Spatiotemporal Fractionation in Radiotherapy

Dissertation

zur

Erlangung der naturwissenschaftlichen Doktorwürde (Dr. sc. nat.)

vorgelegt der

Mathematisch-naturwissenschaftlichen Fakultät

der

Universität Zürich

von

Nathan Torelli

von

Cerentino TI

Promotionskommission

Prof. Dr. Johan Chang
Prof. Dr. Uwe Schneider
Prof. Dr. Martin Pruschy
Prof. Dr. Jan Unkelbach (Vorsitz und Leitung der Dissertation)

Zürich, 2024

Acknowledgements

Many people helped me over these years and I thank all of them!

First of all, I would like to express my sincere gratitude to my advisor, Professor Jan Unkelbach, for his continuous feedback and support. His guidance has had an invaluable impact on my research, and the brainstorming sessions with him were the origin of many fruitful ideas.

I wish to thank Professors Martin Pruschy, Uwe Schneider and Johan Chang for their interest and precious comments.

I am also grateful to Matthias Guckenberger, the chairman of the Department for Radiation Oncology, for allowing me to carry out this research at the University Hospital Zürich.

Many thanks to all the present and past members of the Medical Physics Research Group and the whole team of the Department for Radiation Oncology at the University Hospital Zürich for the countless discussions about work and non-work related topics. I am glad and grateful that we will continue working together.

Finally, I would like to thank my family, my girlfriend and all my friends for their constant encouragement and their unconditional support during these years.

Contents

Abstract

In current clinical practice, radiotherapy treatments are often fractionated, i.e. the total radiation dose is equally divided into small fractions to be delivered daily over a period of few days or weeks. It has recently been shown in silico that spatiotemporal fractionation schemes, i.e. delivering distinct dose distributions in different fractions, can potentially improve the treatment. This is possible if these dose distributions are designed such that different fractions deliver similar doses to normal tissues (i.e. exploit the fractionation effect), but each fraction delivers high single-fraction doses to alternating parts of the tumor (i.e. achieve partial hypofractionation in the tumor). Thereby, the ratio of biological dose in the tumor versus the normal tissue can be improved.

In this project, we further developed this innovative and novel concept. In particular, we focused on:

1. Developing new treatment planning algorithms for spatiotemporal fractionation

2. Identifying potential clinical applications of spatiotemporal fractionation

with the aim of bringing spatiotemporal fractionation towards the design and implementation of a phase I clinical trial.

Spatiotemporal fractionation is associated with higher complexity in treatment planning and delivery. Different plans with distinct dose distributions for different fractions must be designed such that all fractions together deliver the prescribed biological dose to the tumor. To that end, novel mathematical optimization methods for treatment planning have been developed, which are based on the cumulative biological dose rather than the physical dose. In particular, we developed robust treatment planning methods to account for geometric uncertainty in the patient setup and biological uncertainty in the fractionation sensitivity, which may lead to a degradation of the resulting treatment if not accounted for. It was shown that spatiotemporally fractionated treatments can be obtained which are robust against setup errors and

uncertainty in the fractionation sensitivity. At the same time, these robust plans maintain most of their dosimetric benefit over uniformly fractionated plans. Besides liver cancer patients and patients with large arteriovenous malformations, patients with multiple brain metastases were identified to be especially well suited for spatiotemporal fractionation, because of the high accuracy in patient positioning. For theses patients, delivering high doses to different metastases in different fractions allows for fractionation of the normal brain dose in between the metastases while increasing the biological dose within the metastases.

In addition, novel extensions of spatiotemporal fractionation were investigated. Spatiotemporal fractionation has been combined with other degrees of freedom that can be exploited in fractionated radiotherapy treatments, i.e. the combination of different particle types and treatment techniques, and the use of different beam orientations in different fractions. We showed that in the context of combined proton-photon therapy, spatiotemporal fractionation can be used to determine the optimal dose contribution of the proton and photon fractions to the tumor, thereby improving on simple proportional combination of intensity modulated radiotherapy and intensity modulated proton therapy plans. Also, we demonstrated that the quality of spatiotemporally fractionated treatments can be boosted by selecting fraction-specific beam orientations that are beneficial to treat specific regions of the tumor. To that end, a treatment planning algorithm was developed that allows for simultaneous optimization of multiple non-coplanar arc treatments.

Finally, the simultaneous optimization of multiple dose distributions based on the cumulative biological dose is not supported by any commercial treatment planning system. To this end, we implemented a method which allows to import treatment plans optimized using our in-house research treatment planning system into a commercial treatment planning system. Thereby, it is possible to deliver spatiotemporally fractionated treatments in the clinics.

In conclusion, in this dissertation we addressed the main hurdles associated with spatiotemporal fractionation which must be overcome before being clinically implemented. The work performed in this thesis may thus facilitate the design of a clinical phase I trial to investigate the feasibility of spatiotemporal fractionation in the clinics.

Preface

This thesis was carried out at the Department for Radiation Oncology of the University Hospital Zürich and University of Zürich, and was supported by grant Spatiotemporal fractionation in radiotherapy (310030_189285/1) of the Swiss National Science Foundation.

Contributions

This thesis consists of 7 chapters, which describe work that has been either published or submitted as original manuscripts or conference abstracts, or for which a manuscript is in preparation. The main authors' contributions are described in the following.

- **Chapter 2:** This study was conceived by Jan Unkelbach and myself. Dávid Papp contributed to the mathematical formulation of the optimization problem. I implemented the methods and analysed the results.

  This work has been presented as a conference abstract to the "AAPM Annual Meeting 2021" (Optimal Combination of Spatial and Temporal Fractionation for the Treatment of Multiple Brain Metastases. *AAPM ePoster Library.* Torelli N. 07/26/21; 323934; 58590).

- **Chapter 3**: This study was conceived by Jan Unkelbach and myself. The implementation of the methodology, all the computations and the analysis of the results were performed by myself. Dávid Papp and Jan Unkelbach contributed to the interpretation of the results and provided critical feedback to the manuscript that was drafted by me.

  Preliminary work on Chapter 3 has been presented as conference abstracts to the "ESTRO 2021 conference" (PD-0786 Spatiotemporal fractionation schemes for the treatment of multiple brain metastases. N. Torelli, J. Unkelbach. Published in issue: August 2021. S618-S619) and to the "10th edition of the brain metastases research and emerging therapy conference" (A novel spatiotemporal fractination concept

for irradiating multiple brain metastases, Torelli N, Unkelbach J). The latter abstract received the **Best Poster Award**.

The content of Chapter 3 has been published as an original manuscript in *Medical Physics*. (Torelli N, Papp D, and Unkelbach J. Spatiotemporal fractionation schemes for stereotactic radiosurgery of multiple brain metastases. *Med Phys* 2023;50(8):5095-5114. doi:10.1002/mp.16457).

- **Chapter 4:** This study was conceived by Jan Unkelbach and myself. The methodological part was implemented by myself together with Silvia Fabiano.

  A manuscript on the methods developed in this work was published together with Silvia Fabiano in *Physics in Medicine and Biology* in the context of combined proton-photon therapy (Fabiano S, Torelli N, Papp D, and Unkelbach J. A novel stochastic optimization method for handling misalignments of proton and photon doses in combined treatments. *Phys Med Biol.* 2022;67(18):10.1088/1361-6560/ac858f. doi:10.1088/1361-6560/ac858f), to which I contributed to the implementation and interpretation of the results and provided critical feedback.

  The study presented in Chapter 4 applies the same methodology in the context of spatiotemporal fractionation.

- **Chapter 5:** This study was conceived by Jan Unkelbach and myself. I implemented the methods and analyzed the results. This work has not yet been published.

- **Chapter 6:** This study is partly based on Yves Bicker's bachelor thesis, which was conducted under Jan Unkelbach's and my supervision. Jan Unkelbach conceived the idea and I helped to shape the research. I implemented the methodology and Yves Bicker carried out the simulations.

  This work has been presented as a conference abstract to the "SASRO 2022 Annual Meeting" (A novel approach for combined proton-photon therapy of multi-metastatic cancer patients, Torelli N, Bicker Y, Marc L, Fabiano S, Unkelbach J) and a manuscript is in preparation.

- **Chapter 7:** This study was conceived by Jan Unkelbach and myself. The implementation of the methodology, all the computations and the analysis of the results were performed by myself.

An original manuscript has been submitted to *Physics in Medicine and Biology* (Torelli N, Unkelbach J. Fraction-variant radiotherapy treatments: an approach to exploit additional degrees of freedom in radiotherapy planning.).

- **Chapter 8:** This study is partly based on Florian Dietsche's master thesis, which was conducted under Jan Unkelbach's and my supervision. Jan Unkelbach and myself conceived the idea. Florian Dietsche implemented the methodology and I performed the simulations and collected the results.

  This work has not been published yet.

Chapter 1

Introduction

Cancer is the second leading cause of death worldwide [1]. In Switzerland, more than 46'000 new patients were diagnosed with a tumor and more than 17'000 persons died from cancer in 2019 [2]. Due to population aging, environmental factors and better diagnostic tools, the incidence of cancer has been steadily increasing over the past few decades. However, the mortality rate considerably decreased over the same period of time. The implementation of screening programs contributed to detect tumor at the early stages and significant advancements in the treatment of cancer were made.

Besides surgery and chemotherapy, radiotherapy is one of the three main treatment options for cancer patients, with more than half of all tumor patients receiving radiotherapy as part of their treatment [3]. Radiotherapy delivers ionizing radiation to the tumor, which disrupts cancer cells by inducing DNA damage. The energy deposited in the tissue by radiotherapy is quantified by the physical quantity "dose", which has the unit of Gray (1 Gy = 1 J/kg), and can be delivered either from an external or an internal radiation source. The central goal of radiotherapy is to deliver enough radiation dose to the tumor to achieve tumor control, while simultaneously sparing the surrounding normal tissues in order to minimize the risk of serious side effects and preserve the patient's quality of life. The tumor control probability (TCP) and normal tissue complication probability (NTCP) are typically represented as sigmoid curves as a function of the radiation dose (Fig. 1.1). While increasing the dose to the tumor leads to a higher TCP, this will also results in higher normal tissue toxicities, thereby limiting the potential of radiotherapy. The term "therapeutic window" is often used when considering the tradeoff between enhanced radiotherapy efficacy and decreased toxicity.

Radiotherapy achieves a high TPC and a low NTCP via two main concepts: dose conformity and fractionation. Dose conformity means that the dose distribution is precisely shaped to the tumor and dose to sensitive or-

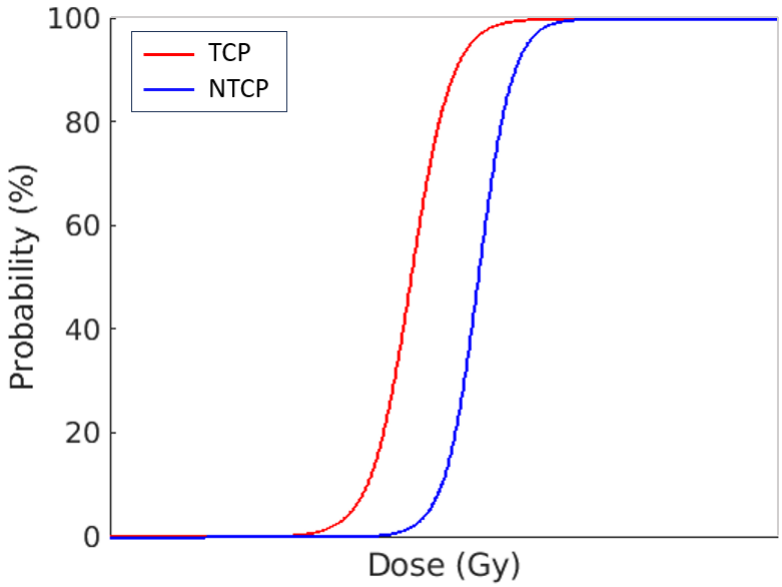

Figure 1.1: *Dose-response curves for the tumor control probability (red) and the normal tissue complication probability (blue).*

gans is minimized. In practice, dose conformity allows to be on different points on the TCP and NTCP curves. The development of intensity modulated radiotherapy (IMRT), which is detailed in the next section, has been a key technological development for achieving this. Fractionation refers to the fact that the total radiation dose is not delivered at once, but is split into many fractions to be delivered daily over a period of few weeks. As it is further discussed in section 1.3, this is motivated by the ability of the normal tissue cells to recover from sub-lethal radiation damage in between fractions. In practice, fractionation moves the TCP and NTCP curves further apart, increasing the therapeutic window.

1.1 Modern radiotherapy techniques

Over the past years, research in medical physics has improved the precision of radiotherapy tremendously. Nowadays, it is possible to shape the radiation dose distribution very precisely to the tumor and minimize the radiation exposure to the surrounding normal tissues. This was rendered possible by the sophistication of the imaging modalities and treatment machines, as well as by the development of new and more advanced radiotherapy techniques.

The most common way of administering radiotherapy is through the use of external radiation sources. Conventional external beam radiotherapy uses

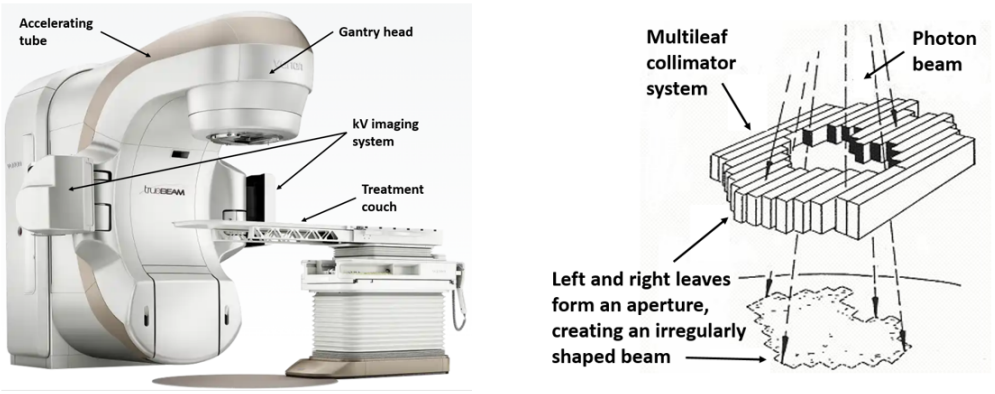

(a) Medical linac (b) Multileaf collimator system

Figure 1.2: *Components of a Linac for photon therapy. The gantry comprises (a) the acceleration tube and the treatment head, and can rotate around the patient that lies on the treatment couch [4]. The imaging system is used for patient positioning verification. The radiation is shaped to the tumor using a multileaf collimator system (b) [5].*

high energy photons (6-20 MV) produced by linear accelerators (Linacs). The main components of a medical linac are shown in Fig. 1.2a, and include an accelerating tube, a gantry head, a treatment couch and imaging systems. In the accelerating tube, electrons are accelerated up to MeV energies and focused on a target (composed by a material with a high atomic number) positioned in the treatment head. Interactions of the electrons with the target produce X-rays through Bremsstrahlung. These X-rays are subsequently precisely shaped to the tumor using a system composed by rectangular collimator jaws and a multileaf collimator (MLC, Fig. 1.2b). Both the accelerating tube and the gantry head are mounted either on a C-arm gantry, ring or robotic treatment unit, which can rotate around the patient to deliver radiation from multiple orientations. Imaging systems are also mounted on the linac and consist of pairs of kV emitters and photon detectors, and can be used to accurately position the patient in each treatment session.

Prior to the development of the MLC, three-dimensional conformal radiotherapy (3D-CRT) was first introduced, which shaped each radiation beam to the projection of the tumor in the beam's eye view by means of patient-specific collimator blocks. Although local and loco-regional could be achieved in many patients with 3D-CRT, limitations arised with irregularly shaped tumors. This led to the development of intensity modulated radiotherapy (IMRT), which marked a milestone in the history of radiotherapy [6]. The defining feature of IMRT is that each of the radiation fluence delivered from

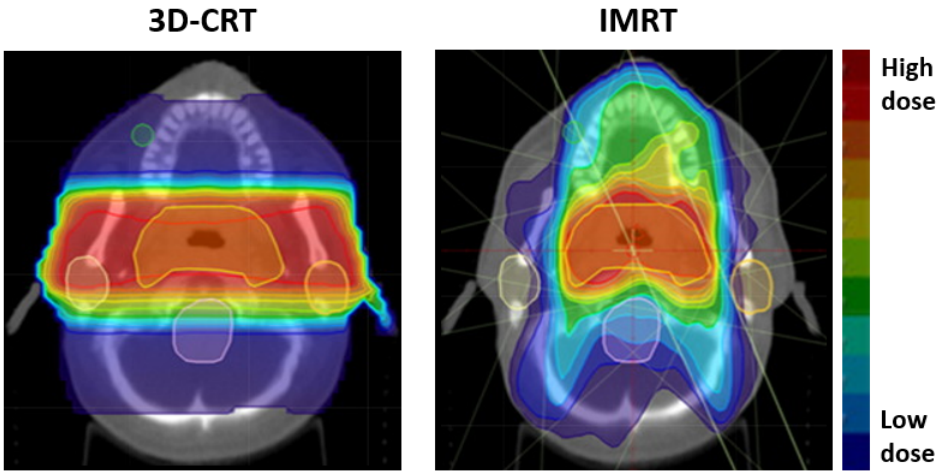

Figure 1.3: *Comparison of dose distributions obtained with 3D-CRT (left) and IMRT (right) [7].*

each beam can be modulated to deliver inhomogeneous dose distributions, using the MLC. This enabled to considerably improve dose conformity compared to 3D-CRT, especially for concave tumors (Fig. 1.3). In order to increase the treatment delivery efficiency, dynamic gantry rotation was further introduced. The resulting volumetric modulated arc therapy (VMAT) has the advantage of considerably decreasing the treatment time compared to IMRT, while maintaining a similar plan quality [8]. IMRT and VMAT are nowadays considered standard of care for many tumor indications.

Latest research investigated novel treatment techniques, which aim to exploit additional degrees of freedom which can be achieved with medical linacs to further improve the quality of radiotherapy plans. For example, the treatment couch can be rotated to increase the set of beam orientations that can be used to treat the tumor and further reduce the dose in the surrounding normal tissue. Also, collimator rotation can be exploited during treatment to achieve better intensity modulation. Treatment techniques such as 4Π radiotherapy [9] and non-coplanar VMAT [10] are currently starting to be used in the clinics and have the potential to further improve dose conformity compared to IMRT and VMAT.

Improvements to dose conformity through technological advances in photon-only treatment techniques seem likely to reach a plateau in the near future [11]. Most of the degrees of freedom to increase the variety of beam directions which can be accessed using current linear accelerators are already exploited by the aforementioned treatment techniques. To overcome this limitation, two ways have been explored recently. On one hand, the plan optimization

is starting to become more biologically oriented, i.e. the radio-sensitivity of tumor and normal tissue is actively included in the treatment objectives. On the other hand, the use of other particle types is being investigated. In that regard, proton therapy was shown to lead to better sparing of the normal tissue and has become established for certain applications [12].

1.2 Treatment plan optimization

Radiotherapy treatment planning refers to the process of determining the best possible treatment plan for every patient that delivers a prescribed dose to the target volume while respecting all dosimetric constraints on the organs-at-risk (OARs) and normal tissue. In this section, we discuss inverse treatment planning for intensity modulated radiotherapy, as opposed to forward planning which has been used in early days to generate 3D-CRT radiotherapy plans. In IMRT planning, each radiation field is discretized into small beam elements (called beamlets), and the intensity of each beamlet is optimized independently. The goal of inverse radiotherapy planning is to determine the optimal beamlets intensities that yield the desired radiation dose to the tumor but minimize the dose to the surrounding OARs [13].

Prior to the optimization of the beamlet's intensities, the target volume and all relevant organs-at-risk (OARs) are delineated, following the applicable guidelines, including the ICRU 50 [14] and ICRU 62 [15] reports (Fig. 1.4). To this end, a computed tomography (CT) scan of the patient is acquired, and the relevant structures are contoured. Other imaging modalities such as magnetic resonance imaging (MRI) or positron-emission tomography (PET) can be used to further improve target volume localization and delineation. First, the gross tumor volume (GTV) is delineated. This represents the tumor mass which is visible on the diagnostic images. However, microscopic disease spread to nearby regions might be present, which is accounted for by adding an extension of the GTV. This is typically referred to as the clinical target volume (CTV) and represents the volume that we want to eradicate with radiotherapy. However, as the tumor might move during treatment (e.g. because of respiratory motion or heart beating), an additional margin is added to the CTV to obtain the internal target volume (ITV). Finally, a margin is applied to compensate for possible uncertainties during the patient positioning, leading to the planning target volume (PTV). Radiotherapy aims to deliver a prescribed dose to the PTV, to ensure that the CTV receives the intended radiation dose, independent of motion and setup uncertainties. To date, the process of target and OARs delineation is performed manually and is very time-consuming. Artificially intelligence technology is being pro-

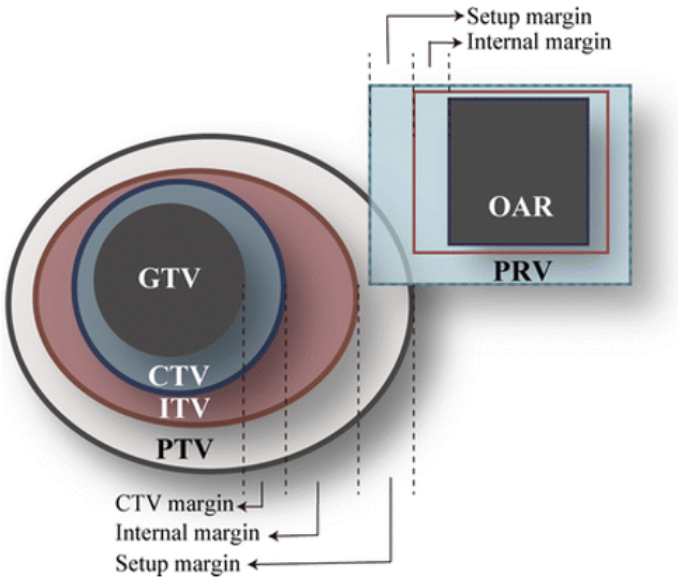

Figure 1.4: *Schematic representation of the main radiotherapy target volumes: the gross tumor volume (GTV), the clinical target volume (CTV), the internal target volume (ITV) and the planning target volume (PTV) [17]. The ITV is obtained from the CTV by adding an internal margin (IM) and the PTV is obtained from the ITV by adding a setup margin (SM). A similar concept can be applied also to organs-at-risk.*

gressively introduced in clinical practice to facilitate auto-delineation of both target volume and OARs [16].

Once all the relevant structures for optimization have been contoured, the dose distribution for each beamlet considered for optimization is calculated. Several dose calculation algorithms can be used, which range from simple pencil beam algorithms [18] to more accurate Monte Carlo methods [19]. These dose distributions are stored in the form of dose-influence matrices D, where each element D_{ij} specifies the dose contribution of beamlet j to voxel i for unit intensity. In this way, the total dose d_i delivered to any voxel i in the patient can be computed as the superposition of all beamlet's dose contributions, scaled by their intensities x_j

$$d_i = \sum_j D_{ij} x_j \tag{1.1}$$

The intensities of each beamlet are subsequently optimized using mathematical optimization algorithms. The clinical goals of achieving a high TCP and a low NTCP are translated into mathematical terms and expressed as

functions to be minimized. Typical objective functions used in radiotherapy planning are piecewise quadratic penalty functions and generalized equivalent uniform dose (gEUD) functions. Quadratic penalty functions are used to penalize doses above or below a certain threshold, and can be expressed as

$$f(\boldsymbol{d}) = \begin{cases} \frac{1}{V_n} \sum_{i=1}^{V_n} (d_i - d_i^{max})_+^2 \\ \frac{1}{V_n} \sum_{i=1}^{V_n} (d_i^{min} - d_i)_+^2 \end{cases} \tag{1.2}$$

For example, quadratic penalty functions are used to ensure that a certain prescribed dose is delivered to any part of the target volume, or to limit the maximum dose to serial OARs. Generalized EUD objectives, instead, can be expressed as

$$f(\boldsymbol{d}) = \left[\frac{1}{V_n} \sum_{i=1}^{V_n} (d_i)^p \right]^{\frac{1}{p}} \tag{1.3}$$

A special form of the gEUD objective is obtained for $p = 1$, and corresponds to the mean dose to a given structure. Mean dose objectives are used to limit the mean dose delivered to parallel OARs.

The optimization problem aims to determine the beamlets intensities which minimize a weighted sum of planning objectives for the target volume and the OARs, and is formulated as

$$\begin{aligned} \underset{\mathbf{x}}{\text{minimize}} \quad & f(\boldsymbol{d}) && && (1.4) \\ \text{subject to} \quad & c_m(\boldsymbol{d}) \leq u_m && \forall m && (1.5) \\ & d_i = \sum_j D_{ij} x_j && \forall i && (1.6) \\ & x_j \geq 0 && \forall j && (1.7) \end{aligned}$$

Depending on the relative weights for the different planning objectives, different, so-called Pareto-optimal plans can be obtained which refer to different tradeoffs between the conflicting goals of delivering a high dose to the target volume and limiting the dose to the surrounding OARs. In clinical practice such tradeoffs are decided on a patient basis, where multiple plans are created and the one with the best tradeoff for a specific situation is selected to be delivered. The quality of a radiotherapy plan is typically evaluated through inspection of the three-dimensional dose distribution, where it is

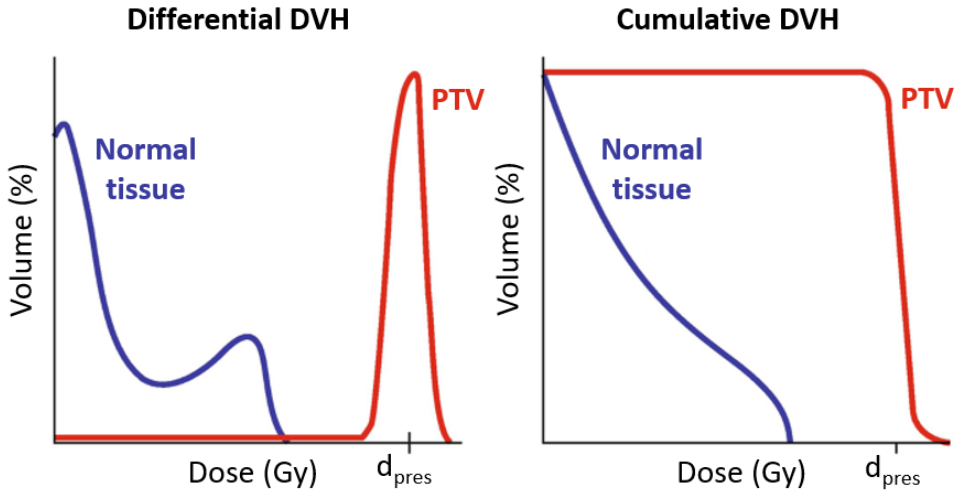

Figure 1.5: *Example of a differential (left) and cumulative (right) dose-volume histogram (DVH) with typical curves for the PTV (red) and the normal tissue (blue).*

checked that the target volume is covered with the intended dose and that the dose in the surrounding normal tissue and OARs is low (i.e. that there are no hot dose spots in unwanted regions). Also, dose-volume histrograms (DVHs) are frequently used, which are easier to interpret (Fig. 1.5).

The optimization problem in Eq. (1.4)-(1.7) is typically referred to as fluence map optimization and results in a set of optimal intensities for each beamlet. To deliver such a plan, fluence maps must be converted into a set of MLC apertures. This can either be achieved using leaf sequencing algorithms, or by directly integrating such machine-specific delivery constraints into the plan optimization. In the latter case, we speak about direct aperture optimization (DAO).

1.3 Fractionation

Besides dose conformity, fractionation is the second major mechanism to limit radiation damage to the normal tissue. Fractionation means that radiotherapy treatments do not deliver the total dose at once, but split the dose over multiple smaller fractions which are delivered daily over a period of 1-6 weeks. This is motivated by the observation that the normal tissue can repair from sublethal radiation damage in between the different fractions, and thereby tolerates a higher total dose. For example, typical maximum tolerated doses by the spinal cord are 10-15 Gy in 1 fraction and 50-60 Gy in 30 fractions

[20]. Tumors have reduced repair mechanisms, but still have some capacity to repair radiation damage and repopulate in between fractions. Therefore, splitting the treatment into more fractions requires that the total radiation dose necessary to maintain the same level of tumor control is increased.

In clinical practice, the biologically effective dose (BED) model is the most widely used concept to describe the fractionation effect and compare different fractionation schemes [21]. The BED model states that the biological dose b is given by

$$b = nd\left(1 + \frac{d}{\alpha/\beta}\right) \tag{1.8}$$

where n is the number of fractions, d is the dose per fraction and α/β is a tissue-specific parameter that quantifies the tissue's sensitivity to fractionation. The idea is that a fixed BED leads to a given clinical effect (e.g. probability of tumor control or normal tissue complication) independent of the number of fractions and the dose per fraction. Hence, for a given α/β value, fractionation schemes with the same BED are assumed to be isoeffective (or isotoxic, respectively). Mathematically, the BED model in Eq. (1.8) describes the clinical observation that a given total dose nd is more effective when the dose per fraction d is large (Fig. 1.6).

Depending on the underlying properties of the tumor and normal tissues, a wide variety of fractionation schemes is used in clinical practice. Traditionally, the majority of the patients are treated with 1.8-2 Gy per fraction, five times per week over a period of 5-6 weeks. However, alternative fractionation schemes such as hyperfractionation or hypofractionation may improve treatment outcomes or reduce the burden of long treatment schedules for patients and health care providers. The BED model has been used to obtain theoretical insight into the optimal fractionation decision, assuming the goal is to minimize the BED in the normal tissue for a given BED prescribed to the tumor [22]. If a dose d_T is delivered to the tumor and a dose d_N is delivered to the normal tissue, it is beneficial to treat the tumor with a large number of fractions if

$$\frac{(\alpha/\beta)_N}{(\alpha/\beta)_T} < \delta \tag{1.9}$$

where $\delta = d_N/d_T$ denotes the ratio between the dose delivered to the normal tissue and the dose delivered to the tumor, whereas $(\alpha/\beta)_N$ and $(\alpha/\beta)_T$ refer to the α/β-ratios of the normal tissue and of the tumor, respectively. Typical values for the α/β-ratio of tumors are 10 Gy or higher [21], whereas normal tissues are mainly characterized by α/β-ratios in the order of 2 Gy (for late-responding tissues) to 10 Gy (for early-reacting tissues) [23].

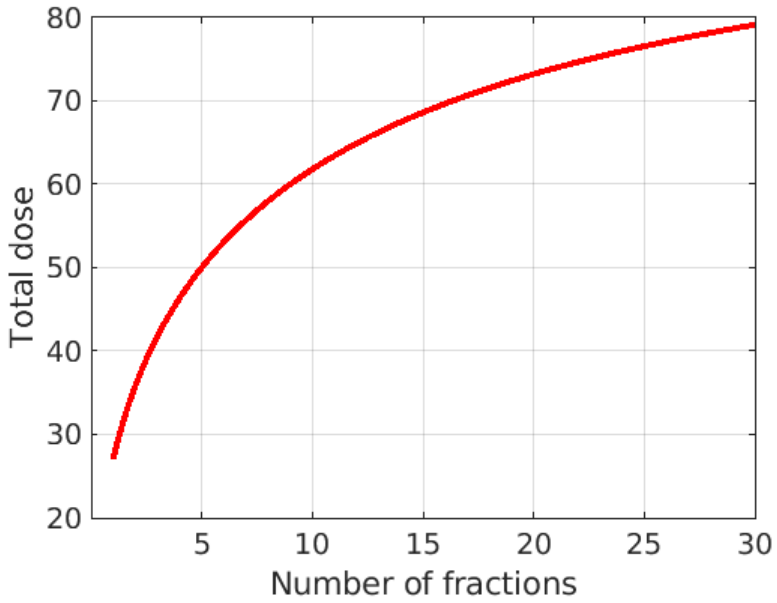

Figure 1.6: *Total physical dose to be delivered in a n-fraction treatment to achieve the same BED as a 5-fraction treatment delivering 10 Gy per fraction, expressed as a function of the number of fractions n. In this example, we assumed $\alpha/\beta = 10$ Gy.*

Thus, the result in Eq. (1.9) provides two justifications for the trend towards hypofractionation that is currently seen in the field of radiation oncology. Due to the improved ability of modern radiotherapy techniques to precisely conform the radiation dose to the tumor and spare the surrounding healthy tissue (thus reducing δ), there has been a trend over the recent years to reduce the number of treatment fractions. Reducing normal tissue dose motivates the use of SRS and SBRT, for example in the treatment of early stage lung cancer [24] or metastatic diseases [25]. In addition, clinical trials have shown that for some tumor, the α/β-ratios are small. This explains the trend towards hypofractionation for prostate cancer [26] and breast cancer [27].

1.4 Spatiotemporal fractionation

Fractionation decisions face tradeoffs between conflicting treatment goals: increasing the number of fractions protects normal tissue; however, this prolongs the total treatment time and requires that the total dose is increased. In that regard, the ideal treatment would fractionate the dose in the normal

tissue (to exploit the fractionation effect), while achieving hypofractionation in the tumor (to reduce the total radiation dose). At first glance, this may appear unattainable. In conventionally fractionated treatments, where the same dose distribution is delivered in every fraction, increasing the dose per fraction to the tumor would also unavoidably increase the dose to the normal tissue. However, it has recently been shown that some degree of hypofractionation in the tumor can be achieved along with near-uniform fractionation in the normal tissue, by delivering distinct dose distributions in different fractions [28-32].

The rationale is illustrated in Fig. 1.7 in the context of arc therapy techniques such as VMAT or tomotherapy. Different dose distributions in distinct fractions can be designed in such a way that each fraction delivers a similar dose bath to the normal tissue surrounding the target volume, thereby achieving the fractionation effect. However, each fraction also delivers a high single-fraction dose to complementary regions of the tumor. Thereby, for a fixed radiation dose, higher biologically effective doses are delivered to the tumor compared to conventional treatments. Since the dose in the surrounding normal tissue is fractionated, this yields a net improvement of the therapeutic ratio.

Treatment planning for spatiotemporal fractionation schemes is performed by simultaneously optimizing treatments for all distinct fractions in a single procedure. This can be done using the same type of objective functions as used in traditional treatment planning, with the only difference that the objective functions are now evaluated for the cumulative BED rather than for the physical dose. In this way, in fact, fractionation effects can be directly incorporated into the treatment plan optimization. The treatment plan optimization problem for spatiotemporal fractionation can then be formulated as

$$\begin{aligned}
\underset{\mathbf{x}_1,\ldots,\mathbf{x}_n}{\text{minimize}} \quad & f(\boldsymbol{b}) && && (1.10)\\
\text{subject to} \quad & c_m(\boldsymbol{b}) \leq u_m && \forall m && (1.11)\\
& b_i = \sum_{t=1}^{n} d_{it}\left(1 + \frac{d_{it}}{(\alpha/\beta)_i}\right) && \forall i && (1.12)\\
& d_{it} = \sum_j D_{ij} x_{jt} && \forall i, \forall t && (1.13)\\
& x_{jt} \geq 0 && \forall j, \forall t && (1.14)
\end{aligned}$$

where d_{it} is the physical dose delivered to voxel i in fraction t. The BED model is generalized to the situation in which different doses can be delivered

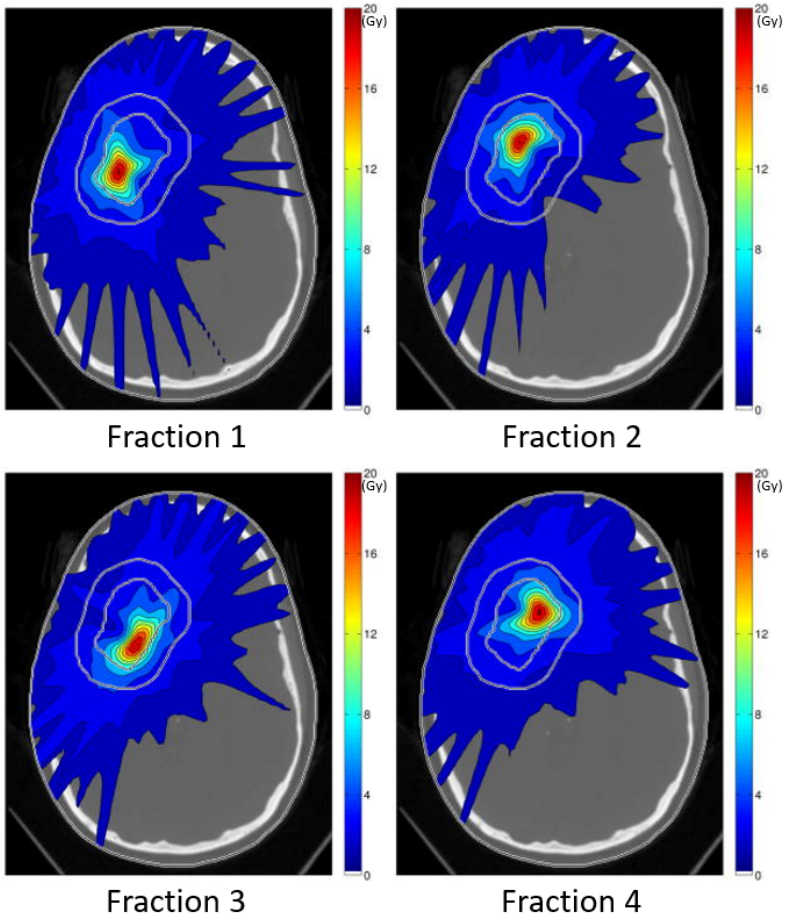

Figure 1.7: *Example of a spatiotemporlly fractionated plan obtained for the treatment of a patient with a large arteriovenus malformation [31].*

in different fractions.

Initial proof-of-principle in-silico planning studies on spatiotemporal fractionation have been performed for large cerebral arteriovenous malformations (AVM) [31], as well as liver tumors [32]. These works showed encouraging results: spatiotemporal fractionation can improve the ratio of tumor to normal tissue BED by approximately 10-20% compared to conventional uniformly fractionated treatments.

1.5 Aim and outline of the thesis

In this thesis, we further develop the innovative and novel concept of spatiotemporal fractionation.

First, we will further develop treatment planning methodology to design spatiotemporally fractionated treatments. Prior work on spatiotemporal fractionation assumed that each fraction will be delivered as planned, such that dose contributions from different fractions add up to the planned cumulative BED in all parts of the target volume. However, some uncertainties in tumor position due to organ motion must be accounted for, despite substantial progress in image guided radiotherapy. A concern is that, as a result of a setup error in one fraction, these dose distributions are shifted relative to each other, potentially causing under-dosing in parts of the tumor. Traditionally, motion uncertainties are accounted for by a margin expansion of the tumor. However, in the context of spatiotemporal fractionation this approach is clearly insufficient. For treatments as illustrated in Fig. 1.7, the target volume is effectively compartmentalized into multiple regions that are treated in different fractions. This compartmentalization occurs automatically during treatment plan optimization and is not manually determined before treatment planning. Therefore, we will develop optimization methods that can incorporate uncertainty directly into treatment plan optimization, resulting in spatiotemporally fractionated treatments which are robust against motion and setup uncertainties. In Chapters 2 and 3, a novel approach to spatiotemporal fractionation is developed for the treatment of patients with multiple brain metastases, where the dose compartmentalization is constrained to follow the anatomical compartmentalization given by the metastases. As each metastasis is defined through an own PTV, robustness against setup errors can be achieved through the traditional safety margin approach. In Chapter 4, a novel efficient stochastic programming method is developed to incorporate setup uncertainties in the optimization of the different fractional dose distributions.

Second, we will develop treatment plan optimization algorithms using extensions of the BED model and methods to incorporate uncertainties in the BED model parameters. All clinical experience is based on delivering the same uniform dose to the entire target volume in every fraction. Therefore, concerns arise about the validity of the standard BED model to accurately describe the response to varying doses per fraction. In particular, there are concerns about the validity of the BED model at very low and very high doses per fraction. Also, there are uncertainties about the BED model parameters to be used (i.e. the α/β-ratio). In Chapter 5, we propose an extension of the BED model which introduces a dose-dependence on the α/β-ratio and can be used to model deviations from the expected biological effect predicted by the standard BED model. Uncertainties in the parameters of the extended BED model are then accounted for during the optimization by stochastic programming methods.

Spatiotemporal fractionation involves varying the dose distribution in between distinct fractions. However, the dose distribution only represents one of the possible degrees of freedom which can be varied in between fractions. For example, different particle types can be utilized in different fractions, or different beam orientations can be used to deliver the plan at each fraction. In Chapter 6, we present a combined proton-photon treatment plan where photon-based plans are delivered in some of the fractions and proton-based plans are delivered in the remaining fractions. Besides exploiting the use of multiple particle types in between different fractions, such a treatment may also broaden the use of proton therapy to a larger population. In Chapter 7, instead, spatiotemporal fractionation optimization is combined with beam orientation optimization. Treatment plans are optimized, where each fraction treats complementary parts of the target volume using fraction-specific beam orientations.

Finally, the optimization of spatiotemporal fractionation schemes is by now only possible in research software. There is no commercial treatment planning system that allows the optimization of multiple dose distributions based on the cumulative BED. For that reason, in Chapter 8 we will develop a treatment planning process that allows to reproduce spatiotemporally fractionated radiotherapy plans generated using a research treatment planning system into a commercial treatment planning system. This will enable the clinical delivery of spatiotemporally fractionated treatments.

Chapter 2

Optimal combination of single-fraction and hypofractionated stereotactic radiosurgery for the treatment of multiple brain metastases

Nathan Torelli[1], Dávid Papp[2], Jan Unkelbach[1]

[1] *Department of Radiation Oncology, University Hospital Zürich and University of Zürich, Switzerland.*
[2] *Department of Mathematics, North Carolina State University, North Carolina, Raleigh, USA.*

2.1 Abstract

Purpose: Stereotactic radiosurgery (SRS) is a standard treatment modality for intracranial metastases. While small lesions are preferably treated in a single fraction, large metastases must be temporally fractionated to reduce brain toxicities. We developed an algorithm that optimally combines single-fraction SRS for some metastases and hypofractionated SRS for other metastases in patients with multiple brain metastases, in an attempt to minimize brain toxicities.
Materials and Methods: For each individual metastasis, a separate non-coplanar VMAT plan is created in the Eclipse treatment planning system (TPS). We then require each metastasis to be either treated to the full dose in one of the fractions or treated uniformly over all fractions. The assignment of each metastasis to one of the fractions or to uniform fractionation is jointly optimized by solving a binary quadratic programming problem, which minimizes the cumulative biologically effective dose BED_2 to the healthy brain, for a fixed tumor BED_{10}. The optimal combination of single-fraction and hypofractionated SRS is investigated for a clinical case consisting of twenty-nine brain metastases of varying sizes to be treated with a BED_{10} of 45 Gy.
Results: By solving the BED-based binary quadratic programming problem, fractionation schemes are obtained which aim to treat small lesions to the full dose in separate fractions to best reduce the integral dose in the brain, while large lesions are temporally fractionated. The fractionation scheme depends on the number of fractions used (the more, the better) and on the planning goals. In particular, reduction of dose-volume objectives for the brain is best achieved through temporal fractionation. For a four-fraction treatment, for example, the resulting fractionation scheme improves on single-fraction SRS by reducing the mean brain BED_2 by 28.1% and the mean BED_2 to a 0.25 cm thick rim structure around the PTV (representing the high dose region) by 15.6%. Compared to a uniformly fractionated 4-fraction SRS treatment, the mean brain BED_2 is reduced by 0.9% for the optimized fractionation scheme, whereas the mean BED_2 to the rim structure slightly increases by 0.4%.
Conclusions: The proposed algorithm allows to combine single-fraction SRS for some metastases and hypofractionated SRS for other metastases, potentially outperforming current state-of-the-art uniform fractionation schemes for the treatment of multiple intracranial metastases. However, the optimization of the fractionation schemes for each individual lesion is performed independently from the optimization of the dose distributions, what may lead to sub-optimal solutions.

2.2 Introduction

Brain metastases are the most common type of brain malignancy, affecting about 10-30% of all cancer patients [33]. Due to better diagnostic modalities and advancements in systemic therapies that enabled cancer patients to live longer, the incidence of brain metastases has been steadily increasing in recent years [34]. In response to this growing issue, current radiotherapy strategies for the treatment of brain metastases have evolved to improve outcomes and minimize radiation-induced toxicities. Whole brain radiotherapy (WBRT), which delivers a prophylactic dose to the entire brain, has been the mainstay of treatment for brain metastases over the past decades. However, WBRT is associated with neurocognitive decline in a large patient population, and has been increasingly replaced by stereotactic radiosurgery (SRS) over the past few years [35]. SRS is a technique which delivers highly focused radiation dose only to the metastatic sites while sparing the surrounding healthy brain, and has reported similar outcomes in terms of local disease control and overall survival as WBRT, but with a reduced risk of neurocognitive impairment [36-40].

Stereotactic radiosurgery is typically delivered either in a single-fraction or fractionated over three to six fractions [41-43]. The selection of the fractionation scheme depends on several factors, including the size and location of the metastases, the patient performance status and other prognostic factors. Single-fraction SRS (SF-SRS) is mainly used to treat small metastases (e.g. with a GTV volume $<$ 3-5 cc), whereas hypofractionated SRS (HF-SRS) is preferred for treating lesions which are large or located close to critical structures, as it allows to better spare the surrounding normal tissue through fractionation. However, while this choice is well motivated for solitary brain metastases, it might not necessarily be optimal for treating patients with multiple brain lesions. In the latter situation, in fact, there may be both small metastases which could benefit from single-fraction SRS and larger lesions that would instead profit from hypofractionated SRS.

In this work, we propose an alternative solution to the fractionation problem for SRS treatments, which consists of jointly optimizing the fractionation scheme for each individual metastasis, while allowing the fractionation scheme for each individual metastasis to be possibly different. By treating different metastases to the full prescribed dose in a single fraction, but distributing the metastases to be treated over different fractions, some degree of fractionation can be achieved in between the different lesions, without the need to increase the total physical dose delivered to the metastases. At the same time, some lesions can be treated uniformly over several fractions to best reduce the brain volume receiving a high dose. A biologically effective

dose (BED) based algorithm is developed which automatically determines what is the optimal fractionation scheme for each metastasis (either SF-SRS or HF-SRS) and optimally assigns metastases to be treated in a single fraction into different fraction groups. This algorithm is demonstrated for a clinical case with twenty-nine brain metastases and compared to both single- and multi-fraction SRS.

2.3 Materials and Methods

2.3.1 Optimization methodology

We consider the situation where a patient with M metastases is treated in a maximum of N fractions. We aim to jointly optimize the fractionation scheme for each individual metastasis in order to minimize the healthy brain toxicities, for a fixed tumor BED. For simplicity and not to overly deviate from current clinical practice, we constrain each lesion to be either treated to the full dose in one single fraction (SF-SRS) or to be treated uniformly over all N fractions (HF-SRS).

Assumption

In this chapter, we assume that treating a metastasis m results in a dose distribution $\mathbf{d}^{(m)}$ which is independent of the dose distributions generated by treating other metastases. This is achieved by creating M separate treatment plans, which irradiate one individual metastasis each. This means that the dose distribution $\mathbf{d}_{tot}$ resulting from treating all metastases $m \in \{1, ..., M\}$ is given by the sum of the dose distributions obtained by treating each metastasis individually:

$$\mathbf{d}_{tot} = \sum_{m=1}^{M} \mathbf{d}^{(m)} \tag{2.1}$$

We can then define the normalized dose distribution $\boldsymbol{\delta}^{(m)}$ in the normal tissue as

$$\boldsymbol{\delta}^{(m)} = \frac{\mathbf{d}^{(m)}}{d_T^{(n)}} \tag{2.2}$$

where $d_T^{(n)}$ denotes the prescribed dose per fraction delivered to metastasis m in a uniformly fractionated n-fraction treatment. We also refer to $\delta_i^{(m)}$ as the

"sparing factor" of voxel i for the dose distribution resulting from treating metastasis m.

BED-based optimization problem

The optimal fractionation scheme for each individual metastasis is then determined by solving the following BED-based optimization problem:

$$\underset{\boldsymbol{x},\ \boldsymbol{y}}{\text{minimize}} \quad f(\boldsymbol{b}) \tag{2.3}$$

$$\text{subject to} \quad b_i = \sum_{f=1}^{N} d_{if} \left(1 + \frac{d_{if}}{(\alpha/\beta)_i}\right) \qquad \forall i \tag{2.4}$$

$$d_{if} = \sum_{m=1}^{M} \left[\left(x_{fm} d_T^{(1)} + y_m d_T^{(N)}\right) \delta_i^{(m)}\right] \qquad \forall i, \forall f \tag{2.5}$$

$$\sum_{f=1}^{N} \left[\left(x_{fm} d_T^{(1)} + y_m d_T^{(N)}\right) + \frac{\left(x_{fm} d_T^{(1)} + y_m d_T^{(N)}\right)^2}{(\alpha/\beta)_T}\right] = b_T^{(m)} \qquad \forall m \tag{2.6}$$

$$x_{fm} \in \{0, 1\} \qquad \forall f, \forall m \tag{2.7}$$

$$y_m \in \{0, 1\} \qquad \forall m \tag{2.8}$$

where $f(\boldsymbol{b})$ is an objective function to be minimized, b_i is the cumulative BED in voxel i and d_{if} is the physical dose delivered to voxel i in fraction f. The optimization variables $x = (x_{fm})_{f\in\{1,\ldots,N\},m\in\{1,\ldots,M\}}$ and $y = (y_m)_{m\in\{1,\ldots,M\}}$ denote whether metastasis m is treated to the full dose $d_T^{(1)}$ in a given fraction f or uniformly over all fractions (with a dose per fraction $d_T^{(N)}$), respectively, where

$$x_{fm} = \begin{cases} 1, & \text{if metastasis } m \text{ is treated to the full dose in fraction } f \\ 0, & \text{otherwise} \end{cases} \tag{2.9}$$

and

$$y_m = \begin{cases} 1, & \text{if metastasis } m \text{ is treated uniformly over all fractions} \\ 0, & \text{otherwise} \end{cases} \tag{2.10}$$

The constraint in Eq. (2.6) requires that every metastasis m is treated to the same cumulative tumor BED $b_T^{(m)}$, independent of the fractionation scheme used.

Binary quadratic programming

Given the binary nature of the optimization variables $\mathbf{x}$ and $\mathbf{y}$, the optimization problem in Eq. (2.3)-(2.8) can be written in the form of a binary quadratic programming problem for an objective function $f(\boldsymbol{b})$ that is linear in the BED. To this end, let's introduce the following notation:

- $\mathbf{z} = \begin{bmatrix} \mathbf{x} \\ \mathbf{y} \end{bmatrix} \in \mathbb{N}^{1\times M(N+1)}$ is the vector of binary optimization variables
- $\mathbf{q}_i = \begin{bmatrix} \mathbf{q}_i^A \\ \mathbf{q}_i^B \end{bmatrix} \in \mathbb{R}^{1\times M(N+1)}$, where
  - $\mathbf{q}_i^A \in \mathbb{R}^{1\times MN}$ with $(\mathbf{q}_i^A)_m = \delta_i^{(m)} d_T^{(1)}$
  - $\mathbf{q}_i^B \in \mathbb{R}^{1\times M}$ with $(\mathbf{q}_i^B)_m = \delta_i^{(m)} d_T^{(N)}$
- $\mathbf{Q}_i = \begin{bmatrix} \mathbf{Q}_i^A & \mathbf{Q}_i^B \\ \mathbf{Q}_i^C & \mathbf{Q}_i^D \end{bmatrix} \in \mathbb{R}^{M(N+1)\times M(N+1)}$, where
  - $\mathbf{Q}_i^A = \mathbf{Q}_i^a \bigoplus \mathbf{Q}_i^a \bigoplus \ldots \bigoplus \mathbf{Q}_i^a \in \mathbb{R}^{MN\times MN}$, where
    - $\mathbf{Q}_i^a \in \mathbb{R}^{M\times M}$ with $(\mathbf{Q}_i^a)_{m_1 m_2} = \frac{\delta_i^{(m_1)}\delta_i^{(m_2)}\left(d_T^{(1)}\right)^2}{(\alpha/\beta)_i}$
  - $\mathbf{Q}_i^B = \begin{bmatrix} \mathbf{Q}_i^b & \mathbf{Q}_i^b & & \mathbf{Q}_i^b \end{bmatrix} \in \mathbb{R}^{M\times MN}$, where
    - $\mathbf{Q}_i^b \in \mathbb{R}^{M\times M}$ with $(\mathbf{Q}_i^b)_{m_1 m_2} = \frac{\delta_i^{(m_1)}\delta_i^{(m_2)} d_T^{(1)} d_T^{(N)}}{(\alpha/\beta)_i}$
  - $\mathbf{Q}_i^C = \left(\mathbf{Q}_i^B\right)^t \in \mathbb{R}^{MN\times M}$
  - $\mathbf{Q}_i^D \in \mathbb{R}^{M\times M}$ with $(\mathbf{Q}_i^D)_{m_1 m_2} = \frac{N\delta_i^{(m_1)}\delta_i^{(m_2)}\left(d_T^{(N)}\right)^2}{(\alpha/\beta)_i}$
- $\mathbf{A} = \begin{bmatrix} \mathbf{I}_{M\times M} & \mathbf{I}_{M\times M} & \ldots & \mathbf{I}_{M\times M} \end{bmatrix} \in \mathbb{N}^{M(N+1)\times M}$, where
  - $\mathbf{I}_{M\times M} \in \mathbb{N}^{M\times M}$ is the identity matrix
- $\mathbf{1}_{1\times M} \in \mathbb{N}^{1\times M}$ is a vector with ones in all entries

The cumulative BED b_i to voxel i in Eq. (2.4) can then be written as:

$$b_i = \mathbf{q}_i^t \mathbf{z} + \mathbf{z}^t \mathbf{Q}_i \mathbf{z} \tag{2.11}$$

Consequently, the optimization problem in Eq. (2.3)-(2.8) can be formulated as follows:

$$\underset{\boldsymbol{z}}{\text{minimize}} \quad \left(f_1(\boldsymbol{q})\right)^t \mathbf{z} + \mathbf{z}^t f_2(\boldsymbol{Q})\mathbf{z} \tag{2.12}$$

$$\text{subject to} \quad \mathbf{A}\mathbf{z} = \mathbf{1}_{1\times M} \tag{2.13}$$

where $f_1 : \mathbb{R}^{1\times M(N+1)} \rightarrow \mathbb{R}^{1\times M(N+1)}$ and $f_2 : \mathbb{R}^{M(N+1)\times M(N+1)} \rightarrow \mathbb{R}^{M(N+1)\times M(N+1)}$ are functions that specify the planning objectives. The linear constraint in Eq. (2.13) requires that each metastasis m is either treated to the full dose in a single fraction or treated uniformly over all fractions (i.e. $\left[\sum_{f=1}^{N} x_{fm}\right] + y_m = 1 \ \forall m$).

Binary quadratic programming problems can be solved efficiently using commercial optimization solvers. In this work, the proposed binary quadratic programming problem in Eq. (2.12)-(2.13) has been implemented in Matlab (The MathWorks Inc., Natick, MA) and solved using the commercial Gurobi optimization software (Gurobi Optimization, LLC). We constrained the optimization time to t=500 s.

2.3.2 Clinical case

We retrospectively investigated the potential benefit of combining single-fraction and hypofractionated SRS for a patient with 29 brain metastases, who has previously been treated with linac-based stereotactic radiosurgery at our institution. The total GTV volume is 14.7 cc (range: 0.1 cc to 9.9 cc) and an isotropic 1.2 mm margin expansion is applied from the GTV to obtain the PTV. The fractionation scheme that has been adopted in the clinical plan aimed to deliver 30 Gy in 6 fractions (6x5 Gy) at the 80% isodose line to each metastasis.

The dose distributions resulting from treating each individual metastasis separately have been generated prior to the optimization of the fractionation scheme using the commercial Eclipse Treatment Planning System v15.6 (Varian Medical Physics, Palo Alto, CA). The selected beam configurations resembled the one used in the clinical plan, and consisted of a full VMAT arc at a couch angle of 0° and three half-arcs from 0° to 180° at couch angles of 45°, 270° and 315°. The HD120 multileaf collimator (Varian Medical Physics, Palo Alto, CA) was used. The following planning objectives have been selected to generate all the dose distributions, i.e.:

1. A physical dose of 30 Gy in 6 fractions was prescribed to the PTV of the selected metastasis, using a piecewise quadratic penalty function (priority = 100). A dose exceeding 37.5 Gy was penalized quadratically (priority = 80).

2. A physical dose of 33.5 Gy was prescribed to the GTV of the selected metastasis, again using a piecewise quadratic penalty function (priority = 100).

3. The mean dose to the brain was minimized (mean dose = 0, priority = 10).

4. The automatic normal tissue objective was used to achieve a good dose conformity (priority = 100).

The VMAT optimization was performed using the Photon Optimizer algorithm (Version 16.1.0), and dose calculation was performed using the Acuros External Beam (Version 16.1.0) algorithm.

Exemplary dose distributions obtained for the treatment of some selected brain metastases, along with dose-volume histograms (DVHs) evaluated for the corresponding PTV and the PTVs of the other metastases, are illustrated in Fig. 2.1. For the selected beam setup and treatment technique, a very steep dose fall off is achieved in the surrounding healthy brain. Consequently, the dose contributions to metastases other than the one treated are very small.

All dose distributions have then been anonymized and exported as DICOM files, together with the corresponding structures set. The normalized dose distributions $\boldsymbol{\delta}^{(m)}$'s have been computed by dividing the dose d_i in each voxel i by $d_T^{(6)} = 30$ Gy, and stored as ".mat"-files in Matlab (The MathWorks Inc., Natick, MA). Masks for the different structures have been obtained using the open-source radiotherapy planning research platform CERR [44].

2.3.3 Assessing the benefit of combining single-fraction and hypofractionated SRS

The fractionation scheme for each individual metastasis has been optimized for the following planning objectives, while constraining each metastasis to receive a BED_{10} of 45 Gy:

1. Minimize the mean BED_2 to the healthy brain (i.e. brain without PTV).

2. Minimize the mean BED_2 to a 0.25 cm thick rim structure around the PTV. This is used to limit the dose in the high dose region, as the

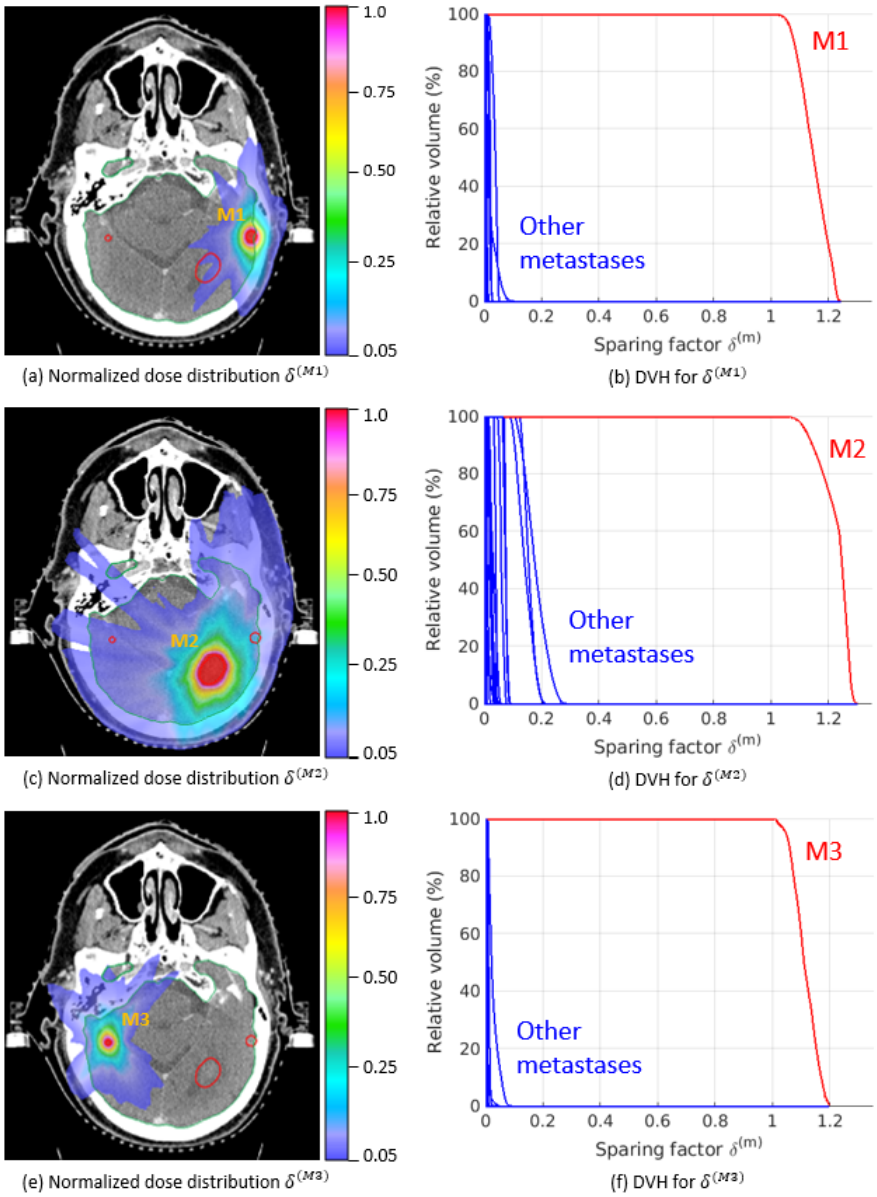

Figure 2.1: *Normalized dose distributions and the corresponding DVHs resulting from treating three selected brain metastases M1, M2 and M3 individually. The DVHs are evaluated for the PTV of the corresponding metastasis (red) and for the PTVs of all other lesions (blue).*

volume of healthy brain exposed to high doses is considered to be a clinically relevant parameter for optimization.

Therefore, the functions f_1 and f_2 in Eq. (2.12) can be expressed as:

$$f_1(\mathbf{q}) = \left[\frac{\omega_1}{|B|}\sum_{i\in B}\mathbf{q}_i\right] + \left[\frac{\omega_2}{|R|}\sum_{j\in R}\mathbf{q}_j\right] \tag{2.14}$$

and

$$f_2(\mathbf{Q}) = \left[\frac{\omega_1}{|B|}\sum_{i\in B}\mathbf{Q}_i\right] + \left[\frac{\omega_2}{|R|}\sum_{j\in R}\mathbf{Q}_j\right] \tag{2.15}$$

where B and R denotes the set of voxels belonging to the healthy brain and to a 0.25 cm thick rim around the PTV, respectively, while ω_1 and ω_2 are the priorities for the objectives 1 and 2 above.

Multiple optimizations have been performed both for different numbers of fractions N and different priorities ω_1 and ω_2, and subsequently compared to both a single-fraction SRS plan and N-fraction uniformly fractionated SRS plans. We optimized the fractionation scheme for values of $N = 2$, $N = 3$, $N = 4$, $N = 5$ and $N = 6$. For each of these cases, 13 different optimization scenarios have been considered with varying objective priorities:

1. $\omega_1 = 100$, $\omega_2 = 1$
2. $\omega_1 = 50$, $\omega_2 = 1$
3. $\omega_1 = 25$, $\omega_2 = 1$
4. $\omega_1 = 10$, $\omega_2 = 1$
5. $\omega_1 = 5$, $\omega_2 = 1$
6. $\omega_1 = 2$, $\omega_2 = 1$
7. $\omega_1 = 1$, $\omega_2 = 1$
8. $\omega_1 = 1$, $\omega_2 = 2$
9. $\omega_1 = 1$, $\omega_2 = 5$
10. $\omega_1 = 1$, $\omega_2 = 10$
11. $\omega_1 = 1$, $\omega_2 = 25$
12. $\omega_1 = 1$, $\omega_2 = 50$
13. $\omega_1 = 1$, $\omega_2 = 100$

Solving the optimization problem in Eq. (2.12)-(2.13) result in a BED_{10} higher than the prescribed BED in some of the metastases due to the dose contribution of multiple dose distributions to the same PTV (see Fig. 2.1). A post-processing step has been performed to obtain SRS plans with a comparable cumulative BED_{10} in all metastases. To this end, we introduce a factor $\boldsymbol{\mu} \in \mathbb{R}^{1\times M(N+1)}$ to up- or down-scale the relative contribution of the dose distributions $\mathbf{d}^{(m)}$, whose entries are optimized such that a given mean cumulative BED_{10} is achieved in each metastasis m. The optimization problem can be formulated as a linear programming problem with quadratic constraints:

$$\begin{aligned}
\underset{\boldsymbol{\mu}}{\text{minimize}} \quad & \mathbf{1}_{M\times 1}\boldsymbol{\mu} && && (2.16)\\
\text{subject to} \quad & \left(\mathbf{1}_{M(N+1)\times 1} - \mathbf{z}\right)^t \boldsymbol{\mu} = 0 && && (2.17)\\
& \mathbf{q}_m^t\boldsymbol{\mu} + \boldsymbol{\mu}^t\mathbf{Q}_m\boldsymbol{\mu} > 0.99c_m && \forall m && (2.18)\\
& \mathbf{q}_m^t\boldsymbol{\mu} + \boldsymbol{\mu}^t\mathbf{Q}_m\boldsymbol{\mu} < 1.01c_m && \forall m && (2.19)
\end{aligned}$$

where

- $\mathbf{q}_m \in \mathbb{R}^{1\times M}$ with $(q_m)_{\tilde{m}} = N\delta^{(\tilde{m})\to(m)}d_T^{(N)}$, where $\delta^{(\tilde{m})\to(m)}$ denotes the mean contribution of the normalized dose distribution $\boldsymbol{\delta}^{(\tilde{m})}$ to metastasis m
- $\mathbf{Q}_m \in \mathbb{R}^{M\times M}$ with $(Q_m)_{m_1m_2} = \frac{N\delta^{(m_1)\to(m)}\delta^{(m_2)\to(m)}\left(d_T^{(N)}\right)^2}{(\alpha/\beta)_T}$
- $c_m \in \mathbb{R}$ is the reference mean cumulative BED_{10} delivered to metastasis m, which in this study was selected to correspond to the mean BED_{10} delivered to metastasis m by the 4-fraction SRS treatment obtained by solving the optimization problem in Eq. (2.12)-(2.13) for the scenario with $\omega_1 = 1$ and $\omega_2 = 1$. The constraints in Eq. (2.18)-(2.19) ensure that the mean BED_{10} in each metastases is close to c_m.

The constraint in Eq. (2.17) ensures that only the dose distributions $\mathbf{d}^{(m)}$ contribute to the fractional dose distribution of fraction f if the corresponding metastases m were selected to be treated in fraction f by solving the binary quadratic programming problem in Eq. (2.12)-(2.13).

The optimization problem with a linear objective and quadratic constraints in Eq. (2.18)-(2.19) has been solved again using the commercial Gurobi optimization software (Gurobi Optimization, LLC). However, the optimization variables were assumed to be continuous real numbers in this latter case.

2.4 Results

2.4.1 Qualitative comparison between different fractionation schedules for a simple situation with $M = 2$ metastases and $N = 2$ fractions

To better understand the potential of both single-fraction and hypofractionated SRS to reduce the brain BED in treatments of patients with multiple brain metastases, we consider a simple situation where $M = 2$ metastases have to be treated in a maximum of $N = 2$ fractions, and compare the following four possible treatment schedules as a function of the sparing factors $\delta_i^{(1)}$ and $\delta_i^{(2)}$ of a voxel i in the healthy brain:

1. *1fx-SRS*: Both metastases are treated to the full dose in fraction 1 (no fractionation).

2. *2fx-SRS*$_{TF}$: Both metastases are treated uniformly in fractions 1 and 2 (temporal fractionation).

3. *2fx-SRS*$_{SF}$: Metastasis 1 is treated to the full dose in fraction 1 and metastasis 2 is treated to the full dose in fraction 2 ("spatial" fractionation).

4. *2fx-SRS*$_{TF+SF}$: Metastasis 1 is treated to the full dose in fraction 1 and metastasis 2 is treated uniformly in both fractions 1 and 2 (temporal and "spatial" fractionation).

Fig. 2.2a shows the difference in BED_2 to voxel i in the healthy brain between *1fx-SRS* and *2fx-SRS*$_{TF}$ as a function of the sparing factors $\delta_i^{(1)}$ and $\delta_i^{(2)}$. Temporally fractionating the dose delivered to the metastases is beneficial if the cumulative physical dose in voxel i is larger than the ratio $\frac{(\alpha/\beta)_B}{(\alpha/\beta)_T}$ of the α/β-values of the healthy brain and target volume (assumed to be 0.2 in this study). The comparison of BED_2 to voxel i in the healthy brain between *1fx-SRS* and *2fx-SRS*$_{SF}$ is shown in Fig. 2.2b. Under the assumption that both metastases have to be treated to the full prescribed dose in a single fraction, it is always beneficial to treat different metastases in different fractions. In such a treatment, every voxel receiving a non-zero dose contribution from both dose distributions experiences a fractionation effect. Fig. 2.2c compares *1fx-SRS* and *2fx-SRS*$_{TF+SF}$, and represents an intermediate solution in between temporal and "spatial" fractionation. Finally, Fig. 2.2d-f illustrate the comparison in brain BED_2 between *2fx-SRS*$_{TF}$ and *2fx-SRS*$_{SF}$,

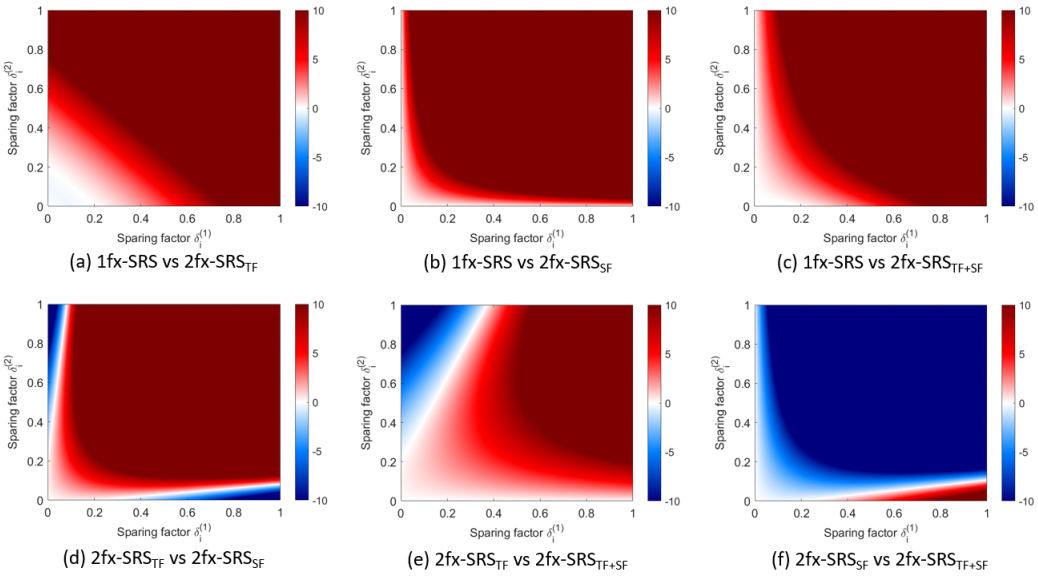

Figure 2.2: *Comparison of difference fractionation schedules as a function of the sparing factors $\delta_i^{(1)}$ and $\delta_i^{(2)}$ of a voxel i in the healthy brain. Differences the brain BED_2 are expressed in unit of Gy.*

2fx-SRS$_{TF}$ and *2fx-SRS$_{TF+SF}$*, and *2fx-SRS$_{SF}$* and *2fx-SRS$_{TF+SF}$*, respectively. In Fig. 2.2d one can observe that, in general, it is beneficial to treat different metastases in separate fractions when the dose contribution of both dose distributions $\mathbf{d}^{(1)}$ and $\mathbf{d}^{(2)}$ to voxel i is large. Uniform fractionation of both metastasis leads to a dosimetric benefit when the dose contribution to voxel i is large for one dose distribution and small for the other one (e.g. in the high dose region close a given metastasis).

2.4.2 Optimal fractionation scheme for a patient with multiple brain metastases

Fig. 2.3 shows the fractional dose distributions obtained for a 4-fraction SRS treatment aiming for the optimal combination of single-fraction and hypofractionated SRS for each individual lesion (for the scenario with $\omega_1 = 1$ and $\omega_2 = 1$), along with the fractional dose distributions for a single-fraction SRS treatment and a 4-fraction uniformly fractionated SRS treatment, respectively. The optimized fractionation scheme aims to treat the very large metastasis (with a PTV volume of 9.9 cc) to the same dose in all fractions, while smaller lesions are treated to the full prescribed dose in one of the fractions. In particular, metastases close to each other tend to be treated in

different fractions to better spare the healthy brain in between the metastases via the fractionation effect. Compared to SRS treatments that treat all the metastases either to the full dose in a single fraction or to the same uniform dose in all fractions, the combination of single-fraction and hypofractionated SRS can reduce the integral brain BED_2, as also illustrated in Fig. 2.4. The mean brain BED_2 is reduced from 29.2 Gy to 21.0 Gy (-28.1%) and the mean BED_2 to the 0.25 cm thick rim around the metastases is reduced from 181.6 Gy to 153.3 Gy (-15.6%) using the optimized fractionation scheme compared to single-fraction SRS. Compared to the 4-fraction uniformly fractionated SRS treatment, the optimized fractionation scheme reduces the mean brain BED_2 by 0.9% (21.0 Gy vs 21.2 Gy), while the mean BED_2 to the 0.25 cm thick rim around the metastases slightly increases by 0.4% (153.3 Gy vs 152.8 Gy). As very well illustrated in Fig. 2.4c, temporally fractionating the doses delivered to a metastasis is beneficial to reduce the biological dose in the high dose region close to the metastasis.

Similar results are also obtained for different weightings of the objective functions and different number of fractions, as illustrated in Fig. 2.5. In general, by increasing the number of fractions, a better sparing of the healthy brain can be achieved. In fact, this allows to distribute the metastases to be treated to the full prescribed dose in a single fraction over more fractions (thereby fractionating even further the dose in between the different lesions), and to achieve a better temporal fractionation of the large metastases. Also, the optimal fractionation scheme varies depending on whether it is more important to reduce the mean brain BED_2 or the BED_2 in the high dose regions close to the metastases. In the latter case, it is more promising to temporally fractionate some of the lesions, whereas the mean brain BED_2 is mostly reduced by treating different metastases to the full dose in distinct fractions. Further details on the different optimized fractionation schemes are reported in the Supplementary material, Appendix A.

2.5 Discussion

The optimal fractionation scheme for stereotactic radiosurgery of multiple brain metastases involves the accurate balance between the delivery of a high single-fraction dose to small lesions and temporal fractionation of the larger metastases. In this study, we developed an optimization approach which allows to minimize the biological dose to the healthy brain by optimally sorting metastases to be either treated to the full prescribed dose in one of the fractions or to be uniformly treated over all fractions. Compared to both single-fraction SRS and uniformly fractionated SRS which are currently

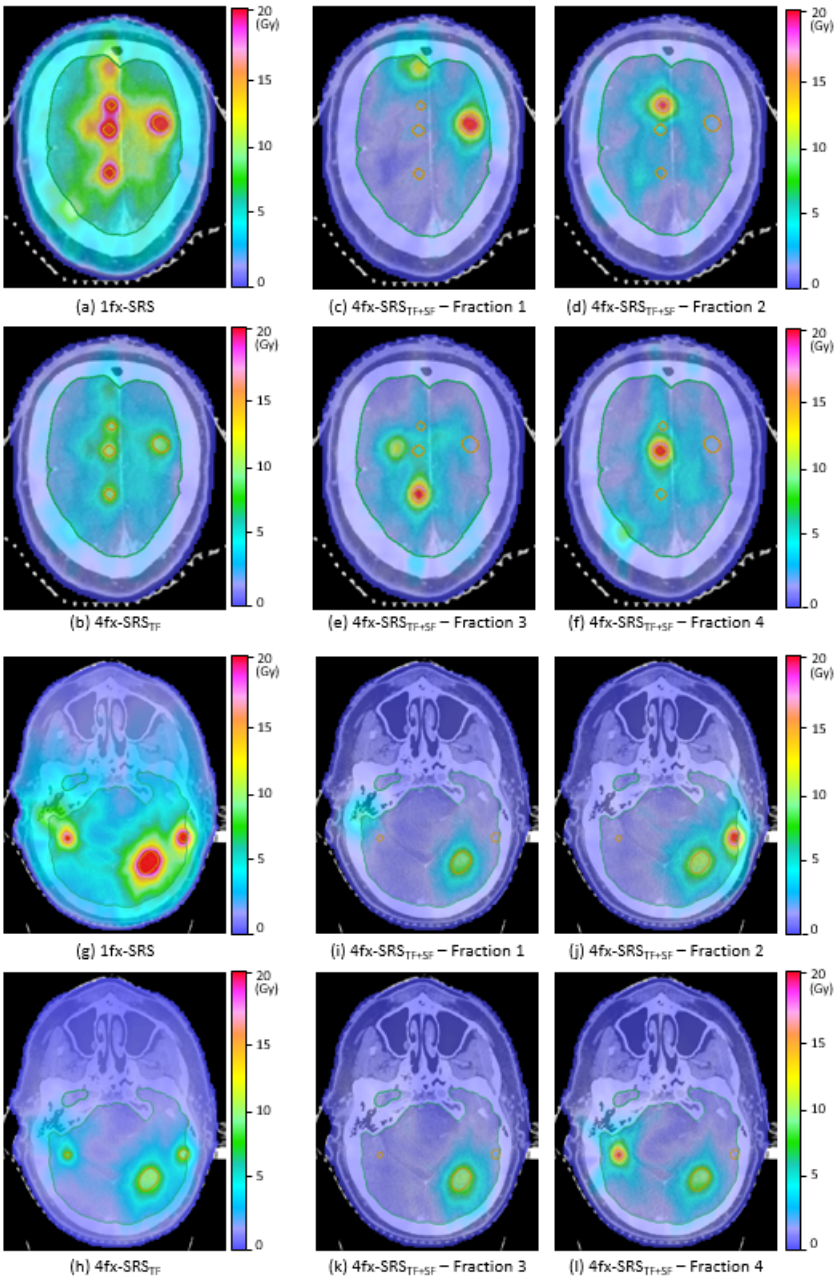

Figure 2.3: *Fractional dose distributions for two different transversal slices for (a)/(g) the single-fraction SRS plan, (b)/(h) the uniformly fractionated 4-fraction SRS plan and (c)-(f)/(i)-(l) the 4-fraction plan combining single-fraction and hypofractionated SRS.*

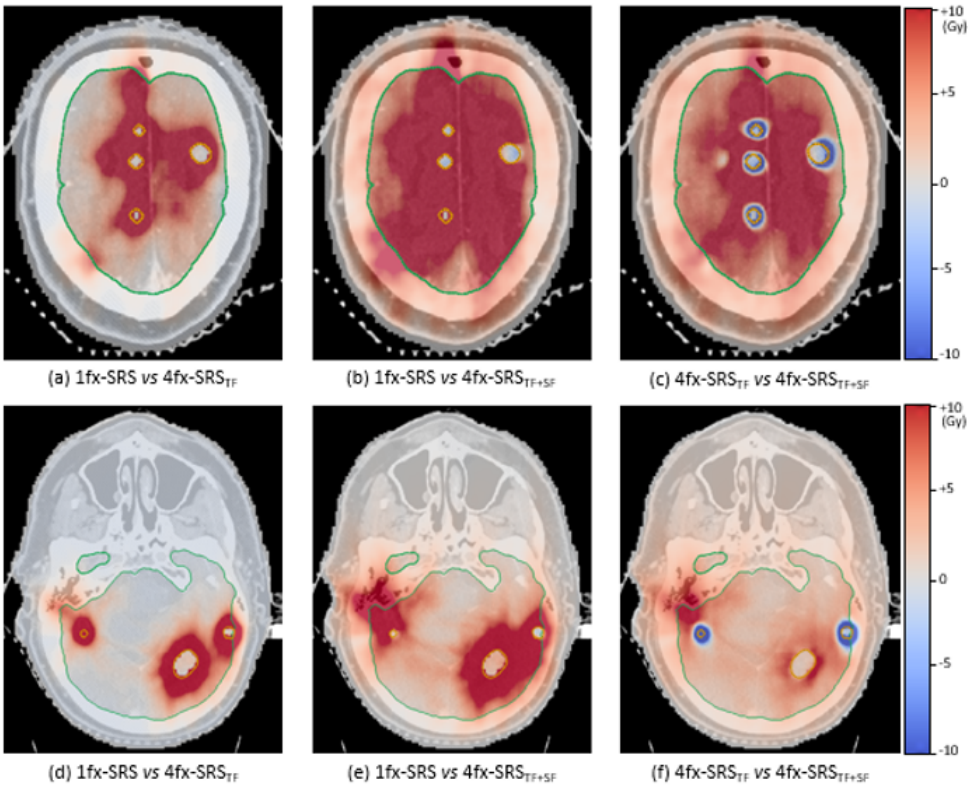

Figure 2.4: *Differences in the cumulative BED distribution for two different transversal slices between (a)/(d) the single-fraction SRS plan and the uniformly fractionated 4-fraction SRS plan, (b)/(e) the single-fraction SRS plan and the optimized SRS plan, and (c)/(f) the uniformly fractionated 4-fraction SRS plan and the optimized SRS plan, respectively.*

used in clinical practice, such an optimal combination of single-fraction and hypofractionate SRS was demonstrated to potentially reduce the biological dose to the healthy brain. In addition, also the delivery time of SRS treatments may be reduced when only a subset of the metastases is treated in every fraction.

Similar approaches aiming to irradiate different subsets of brain metastases in different fractions have already been proposed in the literature [45-47]. In those studies, each lesion was forced to receive the full prescribed dose in a single fraction. In this work, we extend such methods by jointly optimizing the fractionation scheme for all metastases based on the cumulative BED distribution in the healthy brain, while allowing for the fractionation scheme for the individual lesions to be flexible. In this way, not all metastases are treated to the full dose in a single fraction, but a metastasis-specific

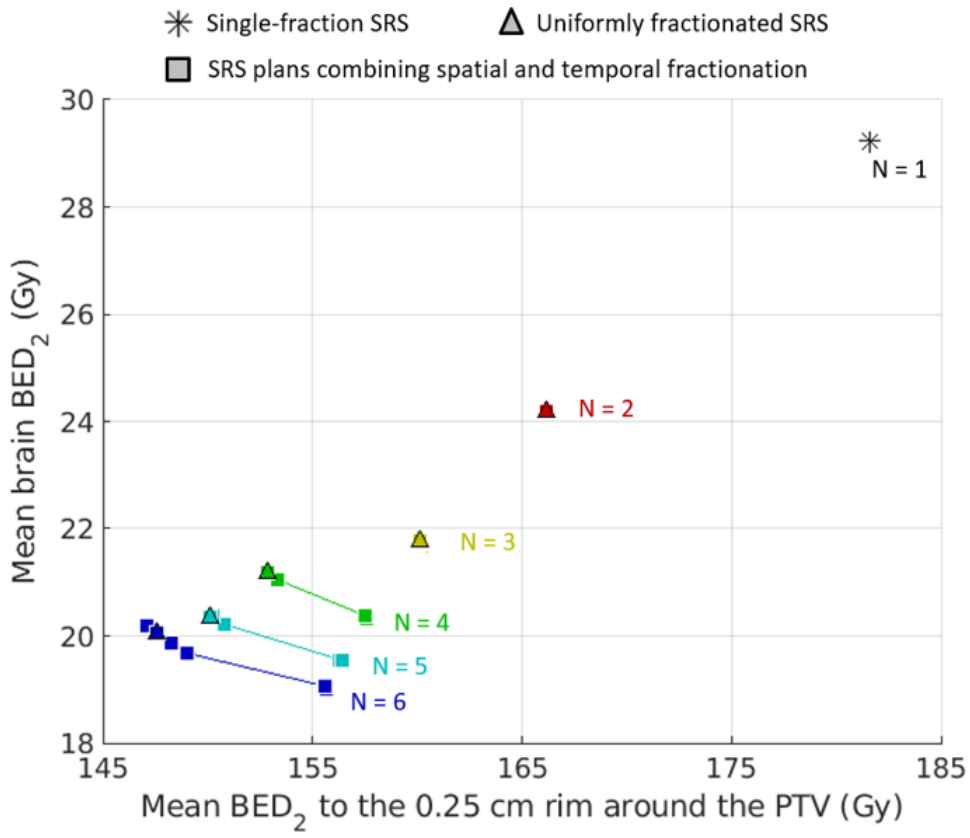

Figure 2.5: *Dosimetric results obtained for the mean brain BED_2 and the mean BED_2 to the 0.25 cm thick rim structure around the PTV for the single-fractions SRS plan, the uniformly fractionated SRS plans and the SRS combining single-fraction and hypofractionate SRS of the metastases for different values of N. For the optimized SRS plans, several results obtained by varying the priorities for the objectives are shown (straight lines connecting the different optimal solutions are only used as visual help and are not associated with any result).*

fractionation scheme is optimized depending on the lesion size and its location relative to other metastases and organs at risk. The ability to uniformly fractionate the dose delivered to some of the lesions is particularly beneficial for metastases which are large or located close to critical structures, as this allows fulfilling dose-volume constraints for the brain in the high dose region.

We could show that the optimized fractionation schemes suggested here improve on a single fraction SRS treatment that irradiates all metastases in the same single fraction. However, the improvement over uniformly frac-

tionated treatments were small. This may be due to one key limitation of the approach presented so far. The main limitation of this work relates to the sequential approach taken here, which separates the optimization of the incident fluence from the optimization of the fractionation scheme. In the first step, separate dose distributions are optimized for individual metastases independently of each other because it is still undetermined which metastases are treated in the same fraction. In the second step, the fractionation scheme is determined, taken fixed dose distributions as input. The incidental dose that the treatment of one metastasis delivers to another metastasis is neither taken into account when creating the dose distributions $d^{(m)}$ nor when solving the binary quadratic problem for determining the fractionation scheme. Although very steep dose gradients can be achieved in current clinical practice using stereotactic radiosurgery, the optimal dose distribution for the treatment of multiple metastases might be different from the sum of the dose distributions obtained by treating each metastasis individually. In particular, the same aperture or beam can be used to deliver dose to more than one lesion. Using the algorithm proposed in this study, in fact, metastases which are located close to each other tend to be treated in different fractions to better spare the healthy brain in between the lesions through fractionation. However, if two metastases are very close to each other, treating one lesion will unavoidably result in a given amount of dose delivered to the adjacent metastasis. With the current algorithm, this dose contribution is not accounted for. In addition, the integral dose might also be distributed differently when a dose distribution is optimized for the treatment of multiple lesions simultaneously, in order not to accumulate dose on the same region of the brain.

An approach to improve on the optimization algorithm presented here, which considers the simultaneous optimization of the dose distribution along with the fractionation scheme and which does not necessarily constrain the fractionation schemes to either deliver the full prescribed dose in a single fraction or an equally divided dose in all fractions to the metastases, is presented in Chapter 3.

2.6 Conclusion

An algorithm to optimize the fractionation scheme in patients with multiple brain lesions has been developed and demonstrated. The algorithm allows different fractionation schemes in individual metastases and optimally assigns metastases to different fractions. The optimal fractionation scheme aims to treat small metastases to the full dose in different fractions, thereby reducing

the physical dose needed for tumor control while still achieving a fractionation effect in between the metastases, whereas large lesions are temporally fractionated to better fulfill the dose-volume constraints for the brain in the high dose region.

2.7 Supplementary material

Appendix A Detailed fractionation schemes

In this section, we detail the fractionation schemes obtained using different weigths for the planning objectives 1 and 2. In Tables 2A.1- 2A.5, it is reported how the different metastases are distributed over the different fractions to be treated to the full dose or assigned to uniform fractionation, respectively, for each of the optimized fractionation scheme. Metastases which are treated to the full dose in a single fraction are quite evenly distributed over the different fractions. While for a small number of fractions all metastases are treated to the full dose in one of the fractions, by increasing the number of fractions more metastases are temporally fractionated over all fractions.

Table 2A.1: *Characteristics of the optimized fractionation schemes obtained for N=2.*

N	Objective weights		Number of metastases treated to the full dose in a single fraction						Number of metastases treated to the same dose in all fractions
	ω_1	ω_2	Fx 1	Fx 2	Fx 3	Fx 4	Fx 5	Fx 6	
2	100	1	16	13	-	-	-	-	0
	50	1	16	13	-	-	-	-	0
	25	1	16	13	-	-	-	-	0
	10	1	15	14	-	-	-	-	0
	5	1	15	14	-	-	-	-	0
	2	1	15	14	-	-	-	-	0
	1	1	15	14	-	-	-	-	0
	1	2	15	14	-	-	-	-	0
	1	5	15	14	-	-	-	-	0
	1	10	15	14	-	-	-	-	0
	1	25	15	14	-	-	-	-	0
	1	50	15	14	-	-	-	-	0
	1	100	15	14	-	-	-	-	0

Table 2A.2: *Characteristics of the optimized fractionation schemes obtained for N=3.*

N	Objective weights		Number of metastases treated to the full dose in a single fraction						Number of metastases treated to the same dose in all fractions
	ω_1	ω_2	Fx 1	Fx 2	Fx 3	Fx 4	Fx 5	Fx 6	
3	100	1	11	10	8	-	-	-	0
	50	1	11	10	8	-	-	-	0
	25	1	12	10	7	-	-	-	0
	10	1	11	11	7	-	-	-	0
	5	1	11	11	7	-	-	-	0
	2	1	13	9	7	-	-	-	0
	1	1	13	9	7	-	-	-	0
	1	2	12	9	8	-	-	-	0
	1	5	12	9	8	-	-	-	0
	1	10	13	9	7	-	-	-	0
	1	25	12	9	8	-	-	-	0
	1	50	13	9	7	-	-	-	0
	1	100	12	9	8	-	-	-	0

Table 2A.3: *Characteristics of the optimized fractionation schemes obtained for N=4.*

N	Objective weights		Number of metastases treated to the full dose in a single fraction						Number of metastases treated to the same dose in all fractions
	ω_1	ω_2	Fx 1	Fx 2	Fx 3	Fx 4	Fx 5	Fx 6	
4	100	1	8	7	7	7	-	-	0
	50	1	8	7	7	7	-	-	0
	25	1	8	8	7	6	-	-	0
	10	1	8	8	7	6	-	-	0
	5	1	8	8	7	6	-	-	0
	2	1	8	8	7	5	-	-	1
	1	1	8	8	7	5	-	-	1
	1	2	8	8	7	4	-	-	2
	1	5	8	8	7	4	-	-	2
	1	10	8	8	7	4	-	-	2
	1	25	8	8	7	4	-	-	2
	1	50	8	8	7	4	-	-	2
	1	100	8	8	7	4	-	-	2

Table 2A.4: *Characteristics of the optimized fractionation schemes obtained for N=5.*

N	Objective weights		Number of metastases treated to the full dose in a single fraction						Number of metastases treated to the same dose in all fractions
	ω_1	ω_2	Fx 1	Fx 2	Fx 3	Fx 4	Fx 5	Fx 6	
5	100	1	8	7	5	5	4	-	0
	50	1	8	7	5	5	4	-	0
	25	1	7	6	6	5	5	-	0
	10	1	7	6	6	5	5	-	0
	5	1	7	7	6	5	4	-	0
	2	1	7	6	6	5	4	-	1
	1	1	7	6	6	5	4	-	1
	1	2	6	6	6	5	4	-	2
	1	5	6	6	6	5	4	-	2
	1	10	6	6	6	5	4	-	2
	1	25	6	6	6	5	4	-	2
	1	50	6	6	6	5	4	-	2
	1	100	6	6	6	5	4	-	2

Table 2A.5: *Characteristics of the optimized fractionation schemes obtained for N=6.*

N	Objective weights		Number of metastases treated to the full dose in a single fraction						Number of metastases treated to the same dose in all fractions
	ω_1	ω_2	Fx 1	Fx 2	Fx 3	Fx 4	Fx 5	Fx 6	
6	100	1	6	5	5	5	4	4	0
	50	1	6	5	5	5	4	4	0
	25	1	6	5	5	5	4	4	0
	10	1	7	6	5	4	4	3	0
	5	1	6	6	5	4	4	3	1
	2	1	5	5	5	5	5	3	1
	1	1	6	5	5	4	4	3	2
	1	2	6	5	5	4	4	3	2
	1	5	5	5	5	4	4	3	3
	1	10	5	5	5	4	4	3	3
	1	25	5	5	5	4	3	3	4
	1	50	5	5	5	4	4	3	3
	1	100	5	5	5	4	4	3	3

Chapter 3

Spatiotemporal fractionation schemes for stereotactic radiosurgery of multiple brain metastases

Nathan Torelli[1], Dávid Papp[2], Jan Unkelbach[1]

[1] *Department of Radiation Oncology, University Hospital Zürich and University of Zürich, Switzerland.*
[2] *Department of Mathematics, North Carolina State University, North Carolina, Raleigh, USA.*

This work has been published in *Medical Physics*

Torelli N, Papp D, Unkelbach J. Spatiotemporal fractionation schemes for stereotactic radiosurgery of multiple brain metastases. Med Phys. 2023;50(8):5095-5114. doi:10.1002/mp.16457

3.1 Abstract

Background: Stereotactic radiosurgery (SRS) is an established treatment for patients with brain metastases (BMs). However, damage to the healthy brain may limit the tumor dose for patients with multiple lesions.
Purpose: In this study, we investigate the potential of spatiotemporal fractionation schemes to reduce the biological dose received by the healthy brain in SRS of multiple BMs, and also demonstrate a novel concept of spatiotemporal fractionation for polymetastatic cancer patients that faces less hurdles for clinical implementation.
Methods: Spatiotemporal fractionation (STF) schemes aim at partial hypofractionation in the metastases along with more uniform fractionation in the healthy brain. This is achieved by delivering distinct dose distributions in different fractions, which are designed based on their cumulative biologically effective dose ($BED_{\alpha/\beta}$) such that each fraction contributes with high doses to complementary parts of target volume, while similar dose baths are delivered to the normal tissue. For patients with multiple brain metastases, a novel constrained approach to spatiotemporal fractionation (cSTF) is proposed, which is more robust against setup and biological uncertainties. The approach aims at irradiating entire metastases with possibly different doses, but spatially similar dose distributions in every fraction, where the optimal dose contribution of every fraction to each metastasis is determined using a new planning objective to be added to the BED-based treatment plan optimization problem. The benefits of spatiotemporal fractionation schemes are evaluated for three patients, each with >25 BMs.
Results: For the same tumor BED_{10} and the same brain volume exposed to high doses in all plans, the mean brain BED_2 can be reduced compared to uniformly fractionated plans by 9-12% with the cSTF plans and by 13-19% with the STF plans. In contrast to the STF plans, the cSTF plans avoid partial irradiation of the individual metastases and are less sensitive to misalignments of the fractional dose distributions when setup errors occur.
Conclusions: Spatiotemporal fractionation schemes represent an approach to lower the biological dose to the healthy brain in SRS-based treatments of multiple BMs. Although cSTF cannot achieve the full BED reduction of STF, it improves on uniform fractionation and is more robust against both setup errors and biological uncertainties related to partial tumor irradiation.

3.2 Introduction

3.2.1 Stereotactic radiosurgery for the treatment of multiple brain metastases

Stereotactic radiosurgery (SRS) has emerged as an established treatment option for patients with a limited number of brain metastases [48,49]. Compared to whole brain radiotherapy (WBRT), which has been the mainstay of treatment for brain metastases over the past few decades, SRS leads to similar outcomes in terms of local disease control and overall survival, but with a reduced risk of neurocognitive impairment [36-40]. Consequently, the use of WBRT is being increasingly replaced by SRS in patients with favorable prognostic factors [35].

The role of SRS in the management of patients with multiple brain metastases is still controversial [50-52]. Major concerns are the prolonged treatment duration and the large integral dose delivered to the healthy brain associated with the concurrent treatment of multiple lesions [53,54]. While recent advances in dose delivery techniques have enabled the efficient treatment of multiple targets using SRS [55], it would be highly desirable to limit the radiation-induced damage to the brain in order to expand the indications for SRS to include selected patients with multiple brain metastases. The volume of brain exposed to high doses is widely considered the most relevant dosimetric parameter [56,57]. However, because of the higher risk of distant brain failure when WBRT is omitted, brain metastases patients must often undergo multiple courses of SRS [58]. In this clinical scenario, it may also be of fundamental importance to minimize the integral brain dose in order to lower the risk of complications after repeated courses of SRS.

3.2.2 Spatiotemporal fractionation schemes

There is a lack of consensus regarding the optimal fractionation scheme for the treatment of brain metastases, with several recent clinical studies reporting similar toxicity levels in the healthy brain between single- and multi-fraction SRS [41-43]. Increasing the number of fractions is beneficial to improve the brain tolerance to high doses. However, the total physical dose must be increased to maintain tumor control [59], and thereby the integral biologically effective dose (BED) delivered to the healthy brain is only slightly affected by the fractionation regimen. In that regard, it would be ideal to simultaneously achieve fractionation in the healthy brain and deliver high single fraction doses to the metastases.

As it has recently been shown for other treatment sites, such a goal can

partly be achieved by delivering non-uniform dose distributions in distinct fractions, in which each fraction contributes with a high dose to complementary parts of the target volume while a similar dose bath is delivered to the surrounding normal tissue. This concept has been named spatiotemporal fractionation and has been demonstrated in in-silico studies to improve the therapeutic ratio compared to conventional uniform fractionation using both proton [28,29] and rotational photon therapy [30-32].

While spatiotemporal fractionation schemes may provide a valuable treatment approach for reducing the integral brain BED in patients with multiple brain metastases treated with SRS, biological and geometrical uncertainties represent a substantial hurdle for clinical implementation. Clinical experience is based on treating an entire lesion in each fraction and the biological effect of irradiating different parts of a lesion in different fractions is unknown. In addition, setup and motion uncertainties represent more of a concern for the accurate delivery of spatiotemporally fractionated plans compared to treatments that deliver the same uniform dose to the target volume in every fraction. If different regions of each individual metastasis are targeted with high doses in distinct fractions, setup and motion errors may lead to misalignments of the dose contributions of the different fractions, causing target underdosage and compromising tumor control. The target compartmentalization is automatically determined in a BED-based treatment plan optimization and is not known a priori. Hence, geometrical uncertainties cannot be accounted for by using margins around the treated volume as in conventional clinical practice.

In the context of polymetastatic diseases, we propose a constrained approach to spatiotemporal fractionation that addresses these issues. The approach forces each fraction to treat the entire volume of a metastasis and avoids partial irradiation of a lesion. However, the approach allows different metastases to be treated to large doses in different fractions. Thereby, the total physical dose needed to control the metastases can be reduced while some degree of fractionation is achieved in the normal tissue in between the metastases, maintaining parts of the benefit of spatiotemporal fractionation. Such a constrained approach to spatiotemporal fractionation is more robust against setup and motion uncertainties than the original approach to spatiotemporal fractionation, because it avoids steep dose gradients within a metastasis in the dose contributions of individual fractions. In addition, the approach yields dose distributions that are more similar to current clinical practice and reduces the biological uncertainties related to partial tumor irradiation. In summary, the constrained approach to spatiotemporal fractionation may face lower hurdles for clinical implementation.

Main contributions of this paper

In this work, we make three main contributions to research on spatiotemporal fractionation. First, we demonstrate the potential of spatiotemporal fractionation schemes for reducing the integral brain BED in SRS-based treatments of patients with multiple brain metastases. This may expand the indications for SRS to include selected patients with multiple brain metastases. Second, we present a conceptual extension of spatiotemporal fractionation and further methodology development by introducing a novel constrained approach to spatiotemporal fractionation, that is applicable to polymetastatic cancer patients. Here, the compartmentalization of the target volume follows the anatomical target compartmentalization defined by each individual metastasis, leading to spatiotemporally fractionated treatments that are more robust against setup and biological uncertainties. Third, by simultaneously optimizing multiple spatial dose distributions and allowing for non-stationary fractionation scheme for individual lesions, we extend on previous studies that aimed to determine the optimal fractionation schedule given a single spatial dose distribution [22,60-32].

3.3 Methods

3.3.1 Planning of spatiotemporally fractionated treatments

Spatiotemporally fractionated treatments are obtained by simultaneously optimizing multiple dose distributions to be delivered in different fractions. In this work, we consider two different approaches to spatiotemporal fractionation, which differ in the way the dose is distributed within the target volume.

Original (unconstrained) approach to spatiotemporal fractionation

The first approach mimics previous studies on spatiotemporal fractionation [29-32]. The target volume, as well as each individual metastasis, can be arbitrarily compartmentalized into distinct regions to be irradiated in different fractions. The optimal dose distributions for each fraction are automatically generated by solving a BED-based treatment plan optimization problem, aiming for the best possible trade-off between hypofractionation in the target volume and more uniform fractionation in the healthy tissue. Such an optimization problem, which is further detailed in the work of Unkelbach et al [31], directly accounts for the fractionation effects by evaluating the planning

objectives and constraints for the cumulative BED $b_i = \sum_{t=1}^{n} d_{it} \left(1 + \frac{d_{it}}{(\alpha/\beta)_i}\right)$ rather than the physical dose. Here, $(\alpha/\beta)_i$ is the α/β-ratio of voxel i, n is the total number of fractions, and $d_{it} = \sum_j D_{ij} x_{jt}$ is the physical dose delivered to voxel i in fraction t (where D_{ij} is the dose-influence matrix term describing the dose contribution of beamlet j to voxel i per unit intensity and x_{jt} is the intensity of beamlet j in fraction t).

Constrained approach to spatiotemporal fractionation

The second approach is specific to patients presenting with polymetastatic diseases. Here, all fractions are restricted to deliver similar (but not necessarily homogeneous) spatial dose distributions within each lesion, to avoid that different parts of the same lesion are treated in different fractions. However, the dose contribution of each fraction to every metastasis can be freely decided to best achieve the desired dosimetric goals. The optimal fractionation scheme for this constrained approach to spatiotemporal fractionation is determined by means of a new planning objective, which is defined as

$$f_{cSTF}(\mathbf{b}, \boldsymbol{\delta}) = \sum_{m=1}^{M} \sum_{t=1}^{n} \sum_{i \in PTV_m} \left[\frac{1}{|PTV_m|} \left(b_{it} - \delta_{mt} \left(\sum_{t=1}^{n} b_{it} \right) \right)^2 \right] \tag{3.1}$$

Here, PTV_m is the set of voxels belonging to metastasis m and M is the total number of metastases. The variables δ_{mt} represent the partial BED contribution of fraction t to metastasis m, and are introduced as additional optimization variables that are determined through the optimization algorithm along with incident beamlet intensities $\mathbf{x}$.

The motivation and intuition behind this objective are as follows. Let us consider the contribution of fraction t and metastasis m to the value of f_{cSTF}. For a given value of δ_{mt}, this contribution is zero if the BED b_{it} delivered in fraction t to voxel i is the same portion δ_{mt} of the total BED $b_i = \sum_{t=1}^{n} b_{it}$ for all voxels $i \in PTV_m$ that belong to metastasis m. Thus, a treatment plan corresponding to a low value of f_{cSTF} has the property that each fraction delivers a spatial dose distribution to a metastasis that is similar to the prescribed cumulative BED distribution, except that it is downscaled by a factor δ_{mt}. In the original unconstrained approach to spatiotemporal fractionation, per contra, a fraction could deliver a large portion of the total cumulative BED in one voxel, and a low portion of the total BED in another voxel of the same metastasis, which corresponds to a large value of f_{cSTF} because the same δ_{mt} applies to all voxels belonging to a given metastasis m. By encouraging such an inter-fraction similarity, the constrained approach

to spatiotemporal fractionation is expected to be more robust against setup uncertainties compared to the original approach, because misalignments of dose contributions from different fractions do not lead to cold spots in the middle of a metastasis. Setup errors only affect coverage of the PTV edge, which can be accounted for by margins as in current clinical practice. In addition, by delivering spatially uniform dose distributions within a lesion in all fractions, the constrained approach to spatiotemporal fractionation may mitigate the biological uncertainties related to partial tumor irradiation.

The formulation of the objective in Eq. (3.1) has two important advantages. First, by introducing δ_{mt}'s as additional optimization variables, it still allows for simultaneous optimization of the incident fluence and the fractionation scheme. The partial BED contributions of every fraction t to each metastasis m are directly optimized together with the cumulative BED distribution and it is therefore not required to manually define a priori how much dose should be delivered to each lesion by which fraction. Second, the proposed planning objective does not make any assumptions on the cumulative BED distribution. Compared, for example, to objective functions which aim at minimizing the variance of the BED distribution of fraction t in metastasis m and thereby force the BED distribution in the PTV to be homogeneous, the objective in Eq. (3.1) allows to deliver inhomogeneous cumulative BED distributions within each lesion (which is clinical practice in SRS of brain metastases).

3.3.2 Patient cases

Three patients, each with a large number of brain metastases (> 25), have been selected to retrospectively investigate the potential benefits of spatiotemporal fractionation schemes. All three cases were treated with linac-based fractionated stereotactic radiosurgery at our institution. Patient 1 has 29 lesions of varying size with a total GTV volume of 14.7 cc and is used for illustration in the results section. Patients 2 and 3 have 27 and 30 metastases, respectively, with total GTV volumes of 22.6 cc and 20.3 cc. More detailed characteristics of the three patients are reported in the Supplementary material, Appendix A.

3.3.3 Treatment planning study

For each of the three brain metastases patients, we generate 3-fraction IMRT treatment plans using non-coplanar 6 MV photon beams, which are designed to approximate a full VMAT arc at a couch angle of 0° and three half-arcs from 0° to 180° at couch angles of 45°, 270° and 315°. The treatment

geometry is assumed to be single-isocenter. The beamlet resolution is 5 x 5 mm[a] and the resolution of the dose grid is 1.2 x 1.2 x 0.6 mm^3 in the x-, y- and z-directions. Calculation of the dose-influence matrix elements D_{ij} is performed with the open-source radiotherapy planning platform CERR [44] using a quadrant infinite beam (QIB) algorithm [63][b].

We attempt to solve the treatment plan optimization problem for the following choice of objective functions and constraints.

Objectives:

1. A BED_{10} of 51.3 Gy is prescribed to the GTV. This is implemented via a quadratic penalty function and corresponds to 27 Gy physical dose delivered in 3 fractions.

2. A BED_{10} of 43.2 Gy is prescribed to the PTV (which is obtained from a isotropic 1.2 mm margin expansion from the GTV[c]), corresponding to 24 Gy physical dose delivered in 3 fractions. A BED_{10} exceeding 60 Gy (i.e. 30 Gy physical dose in 3 fractions) is penalized quadratically[d]. These different dose prescriptions between the GTV and the PTV reflect the clinical practice of prescribing to the 80% isodose line and increasing the dose in the center of the metastases [64].

3. The volume V_{60} of healthy brain (i.e. brain-PTV) receiving a BED_2 larger than 60 Gy is minimized. This corresponds to 10 Gy in a single fraction and is implemented via a continuous relaxation of a dose-volume objective, as further detailed in the Supplementary material, Appendix B.

[a] Although the chosen beamlet size is similar to the diameter of some small metastases, inhomogeneous doses within the lesions and an excellent dose conformity can be achieved with 5 x 5 mm^2 beamlets due to the large number of field directions used. A beamlet size of 2.5 x 2.5 mm^2 may, however, further improve the results.

[b] CERR uses a pencil beam algorithm for calculation of the dose-influence matrix. We performed a comparison of dose profiles computed in CERR to the convolution-superposition algorithm implemented in the commercial planning system Eclipse (Varian Medical Systems). Although some discrepancies can be noticed in the lateral dose profile, the depth dose curves obtained using the QIB algorithm are reliable. In particular, as the brain tissue is quite homogeneous, we expect the dose distributions used in this study to be realistic.

[c] The same PTV margin is applied to every lesion, independently of their distance from the isocenter. The adopted planning margins are intended to be conservative and to hold true also for lesions which are further away from the isocenter.

[d] This over-dose penalty function applies also to all GTV voxels, as GTV $\subset$ PTV.

4. The mean BED_2 to the normal tissue excluding the PTV and the brain is minimized.

5. The mean BED_2 to the healthy brain is minimized.

Constraints:

1. The maximum BED_2 at 5 mm distance from the PTV is constrained to 36 Gy, corresponding to 12 Gy physical dose delivered in 3 fractions (i.e. half of the prescribed PTV dose). This forces the plan to be conformal and prevents hot spots in the normal tissue away from the metastases.

2. The maximum BED_2 to the brainstem is constrained to 120 Gy, corresponding to 24 Gy physical dose delivered in 3 fractions.

We first optimize a uniformly fractionated (UF) 3-fraction SRS treatment plan that delivers the same dose in all fractions, based on a weighted sum of the five objectives. This plan reflects current clinical practice of delivering a hypofractionated SRS treatment to patients with multiple brain metastases and is used as benchmark. Subsequently, two spatiotemporally fractionated plans are generated with both the original (*STF plan*) and the constrained (*cSTF plan*) approaches to spatiotemporal fractionation. The STF plan is obtained by minimizing the mean cumulative brain BED_2, subject to the additional constraints that the values of objectives 1-4 are no worse than in the UF plan. Hence, the entire benefit of spatiotemporal fractionation is directed on reducing the mean BED_2 to the healthy brain. The STF plan is compared to the UF plan to evaluate the maximum achievable benefit of delivering different non-uniform dose distributions in distinct fractions, when no constraints are set on the spatial dose distribution of each fraction. The cSTF plan is obtained by minimizing a weighted sum of the mean brain BED_2 objective and the new objective in Eq. (3.1), subject to the same constraints as for the STF plan, and is compared to both the UF plan and the STF plan in terms of mean brain BED_2 reduction and robustness against setup errors. The spatial dose distribution within the individual metastases in each fraction and the optimal fractionation scheme as a function of the size of the lesions are also compared between the STF and cSTF plans. The cSTF plan is hypothesized to maintain some of the benefit of spatiotemporal fractionation compared to the UF plan, while at the same time being more robust against setup errors and biological uncertainties related to partial tumor irradiation than the STF plan.

To find a local minimum of the optimization problem, we used our own implementation of the L-BFGS quasi-Newton method [65], together with an

augmented Lagrangian method for handling constraints [66]. Fluence maps were initialized with small random intensities (varying in between the different fractions of the spatiotemporally fractionated plans), while the additional optimization variables δ_{mt} used in Eq. (3.1) are initially set to $1/n$. As both the BED-based optimization problem and the new planning objective in Eq. (3.1) are not convex, two additional STF plans and two additional cSTF plans have been generated for patient 1 with different initializations of the fluence maps and of the δ_{mt} parameters, in order to investigate the sensitivity of the planning outcomes to different initializations.

A more detailed description of the treatment plan optimization problem can be found in the Supplementary material, Appendix B.

3.3.4 Variations of the constrained approach to spatiotemporal fractionation

The BED contribution δ_{mt} of fraction t to metastasis m in Eq. (3.1) can, per definition, assume any value in between 0 (i.e. no dose) and 1 (i.e. the full prescribed dose). However, all clinical experience is based on delivering the same dose in every fraction and the effect of delivering very different doses in different fractions is unknown. In that regard, we also consider and investigate two further modifications of the constrained approach to spatiotemporal fractionation, which aim at creating treatments that are even closer to clinical practice.

Adding objectives or constraints on δ_{mt}

Additional constraints or objectives can be defined for the optimization variables δ_{mt}'s to promote specific fractionation schemes. A special case of the constrained approach to spatiotemporal fractionation consists, for example, of assigning each metastasis to be either treated to the full dose in a single fraction (e.g. $\{\delta_{m1}, \delta_{m2}, \delta_{m3}\} = \{1, 0, 0\}$), to be uniformly fractionated over 2 out of 3 fractions (e.g. $\{\delta_{m1}, \delta_{m2}, \delta_{m3}\} = \{1/2, 1/2, 0\}$), or uniformly irradiated over all 3 fractions ($\{\delta_{m1}, \delta_{m2}, \delta_{m3}\} = \{1/3, 1/3, 1/3\}$). Such a fractionation scheme can be promoted by adding the following penalty term to the BED-based optimization problem:

$$f_{cSTF}^{bounds}(\boldsymbol{\delta}) = \sum_{m=1}^{M} \sum_{t=1}^{n} \delta_{mt}^2 \left(\delta_{mt} - \frac{1}{3}\right)^2 \left(\delta_{mt} - \frac{1}{2}\right)^2 (\delta_{mt} - 1)^2 \tag{3.2}$$

The penalty function $f_{cSTF}^{bounds}(\boldsymbol{\delta})$ in Eq. (3.2) is handled as a constraint using augmented Langrangian methods. It can be thought of as constraint

function that adds a term of the form $\lambda f_{cSTF}^{bounds}(\boldsymbol{\delta}) + \mu(f_{cSTF}^{bounds}(\boldsymbol{\delta}))^2$ to the augmented Lagrangian function, where λ is the estimate of a Lagrange multiplier that is iteratively updated and μ is a penalty factor that is iteratively increased as long as the constraint $f_{cSTF}^{bounds}(\boldsymbol{\delta}) = 0$ is violated. Thus, initially the fractional dose distributions and the parameters δ_{mt}'s are jointly optimized as continuous variables using the planning objective in Eq. (3.1). Eventually, δ_{mt} are frozen to the values 0, 1/3, 1/2 and 1 while the cumulative BED distribution is adjusted accordingly.

Not counting the contribution of very small doses per fraction to local tumor control

One specific concern for the application of spatiotemporal fractionation schemes to SRS of brain metastases is that the contribution of very small doses per fraction to local tumor control may be lower than predicted by the standard BED model. To account for such a potential issue, we implemented a method for generating cSTF plans in which only doses per fraction larger than a given threshold value contribute to local tumor control. Based on the cSTF plan obtained by allowing any value for the δ_{mt}'s in the interval [0,1], a second optimization is performed with the constraint that all the prescribed BED_{10} to each lesion is delivered in those fractions in which the cSTF plan contributes with $\delta_{mt}>0.1$ (which corresponds approximately to a physical dose larger than 3.5 Gy). This is achieved by evaluating the planning objectives and constraints for the corresponding metastasis only for the subset of fractions with $\delta_{mt}>0.1$.

Two additional cSTF plans are generated in this study using both the described approaches, to investigate whether alternative formulations of the constrained approach to spatiotemporal fractionation which are even closer to clinical practice might still have a benefit compared to uniform fractionation of all the metastases. These plans are initialized with the results of the cSTF plan obtained using the planning objective in Eq. (3.1) and are optimized using the same planning objectives and constraints.

3.4 Results

Fig. 3.1e and Fig 3.1m show the dose distribution for two different CT slices of patient 1 for the UF plan, in which each metastasis is treated to the same dose in all three fractions. This plan achieves a mean physical dose of 5.13 Gy in the healthy brain, while the brain volume V_{60} receiving a BED_2

larger than 60 Gy is 38.4 cc. The three fractional dose distributions for the STF and cSTF plans are illustrated in Fig. 3.1b-d/Fig. 3.1j-l and Fig. 3.1f-h/Fig. 3.1n-p, respectively. Both plans deliver high doses to complementary parts of the target volume in distinct fractions. In some metastases, maximum single-fraction doses exceed 15 Gy (note that 18.2 Gy delivered in a single fraction corresponds to the prescribed BED_{10} of 51.3 Gy to the GTV). All together, however, the three fractional dose distributions in both spatiotemporally fractionated plans deliver the same prescribed cumulative BED_{10} in each metastasis as in the uniformly fractionated plan (the equieffective dose[e] distributions in patient 1 achieved with the different fractionation schemes are reported in the Supplementary material, Appendix C.1).

Because of partial hypofractionation in the target volume, spatiotemporally fractionated plans achieve the prescribed tumor BED_{10} with less physical dose. This is shown in Fig. 3.1a and Fig. 3.1b, which compare the three plans in terms of the dose-volume histograms (DVH) evaluated for the cumulative physical dose and the equieffective dose, respectively. The mean physical dose to the PTV is 27.2 Gy for the uniformly fractionated plan, while it is reduced to 26.6 Gy (-2.2%) with the cSTF plan and to 25.8 Gy (-5.1%) with the STF plan. As some degree of fractionation is simultaneously achieved in the surrounding healthy brain, this reduction in physical dose leads to a net reduction in the brain BED_2 (Fig. 3.1b). The mean BED_2 to the healthy brain is reduced compared to the uniformly fractionated plan by 9.3% and by 13.2% with the cSTF and STF plans, respectively.

Similar results have been obtained for the other patients. Table 3.1 summarizes the dosimetric results achieved with uniform and spatiotemporal fractionation schemes for all three cases studied, while dose distributions for patients 2 and 3 can be found in the Supplementary material, Appendix C.2. For the same tumor BED_{10} and the same brain volume exposed to high doses in all plans, the mean BED_2 to the healthy brain can be reduced by 9-12% with the cSTF plan and by 13-19% with the STF plan compared to the uniformly fractionated plan. Note that the reduction in the mean brain BED_2 achieved with the spatiotemporally fractionated plans is lower than the corresponding reduction in the mean physical dose. This is due to a deviation from the ideal uniform fractionation in the healthy brain.

Because of the non-convexity of the BED-based optimization problem used in this study, different fractional dose distributions are obtained for both the STF and cSTF plans when the fluence maps are initialized differ-

[e]The equieffective dose $EQDX = \frac{b}{(1+X/(\alpha/\beta)}$ can be interpreted as the total physical dose to be delivered in a uniformly fractionated treatment with a dose per fraction X to achieve a BED b [67].

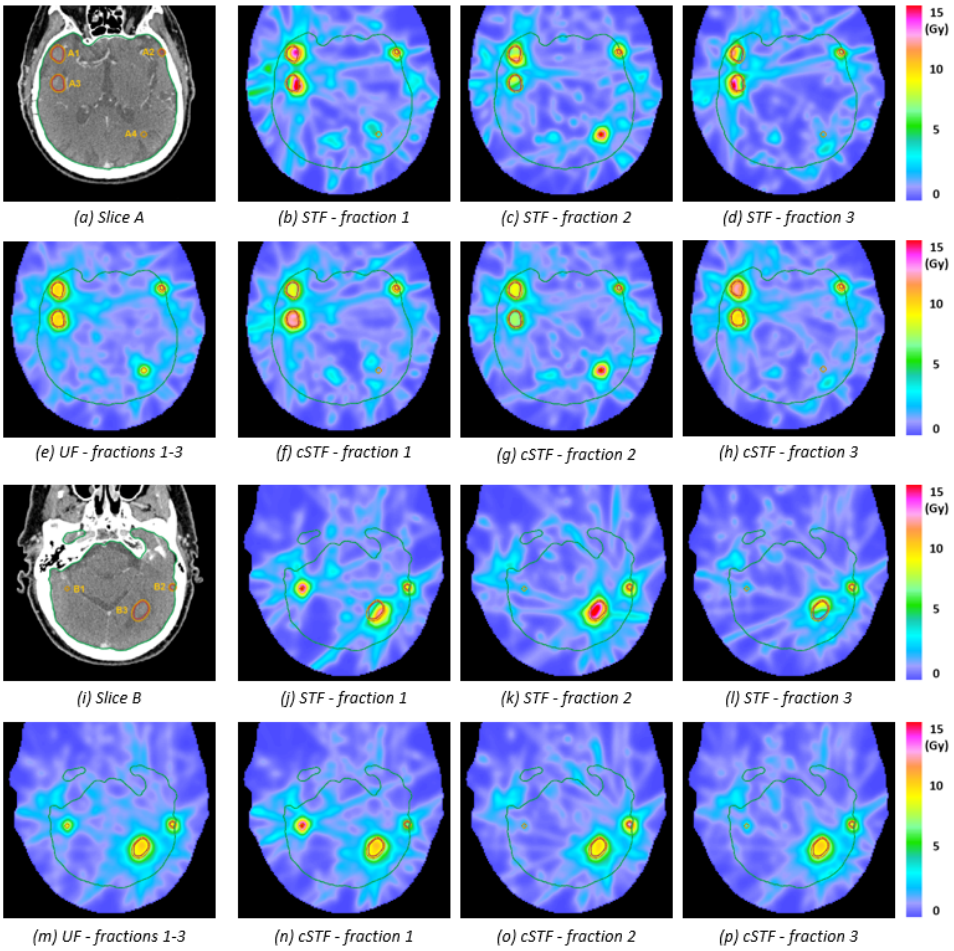

Figure 3.1: *Dose distributions for two CT slices of patient 1 achieved with the different fractionation schemes. In slice A (a), four metastases are visible with PTV volumes of 3.2 cc (A1), 0.3 cc (A2), 2.3 cc (A3) and 0.1 cc (A4). In slice B (i), three metastases are visible with PTV volumes of 0.1 cc (B1), 0.4 cc (B2) and 9.9 cc (B3). For each lesion, contours for the GTV (red) and PTV (orange) are shown. Also shown is the contour of the brain (green).*

ently (this is shown in Fig. 3C.5 in the Supplementary material, Appendix C.3). However, as it has previously been observed by Gaddy et al [68] on a different treatment site, such distinct local minima of the optimization problem correspond to treatments leading to very similar reductions in the mean brain BED_2 compared to the UF plan. These findings have been confirmed in this study for the STF plans, and also demonstrated to hold true for the cSTF plans.

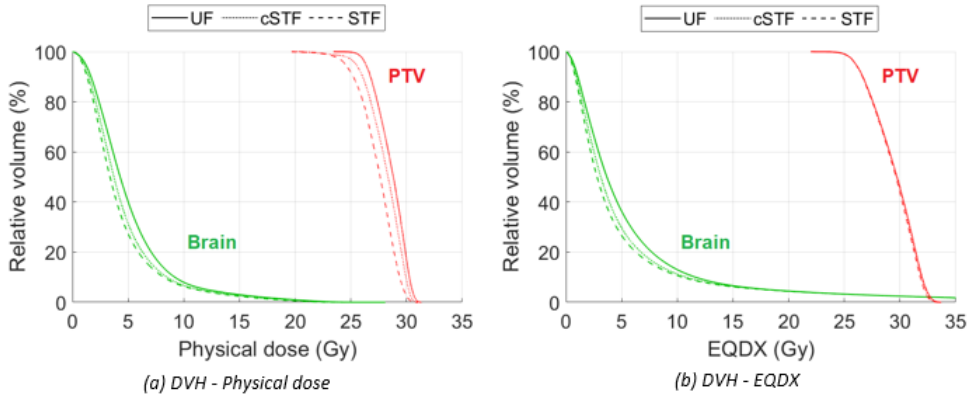

Figure 3.2: *Dose-volume histogram comparison for (a) the cumulative physical dose and (b) the equieffective dose EQDX. The DVHs are evaluated for both the PTV (X = 9 Gy) and the healthy brain (X = 2 Gy).*

Table 3.1: *Summary of the dosimetric results achieved with uniform and spatiotemporal fractionation schemes for all three patients studied. For patient 1, the mean values and standard deviations for the three optimizations with different initializations of the optimization variables are reported. As the mean tumor EQD9 is not directly optimized, slightly lower values for the mean EQD9 may be achieved in the PTV in the spatiotemporally fractionated plans compared to the UF plan. Under- and over-dose quadratic penalty functions for the PTV, however, are at least as good for the cSTF and STF plans as they are for the corresponding UF plan.*

			UF plan	**cSTF plan**	**STF plan**
Patient 1	PTV	Mean dose (Gy)	27.2	26.6 ± 0.0 (-2.2%)	25.8 ± 0.1 (-5.1%)
		Mean EQD9 (Gy)	27.3	27.3 ± 0.0 (=)	27.2 ± 0.0 (-0.4%)
	Healthy brain	Mean dose (Gy)	5.13	4.57 ± 0.1 (-10.9%)	4.29 ± 0.1 (-16.4%)
		Mean EQD2 (Gy)	5.82	5.29 ± 0.1 (-9.1%)	5.06 ± 0.1 (-13.1%)
		V_{60} (cc)	38.4	38.3 ± 0.0 (-0.3%)	38.3 ± 0.0 (-0.3%)
Patient 2	PTV	Mean dose (Gy)	27.2	26.7 (-1.8%)	25.8 (-5.1%)
		Mean EQD9 (Gy)	27.4	27.3 (-0.4%)	27.2 (-0.7%)
	Healthy brain	Mean dose (Gy)	7.47	6.66 (-10.8%)	6.02 (-19.4%)
		Mean EQD2 (Gy)	9.51	8.38 (-11.9%)	7.72 (-18.9%)
		V_{60} (cc)	45.0	45.0 (=)	44.9 (-0.3%)
Patient 3	PTV	Mean dose (Gy)	27.1	26.4 (-2.6%)	25.6 (-5.5%)
		Mean EQD9 (Gy)	27.3	27.2 (-0.4%)	27.1 (-0.7%)
	Healthy brain	Mean dose (Gy)	6.18	5.58 (-9.7%)	5.14 (-16.8%)
		Mean EQD2 (Gy)	7.51	6.84 (-8.9%)	6.39 (-14.9%)
		V_{60} (cc)	47.2	47.1 (-0.2%)	47.2 (=)

3.4.1 Plan sensitivity to random setup errors

The dosimetric results in Table 1 are reported assuming that all dose distributions for the different fractions are delivered as planned and thereby add up to the prescribed BED_{10} in all parts of the target volume. In order to determine the impact of random setup errors on the GTV dose coverage, we performed a robustness analysis. For each of the three fractionation schemes, Fig. 3.3

shows the DVHs evaluated for the EQD9 assuming that random setup errors of ± 1.2 mm in left-right, superior-inferior and anterior-posterior directions apply to the GTV between the different fractions. The magnitude of the setup errors is selected to agree with the GTV-to-PTV margin expansion. Both the UF and the cSTF plans maintain an excellent dose homogeneity within most of the lesions comparable to the situation without setup errors. Only for very small metastases (e.g. metastasis A2) the GTV dose coverage is slightly affected by setup errors, because a larger portion of the GTV moves outside of the high dose region for a 1.2 mm shift. This problem, however, is common to both the UF and cSTF plans, which overall show a very similar sensitivity to geometrical uncertainties. Instead, as a result of the misalignments of the dose contributions of the different fractions within the single metastases, the STF plan presents an increased risk of cold and hot dose spots within the GTV when setup errors are assumed, especially for larger metastases. For instance, the STF plan delivers a mean EQD9 of only 25.3 Gy to the GTV of metastasis A3 in the worst case scenario, whereas the corresponding mean EQD9 reads 29.5 Gy when no setup error is assumed. For smaller lesions, the STF plan is less sensitive to setup errors, because the ability of the STF plan to hypofractionate different parts of the PTV in distinct fractions is reduced for a finite beamlet size (as shown in Fig. 3.5b).

Spatial dose distributions within the individual metastases

In Fig. 3.4, the spatial dose distributions within the individual lesions are analyzed in more detail. For four metastases in patient 1, Fig. 3.4a-d separately display the relative number of voxels receiving a given BED contribution from each of the three fractions in the spatiotemporally fractionated plans. The cSTF plan delivers spatially very homogeneous dose distributions to each metastasis in all fractions, thereby avoiding partial irradiation of the different lesions. Dosimetric improvements over the UF plan are nevertheless obtained by varying the partial dose contribution of each fraction to every lesion. For example, metastasis A4 receives more than 90% of the BED_{10} in the first fraction of the cSTF plan, whereas fractions 2 and 3 only contribute a minor part to the prescribed tumor BED_{10}. In contrast, the STF plan is not constrained to irradiate entire metastases with similar spatial dose distributions and thereby more inhomogeneous doses are delivered within each lesion in separate fractions. This results in an improved trade-off between hypofractionation in the target volume and more uniform fractionation in the healthy brain, and thereby also in a larger brain BED_2 reduction compared to the cSTF plan. However, this may also introduce biological uncertainties related to partial tumor irradiation.

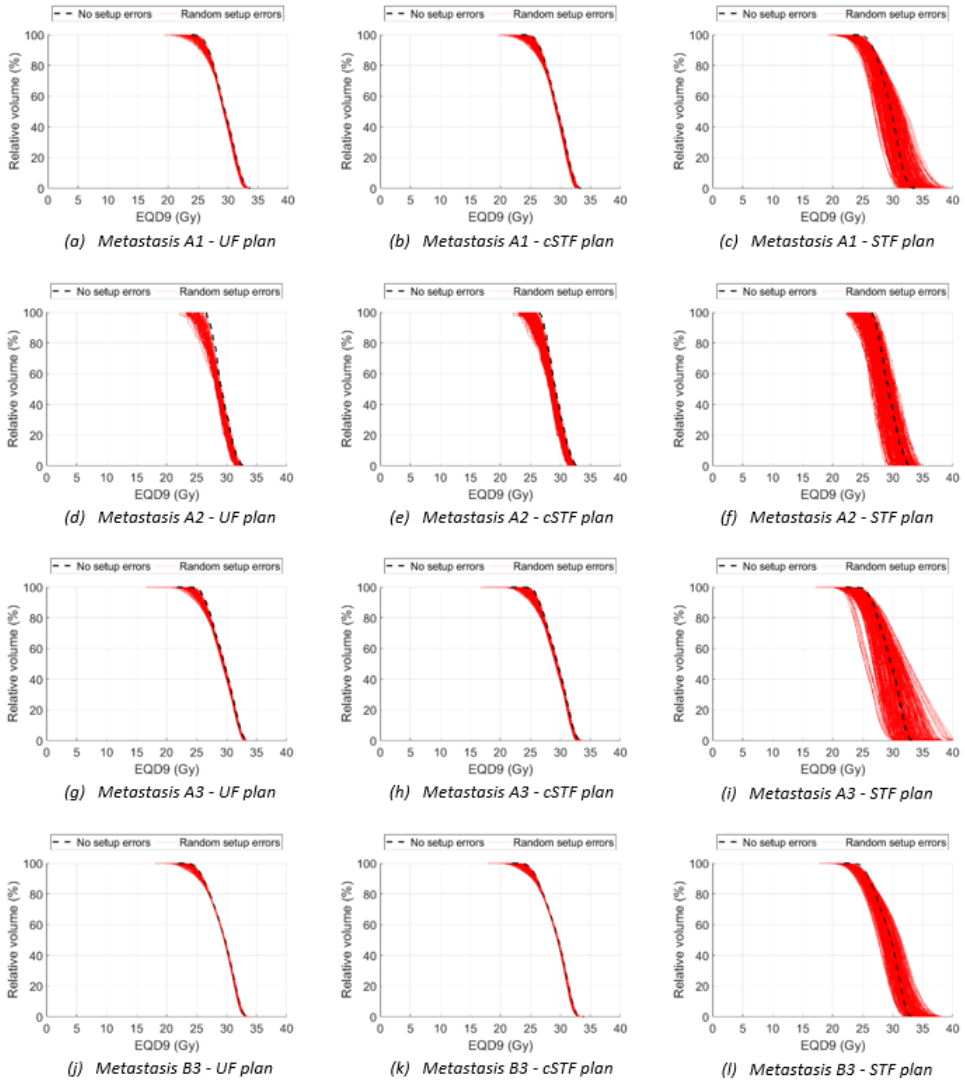

Figure 3.3: *Dose-volume histograms for the GTVs of four individual lesions in patient 1 evaluated for the EQD9, assuming a scenario with no setup errors (black dashed line) and* $7^3 - 1 = 342$ *error scenarios corresponding to all combinations of random setup errors of* ± 1.2 *mm in left-right, superior-inferior and anterior-posterior directions (red solid lines).*

3.4.2 Impact of the size of the metastases on the optimal fractionation scheme

In Fig. 3.5, we analyze how the optimal fractionation scheme depends on the size of the metastases. Fig. 3.5a shows the maximum fractional BED

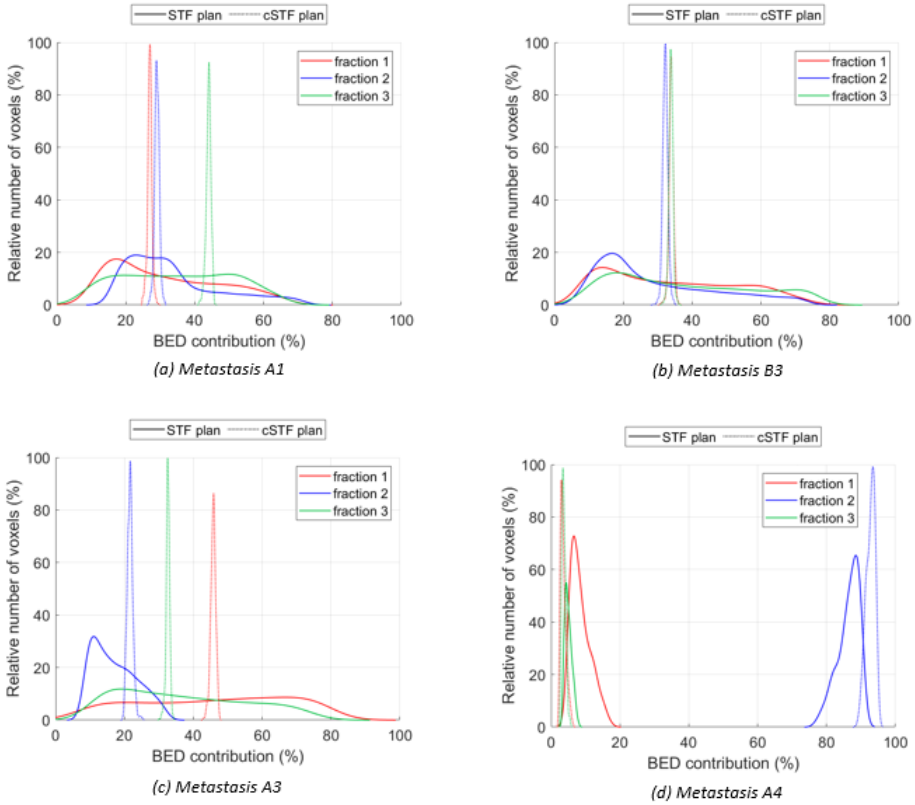

Figure 3.4: *Relative BED contribution of every fraction to four individual metastases in patient 1 for both the cSTF (dashed line) and the STF (solid line) plans.*

contribution $\max_t \delta_{mt}$ to each of the 29 metastases in patient 1 as a function of their size for the cSTF plan, where δ_{mt} are the additional variables defined in Eq. (3.1) for the cSTF plan optimization. Generally, small lesions are treated to high doses in one of the fractions (e.g. metastases A4 and B1 in Fig. 3.1), whereas larger metastases receive a similar dose in all the fractions. For example, the fractionation scheme for the largest lesion with a diameter of 2.7 cm (metastasis B3 in Fig. 3.1) approaches uniform fractionation. As seen in Fig. 3.4b, the partial BED contributions of all three fractions in the cSTF plan to that metastasis range from 32% to 34%. These findings are also well illustrated for patient 3 in the Supplementary material, Appendix C.2.

Fig. 3.5b reports the standard deviation

$$\sigma_{mt} = \sqrt{\frac{1}{|PTV_m|} \sum_{i \in PTV_m} \left(b_{it} - \frac{1}{|PTV_m|} \sum_{i \in PTV_m} b_{it} \right)^2} \tag{3.3}$$

of the BED contributions of every fraction t in the STF plan to all voxels in each of the metastases m in patient 1, as a function of the lesion size. Large values of σ_{mt} occur when complementary parts of the same metastasis are treated to high doses in distinct fractions. For example, metastasis B3 is treated with highly inhomogeneous doses in every fraction of the STF plan (as can be seen in Fig. 3.4b), and the corresponding values for the standard deviation read 10.2 Gy, 9.1 Gy and 10.9 Gy for fractions 1, 2 and 3, respectively. Instead, small values for the standard deviation correspond to a fraction delivering more homogeneous spatial dose distributions within the individual lesions (as it is the case for metastasis A4 in Fig. 3.4d, for which the corresponding values of σ_{mt} are 1.3 Gy, 4.9 Gy and 0.4 Gy for the three contributing fractions). The ability of the STF plan to hypofractionate distinct regions of the same lesion in different fractions is greater for larger metastases, while it almost disappears for lesions with a diameter smaller than 8 mm (note that the beamlet size used in this study is limited to 5 mm).

3.4.3 Alternative cSTF plans with fractional dose contributions which are closer to clinical practice

As shown in Fig. 3.4 and Fig. 3.5a, the optimal BED contribution δ_{mt} of fraction t to metastasis m in the cSTF plan can assume very different values depending on the size of the lesions. In the following, we present the results for two alternative cSTF plans whose fractional dose contributions to the individual lesions are closer to what is conventionally delivered in clinical practice.

cSTF plan obtained by constraining the values of δ_{mt}

The fractional dose distributions for the cSTF plan obtained using the penalty function in Eq. (3.2) are shown in Fig. 3.6 for patient 1. This treatment irradiates each metastasis with fractionation schemes that are conventionally used in clinical practice (i.e. 1 x 16 Gy, 2 x 10 Gy or 3 x 8 Gy), which has the advantage that one does not expect changes in local tumor control. However, with these additional restrictions, such a cSTF plan achieves a mean brain BED_2 reduction of only 1.4% compared to the UF plan (for a similar PTV

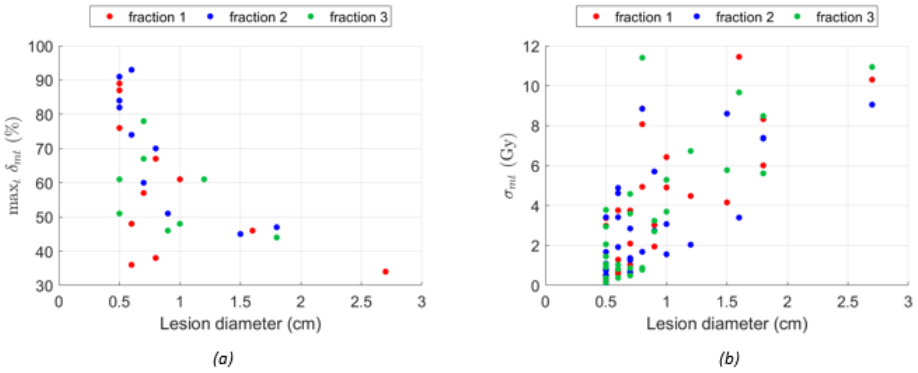

Figure 3.5: *Dependence of the optimal fractionation scheme on the size of the metastases for patient 1. (a) Maximum fractional BED contribution to each metastasis in the cSTF plan, showing that small lesions are treated to high doses in one of the fractions, whereas large metastases receive similar doses in all fractions. (b) Standard deviation of the partial BED contributions of each fraction in the STF plan to the voxels of each individual lesion, showing that the ability of the STF plan to hypofractionate distinct regions of the target volume in different fractions is reduced for small metastases. The sizes of the metastases refer to the planning target volume.*

dose coverage), which is partly explained by the result that 21 out of 29 are assigned to uniform fractionation over all 3 fractions.

cSTF plan obtained by neglecting the contribution of very small doses per fraction to local tumor control

Fig. 3.7 illustrates the result for two selected metastases in patient 1 for the cSTF plan which is obtained by neglecting the contribution to local tumor control of fractions delivering a dose smaller than 3.5 Gy to a metastasis. The method increases the dose contribution of the largest fraction to deliver the entire tumor BED_{10}. While the same PTV dose coverage and volume of brain receiving high doses could be achieved as for the original cSTF plan, the mean brain EQD2 is increased to 5.53 Gy when the contribution of small doses per fraction are neglected. This still represents a 5.0% reduction in the mean brain BED_2 compared to the benchmark UF plan, demonstrating that the benefit of cSTF plans over UF plans is maintained also when it is assumed that small doses per fraction do not contribute to local tumor control. However, the benefit is substantially lower than the 9.1% for the initial cSTF plan, because the method enforces that overall more dose is delivered to the patient.

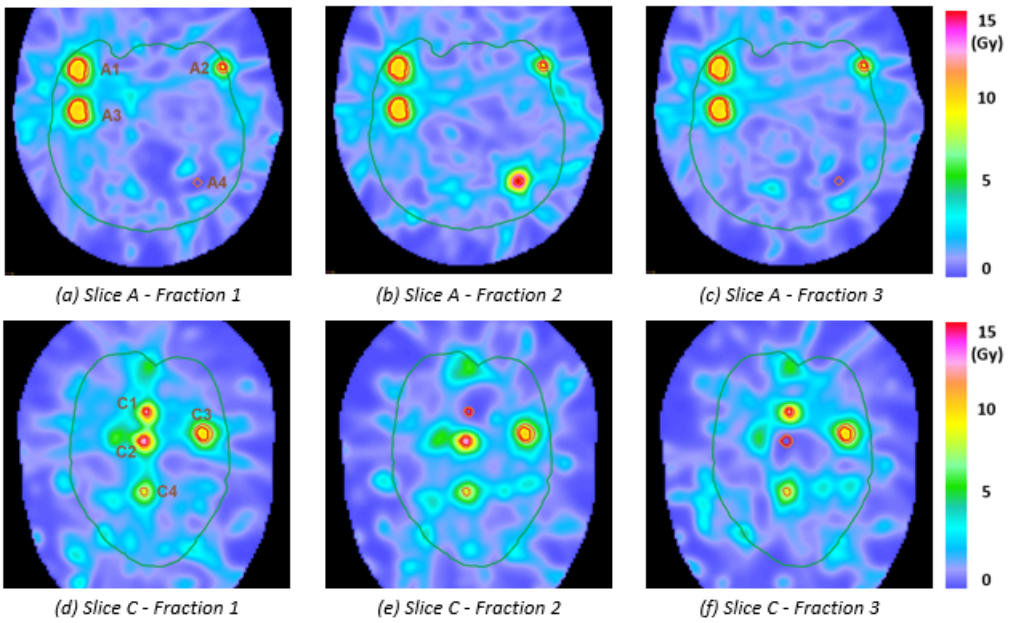

Figure 3.6: *Dose distributions for two CT slices of patient 1 achieved with the cSTF plan obtained using the additional penalty term in Equation (2). All metastases are either treated to the full dose in a single fraction (2/29 lesions; A4), uniformly irradiated over two of the three fractions (6/29 lesions; C1, C2) or uniformly irradiated over all three fractions (21/29 lesions; A1, A2, A3, C3, C4).*

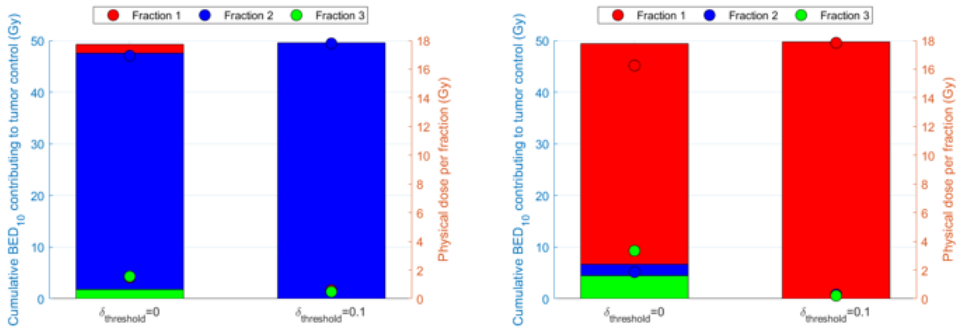

Figure 3.7: *Comparison between the initial cSTF plan and the cSTF plan which considers only fractional dose contributions of at least 3.5 Gy for (a) metastasis A4 and (b) metastasis B1 in patient 1. Round markers represent the physical dose per fraction, whereas the bars represent the contribution to the cumulative target BED_{10} of all fractions with $\delta_{mt} > \delta_{threshold}$.*

3.5 Discussion

The treatment of multiple brain metastases with stereotactic radiosurgery is often limited by the large integral dose delivered to the healthy brain. While uniform fractionation schemes have limited ability to reduce radiation-induced brain toxicities, we demonstrated in this study that by delivering non-uniform dose distributions in distinct fractions, the mean brain BED_2 can be substantially reduced for a fixed prescribed tumor BED_{10}. For each fraction, the dose distributions are designed to achieve partial hypofractionation in the target volume along with more uniform fractionation in the healthy brain, and thereby optimally exploit fractionation effects. Although it is difficult to quantify the clinical benefit of reducing the mean BED_2 in the healthy brain, a lower brain BED_2 may mitigate the risk for neurocognitive decline and give more margin for repeated SRS in brain metastases patients.

Despite the accurate patient positioning typical of SRS treatments, residual setup errors remain a serious concern for the delivery of spatiotemporal fractionation schemes when different parts of the same metastasis are treated to high doses in distinct fractions. Setup errors may, in fact, lead to misalignments of the planned dose distributions of the different fractions, thereby causing non-negligible target underdosage and potentially compromising tumor control. These uncertainties cannot be accounted for by adding margins around the treated volume as in conventional clinical practice, as the optimal dose compartmentalization for the STF plans is automatically determined by solving the BED-based optimization problem and is not known a priori. Stochastic optimization methods to account for geometrical uncertainties in spatiotemporal fractionation schemes have been previously investigated [69]. In this work, we presented a different approach to spatiotemporal fractionation applicable to polymetastatic cancer patients and demonstrated that most of the benefits of STF can be maintained by treating entire metastases with possibly different doses, but spatially similar dose distributions in different fractions. Such constrained approach to spatiotemporal fractionation has two main advantages compared to using stochastic optimization methods. First, by avoiding intra-metastatic fractional dose gradients, robustness against setup and motion uncertainties can be directly achieved by adding margins around the treated volume as in conventional clinical practice. As cSTF plans are obtained by evaluating a single additional planning objective, this method is thereby computationally more efficient than stochastic optimization methods, as it does not require to evaluate multiple error scenarios. Second, the constrained approach to spatiotemporal fractionation potentially mitigates biological uncertainties related to the partial irradiation of a lesion, and thereby represents a practical approach to spatiotemporal fractionation

with lower hurdles for clinical implementation.

In this study, we used a generalization of the standard BED model to quantify the fractionation effects, assuming α/β values of 10 Gy in the tumor and of 2 Gy in the normal brain. While the BED model has been widely used to compare different fractionation schemes, clinical experience is mostly limited to delivering the same dose in each fraction and it is uncertain if the assumed generalization of the BED model adequately describes the effectiveness of treatments that deliver very different doses in different fractions. In that regard, two alternative cSTF approaches have been investigated, which either neglect the contribution of very small doses per fraction to local tumor control or aim at delivering more standard fractionation schemes to each lesion. Both approaches are demonstrated to still outperform the UF plan, but the benefit is lower compared to the cSTF plan obtained by allowing arbitrary fractional dose contributions to the different metastases.

Several prior publications have introduced the concept of irradiating different subsets of metastases in different fractions [45-47]. In those studies, each lesion was forced to receive the full prescribed dose in a single fraction. Chen et al [47] considered gammaknife radiosurgery for multiple brain metastases. In a first step, individual treatment plans were created for each metastasis, and in a second step, the optimal sorting of metastases into the different fraction groups was determined by solving an integer programming problem. In the context of linac-based SRS, this approach has two main limitations that the proposed cSTF approach improves upon. First, in contrast to a sequential approach, it allows for jointly optimizing the incident fluence and the fractional dose contributions to each metastasis. Second, it allows the fractionation scheme for the individual lesions to be flexible. In this way, not all metastases are necessarily treated to the full dose in a single fraction, but a metastasis-specific fractionation scheme is optimized depending on the lesion size and its location relative to other metastases and organs at risk. The ability to uniformly fractionate the dose delivered to some of the lesions is particularly beneficial for metastases which are large or located close to critical structures, as this allows fulfilling dose-volume constraints for the brain in the high dose region. As a special case of cSTF, treatments that irradiate each metastasis to the full dose in one of the fractions can be obtained if Eq. (3.2) is modified as $f_{cSTF}^{bounds}(\boldsymbol{\delta}) = \delta_{mt}^2(\delta_{mt} - 1)^2$. This approach was investigated. However, treatments obtained in this way increased the mean brain BED_2 compared to the UF plan.

Future studies may investigate the potential benefit of the cSTF approach for other treatment sites. Multiple lung or liver metastases might be particularly well suited, as concerns regarding motion uncertainties are even more pressing for the original STF approach. In addition, other methods could be

investigated for making cSTF treatments closer to clinical practice without considerably compromising their dosimetric benefit. This may include alternative formulations of Eq. (3.2) and approaches to address the nonconvexity of the optimization problems, e.g. smart initializations of the optimization variables that yield local minima close to the global optimum.

3.6 Conclusions

Spatiotemporal fractionation schemes lead to lower biological doses in the healthy brain compared to uniform fractionation schemes for patients with multiple brain metastases treated with SRS. A constrained approach to spatiotemporal fractionation that treats entire metastases with possibly different doses, but spatially similar dose distributions in distinct fractions maintains most of the benefits in terms of mean brain BED reduction and presents lower hurdles for clinical implementation.

3.7 Supplementary material

Appendix A Patients

Table 3A.1 reports the characteristics of the three metastastic cancer patients used to investigate the benefits of spatiotemporal fractionation schemes. The selection criteria include patients with more than 25 brain metastases (BMs) treated with hypofractionated SRS at our institution in the year of 2020.

Appendix B Treatment plan optimization

In this section, we detail the treatment plan optimization methods. We provide the mathematical formulation of the planning objectives and constraints used in the treatment plan optimization problem, and discuss the dose calculation algorithm which has been used in this study.

Table 3A.1: *Characteristics of the three clinical cases studied. Volumetric data refer to the gross tumor volume.*

			Volume per BM (cc)		
	No. of metastases	Total volume (cc)	Min	Max	Median
Patient 1	29	14.7	0.1	7.4	0.1
Patient 2	27	22.6	0.1	3.4	0.2
Patient 3	30	20.3	0.1	8.3	0.3

B.1 Optimization of the uniformly fractionated plan

For the uniformly fractionated plan, the BED-based treatment plan optimization problem is solved for a single fluence map $\mathbf{x}$. The following objectives and constraints have been used:

$$\underset{\mathbf{x}}{\text{minimize}} \quad f(\mathbf{b}) = \sum_{m=1}^{M} \frac{1}{|G_m|} \sum_{i \in G_m} (51.3 - b_i)_+^2 \tag{3B.1}$$

$$+ \sum_{m=1}^{M} \frac{1}{|P_m|} \sum_{i \in P_m} \left[\frac{5}{2} (43.2 - b_i)_+^2 + (b_i - 60)_+^2 \right] \tag{3B.2}$$

$$+ \frac{\omega_p}{|B|} \sum_{i \in B} \frac{1}{1 + e^{-(b_i - 60)/0.5}} \tag{3B.3}$$

$$+ \frac{10\omega_p}{|B|} \sum_{i \in B} b_i \tag{3B.4}$$

$$+ \frac{\omega_p}{|N_{rem}|} \sum_{i \in N_{rem}} b_i \tag{3B.5}$$

$$\text{subject to} \quad b_i \leq 36 \qquad \forall i \in N_{5mm} \tag{3B.6}$$

$$b_i \leq 120 \qquad \forall i \in S \tag{3B.7}$$

$$b_i = n d_i \left[1 + \frac{d_i}{(\alpha/\beta)_i} \right] \qquad \forall i \tag{3B.8}$$

$$d_i = \sum_j D_{ij} x_j \qquad \forall i \tag{3B.9}$$

$$x_j \geq 0 \qquad \forall j \tag{3B.10}$$

where ω_p is a patient-specific weighting factor which is set to 1 for patients 1 and 3, and to 1/5 for patient 2. Here, the dose-influence matrix elements D_{ij} describe the physical dose contributions of beamlets j to voxel i for unit fluence, while x_j is the fluence of beamlet j. G_m and P_m (where $G_m \subset P_m$) denote the sets of voxels contained in the GTV and the PTV of metastasis m, respectively; B is the set of voxels in the healthy brain (defined as the brain without the PTV); N_{rem} denotes all voxels in the remaining normal tissue (i.e. the normal tissue without the brain and the PTV); N_{5mm} is the set of voxels belonging to the normal tissue and at a distance equal or larger than 5 mm from the PTV; and S denotes the set of voxels belonging to the brainstem. The planning objective in Eq. (3B.3) is used to control the brain volume exposed to BED_2 values larger than 60 Gy. Differently

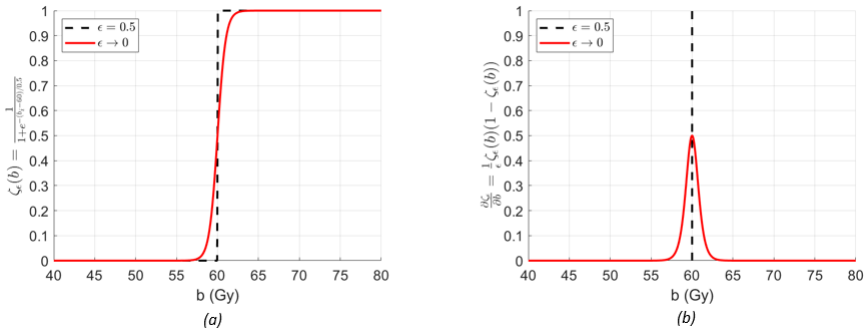

Figure 3B.1: *(a) Logistic sigmoid function and (b) its derivative. In (a), the red solid line is obtained for a smoothness parameter $\epsilon = 0.5$ and corresponds to the continuously differentiable function that is used for the treatment plan optimization in this work, whereas the black dashed line (obtained for $\epsilon \to 0$) corresponds to the Heaviside step function.*

than classical DVH objectives, which are evaluated using the Heaviside step function $\theta(x)$, the objective function in Eq. (3B.3) is evaluated using a continuously differentiable logistic sigmoid function $\zeta_\epsilon(x)$ (Fig. 3B.1a), where ϵ is called smoothness parameter [70]. For $\epsilon \neq 0$, we can define a smooth approximation of a DVH objective with a non-vanishing gradient around b = 60 Gy (Fig. 3B.1b). This makes such planning objective more suitable for gradient-based optimizations, particularly when used as a constraint. In this work, we set the smoothness parameter ϵ to 0.5 (note that $\zeta_\epsilon(x) \to \theta(x)$ for $\epsilon \to 0$).

Note that Eq. (3B.8) and (3B.9) define the relation of the optimization variables $\mathbf{x}$ (i.e. the beamlet intensities), the physical dose, and the cumulative BED (which is used to evaluate the objectives and constraints). These relations are included here as equality constraints only for presentation purposes, but the actual optimization is done by expressing the cumulative BED in terms of the beamlet intensities x_j's, and solving for the optimal fluence map $\mathbf{x}$.

B.2 Optimization of the spatiotemporally fractionated plans

Spatiotemporally fractionated plans may deliver n possibly different dose distributions in each of the n fractions, and thereby the BED-based treatment plan optimization problem is solved for n distinct fluence maps $\{\mathbf{x}_1, ..., \mathbf{x}_n\}$. The corresponding optimization problem reads:

$$\underset{\mathbf{x}_1,\ldots,\mathbf{x}_n}{\text{minimize}} \quad f(\mathbf{b}) = \frac{100}{|B|}\sum_{i\in B}(51.3-b_i)_+^2 \tag{3B.11}$$

$$+\left(\sum_{m=1}^{M}\sum_{t=1}^{n}\sum_{i\in P_m}\left[\frac{1/\omega_p}{|P_m|}\left(b_{it}-\delta_{mt}\left(\sum_{t=1}^{n}b_{it}\right)\right)^2\right]\right) \tag{3B.12}$$

$$\text{subject to} \quad f_{G_m}^{UF} \geq \frac{1}{|G_m|}\sum_{i\in G_m}(51.3-b_i)_+^2 \qquad \forall m \tag{3B.13}$$

$$f_{P_m}^{UF} \geq \frac{1}{|P_m|}\sum_{i\in P_m}\left[\frac{5}{2}(43.2-b_i)_+^2+(b_i-60)_+^2\right] \qquad \forall m \tag{3B.14}$$

$$f_{B,volume}^{UF} \geq \frac{\omega_p}{|B|}\sum_{i\in B}\frac{1}{1+e^{-(b_i-60)/0.5}} \tag{3B.15}$$

$$f_{N_{rem}}^{UF} \geq \frac{\omega_p}{|N_{rem}|}\sum_{i\in N_{rem}} b_i \tag{3B.16}$$

$$b_i = \sum_{t=1}^{n} d_{it}\left[1+\frac{d_{it}}{(\alpha/\beta)_i}\right] \qquad \forall i \tag{3B.17}$$

$$d_{it} = \sum_j D_{ij}x_{jt} \qquad \forall i,\forall t \tag{3B.18}$$

$$x_{jt} \geq 0 \qquad \forall j,\forall t \tag{3B.19}$$

where we denote the objective values for the GTVs, PTVs, brain volume and normal tissue obtained in the uniformly fractionated plan by $f_{G_m}^{UF}$, $f_{P_m}^{UF}$, $f_{B,volume}^{UF}$ and $f_{N_{rem}}^{UF}$. Note that the new planning objective in Eq. (3B.12) is used when optimizing spatiotemporally fractionated plans using the constrained approach.

The computation time for generating spatiotemporally fractionated treatments scales linearly with the number of different dose distributions to optimize. For the 3-fraction SRS treatments considered in this study, the computation time for optimizing the STF and cSTF plans is thereby about 3 times longer than the time needed for optimizing the UF plan given comparable setups. The additional time required to generate the cSTF plans is negligible, as the new planning objective in Eq. (3B.12) is evaluated only for the PTV voxels (which are very few compared to the voxels in the rest of the body).

B.3 Numerical satisfaction of the constraints

The planning constraints in Eq.(3B.6)-(3B.7) and Eq.(3B.13)-(3B.18) are handled using an augmented Lagrangian method. As a penalty method rather than a barrier method, the AL algorithm may satisfy constraints only after a large number of iterations. In fact, for the current study, differently than what is done in current clinical practice, a very large number of iterations (N=2000) was allowed for the L-BFGS algorithm (to have a rigorous comparison), what enables the algorithm to converge until almost constraint satisfaction. Any residual constraint violations in this study were numerically very small compared to the improvements of the STF and cSTF plans over the uniformly fractionated plans. Their impact on the quantitative plan comparisons was negligible for all cases.

Appendix C Results

C.1 EQD9 distributions in patient 1

Fig. 3C.2 shows the EQD9 distributions achieved with the different fractionation schemes for patient 1. Although the spatiotemporally fractionated plans deliver non-uniform doses to the target volume in distinct fractions, the sum of all fractional doses result in the same prescribed BED_{10} within each metastasis as the corresponding uniformly fractionated plan.

C.2 Dose distributions for patients 2 and 3

Fig. 3C.3 and Fig. 3C.4 show the fractional dose distributions obtained with the uniformly and both spatiotemporally fractionated plans for two different slices of patient 2 and patient 3, respectively. Similar to patient 1, the spatiotemporally fractionated plans hypofractionate the dose in the target volume by delivering high doses in distinct fractions. While the STF plans deliver high doses to complementary parts of individual metastases, the plans obtained with the constrained approach to spatiotemporal fractionation scheme do not present dose gradients within the individual lesions between the different fractions. The cSTF plans, in fact, improve on uniformly fractionated plans by treating small metastases to a high dose in alternated fractions, but tend to deliver similar doses to the larger lesions in order to fulfill the dose-volume constraints for the healthy brain. Note also that metastasis B2 in patient 2 is almost uniformly fractionated in the STF and cSTF plans in order not to violate the maximum dose constraint for the brainstem. This demonstrates that not only large metastases may preferably

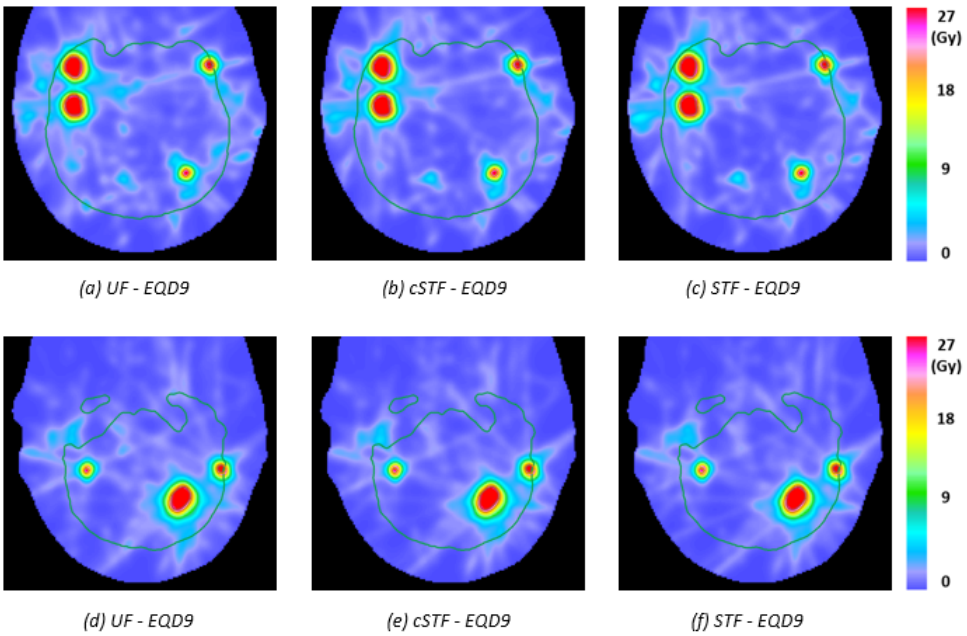

Figure 3C.2: *EQD9 distributions achieved with the different fractionation schemes for (a)-(c) slice A and (d)-(f) slice B of patient 1.*

be treated over multiple uniform fractions, but also lesions which are inside or close to critical organs at risk.

C.3 Dose distributions for patient 1 obtained with different initializations of the optimization variables

Fig. 3C.5 shows the dose distributions obtained for the STF and cSTF plans for two different initializations of the fluence maps (and the additional optimization parameters δ_{mt}'s).

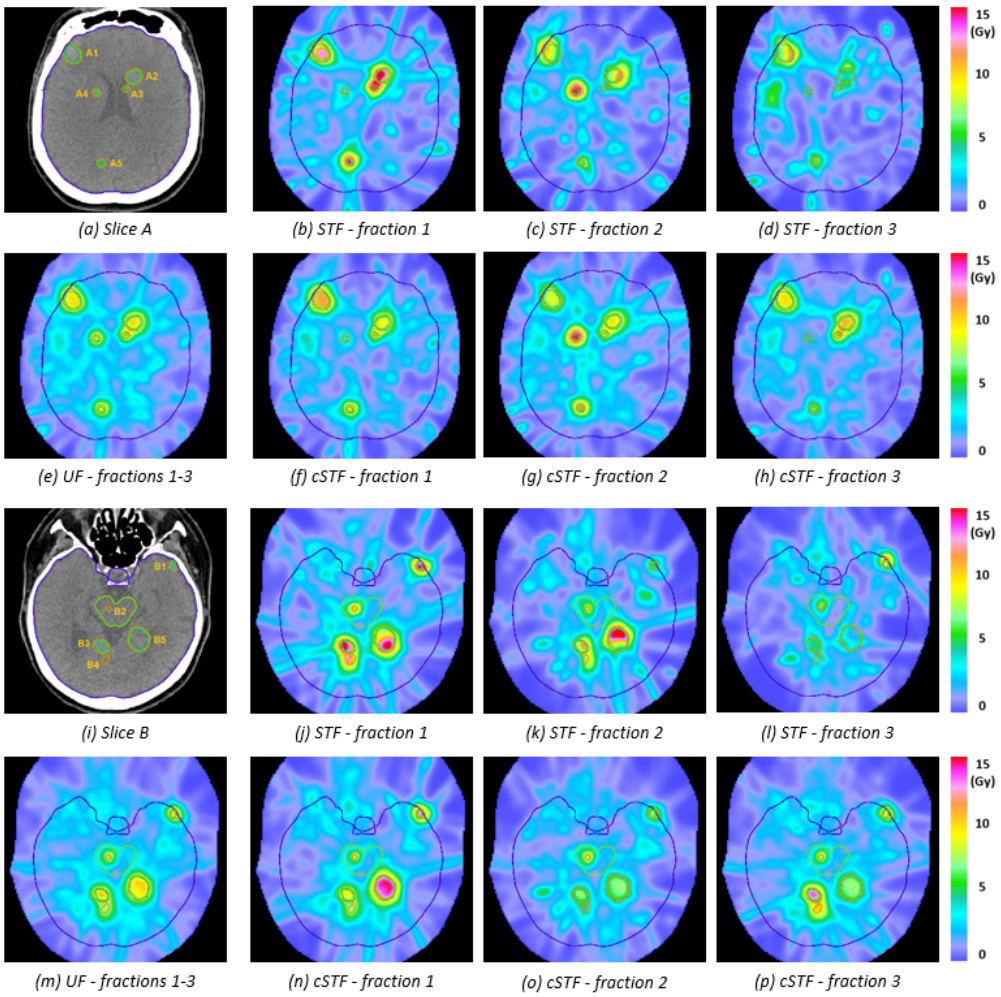

Figure 3C.3: *Dose distributions for two CT slices of patient 2 achieved with the different fractionation schemes. In slice A (a), five metastases are visible with PTV volumes of 3.5 cc (A1), 3.4 cc (A2), 0.2 cc (A3), 0.2 cc (A4) and 0.4 cc (A5). In slice B (i), five metastases are visible with PTV volumes of 0.3 cc (B1), 0.2 cc (B2), 0.6 cc (B3), 4.7 cc (B4) and 4.2 cc (B5). For each lesion, both contours for the GTV (green) and PTV (orange) are shown. Also shown are the contours of the brain (dark blue) and of the brainstem (light green).*

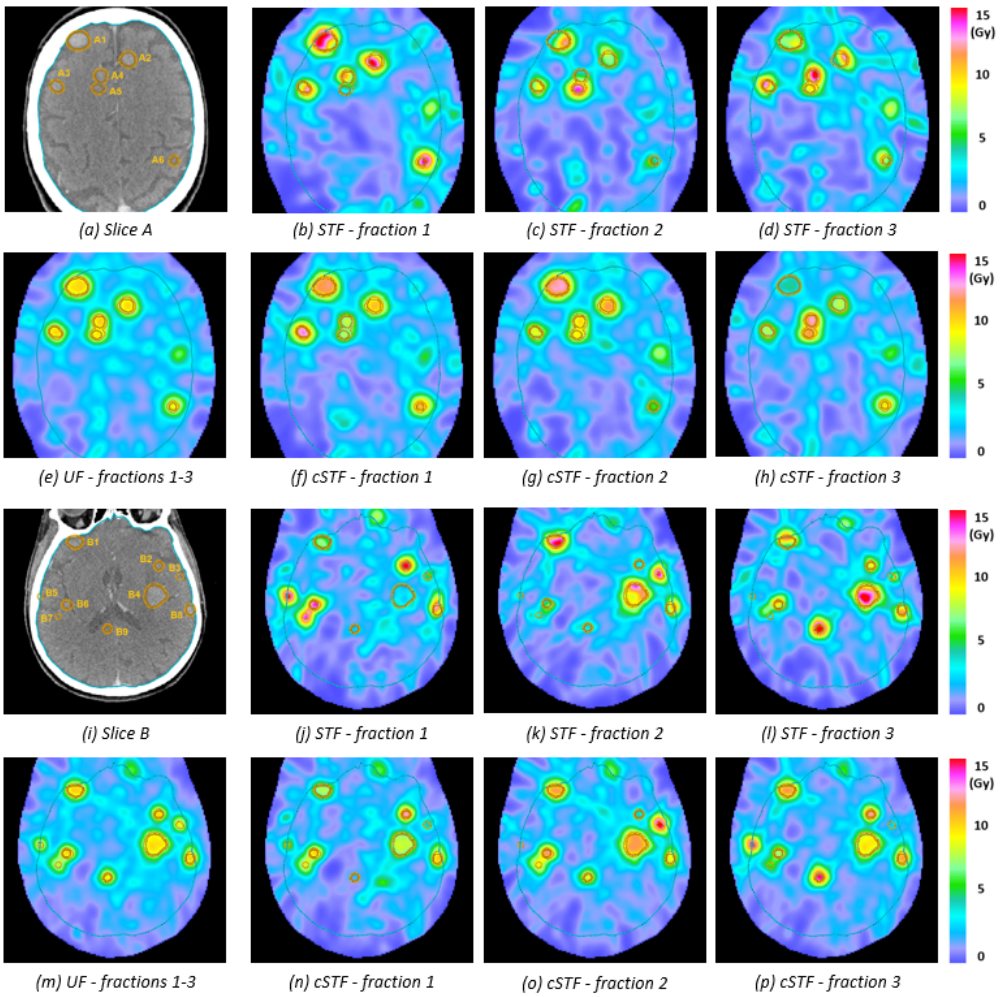

Figure 3C.4: *Dose distributions for two CT slices of patient 3 achieved with the different fractionation schemes. In slice A (a), six metastases are visible with PTV volumes of 1.7 cc (A1), 1.3 cc (A2), 0.5 cc (A3), 0.6 cc (A4), 0.5 cc (A5) and 0.7 cc (A6). In slice B (i), nine metastases are visible with PTV volumes of 1.3 cc (B1), 0.4 cc (B2), 0.4 cc (B3), 10.9 cc (B4), 0.3 cc (B5), 0.4 cc (B6), 1.4 cc (B7), 0.6 cc (B8) and 0.5 cc (B9). For each lesion, both contours for the GTV (brown) and PTV (orange) are shown. Also shown is the contour of the brain (light blue).*

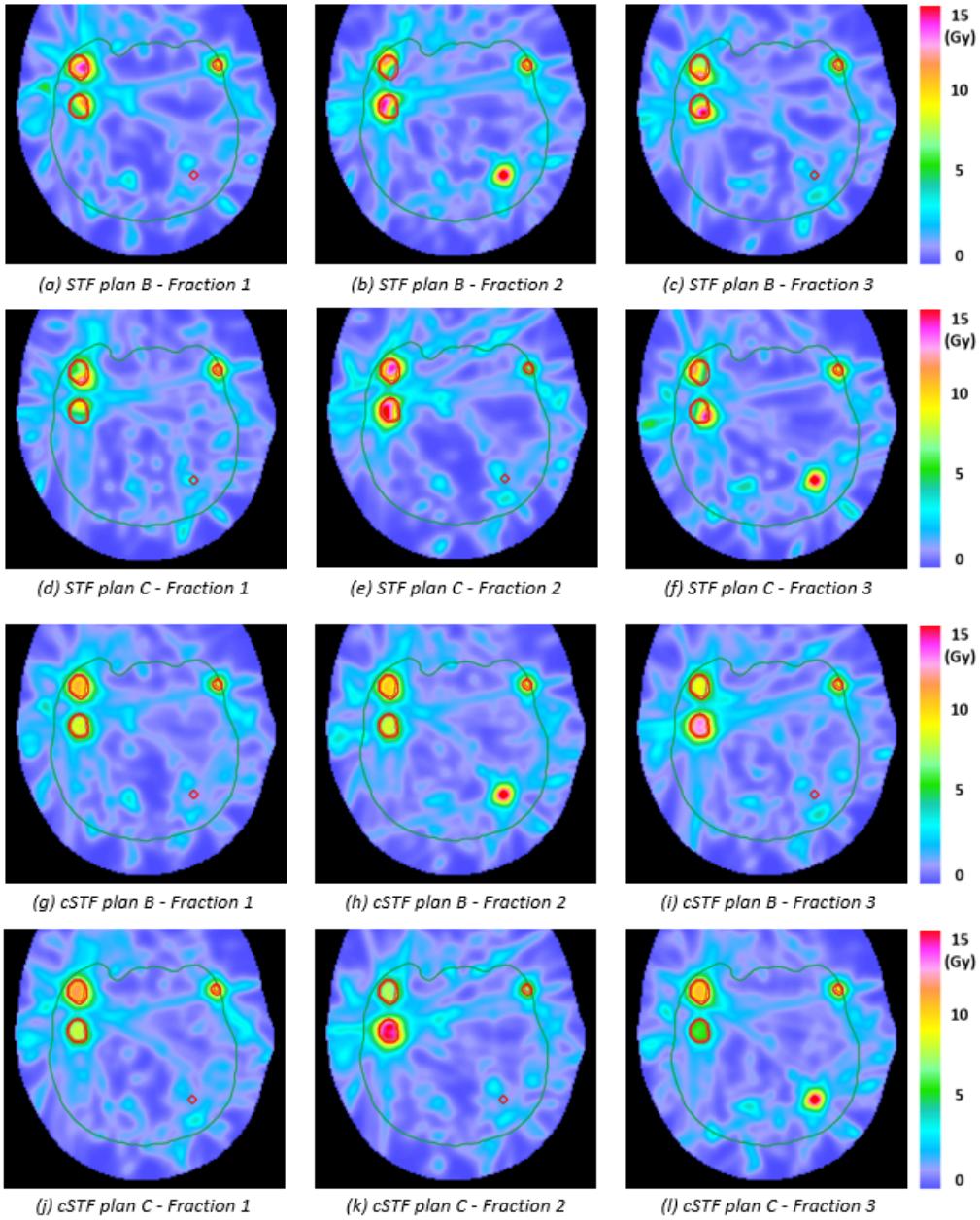

Figure 3C.5: *Dose distributions for the (a)-(f) STF and (g)-(l) cSTF plans in slice A of patient 1 obtained with different initializations of the fluence maps and the additional optimization variables δ_{mt}'s.*

Chapter 4

A novel stochastic optimization approach for handling misalignments in the delivery of spatiotemporally fractionated treatments

Nathan Torelli[1], Silvia Fabiano[1], Dávid Papp[2], Jan Unkelbach[1]

[1] *Department of Radiation Oncology, University Hospital Zürich and University of Zürich, Switzerland.*

[2] *Department of Mathematics, North Carolina State University, North Carolina, Raleigh, USA.*

4.1 Abstract

Purpose: Spatiotemporal fractionation schemes have recently arisen as a promising technique for healthy tissue sparing. However, because spatiotemporally fractionated treatments have a characteristic pattern of delivering high doses to different parts of the tumor in each fraction, uncertainty in patient positioning may cause target underdosage and compromise tumor control. To overcome this issue, we developed a novel stochastic optimization approach which directly accounts for possible setup errors during the optimization of spatiotemporally fractionated treatments.
Methods: The method considers the expected value $\mathbb{E}(b)$ and standard deviation $\sigma(b)$ of the cumulative BED b in every voxel of the target volume, for several discrete error scenarios. To ensure that a good target dose coverage is achieved in any error scenario, a piecewise quadratic penalty function of the form $[b^{min} - (\mathbb{E}(b) - 2\sigma(b))]_+^2$ is minimized. This approach avoids considering all combinations of discrete error scenarios and in thereby computationally tractable. The proposed method has been used to generate both robust uniformly fractionated (UF) and robust spatiotemporally fractionated (STF) plans for a patient with multiple brain metastases, assuming setup errors of approximately ± 1.2 mm in the left-right, anterior-posterior and cranial-caudal directions.
Results: Using the proposed stochastic programming method, a spatiotemporally fractionated treatment plan could be obtained which is robust against patient setup errors. Interestingly, the robust STF plan maintains the characteristic feature of spatiotemporal fractionation schemes of treating some regions of the target volume to a high dose and other regions to a low dose. At the same time, the robust STF plan maintains a dosimetric benefit over the robust UF plan, reduing the mean brain BED_2 6.6% for a similar target coverage.
Conclusions: A stochastic programming method has been implemented that can mitigate the degradation of the target dose coverage for STF plans in the presence of setup errors. This may facilitate the clinical implementation of spatiotemporal fractionation schemes.

4.2 Introduction

In the previous chapter, we showed that spatiotemporally fractionated treatments can be obtained for patients with multiple brain metastases which are robust against setup uncertainties. This was achieved by introducing a novel planning objective that constrains the spatial dose distribution within

each metastatic lesions to be similar in every fraction, while still allowing for the dose contribution of each fraction to every metastasis to be freely optimized. However, this is only one possible approach to mitigate the detrimental impact of misalignments of the different fractional dose distributions. Other optimization approaches have been proposed in the literature to obtain treatment plans that are robust against setup and motion uncertainties [71]. For example, stochastic programming methods can be used to directly account for intra-fraction setup errors during the plan optimization [72]. These methods do not make any assumption on how the spatial dose distributions should be compartmentalized between the different fractions, but rather simultaneously optimize the dose distributions for multiple errors scenarios associated with discrete shifts in the patient position, and require that the prescribed dose is delivered to the target volume in any error scenario.

Conventional stochastic programming approaches have previously been investigated for spatiotemporally fractionated treatments of patients with liver metastases [69]. It was shown that spatiotemporal fractionation schemes maintain their characteristic pattern of delivering high doses to complementary parts of the tumor in distinct fractions only if the setup errors are assumed to be small. For larger setup errors, spatiotemporally fractionated treatments converged to uniformly fractionated treatments, where the entire target volume is treated with a similar dose in every fraction. In this regard, patients with cranial lesions are expected to maintain a benefit for spatiotemporal fractionation schemes also in the presence of setup errors. One limitation of the previous study is that it was only performed for a single two-dimensional slice of each patient to make the computational effort feasible. Existing scenario-based stochastic optimization approaches are not efficient enough to be directly adapted to the optimization of spatiotemporally fractionated treatments. To make such treatments robust with respect to misalignments of dose contributions from different fractions, they rely on the complete enumeration of all combinations of setup errors in every fraction, which grows exponentially.

To circumvent this issue, in this work we developed a novel robust optimization approach that considers piecewise quadratic penalty functions of the expected value and variance of the cumulative BED in every voxel [73]. The method is demonstrated for a patient with multiple brain metastases and both differences and similarities to the constrained approach to spatiotemporal fractionation proposed in Chapter 2 are discussed.

4.3 Materials and methods

4.3.1 Stochastic optimization of spatiotemporally fractionated treatments

Setup uncertainties

Inter-fractional setup uncertainties are modeled via discrete error scenarios. For each error scenario $s \in S$, different dose-influence matrices $D^{(s)}$ are considered, such that the dose $d_i^{(s)}$ delivered to voxel i for a given fluence $\mathbf{x}$ can be computed as

$$d_i^{(s)} = \sum_j D_{ij}^{(s)} x_j \tag{4.1}$$

where j indexes all the beamlets which contribute to the dose in voxel i.

In this work, dose-influence matrices $D^{(s)}$ at different error scenarios s are obtained from the dose-influence matrix $D^{(0)}$ at the nominal scenario via the static dose-cloud approximation. This means that the dose-influence matrices for different error scenarios can be computed starting from the dose-influence matrix in the nominal scenario as follows:

$$D^{(s)}(x, y, z) = D^{(0)}(f_s(x), g_s(y), h_s(z)) \tag{4.2}$$

where

$$f_s : \mathbb{R} \to \mathbb{R}, \quad x \mapsto x + c_x^{(s)} \tag{4.3}$$

$$f_s : \mathbb{R} \to \mathbb{R}, \quad y \mapsto y + c_y^{(s)} \tag{4.4}$$

$$f_s : \mathbb{R} \to \mathbb{R}, \quad z \mapsto z + c_z^{(s)} \tag{4.5}$$

are rigid transformations that link the voxel position at the coordinates (x, y, z) in the error scenario s to the corresponding voxel position in the nominal scenario, and $c^{(s)} = (c_x^{(s)}, c_y^{(s)}, c_z^{(s)})$ denotes the setup error for the error scenario s. This assumption is justified as the brain consists of a very homogeneous tissue, and shifts in the entry position of a photon beamlet only have a minor impact on the resulting dose distribution.

Incorporation of setup errors into the optimization of spatiotemporal fractionation schemes

As discussed in the previous chapters, spatiotemporally fractionated schemes are generated by simultaneously optimizing multiple dose distributions to be delivered in the different fractions. In this work, we directly incorporate possible inter-fractional setup errors in the optimization of spatiotemporal fractionation schemes by developing a novel piecewise quadratic objective function that considers the expected value and variance of the cumulative BED for the different errors scenarios in every voxel of a structure, and penalizes deviations from the prescribed BED values.

$$\mathbb{E}(b_i) = \sum_{t=1}^{N} \mathbb{E}(b_{it}) = \sum_{t=1}^{N} \left(\sum_{s \in S} p_s b_{it}^{(s)} \right) \tag{4.6}$$

and

$$\mathbb{V}(b_i) = \sum_{t=1}^{N} \mathbb{V}(b_{it}) = \sum_{t=1}^{N} \left[\sum_{s \in S} p_s (b_{it}^{(s)})^2 - \mathbb{E}(b_{it})^2 \right] \tag{4.7}$$

where $b_{it}^{(s)}$ is the BED delivered to voxel i in fraction t for scenario s, N is the total number of fractions and p_s denotes the probability for scenario s.

To ensure that target coverage is achieved in the presence of setup uncertainties, the under- and over-dose planning objectives for the target volume are formulated as

$$f_{under}(\mathbf{b}) = \frac{1}{|TV|} \sum_{i \in TV} \left[b^{min} - \left(\mathbb{E}(b_i) - \delta \sqrt{\mathbb{V}(b_i)} \right) \right]_+^2 \tag{4.8}$$

and

$$f_{over}(\mathbf{b}) = \frac{1}{|TV|} \sum_{i \in TV} \left[\left(\mathbb{E}(b_i) + \delta \sqrt{\mathbb{V}(b_i)} \right) - b^{max} \right]_+^2 \tag{4.9}$$

where b^{min} and b^{max} refer to the prescribed minimum and maximum doses in the target volume TV, and δ is a real scalar. Minimization of these objective functions leads to a spatiotemporally fractionated treatments that aims to achieve that in each voxel within the target volume the expected dose minus δ times the standard deviation exceeds the prescribed dose.

Computational cost

The computation time of the objective function and its gradient is dominated by the calculation of the dose distributions for the individual error scenarios,

which requires the multiplication of the dose-influence matrices $D^{(s)}$ with the corresponding beamlet intensities vector $\mathbf{x}$. The gradient of the objective function in Eq. (4.8) with respect to the intensity of beamlet j in fraction t can be expressed as

$$\frac{\partial f_{under}}{\partial x_{jt}} = \frac{2}{|TV|}\left[b^{min} - \left(\mathbb{E}(b_i) - \delta\sqrt{\mathbb{V}(b_i)}\right)\right]_+ \left(-\frac{\partial \mathbb{E}(b_i)}{\partial x_{jt}} + \delta\frac{1}{2\sqrt{\mathbb{V}(b_i)}}\frac{\partial \mathbb{V}(b_i)}{\partial x_{jt}}\right) \quad (4.10)$$

where

$$\frac{\partial \mathbb{E}(b_i)}{\partial x_{jt}} = \sum_{s\in S} p_s D_{ij}^{(s)}\left[1 + \frac{2d_{it}^{(s)}}{(\alpha/\beta)_i}\right] \quad (4.11)$$

and

$$\frac{\partial \mathbb{V}(b_i)}{\partial x_{jt}} = \sum_{s\in S} p_s D_{ij}^{(s)}\left(b_{it}^{(s)} - \mathbb{E}(b_{it})\right)\left[1 + \frac{2d_{it}^{(s)}}{(\alpha/\beta)_i}\right] \quad (4.12)$$

The gradient for the over-dose penalty function in Eq. (4.9) can be derived analogously.

In our approach, the calculation of the gradient of the objective function benefits from the fact that the variance of the cumulative BED distribution separates into the sum of the variances of each different fractional BED distribution. Due to this property, the calculation of the gradient effectively only requires looping once over all non-zero elements of the different scenarios dose-influence matrices $D^{(s)}$, and hence over $N|S|$ scenarios. More conventional stochastic optimization approaches, in which the objective function is formulated as

$$f_{under}(\mathbf{b}) = \sum_{s\in S} p_s\left[\frac{1}{|TV|}\sum_{i\in TV}(b^{min} - b_i^{(s)})_+^2\right] \quad (4.13)$$

instead require looping over $|S|^N$ scenarios. Hence, the proposed approach avoids the curse of dimensionality.

4.3.2 Clinical case, dose prescriptions and planning study

We retrospectively applied the novel stochastic optimization method to a patient with 29 brain metastases. We first generated a robust uniformly fractionated (UF) plan for the following choice of planning objectives:

1. A BED_{10} of 51.3 Gy is prescribed to the GTV in the nominal scenario. This corresponds to a physical dose of 27 Gy in 3 fractions and used to achieve the desired dose gradient within the metastasis.

2. A BED_{10} b^{min}=43.2 Gy (corresponding to 24 Gy physical dose in 3 fractions) is prescribed to the GTV for all error scenarios, using the novel planning objective in Eq. (4.8). A BED_{10} exceeding b^{max}=60 Gy (corresponding to 30 Gy physical dose in 3 fractions) is penalized quadratically using the planning objective in Eq (4.9). In both cases, we set δ=2.

3. The volume V_{60} of healthy brain (defined as the brain without the PTV) receiving a BED_2 larger than 60 Gy is minimized.

4. The mean brain BED_2 is minimized.

5. The mean BED_2 to the normal tissue except the brain is minimized.

In addition, the BED_2 in all voxels at a distance larger than 5 mm from the PTV boundary was constrained to be lower than 36 Gy. The planning objective 2 has been evaluated assuming setup errors of approximately ± 1.2 mm in the left-right, anterior-posterior and cranial-caudal directions, which correspond to a shift of 1 voxel. The probabilities p_s were set to $2/(|S|+1)$ for the nominal scenario and to $1/(|S|+1)$ for all other scenarios.

Subsequently, a robust STF plan is optimized aiming to minimize objective 4 under the additional constraints that the other objectives are no worse than for the UF plan. The robust STF plan was compared to the robust UF plan in terms of brain BED_2 reduction, and the sensitivity of both plans to setup uncertainties was studied.

4.4 Results

The dose distributions for the robust UF and STF plans are shown in Fig. 4.1. For the UF plan, stochastic optimization extended the irradiated region around the GTV of each metastasis to achieve sufficient GTV dose coverage under setup errors, similar to the situation in which a safety margin is used. Interestingly, the STF plan maintains the characteristic pattern of spatiotemporal fractionation schemes also in the presence of setup errors, where distinct regions of the larger metastases are treated to a high dose in different fractions. Compared to STF plans optimized using a safety margin and assuming no setup errors (see Fig. 3.1 in Chapter 3), however, the spatial dose distributions within the individual metastases are more similar

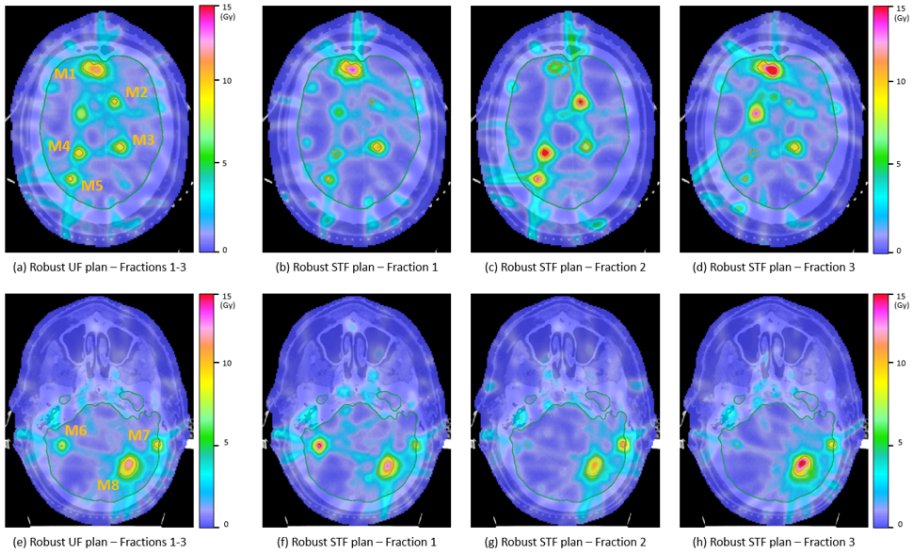

Figure 4.1: *Fractional dose distributions for the robust UF and STF plans, for two different CT slices of the patient.*

in between the different fractions for the robust STF plan. This is illustrated in Fig. 4.2, which compares the dose profiles in the left-right and anterior-posterior directions delivered in the different fractions to metastasis M8 shown in Fig. 4.1e-h for both the robust STF plan and the STF plan obtained using safety margins and assuming no setup errors. Consequently, the robust STF plan is also less sensitive to setup errors. As demonstrated in Fig. 4.3, where the dose-volume histograms for the GTV of metastases M1 and M8 are evaluated for different combinations of setup errors, misalignments of the fractional dose distributions do not lead to a considerable degradation of the GTV dose coverage, similar to the robust UF plan.

Spatiotemporal fractionation schemes maintain a benefit over uniform fractionation schemes also in the presence of setup uncertainties. The mean brain BED_2 is reduced by 6.6% for the robust STF plan compared to the robust UF plan. Although a one-to-one quantitative comparison with the results obtained in Chapter 3 using the safety margin approach is not possible due to slight differences in the optimization settings used to generate the different plans (which result in a different trade-off between target coverage and sparing of the healthy brain), the dosimetric benefit of the robust STF plan over the robust UF plan appears to be reduced compared to the situation when no inter-fractional misalignments are assumed (in that case, the mean brain BED_2 was reduced by 13.1% for the STF plan compared to the UF plan).

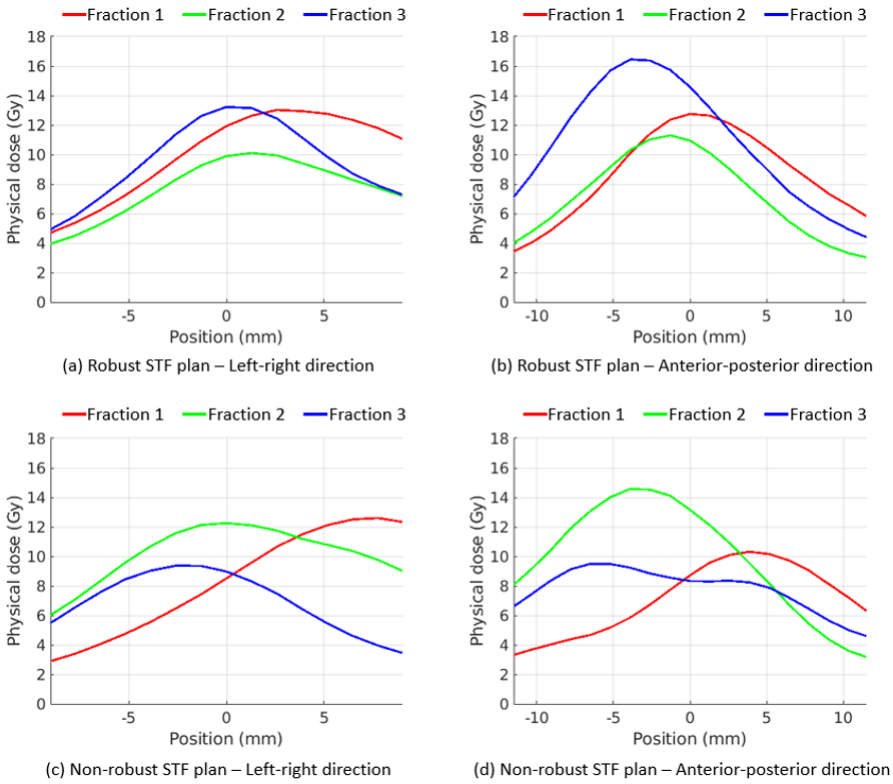

Figure 4.2: *Dose profiles in metastasis M8 along the left-right and anterior-posterior directions for (a)-(b) the robust STF plan and (c)-(d) the STF plan optimized for the nominal scenario using a safety margin.*

4.5 Discussion

In this study, we developed a stochastic programming approach which directly accounts for potential setup errors during the optimization of spatiotemporal fractionation schemes, including misalignments of the dose contributions of different fractions. We demonstrated that robust STF plans can be obtained which still maintain a dosimetric benefit over UF plans and for which good target coverage is maintained also in the presence of setup erros. By considering the expected cumulative BED and the BED variance over the different error scenarios, the proposed robust optimization approach avoids the complete enumeration of all combinations of setup errors in every fraction and is thereby computationally efficient.

Compared to the constrained spatiotemporal fractionation approach presented in Chapter 3, STF plans optimized with the proposed stochastic programming approach are not constrained to deliver a similar spatial dose dis-

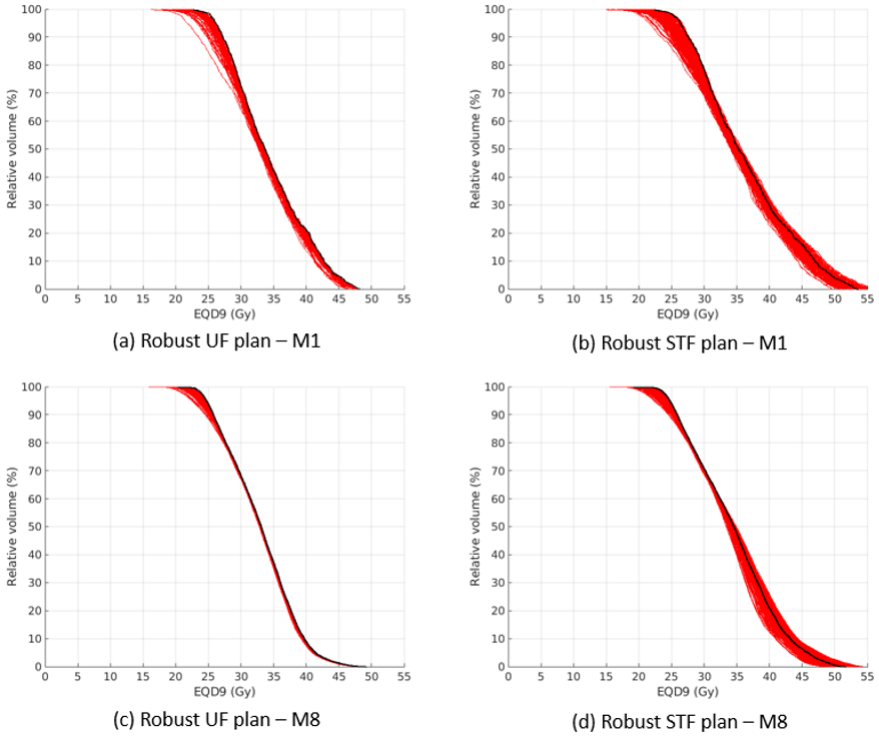

Figure 4.3: *Dose-volume histograms evaluated for the GTVs of metastases M1 and M8 for the nominal scenario (black line) and for all 7^3-1=342 possible combinations of setup errors.*

tribution within each lesion. As a result, STF plans are obtained which still treat certain regions of large metastases to a higher dose and other regions to a lower dose. While this is expected to potentially lead to better dosimetric results, uncertainties regarding the biological response of the metastases to partial tumor irradiation remain. Thereby, robust STF plans obtained using the proposed stochastic programming method represent an intermediate solution between STF plans obtained using the traditional margin approach and optimized for the nominal scenario only, and STF plans obtained using the constrained spatiotemporal fractionation approach proposed in the previous chapter.

Patients with multiple brain metastases are promising candidates for spatiotemporal fractionation schemes, as setup errors are expected to be very small. Additional work may be performed to investigate whether robust STF plans can be obtained which improve on UF plans also for other treatments sites where larger setup errors are possible (e.g. lung or liver cancer).

4.6 Conclusion

Misalignments of the different fractional dose distributions of a spatiotemporally fractionated plan may cause target underdosage. Setup errors can be accounted for via stochastic optimization of spatiotemporally fractionated treatments, while still maintaining a dosimetric benefit over conventional uniformly fractionated treatments.

Chapter 5

Robust optimization of spatiotemporally fractionated radiotherapy treatments to handle uncertainties in the biologically effective dose model

Nathan Torelli[1], Jan Unkelbach[1]

[1] *Department of Radiation Oncology, University Hospital Zürich and University of Zürich, Switzerland.*

A manuscript on this work is in preparation.

5.1 Abstract

Purpose: Spatiotemporal fractionation schemes are optimized based on the cumulative BED in all fractions, assuming fixed α/β-ratios for the tumor and the normal tissue. Although the BED model has been widely used in clinical practice to compare different fractionation schemes, there is uncertainty regarding which fractionation schemes are really isoeffective, which can be interpreted as uncertainty in the BED model parameters. Also, there are concerns about the validity of the BED model at very low and very high doses per fraction. In this work, we investigate the sensitivity of spatiotemporally fractionated treatments to such biological uncertainties and develop a stochastic optimization method to directly account for biological uncertainties in the optimization of spatiotemporal fractionation schemes.
Methods: An extension of the BED model is proposed, which introduces a dose-dependence on the α/β ratio, which allows to model deviations of the expected biological effect from the standard BED model at very low and very high doses per fraction. The sensitivity of both STF and UF plans on variations of the parameters of the extended BED model is investigated for a patient with liver metastases and a patient with a large arteriovenus malformation. A stochastic programming method which optimizes a treatment for multiple discrete scenarios with different model parameters is developed and used to generate robust UF and STF plans.
Results: The UF plans are almost insensitive to variations of the BED model parameters. The STF plans, per counter, present differences in the degree of tumor hypofractionation depending on the different BED model parameters used for the optimization. In particular, the benefit of spatiotemporal fractionation increases for small values of α/β in the tumor, where high single-fraction doses are expected to be more effective. Consequently, the expected target BED_{10} coverage may degrade if a STF plan is optimize for a specific value for the α/β-ratio in the tumor and evaluated for a different α/β-ratio in the tumor. The robustly optimized STF plans, instead, show a much reduced sensitivity to variations of the BED model parameters and at the same time maintain part of the dosiemtric benefit of spatiotemporal fractionation.
Conclusions: The optimal solution to spatiotemporal fractionation is dependent on the BED model parameters used in the optimization. However, the sensitivity of the STF plans to biological uncertainties can be mitigate using an appropriate stochastic optimizations method.

5.2 Introduction

Spatiotemporal fractionation schemes have recently arisen as a promising treatment approach for tumor dose escalation and normal tissue sparing. In contrast to conventional fractionation techniques, spatiotemporally fractionated treatments vary the dose distribution in each fraction, with the aim to exploit the fractionation effect optimally. The goal of spatiotemporal fractionation schemes is to approximate an ideal treatment that would achieve tumor hypofractionation and at the same time deliver a conventionally fractionated dose to the surrounding normal tissue. Spatiotemporal fractionation schemes in part accomplish this by delivering high single-fraction doses to complementary parts of the tumor in every fraction, while distributing the normal tissue dose more uniformly over all fractions. Consequently, spatiotemporal fractionation schemes necessitate a lower cumulative physical dose compared to conventional treatments to achieve the same level of tumor control, what translates into a net reduction of the biological dose in the normal tissue.

Prior in-silico studies have demonstrated the potential of spatiotemporally fractionated treatments to improve the therapeutic ratio compared to conventionally fractionated radiotherapy treatments for multiple treatments sites, using both proton therapy [28,29] and rotational photon therapy [30-32]. However, the impact of biological uncertainties on the quality of spatiotemporal fractionation schemes was not investigated. In all prior work, the biologically effective dose (BED) model was used to describe the fractionation effects, assuming fixed α/β-ratios for the tumor and the normal tissue [21]. Although the BED model has been widely used in clinical practice to compare different fractionation schemes, there are uncertainties regarding which fractionation schemes are really isoeffective, which can be interpreted as uncertainties in the α/β-ratios. Depending on the tumor stage, the selected clinical endpoint and other patient related factors, a wide variation in the α/β-ratios was reported in the literature [74]. In addition, radiobiological experiments in-vitro and in preclinical models raise concerns about the validity of the BED model across a large range from very low to very high doses per fraction [75]. For example, at very low doses some cell lines exhibit a hyper-radiosensitivity and the BED model fails to describe the measured in-vitro cell-survival curves [76]. At very high doses, instead, damage to the vasculatory environment may cause deviations from the radiation response predicted by the standard BED model [77]. It is unclear to what extend such effects observed in a laboratory setting translate into a deviation from the BED in a clinical setting. Nevertheless, uncertainty in biological effectiveness may potentially affect the therapeutic efficacy of spatiotemporal frac-

tionation schemes and must be addressed before a clinical implementation of spatiotemporal fractionation.

Several extensions of the linear-quadratic (LQ) model have been proposed in the literature to better fit the measured in vitro cell survival curves, which may be used to motivate extensions of the standard BED model [78]. For example, the linear-quadratic-cubic model introduces a third fit parameter proportional to the cube of the dose, whereas the linear-quadratic-linear model modifies the LQ model such that it has a maximum slope followed by a linear response at high doses. Other strategies have been explored to provide a more mechanistic explanation for altering the LQ model. These approaches include transitioning smoothly between the LQ model and a multi-target model, or integrating adjustments for dose protraction and lesion interaction. Also, there have been some attempts to describe higher order biological effects, such as incomplete repair of radiation damage between fractions, repopulation of tumors over the course of the treatment, accelerated repopulation effects, the effect of chemotherapeutic agents, and reoxygenation of hypoxic tumors. The latter models typically introduce a time-dependence in the cell response to radiation, and are beyond the scope of this study.

In this work, we incorporate uncertainties in the LQ model by proposing an extension of the standard BED model which describe the situation that the α/β-ratios in the high dose region may be different from those in the low dose region, where a dose-dependent α/β-ratio is suggested. This results in a cubic dependence of the BED on the dose per fraction, similar to the linear-quadratic-cubic model. To account for uncertainties in the extended BED model parameters during the optimization of spatiotemporal fractionation schemes, we use stochastic programming methods. In this way, spatiotemporally fractionated treatments can be obtained which are more robust against biological uncertainties. The impact of biological uncertainties on the expected benefit of spatiotemporal fractionation schemes is investigated for two treatment sites previously considered as promising candidates for spatiotemporal fractionation, i.e. large liver metastases and large arteriovenous malformations.

5.3 Materials and methods

5.3.1 Modeling the fractionation effects

Standard BED model

The standard BED model is commonly used in clinical practice to compare different fractionation schemes. It specifies that two radiotherapy treatments

that deliver the same BED to the tumor (or normal tissue) are isoeffective (or isotoxic), where the BED b_i in voxel i is defined for a n-fraction treatment delivering the same physical dose d_i in all fractions as

$$b_i = n d_i \left(1 + \frac{d_i}{(\alpha/\beta)_i}\right) \tag{5.1}$$

Here, $(\alpha/\beta)_i$ denotes the α/β-ratio of the tissue that voxel i belongs to and quantifies the fractionation sensitivity of that tissue.

In previous studies on spatiotemporal fractionation, Eq. (5.1) has been generalized to the situation in which a treatment delivers possibly different doses in distinct fractions. In such a case, the cumulative BED b_i over the entire treatment is expressed as

$$b_i = \sum_{t=1}^{n} d_{it} \left(1 + \frac{d_{it}}{(\alpha/\beta)_i}\right) \tag{5.2}$$

where d_{it} is the physical dose delivered to voxel i in fraction t.

Extended BED model

To account for possible deviations from the standard BED model when delivering low and high doses to the target volume in distinct fractions, we propose an extension of the standard BED model which describes the situation in which the α/β-ratios in the low dose and high dose regions may be different from the α/β-ratio that is typically used for comparing conventionally fractionated treatments. This extension of the standard BED model is derived by introducing a dose-dependence in the α/β-ratio:

$$\frac{1}{\alpha/\beta} \rightarrow \frac{1}{\alpha/\beta}\left(1 + \kappa(d - d_{ref})\right) \tag{5.3}$$

where d_{ref} is the dose per fraction in a reference fractionation scheme near which the standard BED model is approximately valid and κ is a parameter that can describe deviations from the standard BED model far away from the reference dose per fraction d_{ref}. This leads to the extended BED model

$$b_i^{ext} = \sum_{t=1}^{n} d_{it} \left[1 + \frac{d_{it}}{(\alpha/\beta)_i}\left(1 + \kappa(d - d_{ref})\right)\right] \tag{5.4}$$

Here, we can distinguish between two situations:

- $\kappa > 0$ describes the situation that for large (small) doses per fraction, the BED increases more (less) than predicted by the standard BED

model. In practice, this can be used to model conservative normal tissue constraints (conservative prescription doses for tumors).

- $\kappa < 0$ describes the situation that for large (small) doses per fraction, the BED increases less (more) than predicted by the standard BED model. In practice, this can be used to model conservative prescription doses for tumors (conservative normal tissue constraints).

Mathematically, the extended BED model in Eq. (5.4) leads to a cubic rather than quadratic dependence of the BED on the physical dose, similar to other models proposed in the literature.

In this work, we constrained the parameter κ in the extended BED model to only assume values in a certain range, such that the BED is a monotonically increasing function with respect to the dose per fraction:

$$\frac{\partial b_i^{ext}}{\partial d_i} > 0 \tag{5.5}$$

This leads to the following boundaries for the parameter κ in the extended BED model:

$$\kappa \in \left]-\frac{2d_i + (\alpha/\beta)_i}{|3d_i^2 - 2d_{ref}d_i|}, +\frac{2d_i + (\alpha/\beta)_i}{|3d_i^2 - 2d_{ref}d_i|}\right[\tag{5.6}$$

Examples of fractionation schemes which are assumed to be equieffective according to the extended BED model are shown in Fig. 5.1 for different model parameters α/β and κ. In this example, we assume that a dose of 40 Gy in 5 uniform fractions is prescribed to the PTV. For the standard BED model and α/β=10 Gy this is equieffective to 22.3 Gy in a single fraction or 56.2 Gy in 20 fractions (yellow curve in Fig. 5.1b). Decreasing α/β in the standard BED model makes large doses per fraction more effective and small doses less effective (purple curve). For α/β=5 Gy, a dose of 20.4 Gy in a single fraction is sufficient to achieve the BED equivalent to 40 Gy in 5 fractions. On the other hand, the dose in 20 fractions would have to be increased to 63.6 Gy. Analogously, increasing α/β in the standard BED model makes large doses per fraction less effective and small doses more effective. The extended BED provides a second parameter κ to control the effectiveness of small and large fraction doses independently. The case α/β=10 Gy and κ=0.02 Gy^{-1} (green curve) also makes a single fraction dose of 20.4 Gy equivalent to 40 Gy in 5 fractions. Thus, large doses per fraction are similarly effective as in the standard BED model for α/β=5 Gy. However, small doses per fraction remain relatively effective.

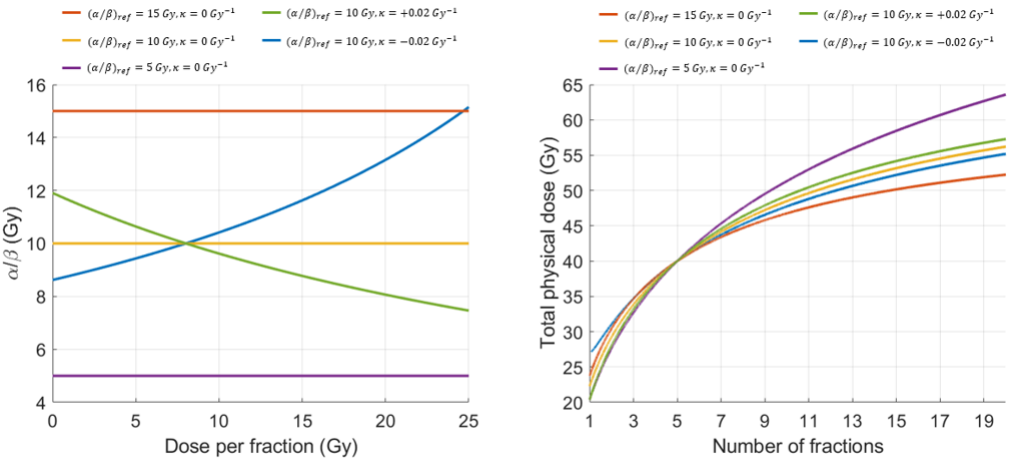

(a) Dose-dependent α/β in the extended BED model

(b) Equieffective fractionation schemes

Figure 5.1: *(a) Value of the dose-dependent α/β-ratio in Eq. (5.3) as a function of different BED model parameters. (b) Equieffective fractionation schemes for different BED model parameters.*

5.3.2 Treatment planning methodology

Optimization of spatiotemporal fractionation schemes

Spatiotemporally fractionated treatments are generated by simultaneously optimizing n possibly distinct fluence maps $\{\mathbf{x}_1, ..., \mathbf{x}_n\}$ for each of the n fractions in an IMRT plan. To directly account for the fractionation effects during the optimization, planning objectives and constraints are evaluated for the cumulative BED rather than for the physical dose. Formally, the treatment plan optimization problem reads

$$\begin{aligned}
\underset{\mathbf{x}_1,\ldots,\mathbf{x}_n}{\text{minimize}} \quad & f(\boldsymbol{b}) && && (5.7)\\
\text{subject to} \quad & c_m(\boldsymbol{b}) \leq u_m && \forall m && (5.8)\\
& b_i = \sum_{t=1}^{n} d_{it}\left(1 + \frac{d_{it}}{(\alpha/\beta)_i}\right) && \forall i && (5.9)\\
& d_{it} = \sum_j D_{ij} x_{jt} && \forall i, \forall t && (5.10)\\
& x_{jt} \geq 0 && \forall j, \forall t && (5.11)
\end{aligned}$$

where f is an objective function to be minimized, c_k are a set of constraints indexed by k with upper bounds u_k and D_{ij} denotes a dose-influence matrix

element storing the physical dose contribution of beamlet j to voxel i per unit intensity.

Stochastic programming methods for handling uncertainties in the BED model parameters

There is uncertainty in the clinical knowledge of which fractionation schemes are truly isoeffective. Mathematically, this corresponds to uncertainties in the BED model parameters (i.e. the α/β-ratio and κ parameters in the extended BED model in Eq. (5.4)). In this work, we directly incorporate such uncertainty in biological effectiveness into the treatment plan optimization through stochastic programming methods. Treatment plan optimization is performed based on a weighted sum of objective functions, where the summation happens over multiple combinations of α/β-ratios and κ parameters. Over- and under-dose quadratic penalty functions for target coverage are then expressed as

$$f_{under}(\mathbf{b}) = \sum_{s\in S} p_s \sum_{i\in TV} \left[\sum_{t=1}^{n} \left(d_{it} + \frac{d_{it}^2}{(\alpha/\beta)_i} \left(1 + \kappa_s (d_{it} - d_{ref})\right) \right) - n_{ref} \left(d_{ref} + \frac{d_{ref}^2}{(\alpha/\beta)_i} \right) \right]_+^2 \quad (5.12)$$

and

$$f_{over}(\mathbf{b}) = \sum_{s\in S} p_s \sum_{i\in TV} \left[n_{ref} \left(d_{ref} + \frac{d_{ref}^2}{(\alpha/\beta)_i} \right) - \sum_{t=1}^{n} \left(d_{it} + \frac{d_{it}^2}{(\alpha/\beta)_i} \left(1 + \kappa_s (d_{it} - d_{ref})\right) \right) \right]_+^2 \quad (5.13)$$

respectively, where d_{ref} is the prescribed dose per fraction to the target volume TV in a reference fractionation scheme with n_{ref} fractions, and p_s denotes the probability of scenario s with α/β-ratio $(\alpha/\beta)_s$ and κ parameter κ_s. Minimization of these objective functions will yield a treatment plan that aims to deliver a biological dose to the target volume that is at least as effective as the reference fractionation scheme for any pair $\{(\alpha/\beta)_s, \kappa_s\}$ assumed in the uncertainty set.

In this work, $(\alpha/\beta)_s$ and κ_s are simulated by randomly sampling from truncated Gaussian distributions with parameters $\{\mu_{\alpha/\beta}, \sigma_{\alpha/\beta}\}$ and $\{\mu_\kappa, \sigma_\kappa\}$, respectively, where only positive values for $(\alpha/\beta)_s$ and values for κ_s in the range $[-1/d_{ref}, +1/d_{ref}]$ are accepted[a]. We set the number of scenarios to S=100 and assign an equal probability $p_s = 1/S$ to each scenario s.

[a] Values for κ_s in this range should fulfill the constraint in Eq. (5.6) for most of the values of $(\alpha/\beta)_s$ assumed in this study and for dose values which are typically adopted in clinical practice.

Optimization algorithm

To find a local minimum of the optimization problem, we use our own implementation of the L-BFGS quasi-Newton method, together with an augmented Lagrangian method for handling constraints. To allow for the dose distributions in the distinct fractions to possibly diverge, fluence maps are initialized with small random intensities (varying in between the different fractions of the spatiotemporally fractionated plans). Calculation of the dose-influence matrix elements D_{ij} is performed with the open-source radiotherapy planning research platform CERR [44] using a quadrant infinite beam (QIB) algorithm [63].

5.3.3 Clinical cases

We retrospectively investigated the impact of biological uncertainties on the quality of spatiotemporal fractionation schemes for two patients, who have previously been identified as promising candidates for spatiotemporal fractionation. Patient 1 has four large metastases located in the right lobe of the liver, and is used for illustration in the results section. The total GTV volume is 319 cc and a 3 mm isotropic margin expansion has been applied to the GTV to obtain the PTV. Patient 2 has a large arteriovenous malformation (AVM) located in the right frontal lobe with a volume of 30 cc.

5.3.4 Treatment planning study

For both patient 1 and patient 2, we generated uniformly fractionated (UF) and spatiotemporally fractionated (STF) plans for different fixed values for the α/β-ratio and the parameter κ in the extended BED model. The dosimetric benefit of spatiotemporal fractionation as compared to conventional uniform fractionation is evaluated for different parameters of the extended BED model, and the sensitivity of the different fractionation schemes to uncertainties in the α/β-ratio and parameter κ are investigated. Afterwards, UF and STF plans are optimized using stochastic programming methods aiming to mitigate the impact of these uncertainties. For simplicity, we only assume uncertainties in the BED model parameters used for the target volume, while the standard BED model with a fixed α/β-ratio is used to model the fractionation effect in the normal tissue.

Patient 1

For patient 1, 5-fraction stereotactic body radiotherapy (SBRT) UF plans are first optimized for the following planning objectives:

1. A $\text{BED}_{\alpha/\beta}$ equivalent to 40 Gy in 5 fractions (i.e. d_{ref}=8 Gy) is prescribed to the PTV (excluding the GTV). A $\text{BED}_{\alpha/\beta}$ exceeding $\text{BED}_{\alpha/\beta}$ values equivalent to 50 Gy in 5 fractions are penalized quadratically.

2. A $\text{BED}_{\alpha/\beta}$ equivalent to 50 Gy in 5 fractions is prescribed to the GTV, again using piecewise quadratic penalty functions.

3. The dose has to be conformal to the PTV. This is implemented via a normal tissue objective which limits the BED_3 to the normal tissue by steepening the dose gradient.

4. The mean BED_3 to the healthy liver (defined as liver without PTV) is minimized.

Subsequently, 5-fraction STF plans are generated aiming to minimize the planning objective 4, under the constraints that the objectives 1-3 are no worse than the corresponding UF plans. Hence, the benefit of spatiotemporal fractionation is directed on reducing the mean liver BED_3. Finally, a robust UF plan and a robust STF plan are optimized for the planning objectives in Eq. (5.12) and Eq. (5.13), assuming the same physical dose prescriptions are for objectives 1 and 2, along with the planning objectives 3 and 4. For these robust optimizations, we assumed $\mu_{\alpha/\beta}$=10 Gy, $\sigma_{\alpha/\beta}$=5 Gy, and μ_κ=0 Gy^{-1} and σ_κ=0.02 Gy^{-1}.

Both the UF and STF plans consisted of 19 equispaced 6 MV photon beams, which approximate a full VMAT arc at a couch angle of 0°. The bixel size is set to 5 x 5 mm^2 and a non-uniform dose grid size is used throughout the body, with small voxels of 5.1 x 5.1 x 2.5 mm^3 in size that are used in the PTV and close to the PTV, where a larger dose gradient is expected. At a distance between 2 cm and 4 cm from the PTV edge, medium-size voxels are used with 8-fold volume, whereas at distances larger than 4 cm from the PTV edge large-size voxels are used with 64-fold volume. All dosimetric results, however, are evaluated based on the finest (small) dose grid size.

Patient 2

Analogously, for patient 2 we generated 4-fraction stereotactic radiotherapy (SRT) plans for different BED model parameters using both uniform and spatiotemporal fractionation schemes. Successively, a robust UF plan and a robust STF plan are optimized for the planning objectives in Eq. (5.12) and Eq. (5.13).

Details regarding the planning objectives and the optimization setup used for patient 2 are reported in the Supplementary material, Appendix A.

5.4 Results

In the following, we present the results obtained for patient 1. Similar results are obtained also for patient 2 and are reported in the Supplementary material, Appendix B.

5.4.1 Characterization of spatiotemporal fractionation schemes for different parameters of the BED model

First, we characterize the STF plans obtained for different BED model parameters. The effect of varying both the α/β-ratio and the parameter κ in the extended BED model on the resulting fractional dose distributions and on the expected benefit over UF plans is studied.

Different α/β-ratios, fixed κ

Fig. 5.2 shows the fractional dose distributions obtained for the UF and STF plans optimized assuming α/β-ratios for the PTV of $(\alpha/\beta)_T$=5 Gy, $(\alpha/\beta)_T$=10 Gy and $(\alpha/\beta)_T$=15 Gy, respectively, and a fixed parameter κ=0 Gy^{-1} (i.e. the standard BED model is considered). Almost no differences are observed between the different UF plans when different α/β-ratios are assumed for the PTV. Also, qualitatively similar STF plans are obtained. A more quantitative analysis reveals that spatiotemporal fractionation schemes present a higher degree of hypofractionation in the target volume for small values of $(\alpha/\beta)_T$. This is illustrated in Fig. 5.4a, which shows the maximum relative single-fraction doses received by all voxels belonging to the PTV for the different STF plans. By achieving such higher degree of hypofractionation in the PTV, the STF plans optimized for small values of $(\alpha/\beta)_T$ necessitate a lower physical dose in the PTV to achieve the same level of tumor control. As the normal tissue dose is distributed more uniformly over all fractions, this translates into a net reduction of the BED_3 in the healthy liver. The mean liver BED_3 for the STF plans is reduced compared to the corresponding UF plans by 18.6% for $(\alpha/\beta)_T$ = 5 Gy, 13.3% for $(\alpha/\beta)_T$ = 10 Gy and 9.8% for $(\alpha/\beta)_T$ = 15 Gy, for a similar PTV dose coverage.

Fixed α/β-ratios, different κ

The fractional dose distributions obtained for the UF and STF plans assuming an α/β-ratio for the tumor of 10 Gy and different parameters κ of -0.02 Gy^{-1}, 0.0 Gy^{-1} and +0.02 Gy^{-1} are illustrated in Fig. 5.3. Again, the UF plans are almost insensitive to variations of the parameter κ. In fact, as

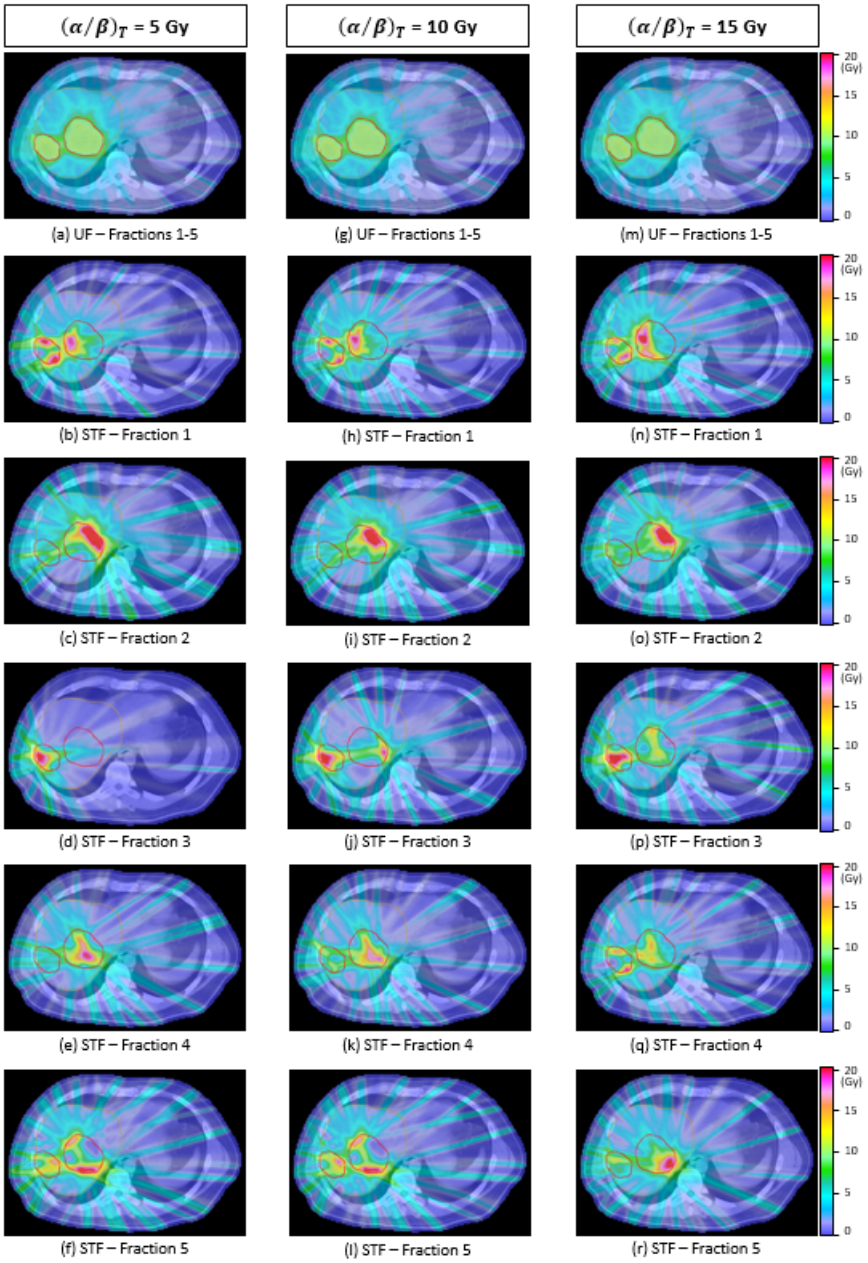

Figure 5.2: *Fractional dose distributions obtained for patient 1 with the UF and STF plans using different α/β-ratios for the target volume of (a)-(f) 5 Gy, (g)-(l) 10 Gy and (m)-(r) 15 Gy, respectively. The parameter κ is fixed to 0 Gy^{-1} for all plans.*

the UF plans aim to deliver a uniform dose d_{ref} to the entire target volume,

the effects of the additional term in the extended BED model only has a very little effect on the cumulative BED delivered to the PTV. On the other hand, changes in the parameter κ of the extended BED model lead to variations of the dose distributions obtained for the STF plans. As also shown in Fig. 5.4b, when negative values for κ are assumed, fewer PTV voxels receive high single-fraction doses. In fact, high doses per fraction are less effective when a negative value of κ is assumed in the extended BED model (Fig. 5.1b), and the corresponding tumor hypofractionation would not compensate for the loss of uniform fractionation in the healthy liver. Positive values of κ, instead, represent a favorable situation for STF (Fig. 5.1b). The mean liver BED_3 for the STF plans is reduced compared to the corresponding UF plans by 6.3% for κ = -0.02 Gy^{-1}, 13.3% for κ = 0 Gy^{-1} and 18.3% for κ = +0.02 Gy^{-1}, for a similar PTV dose coverage.

Sensitivity of the STF and UF plans to uncertainties in the BED model parameters

Fig. 5.5 shows the dose-volume histograms (DVHs) for the PTV for each UF and STF plan (i.e. both optimized for fixed BED model parameters and optimized using the stochastic approach), evaluated for all different scenarios. Although STF plans have the potential to better spare the healthy liver compared to UF plans, STF plans are also more sensitive to uncertainties in the BED model parameters compared to the UF plans. For example, if a STF plan is optimized for $(\alpha/\beta)_T$= 5 Gy but evaluated for $(\alpha/\beta)_T$ = 10 Gy, there will be some underdosage in the hypofractionated PTV regions (Fig. 5.5g). Such underdosage is even more extreme in the situation where $(\alpha/\beta)_T$ = 10 Gy and κ = -0.02 Gy^{-1} (because high doses are even less effective).

5.4.2 Robustly optimized treatment plans

The dose distributions for the STF and UF plans obtained using stochastic programming methods are shown in Fig. 5.6. Thus, the robust STF still shows the characteristic features of spatiotemporal fractionation. The robustly optimized STF plan aims to find a trade-off between the optimal fractionation schemes for the single-scenario situations, and thereby avoids to excessively hypofractionate the dose in the tumor (see also Fig. 5.7). In this manner, such a treatment plan is more robust against biological uncertainties compared to STF plans optimized for fixed values of $(\alpha/\beta)_T$ and κ, and can partly mitigate the detrimental effects of biological uncertainties on the PTV dose coverage. This is demonstrated in Fig. 5.5l.

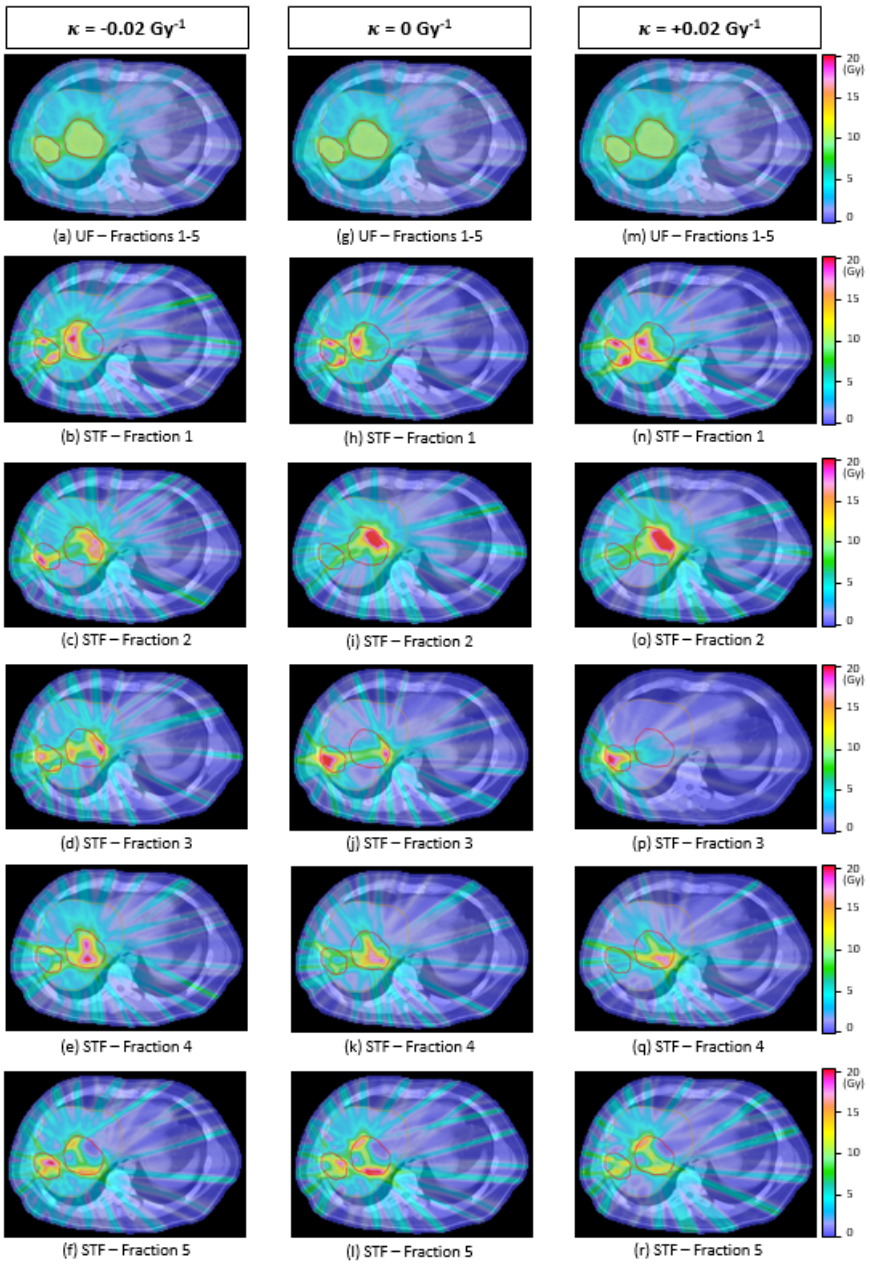

Figure 5.3: *Fractional dose distributions obtained for patient 1 with the UF and STF plans using different κ parameters for the target volume of (a)-(f) -0.02 Gy^{-1}, (g)-(l) 0 Gy^{-1} and (m)-(r) +0.02 Gy^{-1}, respectively. The α/β-ratio is fixed to 10 Gy for all plans.*

At the same time, some of the dosimetric benefits of spatiotemporal fractionation schemes are maintained. The robustly optimized STF plans still

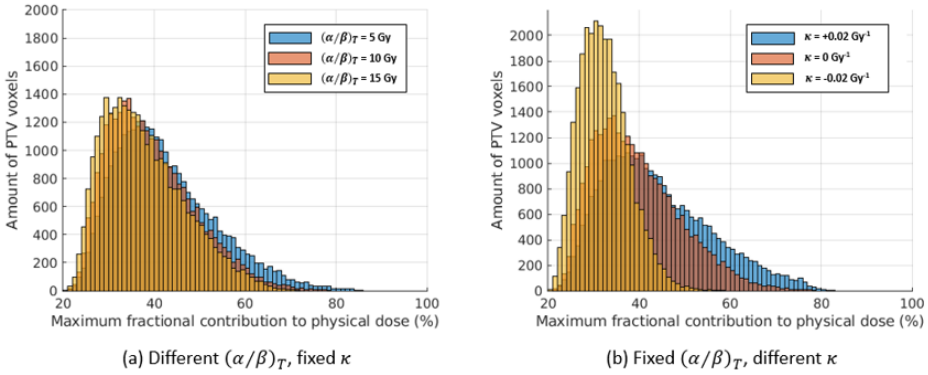

Figure 5.4: *Maximum relative dose contribution of each fraction to the PTV voxels for (a) STF plans obtained using different $(\alpha/\beta)_T$-ratios and a fixed parameter κ, and (b) a fixed $(\alpha/\beta)_T$-ratio and different values for the parameter κ.*

reduces the mean liver BED_3 compared to the robustly optimized UF plan by 4.5%. Thus, the benefit of spatiotemporal fractionation over conventional uniform fractionation is lower compared to STF plans optimized for $(\alpha/\beta)_T$ and κ fixed to their mean values. The residual benefit is comparable to the benefit obtained when STF plans are optimized for unfavorable values of $(\alpha/\beta)_T$ and κ.

5.5 Discussion

In this study, we investigated the impact of uncertainties in the BED model parameters on spatiotemporal fractionation schemes. We first investigated how STF plans vary when optimized for different but fixed values of the BED model parameters α/β and κ in the tumor. It was observed that the qualitative features of STF plans are preserved (for the range of values considered here). However, the benefit of spatiotemporal fractionation schemes over conventional uniform fractionation schemes is higher if the α/β-ratio in the tumor is low, as hypofractionation in the tumor becomes more effective. This result is in line with previous studies which showed that for small values of the ratio $\frac{(\alpha/\beta)_T}{(\alpha/\beta)_{OAR}}$ hypofractionation improves on standard fractionation [22]. In that regard, methods to accurately determine tumor- and patient-specific α/β-ratios would be helpful to identify patients who are expected to benefit the most from spatiotemporal fractionation schemes.

We then investigated the robustness of STF plans optimized for fixed BED model parameters against uncertainty in these parameters. It was demon-

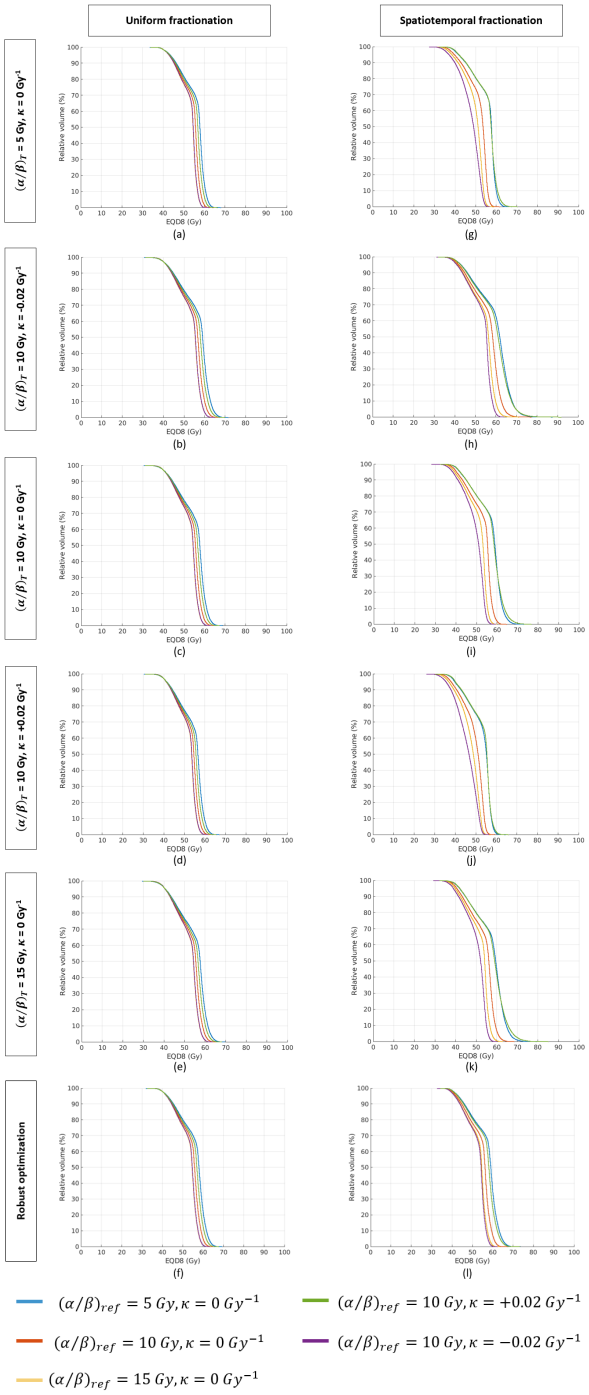

Figure 5.5: *Dose-volume histograms for the PTV evaluated for the equieffective dose EQD8 assuming different values for the BED model parameters* $(\alpha/\beta)_T$ *and* κ*.*

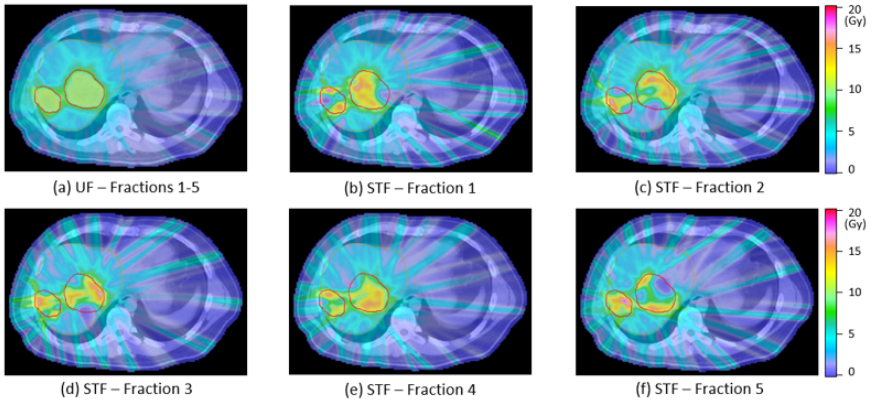

Figure 5.6: *Fractional dose distributions obtained for patient 1 with the UF and STF plans using stochastic programming methods.*

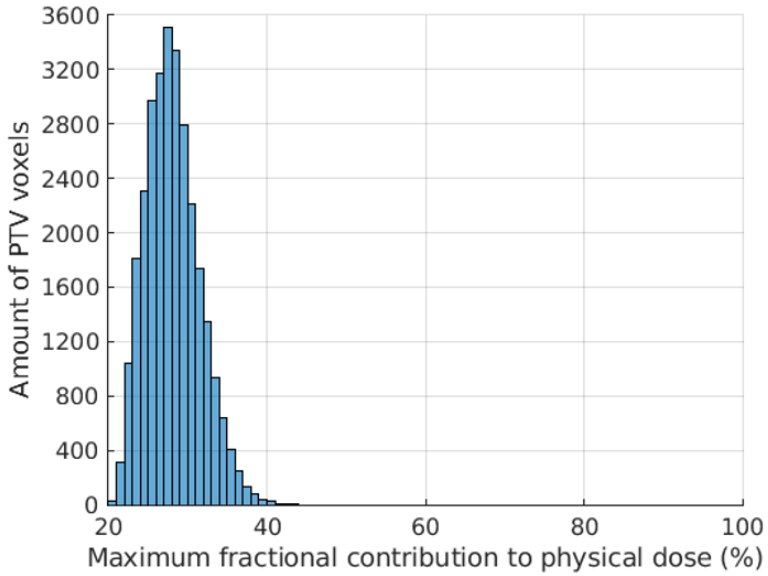

Figure 5.7: *Maximum relative dose contribution of each fraction to the PTV voxels for the robustly optimized STF plan.*

strated that STF plans are quite sensitive to variations of both the α/β-ratio in the tumor and the parameter κ introduced in the extended BED model. These uncertainties may compromise the therapeutic efficacy of spatiotemporal fractionation schemes. To overcome this issue, we proposed a stochastic programming method to directly account for these potential uncertainties in the biological response of the tumor during the plan optimization, and demonstrated that STF plans can be obtained which still maintain a consid-

erable dosimetric benefit over conventional UF plans, while at the same time being more robust against uncertainties in the BED model parameters.

The extended BED model assumed in this work can describe deviations of the biological response from what is predicted by the standard BED model at very low and very high doses per fraction. By introducing a dose-dependent α/β-ratio, it leads to a cubic dependence of the BED on the physical dose, similar to the linear-quadratic-cubic model. Nevertheless, several alternative models have been proposed in the literature to improve on the LQ model, which may have a different impact on the resulting spatiotemporal fractionation schemes. In particular, in this study we did not model biological effects related to partial tumor irradiation, nor effects such as tumor repopulation and development of radiation resistance. Also, we assumed that dose distributions in each fraction are delivered as planned and add up to the prescribed BED in every part of the target volume. However, setup and motion errors may lead to misalignments of the different fractional dose distributions, resulting in cold and hot dose spots within the PTV.

Future work may combine robust optimization approaches to handle biological uncertainties with robust optimization approaches to handle setup and motion uncertainties. Also, research in radiobiology may lead to the development of novel models to describe the fractionation effect, which could then be integrated into the optimization of spatiotemporal fractionation schemes.

5.6 Conclusion

Uncertainties in the BED model and its parameters are a concern regarding the therapeutic efficacy of spatiotemporal fractionation schemes. We developed a stochastic programming approach to directly integrate such uncertainties in the optimization of spatiotemporal fractionation schemes and demonstrated that spatiotemporally fractionated treatment plans can be obtained which are robust against uncertainties in the BED model parameters, while maintaining a dosimetric benefit over uniformly fractionated treatments.

5.7 Supplementary material

Appendix A Treatment plan optimization

In this section, we further detail the treatment plan optimization methods. We provide the mathematical formulation of the planning objectives used in

the treatment plan optimization problem, and discuss the dose calculation algorithm which has been used for computing the dose-influence matrices.

A.1 Patient 1

For patient 1, the objective function in Eq. (5.7) reads as follows:

$$f(\mathbf{b}) = \frac{1}{|GTV|}\sum_{i\in GTV}\left[10\left(50\left(1+\frac{10}{(\alpha/\beta)_T}\right)-b_i^{ext}\right)_+^2+\left(b_i^{ext}-55\left(1+\frac{11}{(\alpha/\beta)_T}\right)\right)_+^2\right] \tag{5A.1}$$

$$+\frac{1}{|P\tilde{T}V|}\sum_{i\in P\tilde{T}V}\left[10\left(40\left(1+\frac{8}{(\alpha/\beta)_T}\right)-b_i^{ext}\right)_+^2+\left(b_i^{ext}-50\left(1+\frac{10}{(\alpha/\beta)_T}\right)\right)_+^2\right] \tag{5A.2}$$

$$+\frac{50}{|NT|}\sum_{i\in NT}(b_i-b_i^{max})_+^2 \tag{5A.3}$$

$$+\frac{10}{|L|}\sum_{i\in L}b_i \tag{5A.4}$$

where GTV denotes the set of voxels belonging to the GTV, $(P\tilde{T}V)$ is the set of voxels belonging to the PTV excluding the GTV voxels, NT denotes the set of voxels belonging to the normal tissue (i.e. the entire body except for the PTV) and L is the set of voxels belonging to the healthy liver (i.e. liver without the PTV). The planning objective in Eq. (5A.3) corresponds to the normal tissue objective (NTO) implemented in the Eclipse Treatment Planning System (Varian Medical Systems, Palo Alto, CA), where b_i^{max} is a voxel-dependent value defined as:

$$b_i^{max} = \begin{cases} b_0, & \text{if } x_i < x_0 \\ b_0 e^{-\kappa(x_i-x_0)} + b_\infty\left(1-e^{-\kappa(x_i-x_0)}\right), & \text{if } x_i \geq x_0 \end{cases} \tag{5A.5}$$

Here, x_i indicates the distance of a normal tissue voxel i from the PTV edge and we set b_0=131.7 Gy, b_∞=15.75 Gy, x_0=0.5 cm and κ=0.6 cm^{-1}. The penalty value b_i^{max} as a function of x_i is schematically illustrated in Fig. 5A.1.

A.2 Patient 2

For patient 2, the different treatment plans are optimized for the following choice of planning objectives:

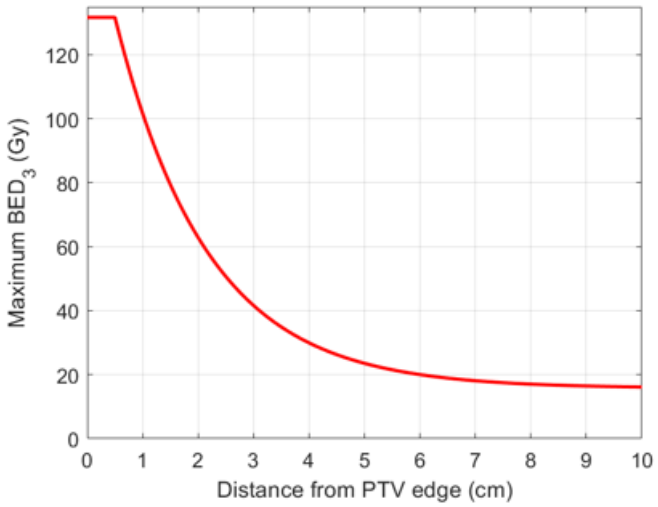

Figure 5A.1: *BED gradient as a function of the distance from the PTV edge required by the normal tissue objective in Eq. (5A.3).*

1. A $\text{BED}_{\alpha/\beta}$ equivalent to 28 Gy in 4 fractions is prescribed to the AVM (implemented via a quadratic penalty function). A $\text{BED}_{\alpha/\beta}$ exceeding $\text{BED}_{\alpha/\beta}$ values equivalent to 40 Gy physical dose in 4 fractions are penalized quadratically.

2. The volume of healthy brain (i.e. brain excluding the AVM) receiving a BED_2 larger than 60 Gy is minimized. This corresponds to a physical dose of 10 Gy in a single fraction and is implemented via a continuous relaxation of a dose-volume objective.

3. The dose has to be conformal to the AVM. This is implemented via a normal tissue objective which limits the dose to the normal tissue by steepening the dose gradient.

4. The mean BED_2 to the healthy brain (i.e. brain without the AVM) is minimized.

Mathematically, these objectives can be expressed as follows:

$$f(\mathbf{b}) = \frac{1}{|AVM|} \sum_{i \in AVM} \left[10 \left(28 \left(1 + \frac{7}{(\alpha/\beta)_T} \right) - b_i^{ext} \right)_+^2 + \left(b_i^{ext} - 40 \left(1 + \frac{10}{(\alpha/\beta)_T} \right) \right)_+^2 \right] \tag{5A.6}$$

$$+ \frac{100}{|B|} \sum_{i \in B} \frac{1}{1 + e^{-(b_i - 60)/0.5}} \tag{5A.7}$$

$$+\frac{1}{|NT|}\sum_{i\in NT}(b_i - b_i^{max})_+^2 \tag{5A.8}$$

$$+\frac{10}{|B|}\sum_{i\in B} b_i \tag{5A.9}$$

where AVM denotes the set of voxels belonging to the arteriovenous malformation, B is the set of voxels belonging to the healthy brain (i.e. brain without the AVM) and NT denotes the set of voxels belonging to the normal tissue (i.e. the entire body except for the AVM).

The parameters for the normal tissue objective in Eq. (5A.7) are set to b_0=115 Gy, b_∞=13.125 Gy, x_0=0.5 cm and κ=0.6 cm^{-1}. For patient 2, we assumed $\mu_{\alpha/\beta}$=4 Gy, $\sigma_{\alpha/\beta}$=2 Gy, and μ_κ=0 Gy^{-1} and σ_κ=0.02 Gy^{-1}. Similar as for patient 1, a non-uniform dose grid size is used, where the size of the smaller voxels is 2.7 x 2.7 x 1.2 mm^3. Nineteen equispaced photon beams are used, with a bixel size of 5 x 5 mm^2 and a photon energy of 6 MV.

A.3 Dose calculation algorithm

Calculation of the dose-influence matrix elements D_{ij} is performed with the open-source radiotherapy planning research platform CERR [59] using a quadrant infinite beam (QIB) algorithm [60].

Appendix B Results for patient 2

In this section, we report the results obtained for patient 2.

B.1 Characterization of spatiotemporal fractionation schemes for different parameters of the BED model

First, we characterize the STF plans obtained for different BED model parameters. The effect of varying both the α/β-ratio and the parameter κ in the extended BED model on the resulting fractional dose distributions and on the expected benefit over UF plans is studied.

B.1.1 Different α/β-ratios, fixed κ

The fractional dose distributions for the UF and STF plans optimized for different α/β-values for the AVM of $(\alpha/\beta)_T$ = 2 Gy, $(\alpha/\beta)_T$ = 4 Gy and $(\alpha/\beta)_T$ = 6 Gy, respectively, and a fixed parameter κ = 0 Gy^{-1} are shown in Fig. 5B.2. Also for patient 2, a higher degree of hypofractionation in the target volume is observed for smaller values of $(\alpha/\beta)_T$. This is also shown in

Fig. 5B.4a. The UF plans do not show any qualitative difference if optimized for different BED model parameters.

The mean brain BED_2 is reduced compared to the corresponding UF plans by 8.1% for the STF plan optimized for $(\alpha/\beta)_T = 2$ Gy, plans by 5.6% for the STF plan optimized for $(\alpha/\beta)_T = 4$ Gy and by 1.9% for the STF plan optimized for $(\alpha/\beta)_T = 6$ Gy. The brain volume V_{60} receiving a BED_2 higher than 60 Gy is reduced by 8.5% for the STF plan optimized for $(\alpha/\beta)_T = 2$ Gy, by 8.7% for the STF plan optimized for $(\alpha/\beta)_T = 4$ Gy and by 3.9% for the STF plan optimized for $(\alpha/\beta)_T = 6$ Gy compared to the corresponding UF plans.

B.1.2 Fixed α/β-ratios, different κ

Fig. 5B.3 illustrates the fractional dose distributions obtained for the UF and STF plans optimized for a fixed α/β-ratio of 4 Gy and different parameters κ of -0.02 Gy^{-1}, 0 Gy^{-1} and +0.02 Gy^{-1}, respectively. Similar to patient 1, much higher doses are delivered to the target volume for positive values of the parameter κ (see Fig. 5B.4b). This also leads to an improved sparing of the healthy brain. Compared to the corresponding UF plan, the STF plan optimized for κ=+0.02 Gy-1 reduces the mean brain BED_2 by 13.2% and the brain volume V_{60} by 14.8%, respectively. The reduction of mean brain BED_2 compared to the corresponding UF plans is 5.6% for the STF plan optimized for κ=0 Gy^{-1} and 1.2% for the STF plan optimized for κ=-0.02 Gy^{-1}, whereas the volume V_{60} of healthy brain exposed to a BED_2 higher than 60 Gy decreases by 8.7% for the STF plan optimized for κ=0 Gy^{-1} and 4.2% for the STF plan optimized for κ=-0.02 Gy^{-1}.

B.1.3 Sensitivity of the STF and UF plans to uncertainties in the BED model parameters

Fig. 5B.5 shows the DVHs for the AVM for each UF and STF plan (i.e. both optimized for fixed BED model parameters and optimized using the stochastic approach), evaluated for all different scenarios. Although STF plans have the potential to better spare the healthy brain compared to UF plans, STF plans are also more sensitive to uncertainties in the BED model parameters compared to the UF plans. For example, if a STF plan is optimized for $(\alpha/\beta)_T = 2$ Gy but evaluated for $(\alpha/\beta)_T = 4$ Gy, there will be some underdosage in the hypofractionated PTV regions (Fig. 5B.5g). Such underdosage is even more extreme in the situation where $(\alpha/\beta)_T = 4$ Gy and κ = -0.02 Gy^{-1}.

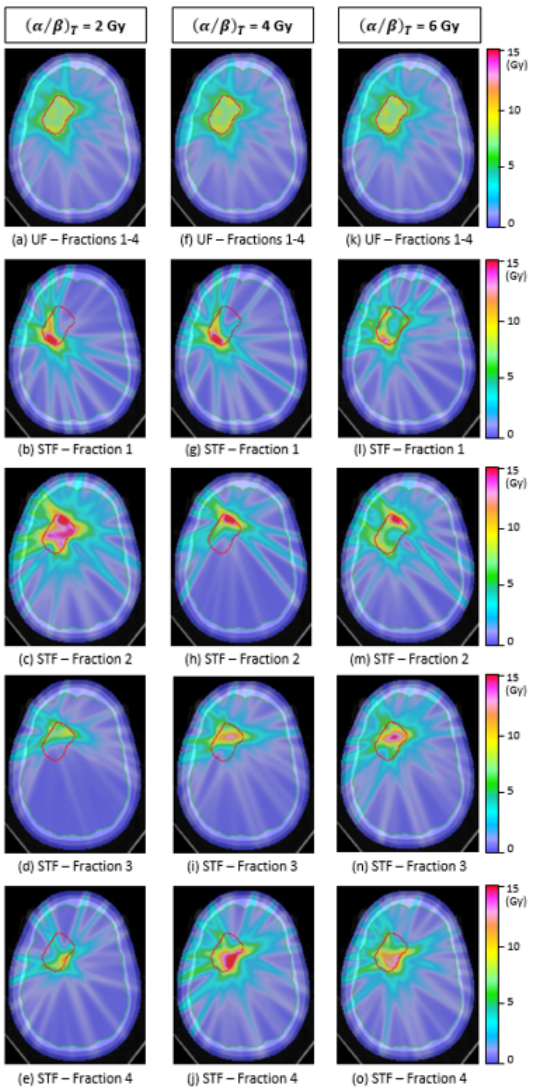

Figure 5B.2: *Fractional dose distributions obtained for patient 2 with the UF and STF plans using different α/β-ratios for the target volume of (a)-(e) 2 Gy, (f)-(j) 4 Gy and (k)-(o) 6 Gy, respectively. The parameter κ is fixed to 0 Gy^{-1} for all plans.*

B.2 Robustly optimized treatment plans

The dose distributions for the STF and UF plans obtained using stochastic programming methods are shown in Fig. 5B.6. Also for patient 2, the robust STF partly preserves the characteristic pattern of treating different parts of the target volume to a higher dose in distinct fractions, while at the same time being very robust against uncertainties in the BED model parameters

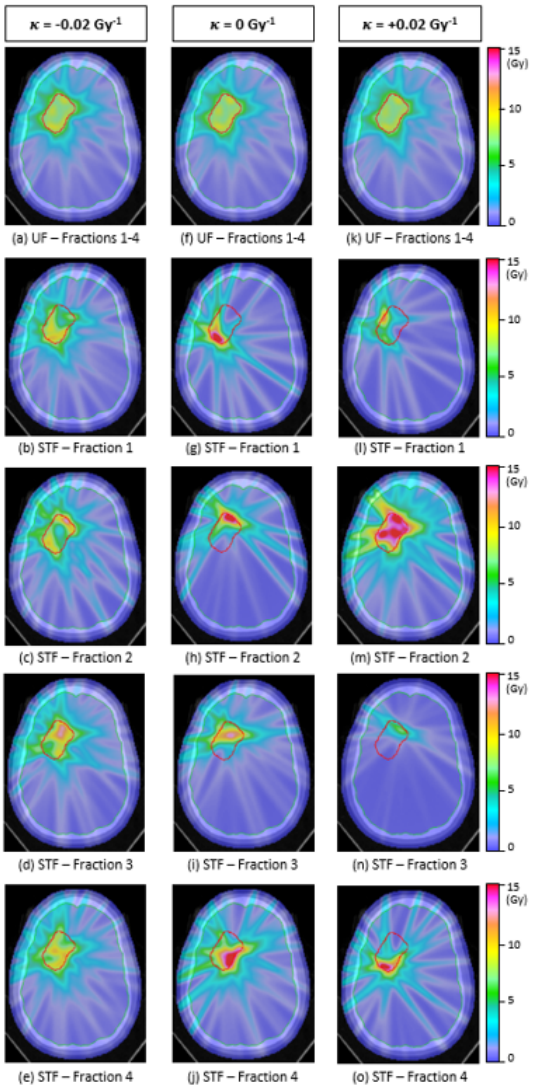

Figure 5B.3: *Fractional dose distributions obtained for patient 2 with the UF and STF plans using different parameters* κ *of (a)-(e) -0.02* Gy^{-1}*, (f)-(j)* 0^{-1} *and (k)-(o)* $+0.02^{-1}$*, respectively. The* α/β*-ratio is fixed to 4 Gy for all plans.*

(Fig. 5B.5l). Nevertheless, the degree of hypofractionation achieved in the target volume for the robust STF plan is lower compared to the degree of hypofractionation achieved for some STF plans optimized for favorable BED model parameters. This is also well illustrated in Fig. 5B.7.

The robust STF plan maintains a dosimetric benefit compared to the robust UF plan. The mean brain BED_2 and brain volume V_{60} receiving a

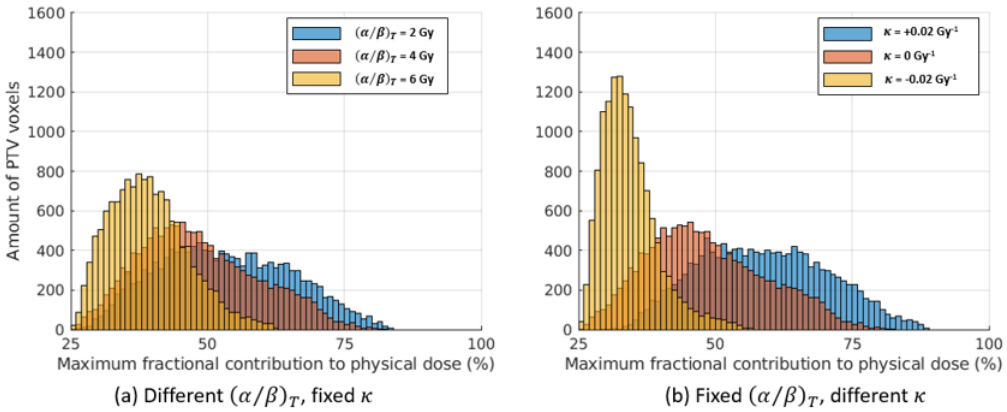

Figure 5B.4: *Maximum relative dose contribution of each fraction to the PTV voxels for (a) STF plans obtained using different $(\alpha/\beta)_T$-ratios and a fixed parameter κ, and (b) a fixed $(\alpha/\beta)_T$-ratio and different values for the parameter κ.*

BED_2 larger than 60 Gy are reduced for the robust STF plan by 3.3% and 8.6%, respectively.

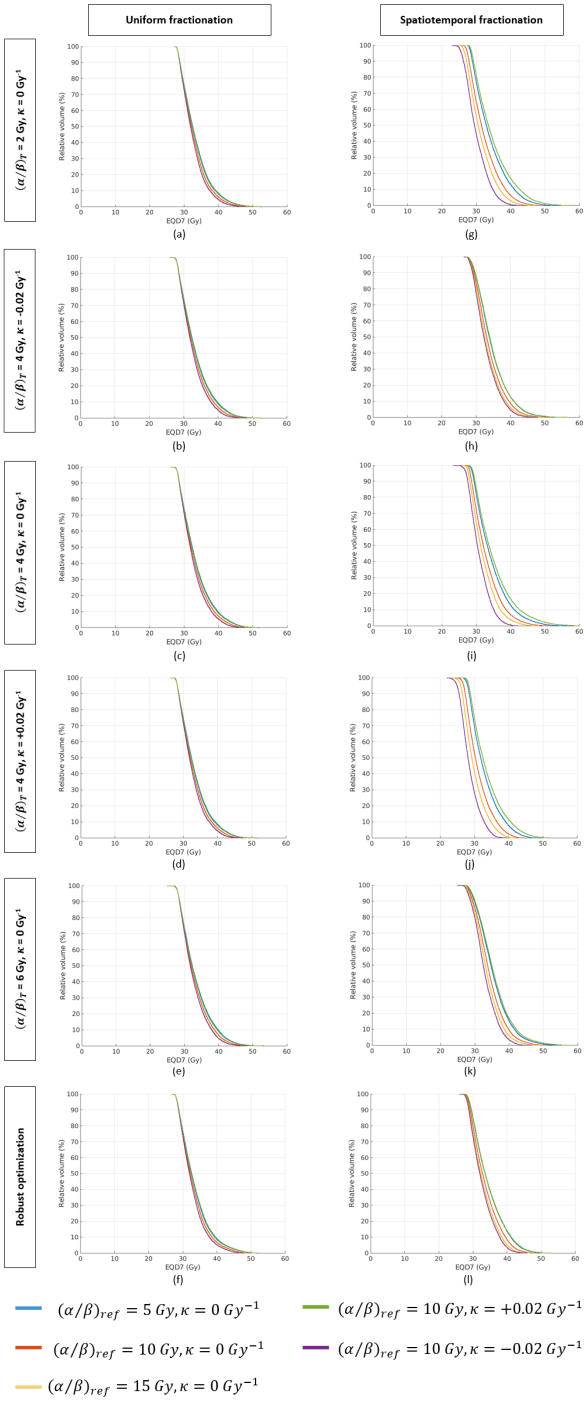

Figure 5B.5: *Dose-volume histograms for the AVM evaluated for the equieffective dose EQD7 assuming different values for the BED model parameters* $(\alpha/\beta)_T$ *and* κ.

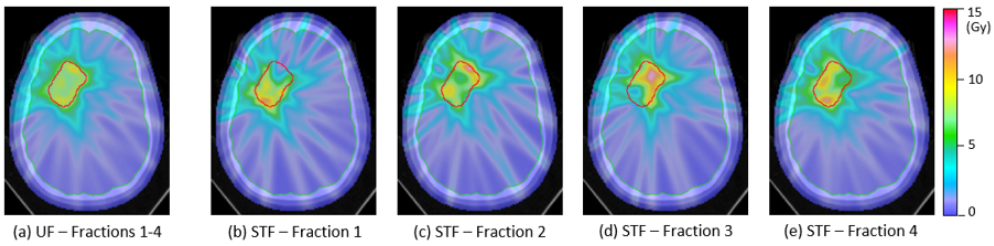

Figure 5B.6: *Fractional dose distributions obtained for patient 2 with the UF and STF plans using stochastic programming methods.*

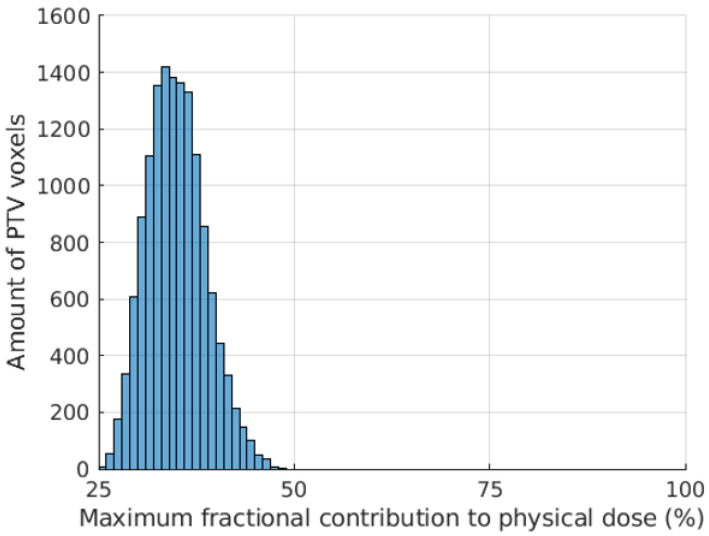

Figure 5B.7: *Maximum relative dose contribution of each fraction to the PTV voxels for the robust STF plan in patient 2.*

Chapter 6

A novel fractionation approach for combined proton-photon therapy of metastatic cancer patients

Nathan Torelli[1], Yves Bicker[1], Louise Marc[1], Silvia Fabiano[1], Jan Unkelbach[1]

[1] *Department of Radiation Oncology, University Hospital Zürich and University of Zürich, Switzerland.*

A manuscript on this work is in preparation.

6.1 Abstract

Purpose: Combined proton-photon therapy (CPPT), where most fractions are delivered with photons and only a few are delivered with protons, may represent a practical approach to optimally use limited proton resources. Previous studies showed that CPPT performs better when an overproportionate dose is delivered to the tumor with the proton fractions. In this study, we extend such an approach by determining the optimal proton and photon dose contributions to individual lesions for patients with multiple metastases.
Methods: CPPT plans are generated by simultaneously optimizing distinct IMPT and IMRT dose distributions based on their cumulative biologically effective dose ($BED_{\alpha/\beta}$). The dose contributions of the proton and photon fractions to each individual metastasis are handled as additional optimization variables in the fluence map optimization problem using a new planning objective, which also ensures that similar spatial dose distributions are delivered within each lesion in all fractions. Five-fraction and three-fraction CPPT plans, in which one fraction is delivered with protons and the remaining fractions with photons, are generated for a patient with 4 liver metastases (patient 1) and a patient with 30 brain metastases (patient 2), respectively, and benchmarked against uniformly fractionated IMRT and IMPT plans.
Results: For patient 1, the IMRT plan achieves a mean liver BED_4 of 29.9 Gy, while this is reduced to 17.0 Gy (-43%) with the CPPT plan and to 16.3 Gy (-45%) with the IMPT plan. Similar results are obtained for patient 2, for which the mean brain BED_2 is reduced compared to the IMRT plan (12.3 Gy) by 27% with the CPPT plan and by 21% with the IMPT plan. The dose contribution of the single proton fraction to the individual metastases varies from 67% to 93% of the tumor BED_{10} for patient 1 and from 24% to 84% of the tumor BED_{10} for patient 2.
Conclusions: CPPT outperforms IMRT in terms of BED reduction to critical organs and approaches (or even improves) the IMPT plan quality, while using only a single proton fraction. The proposed approach allows to deliver different proton dose contributions to distinct metastases, depending on their size and location.

6.2 Introduction

Photon-based stereotactic radiosurgery (SRS) and stereotactic body radiotherapy (SBRT) have recently emerged as promising treatment options for patients with cranial and extra-cranial oligometastatic diseases [79-82], and their role in combination with systemic therapies is well established [83,84].

Per contra, there are only very few clinical studies considering proton therapy for the treatment of oligometastatic cancer patients [85]. Although the superior normal tissue sparing properties of proton beams may considerably reduce the integral dose in selected patients with multiple metastatic lesions, the high cost and scarce availability of proton therapy prevent its wide adoption in the metastatic setting. Most national health policies, in fact, only support the routine commissioning of proton therapy to include tumor indications which are considered curable [86].

To improve the accessibility to proton therapy to a larger patient population, combined proton-photon therapy (CPPT) has recently been proposed [73,87-91]. CPPT treatments aim at delivering some treatment fractions using proton therapy and the remaining fractions using conventional photon therapy. Different from the Dutch model, where it is a binary decision whether to treat a patient with proton-only or photon-only therapy [92], CPPT treatments allow to better distribute the limited proton resources over a larger patient population [87]. Prior research on combined proton-photon therapy focused on how to optimally combine proton and photon fractions. Ten Eikelder et al [88] considered separately generated intensity modulated proton therapy (IMPT) and intensity modulated radiotherapy (IMRT) plans, and optimized the target dose to be delivered with each modality such to minimize the biologically effective dose (BED) in the normal tissue. In most cases, the superior dosimetric properties of proton beams were exploited by delivering a higher dose to the target volume in the IMPT fractions. Unkelbach et al [89] considered simultaneously optimized IMPT and IMRT plans, based on their cumulative BED distribution. They showed that the optimal combination of protons and photons is achieved when non-uniform dose distributions are delivered with the IMPT and IMRT plans, where protons are used to hypofractionate parts of the target volume while photons are used to achieve the fractionation effect in regions of the target volume located close to dose-limiting organs at risk.

While the latter approach may exploit the fractionation effects more optimally, it is also more sensitive to setup and motion errors compared to the method of ten Eikelder et al. As very pronounced dose gradients may appear within the target volume, misalignments of the proton and photon dose distributions could lead to target underdosage and compromise tumor control. This cannot be compensated by adding planning margins around the treated volume, as the dose compartmentalization is automatically determined during the BED-based plan optimization and not decided a priori. For this reason, in this study we consider a novel approach to combined proton-photon therapy for oligometastatic cancer patients, which expands on the work of ten Eikelder et al, while being more robust against setup un-

certainties compared to the method of Unkelbach et al. This approach, which was first proposed by Torelli et al [93] for photon-based stereotactic radiosurgery of multiple brain metastases, consists of treating different metastases to possibly different doses in the IMRT and IMPT fractions, while constraining the spatial dose distribution within each individual metastatic lesion to be homogeneous in every fraction. In this way, some of the metastases can be treated to a high single-fraction dose, what allows to achieve the desired level of tumor control with a lower physical dose. At the same time, a good fractionation effect can be achieved in between the different metastatic lesions and robustness against setup errors can be achieved by adding planning margins around each metastasis as in conventional clinical practice.

In this work, CPPT treatments for oligometastatic cancer patients are created using the proposed planning approach for a patient with multiple brain metastases and a patient with liver metastases, where the optimal dose contribution of the IMRT and IMPT fractions to each metastasis is determined using a novel BED-based objective function. Such CPPT plans are then compared to IMRT-only plans, IMPT-only plans and CPPT plans resulting from a simple proportional combination of IMRT and IMPT plans.

6.3 Materials and methods

6.3.1 Modeling of the fractionation effects

In this work, the fractionation effects are described using the biologically effective dose (BED) model [94]. Similar to the previous work of Unkelbach et al [89], we assume that the standard BED formalism can be generalized to non-stationary fractionation schemes, where different doses may be delivered in the proton and photon fractions. The cumulative BED b_i to voxel i for a CPPT treatment delivering n_X photon fractions and n_p proton fractions is defined as

$$b_i = n^X d_i^X \left(1 + \frac{d_i^X}{(\alpha/\beta)_i}\right) + n^p d_i^p \left(1 + \frac{d_i^p}{(\alpha/\beta)_i}\right) \tag{6.1}$$

where d_i^X and d_i^p are the physical doses delivered to voxel i in the photon and proton fractions, respectively, and $(\alpha/\beta)_i$ is the α/β-ratio of the tissue that voxel i belongs to. The proton dose distribution d^p includes a constant relative biologically effectiveness (RBE) factor of 1.1, which we do not make explicit in Eq. (6.1).

6.3.2 BED-based multi-modality treatment plan optimization

Planning of combined proton-photon treatments is performed by simultaneously optimizing distinct IMRT and IMPT plans, based on their cumulative BED distribution. Formally, the optimization problem reads:

$$\begin{aligned}
\underset{\mathbf{x}^X,\mathbf{x}^p}{\text{minimize}} \quad & f(\mathbf{b}^X + \mathbf{b}^p) && && (6.2)\\
\text{subject to} \quad & c_k(\mathbf{b}^X + \mathbf{b}^p) \leq u_k && \forall k && (6.3)\\
& b_i^\chi = n^\chi d_i^\chi \left(1 + \frac{d_i^\chi}{(\alpha/\beta)_i}\right) && \forall i, \forall \chi && (6.4)\\
& d_i^\chi = \sum_j D_{ij}^\chi x_j^\chi && \forall i, \forall \chi && (6.5)\\
& x_j^\chi \geq 0 && \forall j, \forall \chi && (6.6)
\end{aligned}$$

where $f(\mathbf{b}^X + \mathbf{b}^p)$ is an objective function evaluated for the cumulative BED, $c_k(\mathbf{b}^X + \mathbf{b}^p)$ are a set of constraint functions indexed by k with corresponding upper bounds u_k and $\chi \in \{X, p\}$ denotes the treatment modality used in each fraction (i.e. either photons or protons). For both IMRT and IMPT plans, distinct fluence maps $\mathbf{x}^X$ and $\mathbf{x}^p$ are optimized, which are related to the photon and proton doses via the dose-influence matrices elements D_{ij}^X and D_{ij}^p (storing the dose contribution of photon beamlet or proton pencil beam j to voxel i per unit intensity).

6.3.3 Robust combination of IMRT and IMPT plans for oligometastatic cancer patients

The simultaneous optimization of distinct IMRT and IMPT plans as described in the treatment plan optimization problem in Eq. (6.2)-(6.6) potentially results in highly non-uniform dose distributions within the target volume, when no additional constraints are defined on the individual dose distributions of the photon and proton fractions. This may in turn compromise target coverage in the presence of setup or motion uncertainties. To ensure that a CPPT treatment is robust against inter-fraction setup uncertainties, we constrain both the IMRT and IMPT plans to deliver a similar spatial dose distribution within each metastasis. As a separate planning margin is defined for each metastatic lesion, the resulting CPPT treatment will be less sensitive to setup uncertainties when dose gradients are avoided within each metastasis in both the IMPT and IMRT plans. However, the absolute

dose contribution of each fraction to every individual metastasis is allowed to vary in between the photon and proton fractions, to best achieve the desired dosimetric goals. The optimal photon and proton dose contributions to each metastasis are determined through the following planning objective, which has previously been proposed by Torelli et al [93] for photon-only treatments:

$$f(\mathbf{b}^X, \mathbf{b}^p, \boldsymbol{\delta}^X, \boldsymbol{\delta}^p) = \sum_{m=1}^{M} \sum_{i \in PTV_m} \frac{1}{|PTV|} \left[\left(b_i^X - \delta_m^X (b_i^X + b_i^p) \right)^2 + \left(b_i^p - \delta_m^p (b_i^X + b_i^p) \right)^2 \right] \tag{6.7}$$

Here, M is the total number of metastases and PTV_m is the set of voxels belonging to metastasis m. The parameters δ_m^X and δ_m^p describe the partial BED contributions of the photon and proton fractions to metastasis m, respectively, and are handled as optimization variables to be optimized along with the incident fluences $\mathbf{x}^X$ and $\mathbf{x}^p$. The quadratic penalty terms ensure that similar spatial dose distributions are delivered within each metastasis m in both the IMRT and IMPT plans, corresponding to the cumulative BED $b_i = b_i^X + b_i^p$ scaled by factors δ_m^X and δ_m^p, respectively.

6.3.4 Clinical cases

We retrospectively investigate the proposed approach to CPPT for two metastatic cancer patients. Patient 1 has 30 brain metastases with sizes varying from 0.1 cc to 8.3 cc and a total GTV volume of 20.3 cc. For patient 1, an isotropic margin expansion of 1.2 mm is applied from the GTV to obtain the PTV. Patient 2 has four metastases of varying size located in the right lobe of the liver, with a total GTV volume of 391 cc. For patient 2, an isotropic GTV-to-PTV margin expansion of 3 mm is applied.

6.3.5 Treatment planning study

Multiple brain metastases patient

For patient 1, we first generate a 3-fraction IMPT plan using the following planning objectives:

1. A BED_{10} of 51.3 Gy is prescribed to the GTV. This is implemented via a quadratic penalty function and corresponds to 27 Gy physical dose delivered in 3 fractions.

2. A BED_{10} of 43.2 Gy is prescribed to the PTV (where GTV $\subset$ PTV), corresponding to a physical dose of 24 Gy delivered in 3 fractions. A

BED_{10} exceeding 60 Gy (i.e. 30 Gy physical dose in 3 fractions) is penalized quadratically.

3. The volume V_{60} of healthy brain (i.e. brain-PTV) receiving a BED_2 larger than 60 Gy is minimized. This corresponds to 10 Gy in a single fraction and is implemented via a continuous relaxation of a dose,Äìvolume objective.

4. The mean BED_2 to the normal tissue excluding the PTV and the brain is minimized.

5. The mean BED_2 to the healthy brain is minimized.

The IMPT plan consists of 3 proton beams with gantry and couch angles of (90°, 0°), (270°, 0°) and (90°, 270°), respectively. The proton pencil beams are chosen to have a spacing of 2.5 mm in both the x- and y-directions, with the initial sigma of the Gaussian proton pencil beams at the patient surface ranging from 5.0 mm for a proton energy of 31.7 MeV to 2.3 mm for an energy of 236.1 MeV . The dose-influence matrices for the proton pencil beams are computed using the open-source radiotherapy research platform matRad [95]. Subsequently, a 3-fraction IMRT plan is generated by solving the treatment plan optimization problem in Eq. (6.2)-(6.6) for objective 5, under the additional constraints that objectives 1-4 are no worse than for the IMPT plan. The IMRT plan consists of 46 non-coplanar photon beams, which approximate a full VMAT arc at a couch angle of 0° and three half-arcs from 0° to 180° at couch angles of 45°, 270° and 315°. The beamlet resolution is set to 5x5 mm^2 and the photon energy is set to 6 MV for all beams. Dose calculation for photon beamlets is performed using the open-source radiotherapy research platform CERR [44].

Liver metastases patient

For patient 2, we first generate a 5-fraction IMRT plan using the following planning objectives:

1. A BED_{10} of 100 Gy is prescribed to the GTV. This is implemented via a quadratic penalty function and corresponds to 50 Gy physical dose delivered in 5 fractions.

2. A BED_{10} of 72 Gy is prescribed to the PTV (where GTV $\not\subset$ PTV), corresponding to a physical dose of 40 Gy delivered in 5 fractions. A BED_{10} exceeding 100 Gy is penalized quadratically.

3. The dose has to be conformal to the PTV. This is implemented via normal tissue objective, which limits the BED_4 in the normal tissue by steepening the dose gradient.

4. The mean BED_4 to the normal tissue excluding the PTV and the liver is minimized.

5. The mean BED_4 to the healthy liver is minimized.

The IMRT plan consists of 19 equispaced coplanar beams, which approximate a VMAT arc. Similar to patient 1, the beamlet resolution is set to 5x5 mm^2, the photon energy is set to 6 MV for all beams and dose calculation is performed using the open-source radiotherapy research platform CERR. Then, a 3-fraction IMPT plan is generated by solving the treatment plan optimization problem in Eq. (6.2)-(6.6) for objective 5, under the additional constraints that objectives 1-4 are no worse than for the IMRT plan. The IMPT plan consists of 3 coplanar proton beams at gantry angles of 225°, 270° and 315°. The proton pencil beams are chosen to have a spacing of 5x5 mm in both the x- and y-directions. The dose-influence matrices for the proton pencil beams are computed using the open-source radiotherapy research platform matRad.

6.3.6 Assessing the benefit of CPPT treatments

For both patients, we consider CPPT plans with a single proton fraction and N-1 photon fractions (where N=3 for patient 1 and N=5 for patient 2). To quantify the benefit of the proposed CPPT approach, three CPPT plans are generated with the following characteristics:

I A CPPT plan resulting from a simple proportional combination of the single-modality plans, which treats each metastasis with the same fixed dose in every fraction. We refer to this plan as CPPT_{UF} plan.

II A CPPT plan where the fractional dose contribution to the entire target volume is allowed to be different for the proton and photon fractions, but not for the individual metastases. This plan is optimized using a weighted sum of objectives 5 in both patients and the objective function in Eq. (6.7), under the constraints that the plan is no worse than the IMPT plan (in case of patient 1) and the IMRT plan (in case of patient 2) for all the other objectives 1-4, and that $\delta_m^X = \delta^X \; \forall m$ and $\delta_m^p = \delta^p \; \forall m$. This plan, which is hereafter referred to as $\text{CPPT}_{cSTF}^{(fixed)}$ plan, represents an intermediate scenario in which the superior normal tissue sparing

properties of proton beams can be exploited, but where the fractionation effects are not optimally considered.

III A CPPT plan where the dose contribution of the proton and photon fractions can vary for every individual metastasis. This plan is optimized similar to the previous CPPT plan, but without any constraint on the additional optimization parameters δ_m^X and δ_m^p. This plan can also better exploit the fractionation effects and is hereafter referred to as $\text{CPPT}_{cSTF}^{(variable)}$ plan.

6.4 Results

6.4.1 Multiple brain metastases patient

Fig. 6.1a and Fig. 6.1b show the dose distributions for patient 1 obtained with the IMRT plan and the IMPT plan, respectively, while Fig. 6.1c show the EQD9 distribution of the CPPT_{UF} plan resulting from their simple proportional combination. For a similar PTV dose coverage, the IMPT plan can considerably reduce the mean brain BED_2 compared to the IMRT plan (9.65 Gy vs 12.25 Gy), at the cost of a slightly increased brain volume receiving a BED_2 larger than 60 Gy (42.75 cc vs 41.02 cc). The CPPT_{UF} plan can only slightly improve on the IMRT plan, by reducing the mean brain BED_2 to 11.39 Gy (-7.0%). However, when the dose contribution of the single proton fraction to the PTV is allowed to be increased compared to the dose contribution of the photon fractions, the superior normal tissue sparing properties of the proton beams can be exploited more effectively. The fractional dose distributions for the $\text{CPPT}_{cSTF}^{(fixed)}$ plan are illustrated in Fig. 6.1d-e and their cumulative EQD9 is shown in Fig. 6.1f. The $\text{CPPT}_{cSTF}^{(fixed)}$ plan delivers approximately 11.7 Gy to every metastasis in the single proton fraction, corresponding to 59% of the total prescribed BED_{10} to the PTV (δ_m^p=0.59 $\forall m$). In this way, the mean brain BED_2 can be reduced to 9.22 Gy (-24.7% compared to the IMRT plan), for a similar PTV dose coverage.

By further relaxing the constraint on the fractionation schedule and allowing the proton dose contribution to every individual metastasis to be different, the resulting $\text{CPPT}_{cSTF}^{(variable)}$ plan can make use of the dosimetric properties of the proton beams to hypofractionate some of the metastases, whereas photon beams are used to achieve the fractionation effect in metastases which cannot be treated to a very high single fraction dose (e.g. due to their size or location within the brain) and to improve the dose conformity. The fractional dose distributions and the cumulative EQD9 distribution obtained with the $\text{CPPT}_{cSTF}^{(variable)}$ plan are shown in Fig. 6.1g-h and Fig. 6.1i,

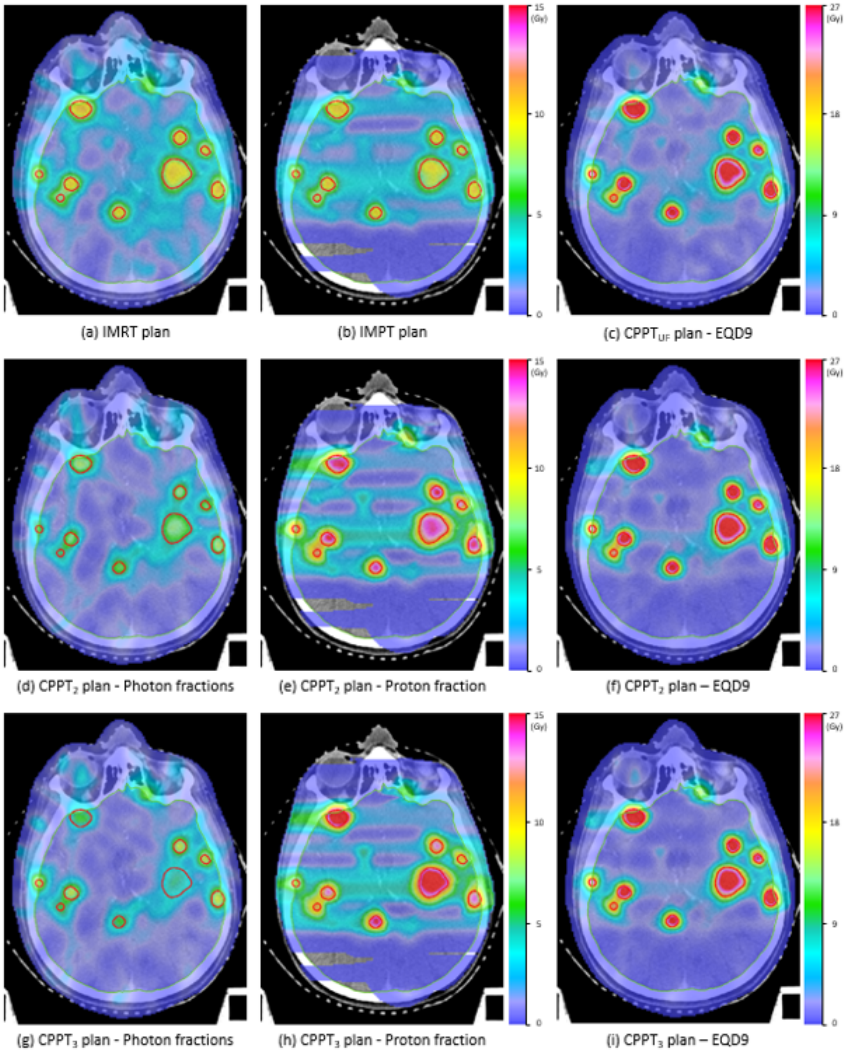

Figure 6.1: *Fractional dose distributions and cumulative EQD9 distributions obtained for patient 1 using the IMRT, IMPT and the three considered CPPT plans.*

respectively. Different from the $CPPT_2$ plan, each metastasis is treated to very different doses in the proton fraction, ranging from 6.3 Gy ($\delta_m^{p(min)}$=0.24) to 14.7 Gy ($\delta_m^{p(max)}$=0.84). The individual dose contributions of the proton fraction to all individual metastases are reported in Fig. 6.2. By more optimally exploiting the fractionation effect, the $CPPT_{cSTF}^{(variable)}$ plan can further reduce the mean brain BED_2 to 9.02 Gy (-26.4% compared to the IMRT plan).

All results are summarized in Table 1.

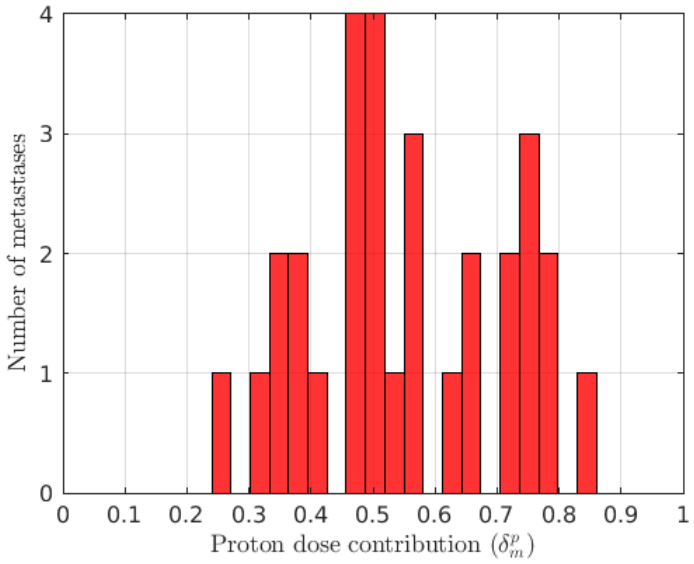

Figure 6.2: *Partial tumor BED_{10} contribution of the single proton fraction of the $CPPT_{cSTF}^{(variable)}$ plan to the 30 brain metastases in patient 1.*

Table 6.1: *Summary of the dosimetric results obtained with the IMRT, IMPT and the three CPPT plans for both patient 1 and patient 2.*

		IMRT	IMPT	$CPPT_{UF}$	$CPPT_{cSTF}^{(fixed)}$	$CPPT_{cSTF}^{(variable)}$
Patient 1	**PTV - Mean BED_{10} (Gy)**	50.3	50.9 (+1.2%)	50.5 (+0.4%)	50.5 (+0.4%)	50.5 (+0.4%)
	Healthy brain - Mean BED_2 (Gy)	12.3	9.7 (-21.2%)	11.4 (-7.0%)	9.2 (-24.7%)	9.0 (-26.4%)
	Healthy brain - V_{60} (cc)	41.0	42.8 (+4.2%)	41.5 (+1.1%)	41.5 (+1.1%)	40.8 (-0.6%)
Patient 2	**PTV - Mean BED_{10} (Gy)**	96.1	95.7 (-0.4 %)	96.1 (-0.1 %)	95.3 (-0.8 %)	95.3 (-0.9 %)
	Healthy liver - Mean BED_4 (Gy)	29.9	16.3 (-45.3%)	27.2 (-9.1%)	18.0 (-39.9%)	17.0 (-43.0%)

6.4.2 Liver metastases patient

Fig. 6.3a-b show the dose distributions obtained for patient 2 using the IMRT and IMPT plans, respectively. The IMPT plan reduces the mean liver BED_4 by 45.3% compared to the IMRT plan (16.33 Gy vs 29.87 Gy), for a similar PTV dose coverage. By simply combining the single-modality plans with the same fixed dose per fraction, a $CPPT_{UF}$ plan is obtained which achieves a mean liver BED_4 of 27.16 Gy (-9.1% compared to the IMRT plan), whose cumulative EQD8 distribution is illustrated in Fig. 6.3c. The fractional dose distributions and the cumulative EQD8 distribution for the $CPPT_{cSTF}^{(fixed)}$ plan are shown in Fig. 6.3d-e and Fig. 6.3f, respectively. Similar as for patient 1, the dose contribution to the PTV is considerably increased in the $CPPT_{cSTF}^{(fixed)}$ plan compared to the $CPPT_{UF}$ plan. The single proton fraction delivers a

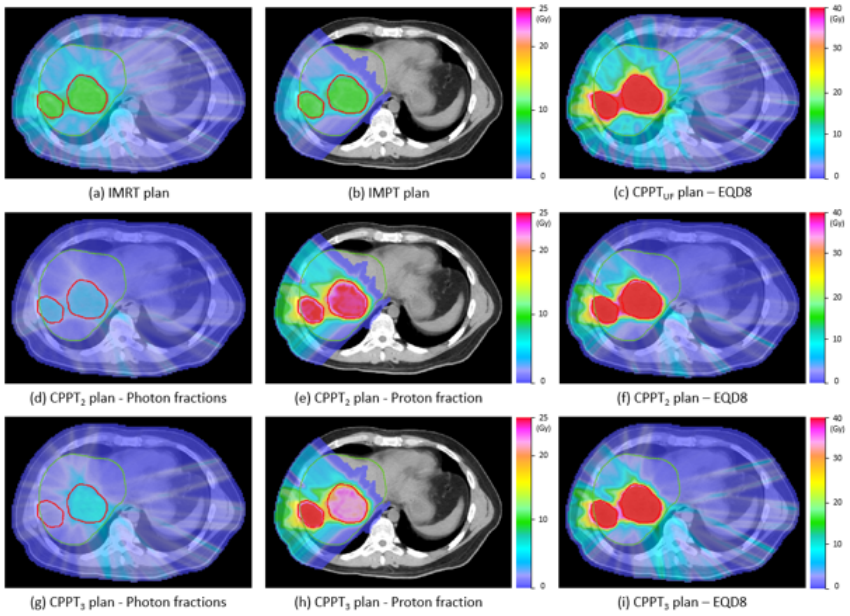

Figure 6.3: *Fractional dose distributions and cumulative EQD8 distributions obtained for patient 2 using the IMRT, IMPT and the three considered CPPT plans.*

dose of approximately 24.2 Gy to all metastases (δ_m^p=0.83 $\forall m$). In this way, the CPPT$_{cSTF}^{(fixed)}$ plan reduces the mean liver BED$_4$ by 39.9% compared to the IMRT plan. When the proton dose contribution to each individual metastasis is allowed to vary, the mean liver BED$_4$ can further be reduced to 17.03 Gy (-43.0% compared to the IMRT plan). The corresponding fractional dose distributions and cumulative EQD8 distribution for the CPPT$_{cSTF}^{(variable)}$ plan are shown in Fig. 6.3g-h and Fig. 6.3i, respectively. In particular, the bridge dose in between the two metastases shown in Fig. 6.3 can better fractionated in the CPPT$_{cSTF}^{(variable)}$ plan, resulting in a lower cumulative EQD8 in between the two metastases. Fig. 6.4 reports the partial BED$_{10}$ contribution of the proton fraction to the individual metastases, which vary from 21.4 Gy ($\delta_m^{p(min)}$=0.67) for the largest lesion to 25.9 Gy ($\delta_m^{p(max)}$=0.93).

The results obtained for patient 2 are summarized in Table 1.

6.5 Discussion

Proton therapy might be an effective treatment modality for oligometastatic cancer patients. Due to their normal tissue sparing properties, proton beams could considerably reduce radiation-induced toxicities, thereby positively im-

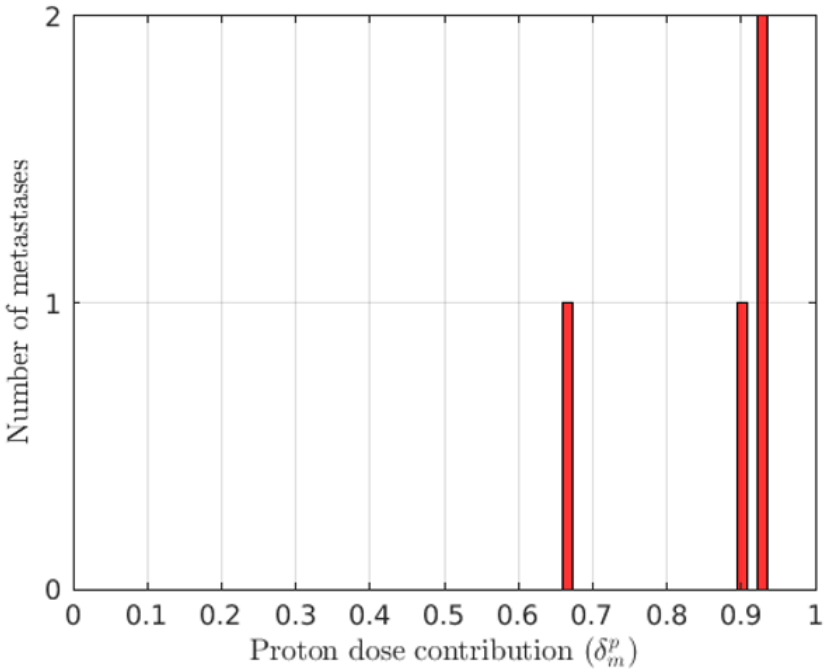

Figure 6.4: *Partial tumor BED_{10} contribution of the single proton fraction of the $CPPT_{cSTF}^{(variable)}$ plan to the 4 liver metastases in patient 2.*

pacting both the overall survival and quality of life. However, proton therapy is still scarcely available and most of the available resources are currently directed onto the treatment of selected tumor indications, preventing the enrollment of oligometastatic cancer patients in clinical studies with proton therapy. In this work, we demonstrated that proton therapy is potentially beneficial for the treatment of oligometastatic diseases and presented an approach to combined proton-photon therapy for metastatic cancer patients which can approximate or even outperform the dosimetric quality of IMPT-only treatments while using only few proton fractions. Combined proton-photon therapy may thereby facilitate the clinical implementation of proton therapy for the treatment of oligometastatic patients, with minor impact on the limited proton resources.

The proposed approach to CPPT treatments is specifically designed for patients with multiple metastases. By determining the optimal proton dose contribution to each individual metastasis, it expands on the previous work of ten Eikelder et al [85], where the same proton dose contribution is delivered to the entire target volume. In this way, not only the more favorable dosimetric properties of proton beams are considered, but also the fractionation effect is more optimally exploited. In addition, compared to previous

work of Unkelbach et al [89], the proposed approach is more robust against misalignments of the proton and photon dose distributions, as dose gradients within the individual metastases are avoided. Robustness is achieved by the evaluation of a single additional planning objective, and is therefore computationally more efficient compared to previously suggested stochastic optimization approaches that consider multiple errors scenarios for setup errors [90]. Finally, this study also extends on the work of Torelli et al [93], including the combination of multiple particle types. Treating different metastases to a different dose in distinct fractions is indeed not only optimal in terms of the fractionation effects, but can also be used to exploit the different dosimetric characteristics of different treatment modalities.

The optimization of CPPT treatments in this study is based on a generalization of the BED model, which assumes that very different doses can be delivered to the target volume in distinct fractions. In addition, a constant RBE factor of 1.1 is assumed for the proton beams. While many extensions of the BED model have been proposed to incorporate higher-order radiobiological effects [96-99] and variable RBE of protons [100], none of these models is yet established in clinical practice. Therefore, even if it is unclear whether the proposed generalization of the BED model adequately describes the fractionation effects over the whole range of doses per fraction, we argue that this does not generally question the proposed approach. Future work may investigate this approach for other metastatic treatment sites. For lung metastases, the use of photons in combination with protons may also be useful to mitigate range uncertainties related to proton therapy, as previously shown by Amstutz et al [101]. Also, more sophisticated radiobiological model including tumor repopulation and an energy-dependent RBE factor might be investigated.

6.6 Conclusion

Proton therapy has the potential to considerably reduce the normal tissue dose in oligometastatic cancer patients. By treating some metastases to high single-fraction proton doses and using photons to fractionate the dose in metastases which are large or located close to critical organs-at-risk, combined proton-photon treatments can exploit most of the benefits of proton therapy while using fewer of the limited proton resources.

Chapter 7

Fraction-variant radiotherapy treatments: an approach to exploit additional degrees of freedom in radiotherapy treatment planning

Nathan Torelli[1], Jan Unkelbach[1]

[1] *Department of Radiation Oncology, University Hospital Zürich, Switzerland.*

This work has been submitted to *Physics in Medicine and Biology* as an original manuscript.

7.1 Abstract

Objective: In current clinical practice, a single treatment plan is typically generated for each patient and repeatedly delivered over several fractions, using the same fixed set of beam orientations. In this work, we investigate the benefit on the quality of radiotherapy treatments of delivering different, possibly non-uniform dose distributions and using different non-coplanar beam orientations in distinct fractions.
Approach: A biologically effective dose (BED)-based direct aperture optimization (DAO) algorithm is developed, which simultaneously optimizes multiple dose distributions to be delivered in different fractions, together with their corresponding set of aperture shapes and MU weights. Each set of apertures specifies a series of control points along a fraction-specific non-coplanar dynamic trajectory, which consists of a 360° gantry arc with dynamic bi-directional couch rotation and whose gantry-couch path is automatically determined during the treatment plan optimization. Fraction-variant non-coplanar stereotactic radiotherapy treatments are generated using the proposed planning approach for a patient with four large liver metastases (patient 1, 3 fractions) and a patient with a large arteriovenous malformation (patient 2, 4 fractions), and benchmarked against state-of-the-art radiotherapy treatments that delivers the same dose distribution in every fraction using coplanar VMAT arcs.
Main results: Fraction-variant radiotherapy treatments deliver highly non-uniform dose distributions in distinct fractions, which hypofractionate the dose in the target volume while delivering a similar dose bath to the normal tissue. In each fraction, different non-coplanar dynamic trajectories are selected. For a similar target BED coverage in both treatments, fraction-variant treatments reduce the mean liver BED_3 in patient 1 by 27.5% and the mean brain BED_2 in patient 2 by 26.5% compared to state-of-the-art VMAT treatments.
Significance: Delivering different non-uniform dose distributions and utilizing different beam orientations in different fractions can considerably improve the dosimetric quality of radiotherapy compared to state-of-the-art treatments that deliver the same plan in every fraction.

7.2 Introduction

Radiotherapy treatment planning aims at generating a patient-personalized treatment plan that delivers a therapeutic radiation dose to the tumor while sparing the surrounding normal tissue as much as possible. Over the past

few decades, developments of new treatment hardware, such as the multileaf collimator [102] and a robotic treatment couch [103], together with the implementation of more sophisticated planning algorithms [7,104-109] allowed to access previously unutilized degrees of freedom in radiotherapy planning and enormously impacted the quality of radiotherapy treatments. Intensity modulated radiotherapy (IMRT) [104,105] and volumetric modulated arc therapy (VMAT) [106], for example, improved dose conformity and organs-at-risk (OAR) sparing compared to three-dimensional conformal radiotherapy (3D-CRT). The use of non-coplanar beam orientations [7,107-109], either manually selected or determined through beam orientation optimization, may further improve the dose distribution.

However, there are still some degrees of freedom which are not yet fully exploited in conventional radiotherapy treatment planning. In current clinical practice, in fact, a single treatment plan is typically generated for each patient and repeatedly delivered over the course of several fractions, using the same fixed set of beam orientations in every fraction. Further improvements to the quality of radiotherapy treatments may be possible through the delivery of different, possibly non-uniform dose distributions and the use of different beam orientations in distinct fractions.

Deviating from the current rigid planning approach and allowing for different dose distributions to be delivered in distinct fractions may improve the quality of radiotherapy treatments for two reasons. First, a better intensity modulation could be achieved. For step-and-shoot IMRT, the incident fluence is represented by a restricted number of apertures per beam angle [110], and for VMAT only a single aperture per gantry angle is used to limit the treatment delivery time [111]. By allowing different aperture shapes and weights to be delivered in distinct fractions, overall more apertures could be used to approximate the optimal fluence map without increasing the delivery time per fraction. Second, the fractionation effects can be more optimally exploited. Delivering the same dose distribution over multiple fractions is beneficial as most normal tissues can better repair from radiation damage in between the different fractions compared to most tumors. However, tumor cells can also partly repair and repopulate, and thereby a higher total physical dose must be delivered to the tumor to achieve the same level of response when a treatment is fractionated [59]. By delivering different non-uniform dose distributions in distinct fractions, where each fraction treats complementary parts of the target volume to a high dose while the normal tissue dose is more uniformly distributed over all fractions, some degree of hypofractionation can be achieved in the tumor while still exploiting the fractionation effect in the normal tissue. This approach has first been proposed by Unkelbach et al and referred to as spatiotemporal fractionation [31]. Spa-

tiotemporally fractionated treatments have been demonstrated in in-silico studies to considerably improve the therapeutic ratio for several treatment sites compared to treatments that deliver the same dose distribution in every fraction [28,30-32].

Utilizing different beam orientations for the delivery of the different treatment fractions, on the other hand, may allow to use overall more beam angles over the entire treatment course. Typically, the more beam orientations are used for generating a treatment plan, the better the plan quality will be [112]. However, if the same beam orientations are used in each fraction, then the total delivery time increases when a larger number of beam orientations are used, what poses a limit on the maximum achievable dosimetric benefit. O'Connor et al [113] and Gu et al [114] showed for both non-coplanar IMRT and intensity modulated proton therapy (IMPT) treatments that the use of different beam orientations in distinct fractions may either improve the dosimetric quality of a treatment while keeping the delivery time per fraction viable, or alternatively can maintain a good plan quality while lowering the delivery time. In their study, however, a similar dose distribution was delivered within the target volume in every fraction. By combining the use of different beam orientations and the delivery of different non-uniform dose distributions in distinct fractions, the treatment plan quality might be further improved by selecting specific beam orientations for each fraction which are beneficial for treating specific parts of the tumor.

In this study, we investigate the impact on both the dosimetric quality and the delivery efficiency of using different beam orientations and delivering different, possibly non-uniform dose distributions in distinct fractions. A direct aperture optimization algorithm is proposed that simultaneously optimizes multiple dose distributions to be delivered in different fractions, together with their corresponding fraction-specific non-coplanar dynamic trajectories. Non-coplanar dynamic trajectories consist of a treatment technique combining dynamic gantry and couch rotation, and represent an efficient way of delivering non-coplanar radiotherapy treatments using conventional C-arm linear accelerators [8,115-122]. The proposed approach, which extends state-of-the-art radiotherapy practice by exploiting fraction-variant intensity modulation, the use of different non-uniform dose distributions in distinct fractions and patient- and fraction-specific beam orientation optimization, is demonstrated for a patient with large liver metastases and a patient with a large arteriovenous malformation.

7.3 Materials and methods

7.3.1 Optimization methodology

Treatment plans in this study are generated by simultaneously optimizing multiple dose distributions to be delivered in the different fractions, together with their corresponding sets of multileaf collimated apertures and monitor unit (MU) weights. Each set of apertures specifies a series of control points along a fraction-specific non-coplanar dynamic trajectory, which consists of a 360° gantry arc with dynamic bi-directional couch rotation and whose gantry-couch path is automatically determined during the treatment plan optimization. To account for the fractionation effects when different non-uniform dose distributions are delivered in distinct fractions, the cumulative biologically effective dose (BED) is optimized rather than the cumulative physical dose.

The proposed BED-based optimization problem is solved using a direct aperture optimization (DAO) algorithm that has been implemented into our in-house research optimization software. The algorithm combines a column generation based method to iteratively add apertures from promising beam orientations together with a gradient based method for DAO that refines MU weights and aperture shapes at each iteration. The optimization workflow is schematically illustrated in Fig. 7.1 and further detailed in the following.

Column generation based method for selecting apertures from promising beam orientations

Favorable non-coplanar dynamic trajectories for the delivery of each treatment fraction are determined using a column generation based method. This is a heuristic algorithm which iteratively adds suitable apertures from promising beam orientations to a treatment fraction, until all control points along the fraction-specific non-coplanar dynamic trajectories are populated. The algorithm starts by assuming an empty set of apertures $K_t = \emptyset$ for all the fractions $t \in \{1, ..., n\}$ (where n is the total number of fractions). Given a set B of feasible beam orientations, the most promising multileaf collimator (MLC)-based apertures per field and per fraction are determined by evaluating the first-order perturbation for each bixel on the objective function (solving a so called pricing problem [3]). The resulting candidate apertures have an associated price, given by the sum of the gradient contributions of each of the bixels not covered by the MLC, and the apertures with the lowest price in each fraction are added to the treatment plan at each iteration

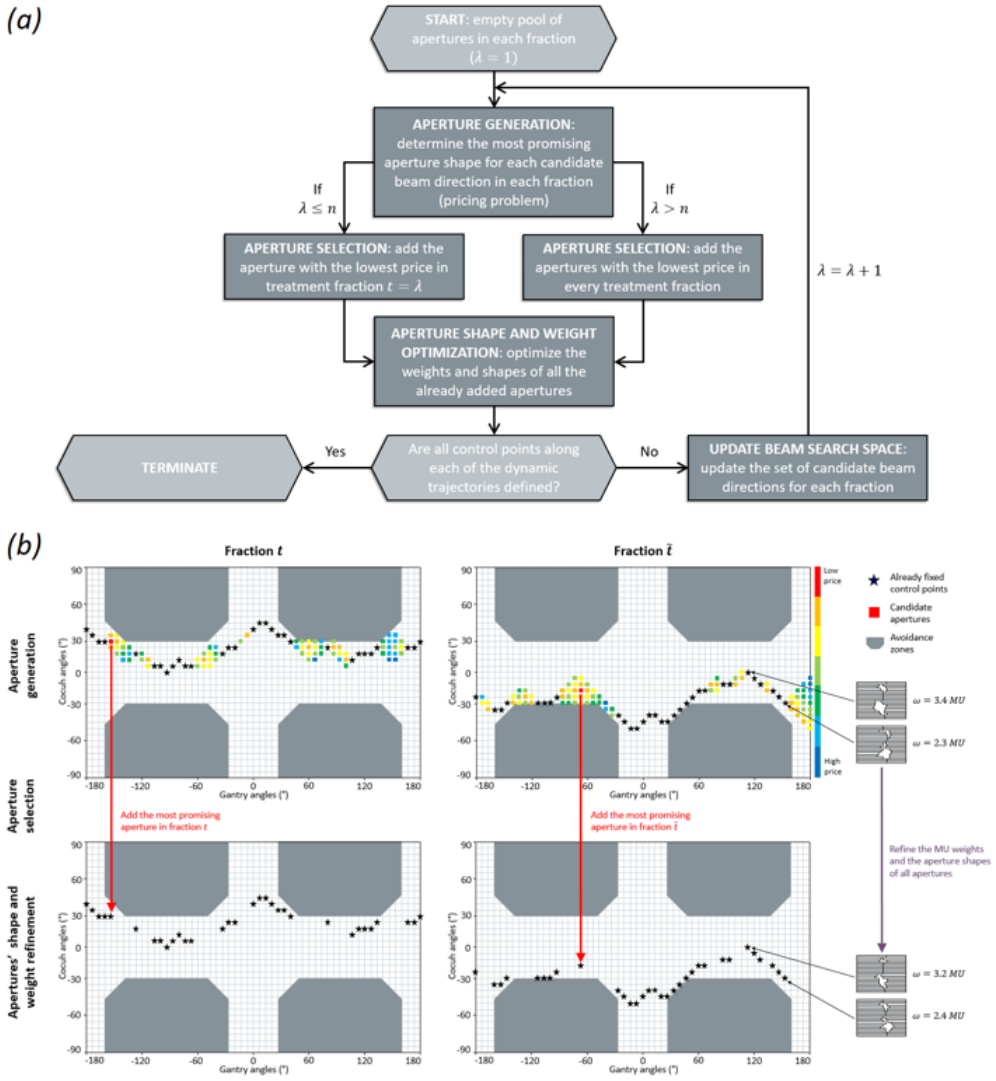

Figure 7.1: *(a) Workflow of the direct aperture optimization algorithm. The index λ refers to the iteration number in the column generation based method and n is the total number of fractions in the treatment. (b) Schematic illustration of iteration $\lambda > n$ of the DAO algorithm for two exemplary fractions t and $\tilde{t}$. The black stars indicate control points for which an aperture has already been fixed. First, candidate apertures are generated for each of the beam orientations which can still be efficiently reached by the non-coplanar dynamic trajectories. The apertures with the lowest price in each fraction are subsequently added to the treatment plan. Both the MU weights and shapes of all the already added apertures are finally refined.*

(see Fig. 7.1b[a]). To allow for the dose distributions delivered in the different fractions to possibly diverge, during the first $\lambda \in \{1, ..., n\}$ iterations of the column generation method, only one single aperture is added to the treatment plan for fraction $t = \lambda$. This is necessary as the gradient information for all fractions with an empty pool of apertures is the same.

Similar to the work of Mullins et al [122], the set B of candidate beam orientations (which is initially the same for all fractions) spans multiple potential control points for the non-coplanar dynamic trajectories, each defined by different pairs of gantry-couch angles. The search space for candidate beam orientations considered for the pricing problem varies dynamically with the addition of each new aperture. Both control points for which an aperture has already been defined and control points that cannot be reached efficiently by a dynamic trajectory due to delivery-efficiency constraints (which are further detailed below) are excluded from the search space B. This makes solving the pricing problem more efficient after the addition of each new aperture. In this study, the control points grid resolution is set to $\Delta\theta = 5°$ for the gantry angles and to $\Delta\phi = 2.5°$ for the couch angles, with gantry angles ranging from -180° to +180° and couch angles ranging from -90° to +90°. Avoidance zones for gantry-couch angle pairs leading to collisions are determined for typical patient geometries and treatment sites (i.e. they are not patient specific) and are excluded from the set of candidate beam orientations. The collimator angle is not optimized and is fixed to 0°.

Gradient based DAO method for apertures' shape and MU weight refinement

After the addition of each aperture to the treatment plan, both the MU weights and the shapes of all the already defined apertures are refined using a gradient based DAO approach, aiming to minimize an objective function $f(\mathbf{b})$ evaluated for the cumulative BED distribution b. Formally, the treatment plan optimization problem reads:

$$\text{minimize} \qquad f(\mathbf{b}) \tag{7.1}$$

$$\text{subject to} \qquad b_i = \sum t = 1^n d_{it} \left[1 + \frac{d_{it}}{(\alpha/\beta)_i}\right] \qquad \forall i \tag{7.2}$$

$$d_{it} = \sum_{k \in K_t} \omega_k \sum_{l \in L_k} \Phi_i^{kl}(x_L^{kl}, x_R^{kl}) \qquad \forall i, \forall t \tag{7.3}$$

[a] In case that multiple non-coplanar dynamic trajectories are used in a single fraction and the same apertures are generated for all trajectories, then the most promising aperture is (per construction) added to the first non-coplanar dynamic trajectory.

$$\omega_k \geq 0 \qquad \forall k \qquad (7.4)$$

$$|x_L^{(k-1)l} - x_L^{kl}| \leq \Delta x_{max} \qquad \forall k \leq 1, \forall l \qquad (7.5)$$

$$|x_R^{(k-1)l} - x_R^{kl}| \leq \Delta x_{max} \qquad \forall k \leq 1, \forall l \qquad (7.6)$$

$$x_L^{kl} \leq x_R^{kl} \qquad \forall k, \forall l \qquad (7.7)$$

where b_i is the cumulative BED to voxel i, $(\alpha/\beta)_i$ is the α/β-ratio of the tissue that voxel i belongs to, d_{it} is the physical dose delivered to voxel i in fraction t by all the contributing MLC-based apertures $k \in K_t$, Φ_i^{kl} is the dose contribution of the l-th leaf pair of aperture k to voxel i per unit intensity and $_k$ is the MU weight of aperture k. The parameters x_L^{kl} and x_R^{kl} describe the positions of the left and right MLC leaves in the l-th leaf pair of aperture k, respectively, and L_k is the set of all MLC leaf pairs in aperture k. The constraints in Eq. (7.5)-(7.6) are used to limit the MLC displacement between neighboring control points by a maximum distance Δx_{max}, as further detailed below[b].

The proposed gradient based DAO approach, which is inspired by the work of Cassioli and Unkelbach [123], exploits gradient information to locally optimize the positions of the MLC leaves and the MU weights in an iterative way. At each iteration of the gradient based DAO method, a restricted optimization problem is solved, where the left and right MLC leaf positions for all leaf pairs $l \in L_k$ and for all apertures $k \in K_t$ are constrained to the bixels b_L^{kl} and b_R^{kl} they are positioned in. Under this assumption, the dose contribution $\Phi_i^{kl}(x_L^{kl}, x_R^{kl})$ to voxel i in Eq. (7.3) can be decomposed into three separate terms describing the dose contributions of the bixels that are in between the two leaves and are thereby completely exposed, and the dose contributions of the partially exposed bixels on the left and on the right, respectively,

$$\Phi_i^{kl}(x_L^{kl}, x_R^{kl}) = \delta_L^{kl} D_{ib_L^{kl}} + \delta_R^{kl} D_{ib_R^{kl}} + \sum_{j=b_L^{kl}+1}^{b_R^{kl}-1} D_{ij} \qquad (7.8)$$

Here, $\delta_L^{kl} \in [0,1]$ and $\delta_R^{kl} \in [0,1]$ describe the fractional opening of the bixles that the left and right MLC leaves are restricted to, and D_{ij} is the dose-influence matrix term storing the dose contribution of bixel j to voxel i per unit intensity. Within each bixel, the dose contribution can be approximated by a linear function of the corresponding dose-influence matrix term. This

[b]Note that for the first and last control points along a dynamic trajectory (i.e. at θ=-180° and θ=+180°), only the MLC displacement from a single neighboring control point is considered.

leads to a well-behaved optimization problem for the leaf positions and the aperture weights, which can be solved efficiently using standard gradient-based algorithms. In this study, we use our in-house implementation of the L-BFGS quasi-Newton method [63], where the constraints $\delta_L^{kl} \in [0,1]$ and $\delta_R^{kl} \in [0,1]$ are handled by projection methods.

If a MLC leaf is moved at the edge of a bixel after an iteration of the gradient based DAO method (e.g. $\delta_L^{kl} \in \{0,1\}$ or $\delta_R^{kl} \in \{0,1\}$), its position can be confined to the neighboring bixel in the next iteration (details on the leaf-to-bixel assignment procedure are discussed in the work of Cassioli and Unkelbach [120]). This allows for larger MLC leaf displacements over multiple iterations. In this work, the iterative refinement of the MLC leaf positions and the MU weights stops either after 20 iterations of the gradient based DAO algorithm or sooner if the decrease in the relative value of the objective function between two consecutive iterations is smaller than ϵ=10^{-6}.

Delivery efficiency constraints

To keep the delivery time of non-coplanar dynamic trajectories practical, delivery efficiency constraints are implemented. Similar to Peng et al [124], we first constrain the MLC leaf displacement Δx_{max} between consecutive control points. The maximum MLC leaf position displacement from one control point to the neighboring one is determined by the maximum leaf speed $\left(\frac{dx}{dt}\right)_{max}$ and the minimum time which the system composed by gantry and couch needs to move between the two control points. For the delivery of non-coplanar dynamic trajectories, this is determined either by the inverse of the maximum gantry angular speed $\left(\frac{d\theta}{dt}\right)^{-1}_{max}$ or by the inverse of the maximum couch angular speed $\left(\frac{d\phi}{dt}\right)^{-1}_{max}$

$$\Delta x_{max} = max\left[\left(\frac{dx}{dt}\right)_{max}\left(\frac{d\theta}{dt}\right)^{-1}_{max}\Delta\theta, \left(\frac{dx}{dt}\right)_{max}\left(\frac{d\phi}{dt}\right)^{-1}_{max}\Delta\phi\right] \quad (7.9)$$

where $\Delta\theta$ and $\Delta\phi$ denote the difference in gantry and couch angles between neighboring control points, respectively[c]. In this study, the maximum MLC leaf speed is set to 2.5 cm/s, the maximum rotation speed of the gantry is set to 6°/s and the maximum rotation speed of the couch is set to 3°/s. These values correspond to the dynamic parameters for a TrueBeam (Varian

[c]Note that $\Delta\theta$ and $\Delta\phi$ in Eq. (7.9) can assume values which are integer multiples of the gantry-couch grid resolution, in case that the two considered control points are not to be delivered consecutively (i.e. if apertures at intermediate control points have not been added yet to the treatment plan).

Medical Systems, Palo Alto, CA) treatment unit equipped with a Millennium MLC 120 (Varian Medical Systems, Palo Alto, CA). For the chosen gantry-couch grid resolution (i.e. $\Delta\theta$=5° and $\Delta\phi$=2.5°), the travel time from one control point to the neighboring one corresponds to 0.83 s and the maximum leaf travel between consecutive control points is thereby limited to 2.08 cm. This constraint on the maximum MLC leaf displacement is incorporated both in the column generation based method (within the pricing problem) and in the gradient based DAO method (within the leaf-to-bixel assignment procedure).

Second, we constrain the delivery time for a non-coplanar dynamic trajectory to be approximately the same as the delivery time for a full coplanar VMAT arc. Potential improvements in the treatment plan quality when using non-coplanar dynamic trajectories are thereby not associated with a decreased delivery efficiency. The maximum couch rotation $\Delta\phi_{max}$ between consecutive control points (defined by monotonically increasing gantry angles) is restricted to

$$\Delta\phi_{max} = \left(\frac{d\phi}{dt}\right)_{max} \left(\frac{d\theta}{dt}\right)^{-1}_{max} \Delta\theta \tag{7.10}$$

To satisfy the constraint in Eq. (7.10) and still obtain a continuous dynamic trajectory spanning a 360° gantry arc, control points which cannot be reached efficiently by a dynamic trajectory while avoiding the collision zones are excluded from the initial beam search space B.

In this work, we do not define any constraint on the maximum MU rate. It is therefore possible that the speed of the mechanical linear accelerator components must be adjusted if a too large number of MUs has to be delivered between consecutive control points.

7.3.2 Patient cases

The proposed DAO algorithm is demonstrated for two patients which have previously been investigated in the context of spatiotemporal fractionation research [29,30]. Patient 1 has four metastases of varying size located in the right lobe of the liver and is used for illustration in the results section. The total GTV volume is 319 cc, and a 3 mm isotropic margin expansion is applied from the GTV to obtain the PTV. Patient 2 has a large arteriovenous malformation (AVM) located in the right frontal lobe with a volume of 30 cc.

7.3.3 Treatment planning study and algorithm validation

Patient 1

For patient 1, a 3-fraction stereotactic body radiotherapy (SBRT) plan is generated using the proposed planning approach. For each fraction, a different non-uniform dose distribution is optimized which is delivered using two fraction-specific non-coplanar dynamic trajectories. Both non-coplanar dynamic trajectories are constrained to share the same gantry-couch path, which is automatically optimized along with the corresponding dose distribution and consists of 73 control points selected from 1463 feasible beam orientations. This fraction-variant SBRT plan (which hereafter is referred to as SBRT_{FV}) is benchmarked against a 3-fraction SBRT plan that delivers the same dose distribution in every fraction and is obtained using two coplanar VMAT arcs at a fixed couch angle of $\phi = 0°$ in every fraction (hereafter referred to as SBRT_{std}). In the latter case, only one single dose distribution is optimized for all fractions using a pre-defined and fixed set of beam orientations $B_0 = \{(\theta_k, \phi_k)\}|\theta_k = -180° + k{\cdot}5°, \phi_k = 0°\forall k \in \{0, 1, ..., 72\}\}$.

Both plans are optimized for the following choice of planning objectives:

1. A BED_{10} of 100.8 Gy is prescribed to the GTV (implemented via a quadratic penalty function), corresponding to a physical dose of 42 Gy in 3 fractions. A BED_{10} exceeding 112.5 Gy (equivalent to 45 Gy physical dose in 3 fractions) is penalized quadratically.

2. A BED_{10} of 79.2 Gy (equivalent to 36 Gy physical dose in 3 fractions) is prescribed to the PTV (excluding the GTV voxels), while BED_{10} values exceeding 100.8 Gy are penalized quadratically.

3. The dose has to be conformal to the PTV. This is implemented via a normal tissue objective which limits the BED_3 to the normal tissue by steepening the dose gradient.

4. The mean BED_3 to the non-involved liver (i.e. liver without PTV) is minimized.

The bixel size is set to 5 x 5 mm^2 and the photon energy is 6 MV for all candidate beam orientations. A non-uniform dose grid size is used throughout the body, with small voxels of 5.1 x 5.1 x 2.5 mm^3 in size that are used in the PTV and close to the PTV, where a larger dose gradient is expected. At a distance between 2 cm and 4 cm from the PTV edge, medium-size voxels are used with 8-fold volume, whereas at distances larger than 4 cm from

the PTV edge large-size voxels are used with 64-fold volume. As previously shown by Mueller et al [125], the use of a non-uniform dose grid size allows to considerably enhance the computational efficiency with negligible trade-offs on the plan accuracy. All dosimetric results, however, are evaluated based on the finest (small) dose grid size.

Patient 2

Analogously, for patient 2 we generate a 4-fraction stereotactic radiotherapy (SRT) plan using the proposed planning approach, where different dose distributions are optimized for each fraction utilizing two fraction-specific non-coplanar dynamic trajectories (both defined through the same 73 control points selected from 3035 candidate beam orientations). This fraction-variant SRT plan (which hereafter is referred to as SRT_{FV}) is benchmarked against a 4-fraction uniformly fractionated SRT plan that uses two coplanar VMAT arcs at a fixed couch angle of $\phi = 0°$ in every fraction (hereafter referred to as SRT_{std}).

The planning objectives and the optimization settings used for patient 2, as well as additional details on the computational setup can be found in the Supplementary material, Appendix A.

Algorithm validation

To test the ability of the proposed DAO algorithm to determine non-coplanar dynamic trajectories that are beneficial for the delivery of each specific fractional dose distribution, N=25 additional treatment plans are generated for patient 1 utilizing different randomly generated non-coplanar dynamic trajectories in different fractions and allowing for different non-uniform dose distributions to be delivered in each distinct fraction. Random dynamic trajectories are determined a priori by randomly sampling feasible beam orientations in an iterative way until a complete set of beam orientations B_{rnd} describing a non-coplanar dynamic trajectory is obtained (which again must satisfy the delivery-efficiency constraints). The different sets of beam orientations B_{rnd} for each fraction are then used as input for the optimization and the resulting plans are compared to the SBRT_{FV} plan obtained with optimized non-coplanar dynamic trajectories (i.e. where the set B of all feasible beam orientations is used as input for the optimization), using the objective function value as a measure for plan quality.

Investigating the impact of each additional degree of freedom on the treatment plan quality and delivery efficiency

Compared to state-of-the-art radiotherapy treatments that deliver the same dose in every fraction and for which the beam orientations are manually defined and fixed for all fractions, treatments generated in this study exploit the following additional degrees of freedom:

- Fraction-variant intensity modulation (which refers to the use of possibly different MLC-based apertures and MU weights in different fractions)
- Delivery of different non-uniform dose distributions in distinct fractions (spatiotemporal fractionation)
- Patient- and fraction-specific beam angle selection

(Note that fraction-variant intensity modulation is an intrinsic characteristic of plans exploiting spatiotemporal fractionation schemes and fraction-specific beam angle selection.) To separately investigate the impact of each of these individual degrees of freedom on the treatment plan quality, the following additional treatment plans are also generated for both patients:

I A plan that exploits fraction-variant intensity modulation only (hereafter referred to as SBRT_{FVIM}/SRT_{FVIM}). This plan allows for the shapes and MU weights of the apertures to vary in between the different fractions, but requires that a uniform dose distribution is delivered within the PTV in every fraction using coplanar VMAT arcs. To ensure that a uniform dose distribution is delivered within the target volume in every fraction, additional planning objectives are defined which require that 1/n of the total prescribed BED is delivered to each voxel of the target volume in every fraction (as further detailed in the Supplementary material, Appendix A).

II A plan that exploits spatiotemporal fractionation schemes only (hereafter referred to as SBRT_{STF}/SRT_{STF}). This plan delivers different non-uniform dose distributions in every fraction, but using two coplanar VMAT arcs in all fractions (thereby neither patient- nor fraction-specific beam angle selection is exploited, similar to previous studies on spatiotemporal fractionation schemes [13-17]). The set of aperture shapes and intensities is allowed to vary between the different fractions, but no constraint is defined on the spatial dose distribution within the target volume at each fraction.

III A plan that exploits fraction-specific beam angle selection only (hereafter referred to as SBRT_{FSBAS}/SRT_{FSBAS}). This plan delivers a uniform dose distribution within the target volume in each fraction, using fraction-specific non-coplanar dynamic trajectories. In this case, we allow to select different non-coplanar dynamic trajectories in different fractions, but require that the dose is distributed near uniformly within the target volume in every fraction (again by adding planning objectives which require that $1/n$ of the total prescribed BED is delivered to each voxel of the target volume in every fraction).

The use of fraction-variant intensity modulation and fraction-specific beam angle selection has also the potential of improving the delivery efficiency of radiotherapy treatments without compromising the plan quality. To investigate the trade-off between plan quality and delivery efficiency, we also generate for both patients an additional plan which is allowed to deliver non-uniform dose distributions in different fractions, but which utilizes only one single fraction-specific non-coplanar dynamic trajectory in each fraction (instead of two VMAT arcs or two dynamic trajectories as for the other plans) and thereby requires a shorter delivery time (hereafter referred to as $\text{SBRT}^{(1)}_{FV}$/$\text{SRT}^{(1)}_{FV}$). The delivery time is estimated by considering the dynamic delivery constraint discussed in the previous section and assuming a maximum MU rate of 10 MU/s.

7.4 Results

Fig. 7.2 shows the fractional dose distributions for patient 1 obtained with the SBRT_{std} plan and the SBRT_{FV} plan, respectively, along with the corresponding gantry-couch paths followed by the VMAT arcs and non-coplanar dynamic trajectories used in each fraction. The SBRT_{FV} plan delivers highly non-uniform dose distributions in different fractions, each treating complementary parts of the PTV to a high dose of up to 20 Gy. In this way, the prescribed BED_{10} to the PTV is achieved with a lower physical dose (the mean physical dose within the PTV is 42.0 Gy for the SBRT_{std} plan and 39.4 Gy for the SBRT_{FV} plan). At the same time, a similar dose bath is delivered to the normal tissue in every fraction, thereby exploiting the fractionation effect. Along with the use of non-coplanar beam orientations, which allow to better distribute the integral dose over a broader volume, this leads to a net reduction in the mean BED_3 to the healthy liver. Compared to the SBRT_{std} plan, which utilizes the same two coplanar VMAT arcs and delivers the same uniform dose distribution in every fraction, the mean liver BED_3 is

reduced from 45.4 Gy to 32.9 (-27.5%) with the SBRT$_{FV}$ plan. The cumulative BED$_{10}$ in the PTV, instead, is approximately the same in both plans. As illustrated in Fig. 7B.1 in the Supplementary material (Appendix B), in fact, the three fractional dose distributions of the SBRT$_{FV}$ plan add up to prescribed equieffective dose in all parts of the target volume.

Interestingly, depending on which part of the target volume is treated in each fraction of the SBRT$_{FV}$ plan, very different non-coplanar dynamic trajectories are used (as shown in Fig. 7.2d/h/l). Although it is difficult to visually interpret why specific beam orientations are used in each fraction, the SBRT$_{FV}$ plan always leads to a lower objective function value (on average -6.97%) compared to the N=25 additional plans obtained by using different randomly generated non-coplanar dynamic trajectories in distinct fractions.

7.4.1 Dosimetric benefit of fraction-variant intensity modulation

Fig. 7.3a-c show the three fractional dose distributions obtained with the SBRT$_{FVIM}$ plan. By allowing different sets of aperture shapes and MU weights to be used in the different fractions (Fig. 7.2d), overall more apertures can be used over the course of the treatment, what allows to better reproduce an ideal intensity modulation. This is demonstrated in Fig. 7.2e, which compares the objective value as a function of the number of apertures per fraction for the SBRT$_{std}$ plan, the SBRT$_{FVIM}$ plan and a plan generated using fluence map optimization[d] for each beam orientation (representing the upper bound for the achievable plan quality), respectively. The SBRT$_{FVIM}$ plan improves on the SBRT$_{std}$ plan by achieving a mean liver BED$_3$ of 42.7 Gy (-5.9%). In addition, differently than for the SBRT$_{std}$ plan, the dose spikes entering the normal tissue (which must be typically kept low) in the SBRT$_{FVIM}$ plan are not constrained to be located at the same position in every fraction, thereby improving on dose conformity.

7.4.2 Dosimetric benefit of spatiotemporal fractionation

The three fractional dose distributions obtained with the SBRT$_{STF}$ plan are shown in Fig. 7.4a-c. By optimally exploiting the fractionation effects, this plan reduces the mean liver BED$_3$ by 16.1% compared to the SBRT$_{std}$ plan (38.1 Gy vs 45.4 Gy). However, since the beam orientations are not optimized and fixed for all fractions, it leads to a lower mean liver BED$_3$ reduction

[d] Fluence map optimization is performed for the same planning objectives and priorities using the L-BFGS quasi-Newton method [32].

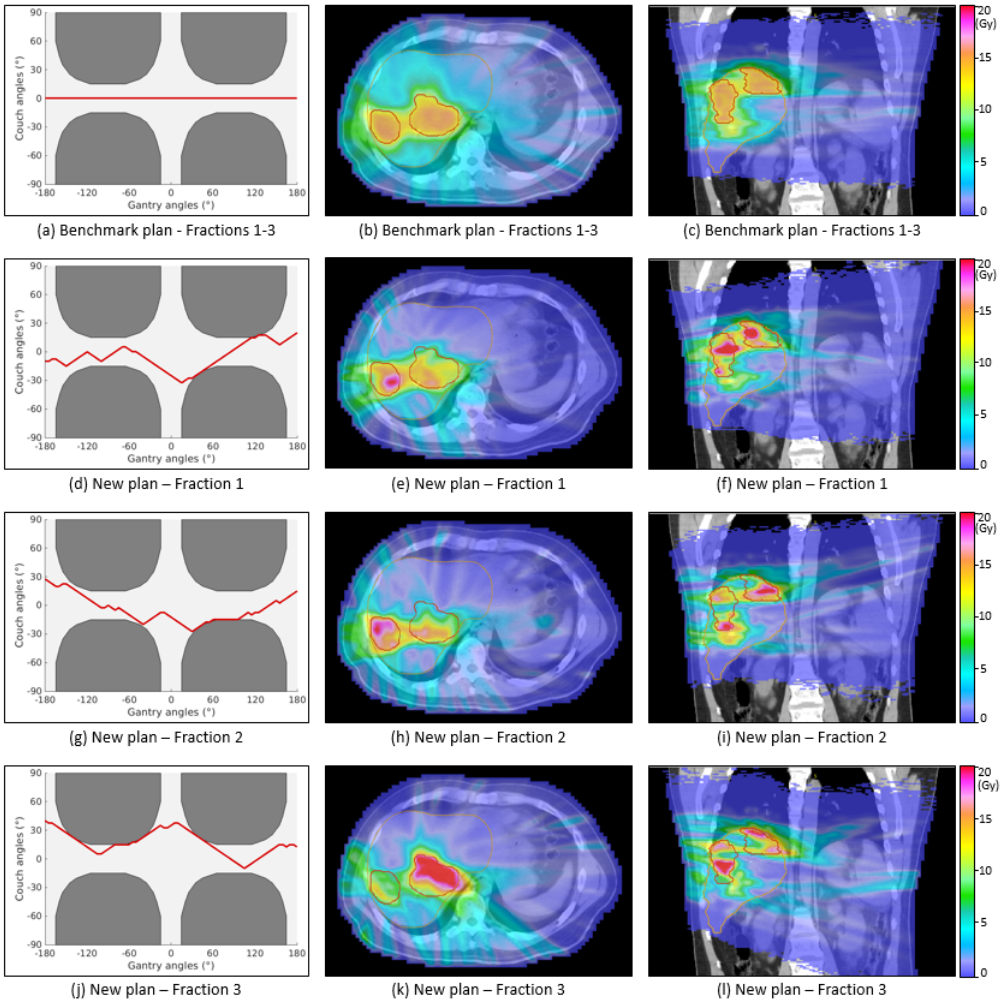

Figure 7.2: *Fractional dose distributions on the transversal (middle) and coronal planes (right) and the corresponding gantry-couch paths (left) for (a)-(c) the $SBRT_{std}$ plan and (d)-(l) the $SBRT_{FV}$ plan for patient 1. The dark grey regions on the gantry-couch map refer to beam orientations leading to collisions between the gantry and the couch.*

compared to the SBRT_{FV} plan. Also, the way the dose is compartmentalized is different, indicating that the decision on which parts of the target volume to treat to a high dose depends on the beam orientations that are used in the BED-based treatment plan optimization problem.

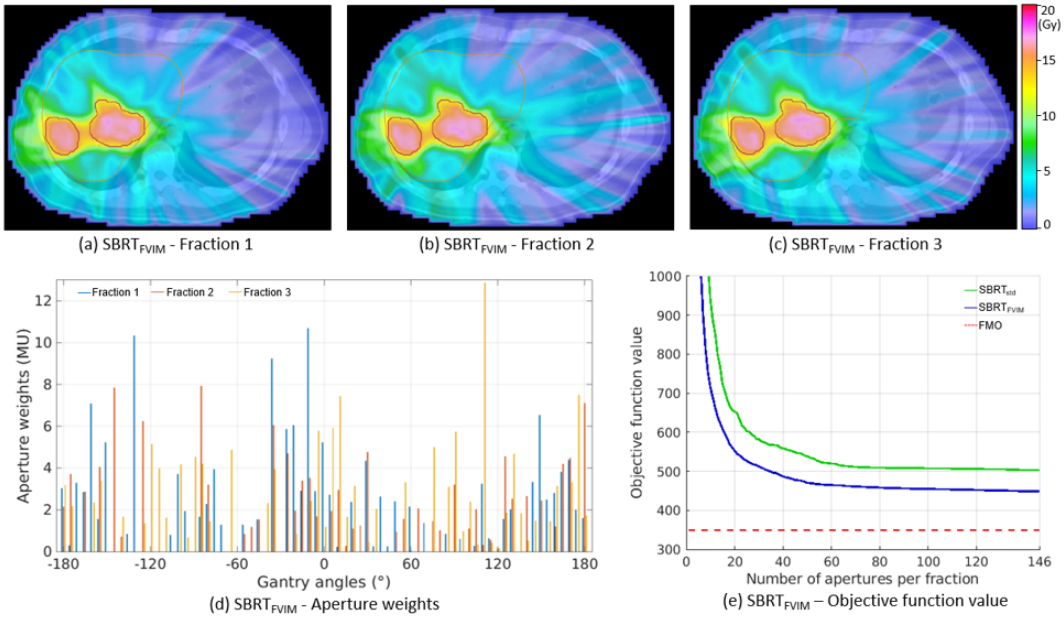

Figure 7.3: *Characteristics of the $SBRT_{FVIM}$ plan: (a)-(c) fractional dose distributions obtained by exploiting only fraction-variant intensity modulation; (d) amount of MUs delivered from each control point in the three different fractions of the $SBRT_{FVIM}$ plan; (e) comparison of the objective value as a function of the number of apertures per fraction for the $SBRT_{std}$, $SBRT_{FVIM}$ and fluence map optimization based plans.*

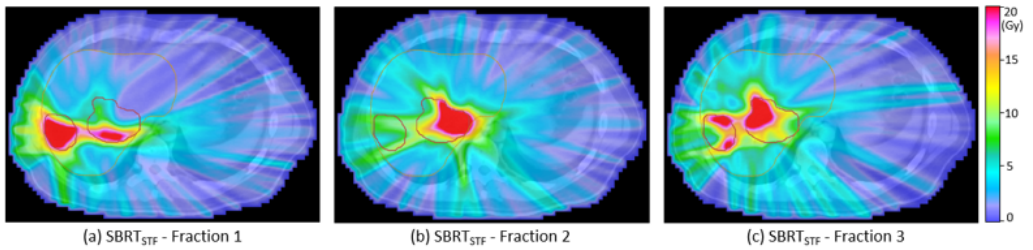

Figure 7.4: *Fractional dose distributions obtained for patient 1 with the $SBRT_{STF}$ plan.*

7.4.3 Dosimetric benefit of fraction-variant beam angle selection

Fig. 7.5a-c show the fractional dose distributions obtained with the SBRT$_{FSBAS}$ plan. This plan achieves a mean liver BED$_3$ of 38.4 Gy (-15.4% compared to the SBRT$_{std}$ plan). As illustrated in Fig. 7.5d-f, different non-coplanar dy-

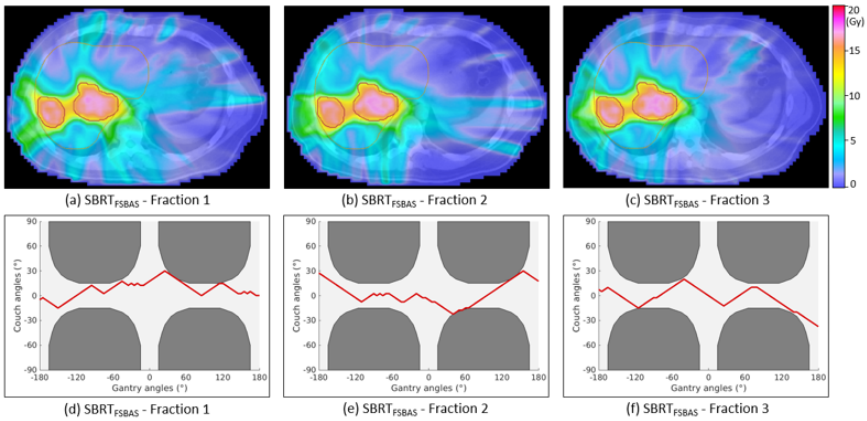

Figure 7.5: *Fractional dose distributions and the corresponding gantry-couch paths for the $SBRT_{FSBAS}$ plan for patient 1. The dark grey regions on the gantry-couch map refer to beam orientations leading to collisions between the gantry and the couch.*

namic trajectories are used in different fractions. Compared to the SBRT_{FV} plan, however, the chosen gantry-couch paths are different. As a similar dose distribution is delivered within the PTV in every fraction, in fact, the benefit of using different non-coplanar dynamic trajectories in distinct fractions mainly lies in the utilization of overall more beam orientations and not in the selection of specific beam orientations which are beneficial for the treatment of specific regions of the target volume.

7.4.4 Trade off between plan quality and delivery time

By utilizing only a single non-coplanar dynamic trajectory in every fraction, the mean delivery time per fraction can be considerably reduced compared to the corresponding SBRT_{FV} plan obtained using two non-coplanar dynamic trajectories per fraction (67 s vs 132 s). Nevertheless, most of the dosimetric benefits could be maintained. The mean liver BED_3 achieved by the $\text{SBRT}_{FV}^{(1)}$ plan, in fact, is 39.9 Gy (i.e. -12.1% compared to the SBRT_{std} plan). The corresponding dose distributions are reported in Fig. 7B.2 in the Supplementary material, Appendix B.

7.4.5 Summary of the results

Table 7.1 summarizes the results obtained for patient 1 using all the different plans which have been discussed, while Fig. 7.6 shows the corresponding dose-volume histograms for the PTV and healthy liver. For a similar PTV dose

Table 7.1: *Dosimetric results and delivery times for the different treatments plans generated for patient 1.*

Plans	Number of arcs per fraction	Mean BED_{10} to the PTV (Gy)	Mean liver BED_3 (Gy)	Mean delivery time per fraction (s)
$SBRT_{std}$	2	101.2	45.4	120
$SBRT_{FVIM}$	2	100.6 (-0.6%)	42.7 (-5.9%)	121 (+0.8%)
$SBRT_{STF}$	2	99.9 (-1.3%)	38.1 (-16.1%)	127 (+5.8%)
$SBRT_{FSBAS}$	2	100.1 (-1.1%)	38.4 (-15.4%)	123 (+2.5%)
$SBRT_{FV}$	2	100.1 (-1.1%)	32.9 (-27.5%)	132 (+10.0%)
$SBRT_{FV}^{(1)}$	1	101.1 (-0.1%)	39.9 (-12.1%)	67 (-44.2%)

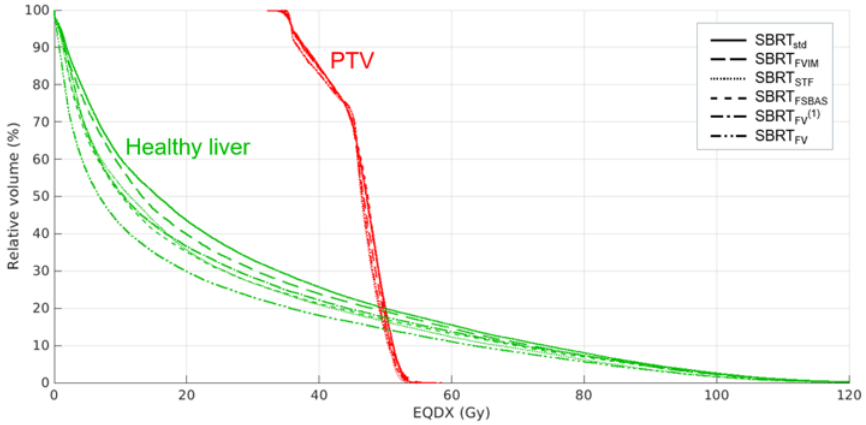

Figure 7.6: *Dose-volume histograms for the PTV (red, X=12 Gy) and healthy liver (green, X=2 Gy) evaluated for the equieffective dose [64]. The equieffective dose* $EQDX = \frac{b}{1+X/(\alpha/\beta)}$) *corresponds to the total physical dose that needs to be delivered in a uniformly fractionated treatment with a dose per fraction X to achieve a BED b, and is linearly proportional to the BED.*

coverage in all plans, each of the degrees of freedom considered in this study leads to an improvement in terms of mean liver BED_3 reduction. Combining fraction-variant intensity modulation, the delivery of non-uniform dose distributions in different fractions and fraction-specific beam angle selection all together, a significant improvement in treatment plan quality (and/or delivery efficiency) can be achieved compared to exploiting each degree of freedom separately.

Similar results have been obtained also for patient 2 and are summarized in Table 2. The corresponding dose distributions and DVHs are reported in the Supplementary material, Appendix B. Note that for patient 2, the use of fraction-variant intensity modulation alone is less beneficial compared to patient 1, as the tumor geometry is less complex.

Table 7.2: *Dosimetric results and delivery times for the different treatments plans generated for patient 2.*

Plans	Number of arcs per fraction	Mean BED_4 to the AVM (Gy)	Brain V_{60} (cc)	Mean brain BED_2 (Gy)	Mean delivery time per fraction (s)
SRT_{std}	2	100.5	28.4	7.01	120
SRT_{FVIM}	2	99.4 (-1.1%)	28.7 (+1.1%)	6.96 (-0.7%)	120 (=)
SRT_{STF}	2	98.6 (-1.9%)	26.2 (-7.7%)	6.31 (-10.0%)	121 (+0.8%)
SRT_{FSBAS}	2	101.5 (+1.0%)	22.5 (-20.8%)	6.18 (-11.8%)	123 (+2.5%)
SRT_{FV}	2	102.0 (+1.5%)	21.2 (-5.4%)	5.15 (-26.5%)	126 (+5.0%)
$SRT_{FV}^{(1)}$	1	101.7 (+1.2%)	21.5 (-24.3%)	5.46 (-22.1%)	64 (-46.7%)

7.5 Discussion

In conventional clinical practice, a single treatment plan is generated for each patient. Such a plan utilizes the same beam orientations and delivers the same uniform dose distribution in every fraction. In this work, we showed that by removing these constraints and varying the beam orientations and the dose distributions in between the different fractions, treatment plans can be generated which considerably reduce the integral BED to critical OARs, for a similar PTV dose coverage. The dose distributions are designed such that distinct regions of the target volume are treated to a high dose in different fractions, while the normal tissue dose is more uniformly distributed over all fractions, and beam orientations are used in every fraction which are optimal for treating each part of the target volume. These treatment plans are generated using a novel direct aperture optimization algorithm that allows to simultaneously optimize multiple dose distributions together with corresponding fraction-specific non-coplanar dynamic trajectories. The DAO algorithm has been successfully validated for a patient with large liver metastases and a patient with a large arteriovenous malformation, and demonstrated to improve on plans obtained using randomly determined beam orientations.

Besides to leading to a considerable dosimetric benefit, the generated treatments have been shown to also possibly enhance the delivery efficiency of radiotherapy treatments without compromising the dosimetric quality. In particular, utilizing different sets of aperture shapes and MU weights in different fractions allows to better reproduce an ideal intensity modulation while using fewer apertures/arcs per fraction. By varying the set of beam orientations which are used in the different fractions, instead, a larger number of non-coplanar beam orientations can be used over the treatment course without increasing the delivery time per fraction. Decreasing the delivery time of radiotherapy treatments may positively impact clinical practice by reducing the uncertainties related to intra-fraction motion and diminishing the discomfort for the patients.

The delivery of different non-uniform dose distributions in distinct fractions using fraction-specific non-coplanar dynamic trajectories is technically feasible using conventional C-arm linear accelerators. However, the following aspects must be carefully considered prior to an eventual clinical implementation of the proposed method:

- First, in this work we assumed that fractionation effects can be modeled using a generalization of the standard BED model, which accounts for different dose distributions to be possibly delivered in different fractions. However, this assumption challenges a decade-old paradigm in radiation therapy, namely that the same dose is delivered in every fraction. Nevertheless, this is a plausible working hypothesis for exploring new fractionation approaches and recently published pre-clinical investigations on the delivery of non-uniform dose distributions in distinct fractions support the assumptions made in this work [126].

- Second, results have been presented in this study by assuming that each dose distribution is delivered as planned. Inter- and intra-fraction setup and motion uncertainties may, however, lead to misalignments of the different dose distributions when different parts of the target volume are treated in distinct fractions, thereby potentially causing target over- or under-dosage. The dose gradients within the target volume can be controlled by adding additional planning objectives on the spatial dose distributions within the target volume, as it has been done for the SBRT_{FSBAS}/SRT_{FSBAS} plans in this study. The priority of these objectives can be used to select a preferred trade-off between robustness against setup errors (high priority) and dosimetric quality (low priority). Image-guided radiotherapy or robust optimization approaches may also be used to guarantee a good therapeutic accuracy when delivering non-uniform dose distributions in different fractions [68].

- Third, although the simultaneous rotation of gantry and couch is supported by most commercial C-arm linear accelerators, the clinical implementation of non-coplanar dynamic trajectories still faces some potential problems, like the increased risk of collision between the gantry head and the system composed by couch and patient, and intra-fraction patient motion due to the continuous couch rotation. Development of more accurate collision prediction models and the use of adequate immobilization devices may be warranted for a clinical use of non-coplanar dynamic trajectories.

- Finally, both the optimization time needed for generating multiple fraction-specific treatment plans and the time necessary for performing quality assurance of the different daily plans are increased. For patient 1, the optimization time needed to generate the SBRT_{FV} plan is approximately 3.4 times longer than the optimization time needed for obtaining the SBRT_{std} plan, while for patient 2 the optimization time increases by 7.4 times. However, this is unlikely to be an insurmountable difficulty, as the continuous development in computational hardware makes optimization increasingly faster, and the development of plan complexity metrics may reduce the need for plan-specific quality assurance [127].

Despite these challenges, fraction-variant radiotherapy treatments show a great potential to considerably improve the quality of radiotherapy compared to state-of-the-art treatments that deliver the same dose distribution in every fraction using fixed and manually defined beam directions in every fraction. Future work can be performed to include even more degrees of freedom which are conventionally not exploited in standard radiotherapy treatment planning, like the combination of multiple treatment modalities and particle types (e.g. combined proton-photon radiotherapy [90] or combined photon-electron radiotherapy [128]). As it has been shown in this study, in fact, combining multiple degrees of freedom leads to an incremental benefit compared to exploiting each degree of freedom separately.

7.6 Conclusion

A BED-based direct aperture optimization algorithm which allows to simultaneously optimize multiple dose distributions to be delivered in distinct fractions along with fraction-specific non-coplanar dynamic trajectories has been successfully implemented and demonstrated. Fraction-variant radiotherapy treatments generated by delivering different, possibly non-uniform dose distributions and utilizing different beam orientations in distinct fractions outperform state-of-the-art radiotherapy treatments which deliver the same dose in every fraction using a fixed and pre-determined set of beam orientations, in terms of both dosimetric quality and delivery efficiency.

7.7 Supplementary material

Appendix A Treatment plan optimization

In this section, we further detail the treatment plan optimization methods. We provide the mathematical formulation of the planning objectives used in the treatment plan optimization problem, and discuss the dose calculation algorithm which has been used for computing the dose-influence matrices.

A.1 Patient 1

For patient 1, the objective function in Eq. (7.1) reads as follows:

$$
\begin{aligned}
f(\mathbf{b}) \quad =& \frac{1}{|GTV|} \sum_{i \in GTV} \left[\omega_1^{lower} \left(100.8 - b_i\right)_+^2 + \omega_1^{upper} \left(b_i - 112.5\right)_+^2 \right] && \text{(7A.1)} \\
&+ \frac{1}{|P\tilde{T}V|} \sum_{i \in P\tilde{T}V} \left[\omega_2^{lower} \left(79.2 - b_i\right)_+^2 + \omega_2^{upper} \left(b_i - 100.8\right)_+^2 \right] && \text{(7A.2)} \\
&+ \frac{\omega_3}{|NT|} \sum_{i \in NT} \left(b_i - b_i^{max}\right)_+^2 && \text{(7A.3)} \\
&+ \frac{\omega_4}{|L|} \sum_{i \in L} b_i && \text{(7A.4)}
\end{aligned}
$$

where GTV denotes the set of voxels belonging to the GTV, $(P\tilde{T}V)$ is the set of voxels belonging to the PTV excluding the GTV voxels, NT denotes the set of voxels belonging to the normal tissue (i.e. the entire body except for the PTV) and L is the set of voxels belonging to the healthy liver (i.e. liver without the PTV). For the planning objective in Eq. (7A.3) we set b_0=131.7 Gy, b_∞=15.75 Gy, x_0=0.5 cm and κ=0.6 cm^{-1}.

The priorities ω_1^{lower}, ω_1^{upper}, ω_2^{lower}, ω_2^{upper}, ω_3 and ω_4 for the planning objectives in Eq. (7A.1)-(7A.4) are set differently for the different treatment plans in order to achieve a similar target BED_{10} coverage and similar dose conformity in all plans:

- SBRT_{std}: $\omega_1^{lower} = 20$, $\omega_1^{upper} = 2$, $\omega_2^{lower} = 10$, $\omega_2^{upper} = 1$, $\omega_3 = 7.5$, $\omega_4 = 6$
- SBRT_{FVIM}: $\omega_1^{lower} = 20$, $\omega_1^{upper} = 2$, $\omega_2^{lower} = 10$, $\omega_2^{upper} = 1$, $\omega_3 = 7.5$, $\omega_4 = 6$

- SBRT$_{STF}$: $\omega_1^{lower} = 20$, $\omega_1^{upper} = 2$, $\omega_2^{lower} = 12$, $\omega_2^{upper} = 1.2$, $\omega_3 = 7.5$, $\omega_4 = 4.5$
- SBRT$_{FSBAS}$: $\omega_1^{lower} = 8$, $\omega_1^{upper} = 0.8$, $\omega_2^{lower} = 8$, $\omega_2^{upper} = 0.8$, $\omega_3 = 10$, $\omega_4 = 2.5$
- SBRT$_{FV}$: $\omega_1^{lower} = 10$, $\omega_1^{upper} = 1$, $\omega_2^{lower} = 10$, $\omega_2^{upper} = 1$, $\omega_3 = 10$, $\omega_4 = 2$
- SBRT$_{FV}^{(1)}$: $\omega_1^{lower} = 10$, $\omega_1^{upper} = 1$, $\omega_2^{lower} = 10$, $\omega_2^{upper} = 1$, $\omega_3 = 10$, $\omega_4 = 2$

A.2 Patient 2

For patient 2, the different treatment plans are optimized for the following choice of planning objectives:

1. A BED_4 of 77 Gy is prescribed to the AVM (implemented via a quadratic penalty function), corresponding to a physical dose of 28 Gy in 4 fractions. A BED_4 exceeding 140 Gy (equivalent to 40 Gy physical dose in 4 fractions) is penalized quadratically.
2. The volume of healthy brain (i.e. brain excluding the AVM) receiving a BED_2 larger than 60 Gy is minimized. This corresponds to a physical dose of 10 Gy in a single fraction and is implemented via a continuous relaxation of a dose-volume objective.
3. The dose has to be conformal to the AVM. This is implemented via a normal tissue objective which limits the dose to the normal tissue by steepening the dose gradient.
4. The mean BED_4 to the healthy brain (i.e. brain without the AVM) is minimized.

Mathematically, these objectives can be expressed as follows:

$$f(\mathbf{b}) = \frac{1}{|AVM|} \sum_{i \in AVM} \left[\omega_5^{lower} (77 - b_i)_+^2 + \omega_5^{upper} (b_i - 140)_+^2 \right] \tag{7A.5}$$

$$+ \frac{\omega_6}{|B|} \sum_{i \in B} \frac{1}{1 + e^{-(b_i - 60)/0.5}} \tag{7A.6}$$

$$+ \frac{\omega_7}{|NT|} \sum_{i \in NT} (b_i - b_i^{max})_+^2 \tag{7A.7}$$

$$+\frac{\omega_8}{|B|}\sum_{i\in B} b_i \tag{7A.8}$$

where AVM denotes the set of voxels belonging to the arteriovenous malformation, B is the set of voxels belonging to the healthy brain (i.e. brain without the AVM) and NT denotes the set of voxels belonging to the normal tissue (i.e. the entire body except for the AVM).

The parameters for the normal tissue objective in Eq. (7A.7) are set to b_0=115 Gy, b_∞=13.125 Gy, x_0=0.5 cm and κ=0.6 cm^{-1}. Analogously to patient 1, the priorities ω_5^{lower}, ω_5^{upper}, ω_6, ω_7 and ω_8 for the planning objectives in Eq. (A5)-(A8) are set differently for the different treatment plans in order to achieve a similar BED_4 coverage of the AVM in all plans:

- SRT_{std}: $\omega_5^{lower} = 10$, $\omega_5^{upper} = 1$, $\omega_6 = 100$, $\omega_7 = 1$, $\omega_8 = 10$
- SRT_{FVIM}: $\omega_5^{lower} = 10$, $\omega_5^{upper} = 1$, $\omega_6 = 100$, $\omega_7 = 1$, $\omega_8 = 10$
- SRT_{STF}: $\omega_5^{lower} = 10$, $\omega_5^{upper} = 2$, $\omega_6 = 100$, $\omega_7 = 1$, $\omega_8 = 10$
- SRT_{FSBAS}: $\omega_5^{lower} = 10$, $\omega_5^{upper} = 1$, $\omega_6 = 100$, $\omega_7 = 3$, $\omega_8 = 5$
- SRT_{FV}: $\omega_5^{lower} = 10$, $\omega_5^{upper} = 1$, $\omega_6 = 100$, $\omega_7 = 4$, $\omega_8 = 5$
- $\text{SRT}_{FV}^{(1)}$: $\omega_5^{lower} = 10$, $\omega_5^{upper} = 1$, $\omega_6 = 100$, $\omega_7 = 4$, $\omega_8 = 5$

Similar as for patient 1, a non-uniform dose grid size is used, where the size of the smaller voxels is 2.7 x 2.7 x 1.2 mm^3. The bixel size is set to 5 x 5 mm^2 and the photon energy is 6 MV for all candidate beam orientations.

A.3 Additional planning objectives used to optimize the SBRT_{FVIM}/SRT_{FVIM} and SBRT_{FSBAS}/SRT_{FSBAS} plans

The additional planning objectives that are used to constrain the dose distribution within the target volume to be uniform in every fraction of the SBRT_{FVIM}/SRT_{FVIM} and SBRT_{FSBAS}/SRT_{FSBAS} plans, respectively, read

$$f(\mathbf{b}) = \sum_{t=1}^{3}\left[\frac{1}{|GTV|}\sum_{i\in GTV}\left[\omega_9^{lower}\left(\frac{100.8}{3}-b_{it}\right)_+^2+\omega_9^{upper}\left(b_{it}-\frac{112.5}{3}\right)_+^2\right]\right] \tag{7A.9}$$

$$+\sum_{t=1}^{3}\left[\frac{1}{|P\tilde{T}V|}\sum_{i\in P\tilde{T}V}\left[\omega_{10}^{lower}\left(\frac{79.2}{3}-b_{it}\right)_+^2+\omega_{10}^{upper}\left(b_{it}-\frac{100.8}{3}\right)_+^2\right]\right] \tag{7A.10}$$

for patient 1, and

$$f(\mathbf{b}) \quad = \sum_{t=1}^{4} \left[\frac{1}{|AVM|} \sum_{i \in AVM} \left[\omega_{11}^{lower} \left(\frac{77}{4} - b_{it} \right)_+^2 + \omega_{11}^{upper} \left(b_{it} - \frac{140}{4} \right)_+^2 \right] \right] \tag{7A.11}$$

for patient 2, where b_{it} is biologically effective dose delivered to voxel i in fraction t.

The priorities for the planning objectives in Eq. (A9)-(A10) are set to ω_9^{lower}=10, ω_9^{upper}=1, ω_{10}^{lower}=10 and ω_{10}^{upper}=1 for both the SBRT$_{FVIM}$ and SBRT$_{FSBAS}$ plans, whereas the priorities for the planning objective in Equation (A11) are set to ω_{11}^{lower}=10 and ω_{11}^{upper}=1 for both the SRT$_{FVIM}$ and SRT$_{FSBAS}$ plans.

A.4 Dose calculation algorithm

Calculation of the dose-influence matrix elements D_{ij} is performed with the open-source radiotherapy planning research platform CERR [44] using a quadrant infinite beam (QIB) algorithm [63].

Appendix B Results

B.1 Patient 1

B.1.1 EQD8 distribution for the SBRTstd and SBRTFV plans

Fig. 7B.1 shows the equieffective dose (EQD8) distributions achieved with the SBRT$_{std}$ and SBRT$_{FV}$ plans in patient 1. The equieffective dose $EQDX$ can be interpreted as the total physical dose to be delivered in a uniformly fractionated treatment with a dose per fraction X to achieve a BED b

$$EQDX = \frac{b}{1 + X/(\alpha/\beta)} \tag{7B.12}$$

and is linearly related to the cumulative BED. Although the SBRT$_{FV}$ plan delivers non-uniform doses to the target volume in distinct fractions, the sum of all fractional doses results in the same prescribed BED$_{10}$ within the PTV as in the SBRT$_{std}$ plan.

B.1.2 SBRT$_{FV}^{(1)}$ plan obtained using a single non-coplanar dynamic trajectory per fraction

Fig. 7B.2 shows the fractional dose distributions and the corresponding gantry-couch paths for the SBRT$_{FV}^{(1)}$ plan obtained using a single non-coplanar dynamic trajectory in each fraction.

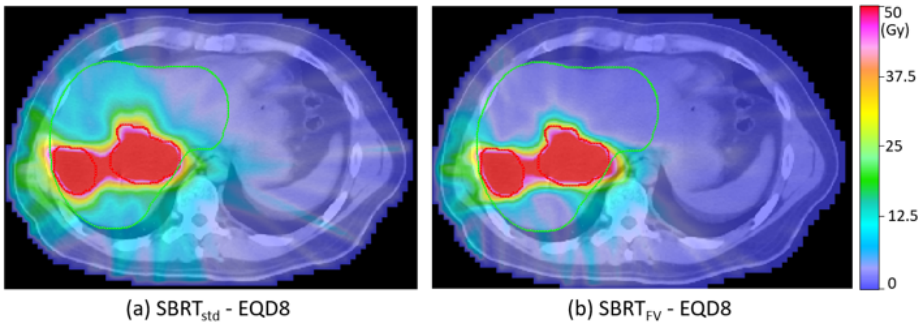

Figure 7B.1: *EQD8 distributions for the $SBRT_{std}$ and $SBRT_{FV}$ plans in patient 1.*

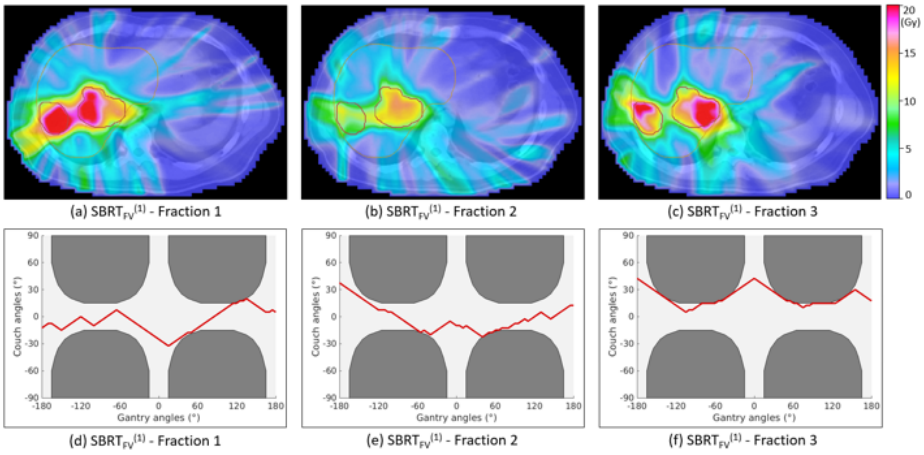

Figure 7B.2: *Fractional dose distributions and the corresponding gantry-couch paths for the $SBRT_{FV}^{(1)}$ plan for patient 1. The dark grey regions on the gantry-couch map refer to beam orientations leading to collisions between the gantry and the couch.*

B.1 Patient 2

B.1.4 Dose distributions for patient 2

Fig. 7B.3 and Fig. 7B.4 show the dose distributions and the corresponding gantry-couch paths for the SRT_{std} and SRT_{FV} plans for patient 2, respectively. The fractional dose distributions for the SRT_{FVIM} and SRT_{STF} plans are reported in Fig. 7B.5 and Fig. 7B.6, while the dose distributions and gantry-couch paths for the SRT_{FSBAS} are illustrated in Fig. 7B.7. Finally, Fig. 7B.8 show the dose distributions and the corresponding gantry-couch paths for the $SRT_{FV}^{(1)}$ plan.

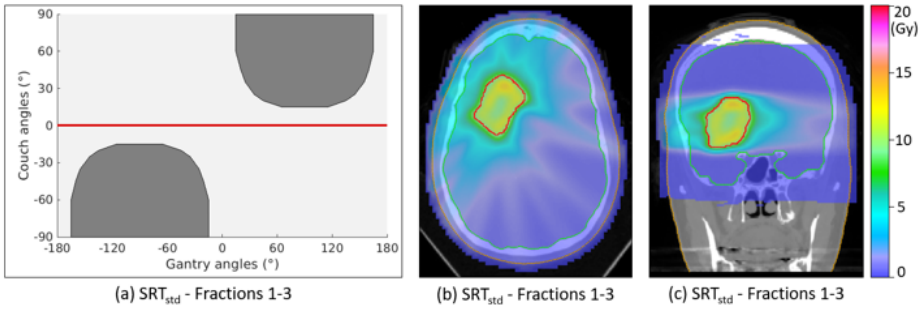

Figure 7B.3: *Dose distribution and the corresponding gantry-couch path for the SRT_{std} plan for patient 2. The dark grey regions on the gantry-couch map refer to beam orientations leading to collisions between the gantry and the couch.*

B.1.5 Dose-volume histograms for patient 2

Fig. 7B.9 shows the DVHs for the AVM and healthy brain evaluated for the equieffective dose.

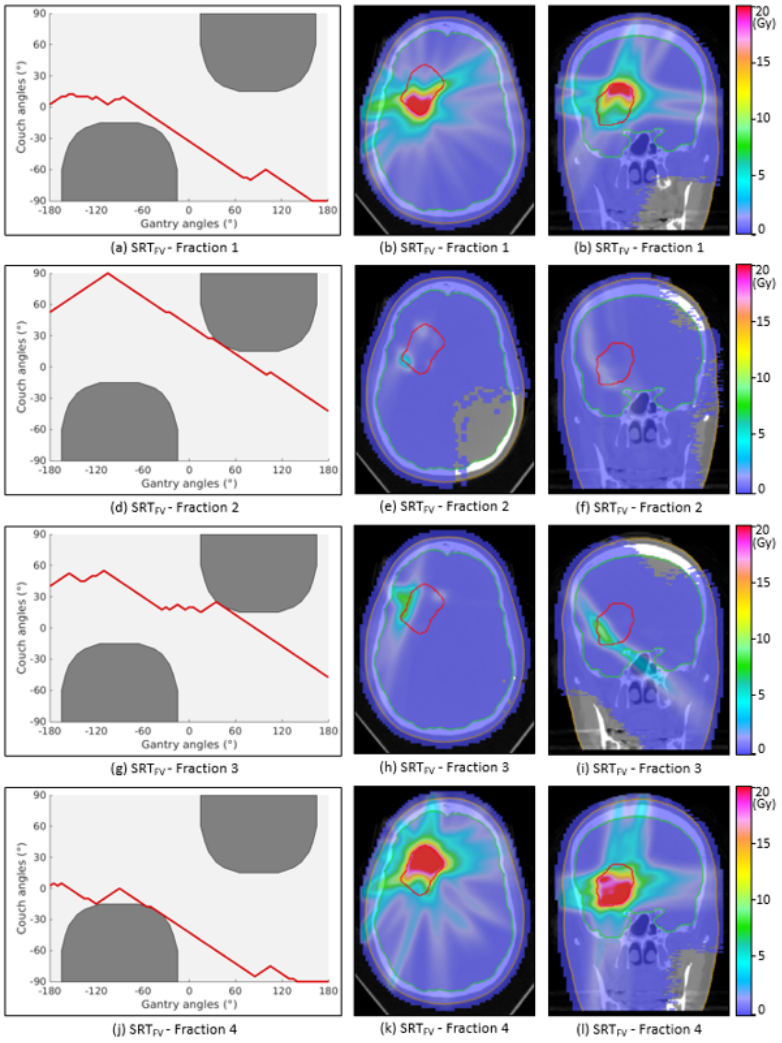

Figure 7B.4: *Fractional dose distributions and the corresponding gantry-couch paths for the SRT_{FV} plan for patient 2. The dark grey regions on the gantry-couch map refer to beam orientations leading to collisions between the gantry and the couch.*

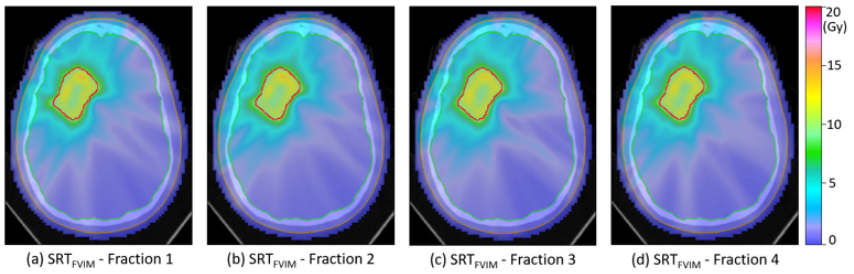

Figure 7B.5: *Fractional dose distributions for the SRT_{FVIM} plan for patient 2.*

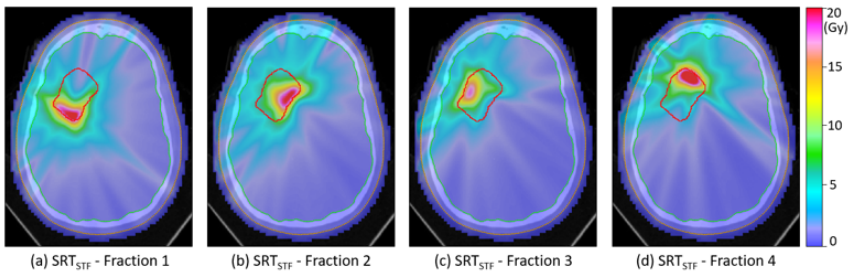

Figure 7B.6: *Fractional dose distributions for the SRT_{STF} plan for patient 2.*

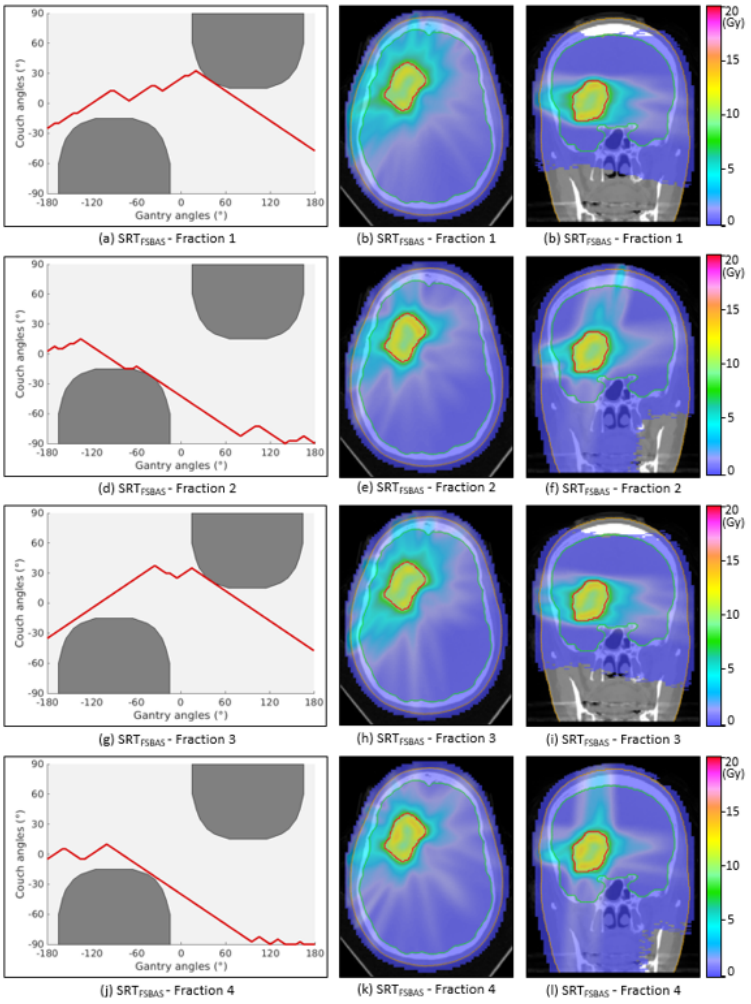

Figure 7B.7: *Fractional dose distributions and the corresponding gantry-couch paths for the SRT_{FSBAS} plan for patient 2. The dark grey regions on the gantry-couch map refer to beam orientations leading to collisions between the gantry and the couch.*

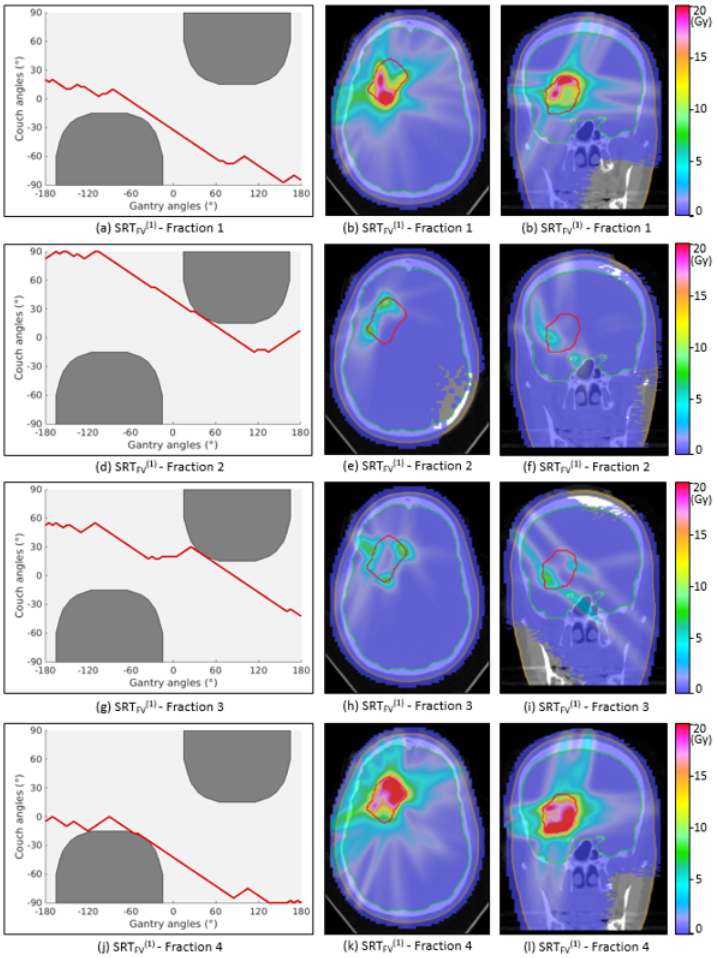

Figure 7B.8: *Fractional dose distributions and the corresponding gantry-couch paths for the $SRT_{FV}^{(1)}$ plan for patient 2. The dark grey regions on the gantry-couch map refer to beam orientations leading to collisions between the gantry and the couch.*

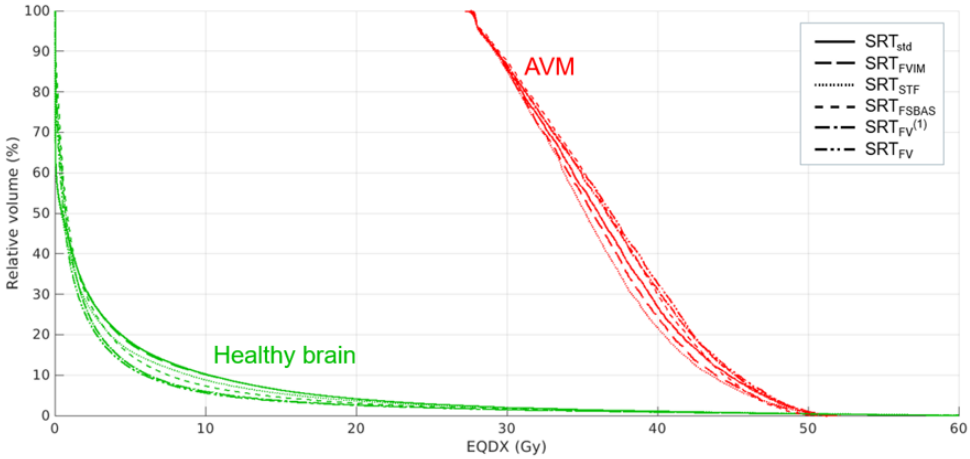

Figure 7B.9: *Dose-volume histograms for the AVM (red, X=7 Gy) and healthy brain (green, X=2 Gy) evaluated for the equieffective dose EQDX.*

Chapter 8

Development of a workflow for generating clinically deliverable spatiotemporally fractionated radiotherapy plans using the Eclipse scripting API

Nathan Torelli[1], Florian Dietsche[1], Jan Unkelbach[1]

[1] *Department of Radiation Oncology, University Hospital Zürich and University of Zürich, Switzerland.*

8.1 Abstract

Purpose: The optimization of spatiotemporally fractionated treatments is so far only supported by research treatment planning systems (TPS). However, research TPS are not approved medical products and lack the rigorous testing of commercial TPS. In this work, we developed a tool to upload treatment plans generated with our in-house TPS into the Eclipse TPS (Varian Medical Systems, Palo Alto, CA).
Methods: Treatment plans generated with our in-house TPS are characterized by a set of multileaf collimator (MLC)-based apertures at different control points. Using the Eclipse Scripting API (ESAPI), treatment plans are created in the Eclipse TPS for the corresponding patient for discrete beam orientations or dynamic arcs, and initialized with control points whose MLC positions are set to the apertures specified in the in-house TPS. Dose distributions for each individual aperture are then computed using Eclipse' commissioned dose calculation algorithms and exported through ESAPI as dose matrices. To mitigate the impact of tongue-and-groove effect, transmission through the MLC and discrepancies between dose calculation algorithms, the fluence of each aperture are re-optimized in the in-house TPS using the exported information. The new monitor unit weights for each aperture are finally uploaded to the Eclipse TPS.
Results: The proposed workflow was tested for a prostate cancer patient. An intensity modulated radiotherapy (IMRT) treatment generated in the in-house TPS was uploaded to the Eclipse TPS and compared to a corresponding IMRT plan generated directly in the Eclipse TPS, where the same fields and same planning objectives were used. The dosimetric quality of the treatments generated in the in-house TPS and Eclipse TPS were similar.
Conclusions: A tool for uploading treatment plans generated using our in-house TPS into the Eclipse TPS was developed. This potentially enables the clinical delivery of spatiotemporally fractionated treatment plans that can only be obtained using our in-house research TPS and not directly in commercial TPS.

8.2 Introduction

In the previous chapters, the potential benefit of spatiotemporal fractionation was investigated in in-silico planning studies for several tumor sites, including patients with large arteriovenous malformations, patients with large liver metastases and patients with multiple brain metastases. Using our in-house research treatment planning software, spatiotemporally fractionated treat-

ments were generated which may reduce the mean BED to the normal tissue surrounding the tumor by approximately 10-20% compared to conventional uniformly fractionated treatments, making these treatment sites interesting candidates for clinical translation in a phase I feasibility trial. However, additional extensions of the in-house research platform are necessary to enable the delivery of spatiotemporal fractionation schemes using commercial linear accelerators.

Research treatment planning systems (TPS) can be easily extended to address research questions. However, research TPS lack of proper quality assurance and are not commissioned for clinical use. Therefore, treatment plans that are entirely generated using a research TPS cannot be delivered to patients. Commercial TPS, on the other hand, are certified medical devices and are commissioned for specific treatment machines. However, commercial TPS only offer established planning approaches and do not support latest planning approaches developed in research. To the best of our knowledge, there is no commercial TPS that supports the simultaneous optimization of multiple dose distributions based on their cumulative biologically effective dose (BED), which is the foundation of spatiotemporal fractionation optimization.

To address this issue and enable the clinical implementation of spatiotemporal fractionation, we developed a treatment planning process in which a treatment plan is first generated using our in-house research TPS, and subsequently a similar plan with the same characteristics (i.e. the same set of multileaf collimated apertures and monitor unit weights) is re-created in the commercial Eclipse TPS (Varian Medical Physics, Palo Alto, CA) using the Eclipse scripting API (EASPI). In this way, treatment plans can be generated using latest optimization approaches, but evaluated using a medically certified TPS. If a plan and its corresponding dose distribution are evaluated directly on a certified commercial TPS and deemed clinically acceptable, there is no legal need to perform quality assurance on the research TPS. The proposed treatment planning process has been validated for a prostate cancer patient and used to generate clinically deliverable spatiotemporally fractionated plans.

8.3 Materials and methods

8.3.1 Treatment planning process

The treatment planning process adopted in the commercial Eclipse TPS is schematically illustrated in Fig. 8.1a. It involves the delineation of the target

volume and relevant organs-at-risk (OARs), the selection of the treatment technique and beam orientations, along with the calculation of the corresponding beamlet dose distributions, the optimization of the incident radiation fluence, a final dose calculation and the plan evaluation. In this work, we extended the treatment planning process to allow the plan optimization to be performed using the in-house TPS (Fig. 8.1b), while still evaluating the resulting plan in the commercial Eclipse TPS. To this end, the Eclipse Scripting API (ESAPI) has been used to export and import files between the Eclipse TPS and the in-house research TPS. In the following, we discuss in more detail the different steps that are performed to allow uploading treatment plans generated in the in-house TPS into the Eclipse TPS.

Beamlet dose calculation and generation of other input files needed for the plan optimization

Once the target volume and all other relevant structures (including the critical OARs) have been contoured in the Eclipse TPS, DICOM files for the patient CT and the structure set are anonymized and exported to the research environment using ESAPI scripts. These files are then imported into the open-source research software CERR [44], which is interfaced with Matlab. In CERR, the patient geometry can be visualized along with the delineated structures, and dose-influence matrices for the selected beam orientations are computed using a quadrant infinite beam (QIB) algorithm [60]. This step is necessary, as it is not possible to directly access the dose-influence matrices used for optimization in the Eclipse TPS. Other files needed as input for the plan optimization, including masks for the relevant structures and other geometrical information, are also generated in CERR.

Treatment plan optimization

A treatment plan is then generated using the in-house research TPS, which besides standard optimization algorithms also supports several novel optimization approaches. These include BED-based optimization, the simultaneous optimization of multiple dose distributions, beam orientation optimization, collimator angle optimization, robust optimization approaches using stochastic programming methods and the use of non-standard planning objectives and constraints such as tumor control probability and equivalent uniform dose. Treatment plans can be optimized in the in-house TPS both using a two-step approach with fluence map optimization followed by leaf sequencing, as well as using direct aperture optimization. Ultimately, treatment plans are generated which consists of a set of multileaf collimator

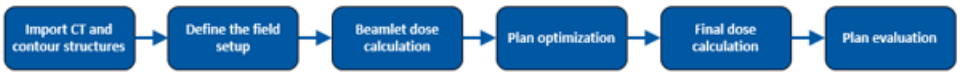

(a) Treament planning process to generate treatment plans within the commercial Eclipse TPS

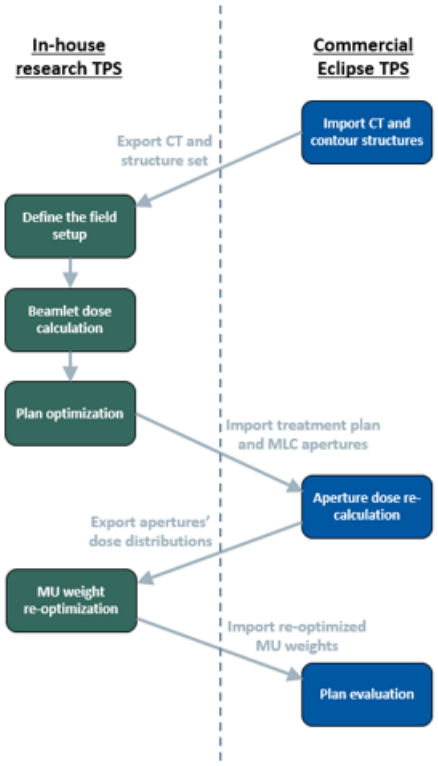

(b) Treament planning process to generate treatment plans starting from the in-house research TPS

Figure 8.1: *Workflows for the treatment planning process used (a) to generate a treatment plan entirely in the Eclipse TPS and (b) to generate a treatment plan using the in-house research TPS and uploading the final plan to the Eclipse TPS.*

(MLC)-based apertures at different beam orientations and their corresponding weights. Each plan is stored as a ".csv" file, which for each aperture includes the information reported in Table 8.1.

Import of the treatment plan into the Eclipse TPS

The files storing the plan information generated by the in-house TPS are subsequently imported into the Eclipse TPS, again using ESAPI scripts. At this step, additional information are manually provided regarding the fractionation scheme, the selection of a target structure, the treatment technique

Table 8.1: *Plan information stored for each MLC-based aperture in the treatment plan optimized using the in-house TPS in a ".csv"-file.*

Variable	Description
Instance number	Denotes the number of the instance that the aperture belongs to, where an instance refers to a specific dose distribution to be delivered in a given fraction (in case a treatment consists of multiple dose distributions to be delivered in distinct fractions)
Beam number	Indexes the number of the beam in the instance
Gantry angle	Denotes the gantry angle of the beam from which the aperture is delivered
Table angle	Denotes the table angle of the beam from which the aperture is delivered
Collimator angle	Denotes the collimator angle for the beam from which the aperture is delivered
Isocenter position	Denotes the isocenter position for the beam from which the aperture is delivered (in the patient's reference frame)
Aperture number	Indexes the number of the aperture
Leaf positions	Denote the x and y coordinates of each MLC leaf pair shaping the aperture
Weight	Denotes the weight of the aperture (not necessarily normalized to monitor units)

(i.e. step-and-shoot intensity modulated radiotherapy (IMRT) or dynamic volumetric modulated arc therapy (VMAT)) and the treatment machine to be used for the delivery of the plan. To create a treatment plan in the Eclipse TPS with the same characteristics (i.e. same beam orientations and same MLC apertures' shapes and weights) of the plan generated using the in-house TPS, the information contained in the input ".csv"-file is first pre-processed to create a hierarchical grouping of different class objects that mirrors the intrinsic class structure for objects in the Eclipse TPS (Fig. 8.2a), i.e. Treatment → Instance → Beam → Aperture → LeafPosition, where:

- The Treatment class is the parent node of the structure. It contains all other class objects and is only initialized once. It contains only one class attribute, which is a list of Instance objects.
- The total amount of Instance objects corresponds to the number of different instances (i.e. dose distributions) within the plan. Each Instance object in turn contains a list of Beam objects.
- Beam objects store the attributes of the beam to be used, namely the gantry, table and collimator angle, as well as the sum of the aperture weights. Additionally, a list of Aperture objects is stored for each beam, which corresponds to all apertures generated in the in-house TPS belonging to this specific beam number and instance number.

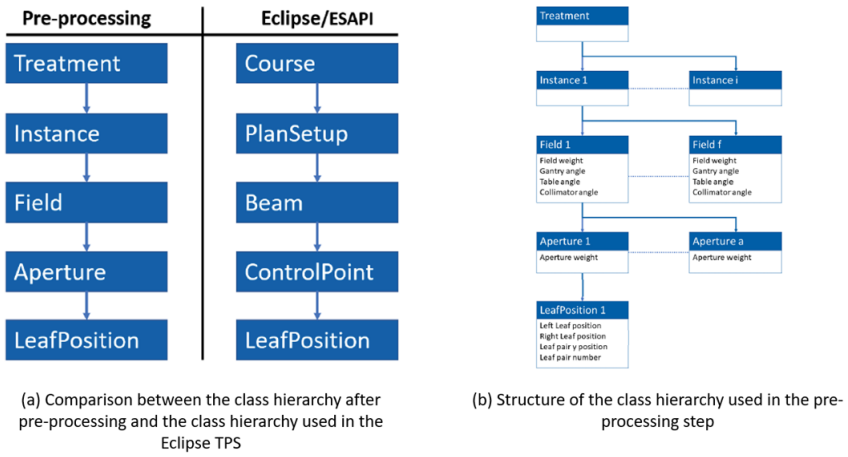

(a) Comparison between the class hierarchy after pre-processing and the class hierarchy used in the Eclipse TPS

(b) Structure of the class hierarchy used in the pre-processing step

Figure 8.2: *Details about the hierarchical structure used to handle treatment plans in the Eclipse, which has been mirrored in the pre-processing step.*

- Aperture objects contain information about the aperture weight, and a list of LeafPosition objects.
- LeafPosition objects store the positions of the left and right MLC leaves for a specific leaf pair and the y coordinate of the corresponding leaf pair. Given this y coordinate, the corresponding leaf number for a machine can then be calculated by using information about the width of the outer and inner MLC leaves. This is also summarized in Figure 2b, which displays the class hierarchy alongside the layers at which certain parameters are stored.

This is also summarized in Fig. 8.2b, which displays the class hierarchy alongside the layers at which certain parameters are stored.

After this pre-processing step, a treatment course is created in the Eclipse TPS, including different plan objects for each instance-specific dose distribution, which are characterized by the same beam orientations and the same set of MLC apertures as obtained from the in-house TPS. This step was performed following the Model-View-ViewModel (MVVM) architecture, which is the accepted standard for Windows presentation foundation (WPF) applications and is the application type of binary plug-ins for the Eclipse TPS.

Dose re-calculation in the Eclipse TPS

For each of the MLC-based aperture imported into the Eclipse TPS, a dose re-calculation is performed using built-in Eclipse dose calculation algorithms. This is necessary for several reasons. First, the dose calculation algorithm

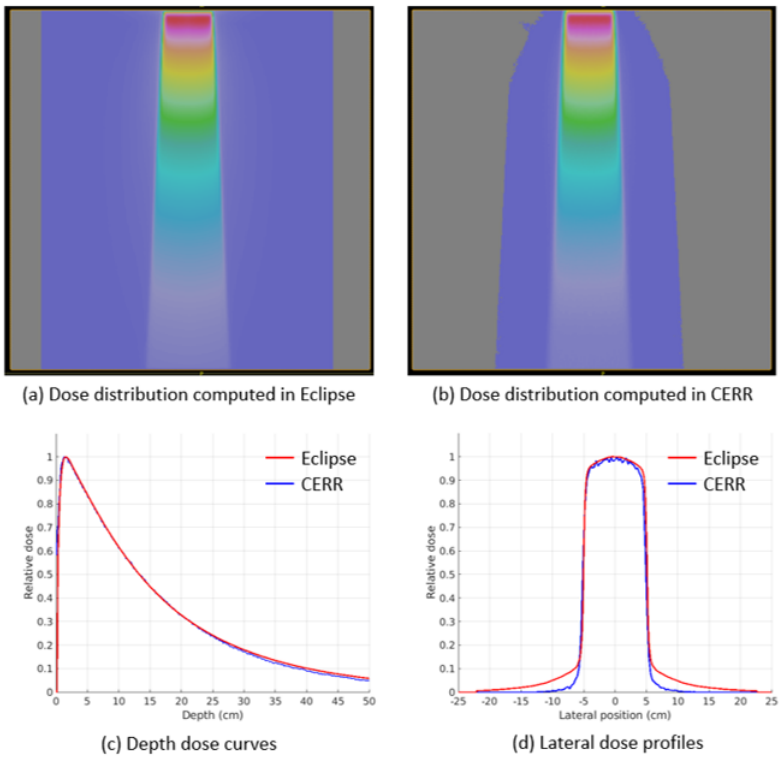

Figure 8.3: *Dose distributions obtained for a 10 x 10 cm^2 field at a SSD of 100 cm impinging on a homogeneous 50 x 50 x 50 cm^3 water phantom computed with (a) the Acuros16.1.0 algorithm in the Eclipse TPS and (b) the QIB algorithm in CERR. Also shown are a comparison of the depth dose curves and the lateral dose profiles, which have been normalized to the maximum voxel dose.*

used to compute the beamlets dose distributions in CERR which have then been used for plan optimization in the in-house TPS is not commissioned for clinical use, whereas dose calculation algorithms in the Eclipse TPS have been validated to match the measured dose distributions for each specific treatment machine used in the clinics. This may introduce some slight discrepancies between the dose distribution computed in CERR and the dose distribution computed in the Eclipse TPS. An example of dose distributions for a 10 x 10 cm^2 field at a source-to-surface distance (SSD) of 100 cm impinging on a homogeneous 50 x 50 x 50 cm^3 water phantom computed with the QIB algorithm in CERR and the Acuros16.1.0 algorithm in the Eclipse TPS, respectively, are shown in Fig. 8.3. While similar depth dose curves are obtained using both algorithms, the dose calculation algorithm used in CERR tends to underestimate the lateral dose.

Second, effects like the tongue-and-groove effect and transmission through the MLC are not considered during plan optimization. Consequently, the dose distribution resulting from the delivery of radiation through an aperture does not necessarily corresponds to the sum of the dose distributions for each of the exposed beamlets, as assumed during the treatment plan optimization. Finally, the dose-influence matrices computed in CERR are not normalized to monitor units (MUs) of a specific treatment machine. Thus, using the same aperture weights as obtained in the in-house TPS does not result in the intended total tumor dose.

Export of aperture-specific dose distributions and aperture weight re-optimization

To mitigate the effect of such discrepancies in the apertures' dose distributions and correct for the MU weight normalization, an additional re-optimization of the aperture weights is performed in the in-house TPS. The dose distributions calculated in the Eclipse TPS are normalized to 1 MU and exported to the research platform. The MU weights of all the apertures are then simultaneously optimized using the in-house TPS for the same planning objectives and constraints as used in the first treatment plan optimization. The shapes of the apertures are not modified.

Import of the re-optimized apertures' weights into the Eclipse TPS and dose evaluation

Finally, the new MU weights for all apertures are imported into the Eclipse TPS, where the dose distributions can be evaluated. To evaluate the quality of spatiotemporal fractionation schemes, an ESAPI script has been used that converts physical dose distributions in the Eclipse TPS into BED distributions.

8.3.2 Assessment of the quality of treatment plans generated using the proposed treatment planning process

The treatment planning process discussed in the previous section has been tested for a prostate cancer patient, by comparing an IMRT treatment plan generated using the proposed workflow to an IMRT plan generated entirely in the Eclipse TPS. However, the optimization and upload of dynamic VMAT plans are also supported. Prostate cancer was chosen for such a comparison because radiotherapy treatment planning for prostate cancer is very well

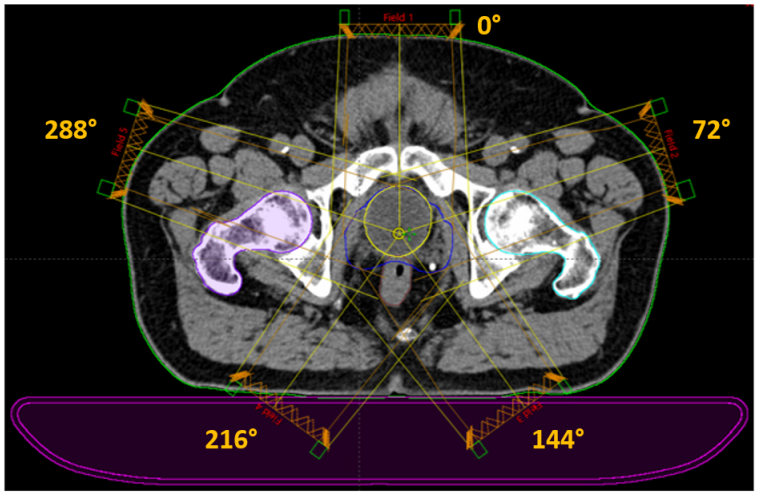

Figure 8.4: *CT of the prostate cancer patient along with the field setup used to generate the step-and-shoot IMRT plan. Shown are the contours of the PTV (blue, which measures 118.3 cc and includes the whole prostate gland), rectum (brown), bladder (yellow) and femoral heads (cyan and violet).*

standardized Thereby, it was possible to better evaluate eventual benefits or shortcomings of the treatment planning process.

First, a step-and-shoot IMRT plan has been generated in the Eclipse TPS. The IMRT plan consists of 5 equispaced fields at gantry angles of 0°, 72°, 144°, 216° and 288° (Fig. 8.4), respectively, and N=10 apertures are used to discretize the optimal fluence of each single beam (i.e. in total 50 apertures are used in the IMRT plan). A dose of 60 Gy in 30 fractions has been prescribed to the PTV in both plans, and dose-volume planning objectives for limiting the dose to bladder, bowel, femoral heads and rectum have been used (as further detailed in the Supplementary material, Appendix A). Additionally, a normal tissue objective was used to penalize high doses outside of the PTV. For the plan optimization the PO16.1.0 algorithm has been used, while dose calculation has been performed using the Acuros16.1.0 algorithm.

Afterwards, the same treatment plan has been re-optimized using the in-house TPS. Dose calculation has been performed using the QIB algorithm in CERR and the plan optimization was performed for the same planning objectives, using an in-house implemented column generation based direct aperture optimization algorithm (further details on the optimization algorithm are discussed in the Supplementary material, Appendix B). The resulting apertures have successively been uploaded into the Eclipse TPS and apertures' dose re-calculation was performed using the Acuros16.1.0 algo-

rithm. Finally, the MU weights of the apertures have been re-optimized in the in-house TPS using a quasi-Newton L-BFGS algorithm, and modified in the Eclipse TPS. For comparison, both plans have been normalized such that the prescribed dose is delivered to 50% of the target volume.

Besides comparing the resulting dosimetric quality of treatment plans generated entirely in the Eclipse TPS and generated using the proposed TPP, respectively, we also analyzed whether the quality of the plan generated using the proposed TPP is affected by the different dose calculation algorithms used. In particular, the quality of the treatment plan obtained assuming the dose-influence matrices computed in CERR has been compared to the quality of the plan obtained after the weight re-optimization. The degree to which the apertures' weights are adjusted was also studied.

8.4 Results

The dose distributions for the IMRT plans generated entirely using the Eclipse TPS and using the proposed treatment planning process, respectively, are shown in Fig. 8.5. The corresponding dose-volume histograms (DVHs) evaluated for the PTV and the most relevant OARs are shown in Fig. 8.6. Overall, the IMRT plan generated using the proposed treatment planning process is very similar to the IMRT plan generated entirely using the Eclipse TPS. In particular, both plans achieve a similar sparing of the OARs. However, the PTV dose coverage is slightly worse for the plan generated using the proposed treatment planning process. This is likely due to discrepancies in the dose calculation algorithms, which can only be partly mitigated by the re-optimization of the apertures' weights. A DVH comparison between the IMRT plan obtained after DAO optimization based on the dose-influence matrices computed in CERR and the plan obtained after re-optimization of the apertures' weights based on the dose distributions computed using the Acuros16.1.0 algorithm in the Eclipse TPS is shown in Fig. 8.7a, demonstrating that a very high plan quality and a good target coverage could be achieved with the in-house research optimizer. Fig. 8.7b illustrates how the weights of the different apertures have been adjusted after the weight re-optimization.

8.5 Discussion

In this work, we developed a treatment planning process which allows to upload treatment plans generated using our in-house TPS into the commercial

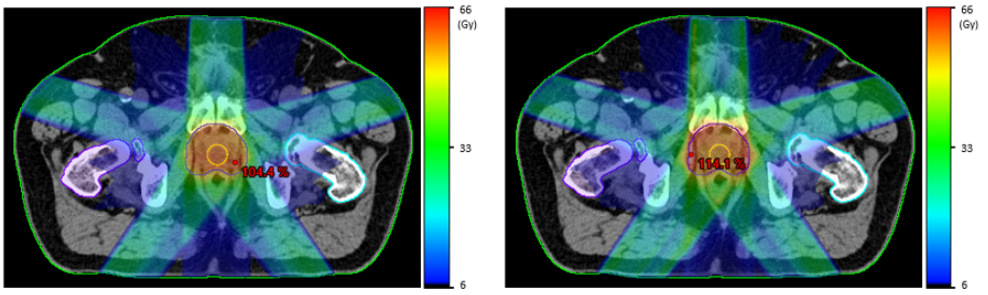

(a) IMRT plan generated entirely using the Eclipse TPS

(b) IMRT plan generated using the proposed treatment planning process

Figure 8.5: *Dose distributions for the IMRT plans generated (a) using the Eclipse TPS and (b) using the proposed treatment planning process.*

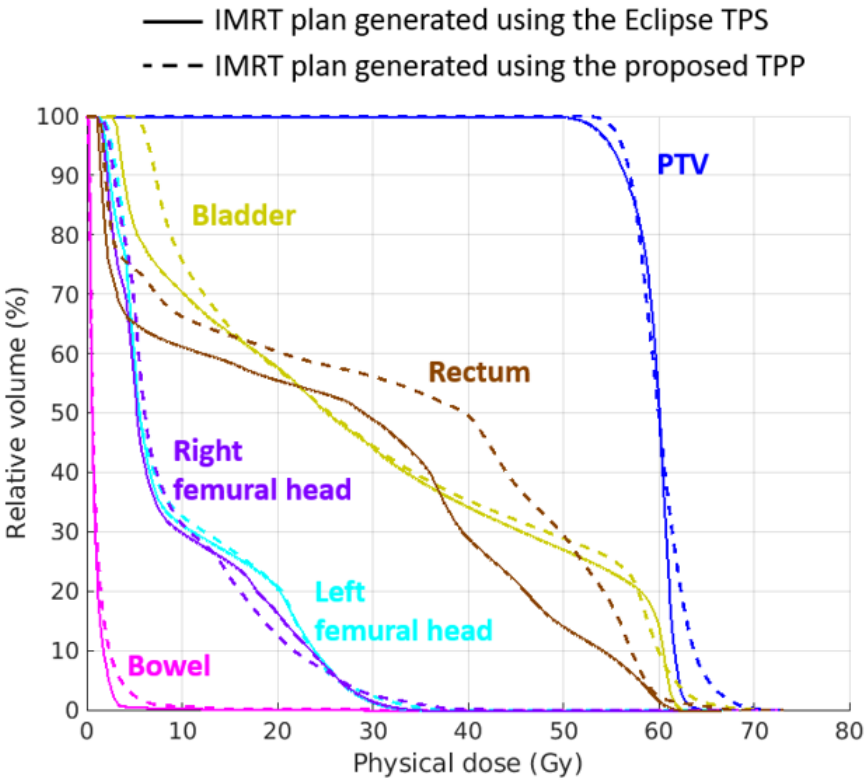

Figure 8.6: *Dose-volume histograms for the IMRT plans obtained using the Eclipse TPS (solid line) and using the proposed treatment planning process (dashed line).*

Eclipse TPS. Such treatment planning process has been successfully validated for a prostate cancer patient, by showing that step-and-shoot IMRT treatment plans can be obtained which have a similar quality as IMRT plans

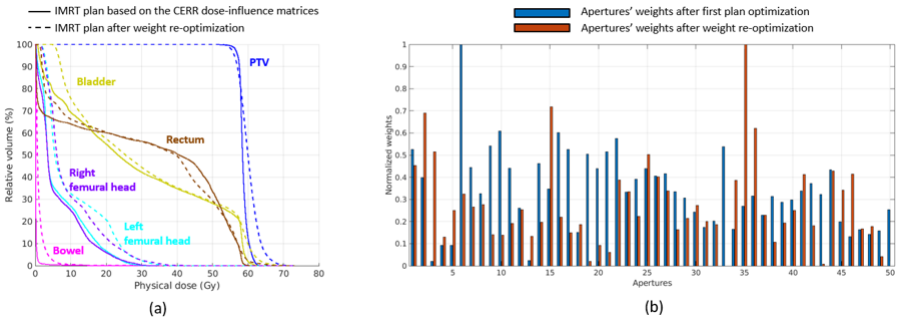

Figure 8.7: *Comparison between the IMRT plans obtained using the proposed treatment planning process after the first plan optimization (i.e. based on the dose-influence matrices computed in CERR) and after re-optimization of the apertures' weights (based on the dose distributions calculated in the Eclipse TPS). In particular, we compared (a) the dose-volume histograms and (b) the apertures' weights.*

generated entirely in the Eclipse TPS. In this way, latest treatment planning approaches developed in research can potentially be used to generated clinically deliverable treatment plans. If dose distributions can be re-created in the Eclipse TPS that meet all clinical standards, in fact, there is no legal need to perform quality assurance of the in-house research TPS.

Despite the promising results obtained in this work, concerns remain regarding some practical aspects of the treatment planning process. In particular, differences in the dose calculation algorithms between CERR and the Eclipse TPS were shown to lead to a slight degradation of the plan quality before and after importing the plan into the Eclipse TPS. Although discrepancies in the apertures' dose distributions could be partly mitigated by the apertures' weights re-optimization step, such an issue may lead to sub-optimal apertures' shapes. Better dose calculation algorithms, for example by using Monte Carlo methods, are necessary for improving the quality of plans generated using the proposed treatment planning process. Also, the need to switch between the in-house research TPS and the Eclipse TPS makes the whole treatment planning process more cumbersome and error-prone compared to generating a treatment plan entirely in the Eclipse TPS. Better automation could reduce this issue.

8.6 Conclusion

Radiotherapy plans generated using a research TPS cannot be delivered clinically without proper quality assurance of the research TPS. To circumvent

this issue, we implemented and tested a treatment planning process which allows reproduce treatment plans optimized using latest planning approaches available in our in-house research TPS within the medically certified commercial Eclipse TPS.

8.7 Supplementary material

Appendix A Planning objectives used to generate the IMRT plans

In this section, we detail and provide the mathematical formulation of the planning objectives used for the optimization of the IMRT plans. The same planning objectives are used both to optimize the plan generated entirely in the Eclipse TPS and the plan generated using the proposed treatment planning process, and are the following:

1. A physical dose of 58 Gy is prescribed to the PTV (using a piecewise quadratic penalty function) and dose values exceeding 62 Gy are penalized quadratically.
2. The mean dose to the bladder is minimized.
3. The mean dose to the left femoral head is minimized.
4. The mean dose to the right femoral head is minimized.
5. Dose values exceeding 59 Gy in the rectum are penalized quadratically.
6. Dose values exceeding 20 Gy in the bowel are penalized quadratically.
7. The dose must be conformal to the PTV. This has been implemented using a normal tissue objective.

Mathematically, these planning objectives are formulated as follows:

$$f(\mathbf{d}) = \frac{100}{|PTV|} \sum_{i \in PTV} \left[(58 - d_i)_+^2 + (d_i - 62)_+^2 \right] \tag{8A.1}$$

$$+ \frac{100}{|BL|} \sum_{i \in BL} d_i \tag{8A.2}$$

$$+ \frac{100}{|FHL|} \sum_{i \in FHL} d_i \tag{8A.3}$$

$$+\frac{100}{|FHR|}\sum_{i\in FHR} d_i \tag{8A.4}$$

$$+\frac{50}{|R|}\sum_{i\in R}(59-d_i)_+^2 \tag{8A.5}$$

$$+\frac{50}{|BW|}\sum_{i\in BW}(20-d_i)_+^2 \tag{8A.6}$$

$$+\frac{100}{|NT|}\sum_{i\in NT}(b_i-b_i^{max})_+^2 \tag{8A.7}$$

where PTV denotes the set of voxels belonging to the PTV, BL is the set of voxels belongin to the bladder, FHL and FHR are the set of voxels belonging to the left and right femoral head, respectively, R denotes the set of voxels belonging to the rectum, BW is the set of voxels belonging to the bowel and NT represents all voxels in the normal tissue. The parameters used for the normal tissue objective are: d_0=57 Gy, d_∞=6 Gy, x_0=0.2 cm and κ=0.2 cm^{-1}.

Appendix B Direct aperture optimization

The step-and-shoot IMRT plan in the research TPS has been optimized using a column generation based direct aperture optimization (DAO) algorithm. The DAO algorithm is very similar to the one described in Chapter 7, where promising apertures are iteratively generated and added to the plan using the a column generation algorithm, and subsequently their shapes and weights are re-optimized using a gradient based DAO approach. Compared to the DAO algorithm used in Chapter 7, however, no delivery efficiency constraints are defined for the optimization of IMRT plans.

The optimization problem thereby reads

$$\begin{aligned}
&\text{minimize} && f(\mathbf{d}) && && (8B.8)\\
&\text{subject to} && d_i = \sum_{k\in K}\omega_k \sum_{l\in L_k}\Phi_i^{kl}(x_L^{kl}, x_R^{kl}) && \forall i, \forall t && (8B.9)\\
& && \omega_k \geq 0 && \forall k && (8B.10)\\
& && x_L^{kl} \leq x_R^{kl} && \forall k, \forall l && (8B.11)
\end{aligned}$$

where d_i is the physical dose delivered to voxel i by all the contributing MLC-based apertures $k \in K$, Φ_i^{kl} is the dose contribution of the l-th leaf pair of aperture k to voxel i per unit intensity and ω_k is the MU weight of aperture

k. The parameters x_L^{kl} and x_R^{kl} describe the positions of the left and right MLC leaves in the l-th leaf pair of aperture k, respectively, and L_k is the set of all MLC leaf pairs in aperture k. The apertures' shape refinement stop after 20 iterations of the gradient based DAO approach.

Compared to IMRT plans generated using the built-in Eclipse optimization algorithm PO16.1.0, which performs first fluence map optimization and then applies a leaf-sequencing algorithm to sequence the optimal fluence into a user-defined number of apertures per beam, with our approach the number of apertures per beam is not constrained to be the same.

Chapter 9

Discussion and Conclusion

Developments in radiotherapy have mainly been driven by advances in the treatment delivery hardware and in the planning algorithms, which allowed to progressively improve the conformity of the dose distribution to the tumor while minimizing the dose to the surrounding normal tissue. However, improvements in dose conformity seem like to reach a plateau in the near future. In that regard, biologically oriented treatment plan optimization is gaining a lot of interest.

In this thesis, we investigated the concept of spatiotemporal fractionation. Unlike traditional uniformly fractionated treatments, spatiotemporally fractionated treatments alter the dose distribution in the different fractions to best achieve hypofractionation in the tumor and uniform fractionation in the surrounding normal tissue. This is achieved by treating distinct regions of the target volume to a high dose in different fractions, thereby reducing the total physical dose needed to achieve tumor control. At the same time, a similar dose bath is delivered to the normal tissue in every fraction, thus exploiting the fractionation effect. These two effects combined lead to an improved ratio between the biological dose delivered to the tumor and the biological dose delivered to the normal tissue in comparison to uniform fractionation schemes. However, spatiotemporal fractionation also increases the complexity of radiotherapy treatments, which must be considered before a translation of spatiotemporal fractionation schemes into clinical practice.

The aim of this thesis was to bring the concept of spatiotemporal fractionation towards the design and implementation of a phase I clinical trial to facilitate a first clinical application. This has been achieved in two ways:

1. The treatment planning methodology to design spatiotemporally fractionated treatments has been further developed. In particular, both limitations of the standard BED model and uncertainty in the biologi-

cal parameters, as well as patient setup uncertainty, have been extensively investigated and integrated into the treatment plan optimization to generate spatiotemporally fractionated treatments which are robust.

2. Additional promising clinical applications for spatiotemporal fractionation have been identified, which may inform the design of future clinical trials.

In the following sections, we will discuss in more detail the main findings of this thesis and summarize the current status of spatiotemporal fractionation. Finally, we will outline avenues for future research and draw conclusions.

9.1 Robustness of spatiotemporally fractionated treatments against biological and geometrical uncertainties

The most pressing concern for spatiotemporal fractionation schemes is their sensitivity to both setup errors and uncertainties in the BED model and the model parameters. Despite the promising dosimetric results which are obtained in in-silico studies, where spatiotemporal fractionation schemes are shown to potentially reduce the integral BED to critical OARs by approximately 10-20% compared to conventional uniform fractionation schemes for a comparable BED in the target volume, potential misalignments of the fractional dose distributions in between the different fractions may lead to tumor under-dosage and thereby compromise tumor control. This has been shown in Chapters 2 and 3, where already setup errors in the order of few millimeters could considerably degrade the treatment plan quality. Also, deviations of the from the assumed fractionation sensitivity were shown in Chapter 4 to possibly deteriorate the therapeutic efficacy of spatiotemporal fractionation.

Such uncertainties can nevertheless be directly accounted for during the optimization of spatiotemporally fractionated treatments. More specifically, in this thesis we developed stochastic optimization methods for handling both biological uncertainties (Chapter 4) and uncertainties in the patient setup (Chapter 3). We demonstrated that robust spatiotemporally fractionated treatment plans can be obtained which maintain parts of the benefits of spatiotemporal fractionation schemes over uniform fractionation schemes. In Chapters 1 and 2, we investigated a different approach which can be adopted to reduce the impact of setup errors and biological uncertainties related to partial tumor irradiation for patients with multiple brain metastases. This approach constrains the dose compartmentalization of the target volume to

follow the anatomical compartmentalization given by the distinct metastatic lesions, while still accounting for setup uncertainties using a safety margin.

Although robust optimization of spatiotemporally fractionated treatments were shown to reduce the expected dosimetric benefit of spatiotemporal fractionation schemes over conventional uniform fractionation schemes, the methods developed in this thesis may be used to facilitate the clinical implementation of spatiotemporal fractionation schemes by reducing the sources of uncertainties which might impact the treatment outcomes.

9.2 Promising candidates for spatiotemporal fractionation

Prior to this study, spatiotemporal fractionation has been mainly investigated for patients with large arteriovenous malformations and patients with liver metastases. These patients have been further investigated in this thesis utilizing both robust optimization approaches (Chapter 5) and combining spatiotemporal fractionation with other interesting approaches, such as combined proton-photon therapy (Chapter 6) and the use of fraction-variant beam orientations (Chapter 7).

In particular, arteriovenous malformations are characterized by a low α/β-ratio, comparable to the α/β-ratio of the surrounding healthy brain. This is advantageous for spatiotemporal fractionation schemes, as high doses per fraction are very effective and an improved trade-off between hypofractionation in the target volume and uniform fractionation in the surrounding healthy brain can be achieved. However, large arteriovenous malformations are rare and only very few patients are diagnosed with large arteriovenous malformations per year. This would make performing a clinical I trial complicated.

Patients with primary or metastatic liver cancer, on the other hand, are more common. Spatiotemporal fractionation schemes have been shown to be a promising treatment approach for patients with large tumor burden that allows dose escalation when the prescription dose is limited by the mean liver dose. Also, the fact that the liver is a parallel organ acts in favor of spatiotemporal fractionation. Spatiotemporally fractionated treatments require that a large portion of the target volume can be hypofractionated in order to be effective. While this is typically not possible when the target volume is very close to serial OARs, it is definitely possible for tumors which are embedded into the liver. However, liver tumors may present significant intrafraction motion, as well as inter-fraction anatomical variation, which may

negatively impact the accuracy of spatiotemporally fractionated treatments. In that regard, future improvements in tumor tracking and deformable image registration may pave the way for a successful clinical implementation of spatiotemporal fractionation schemes for the treatment of patients with liver metastases.

In this thesis, a new and very promising potential application for spatiotemporal fractionation has been extensively investigated, namely patients with multiple brain metastases. Spatiotemporal fractionation schemes may not be necessarily advantageous for solitary brain tumors due to the unfavorable ratio between high α/β in the tumor and low α/β in the surrounding healthy brain. However, for patients with multiple lesions, it is possible to treat different metastases to a high dose in different fractions while at the same time achieving fractionation in the healthy brain in between the different lesions. In Chapters 2, 3 and 4, we demonstrated that spatiotemporally fractionated treatments can considerably reduce the mean brain BED compared to established stereotactic radiosurgery treatments. One special advantage of patients with multiple brain metastases, which makes them a very interesting and promising application for spatiotemporal fractionation, is that intra-cranial metastases only present negligible anatomical changes during the treatment and existing immobilization devices together with image guidance ensures high reproducibility of the patient setup in between the different fractions. Consequently, spatiotemporally fractionated treatments could guarantee an accurate tumor dose coverage. With the increasing efficacy of systemic therapies, which increase the life expectancy for patients with multiple brain metastases, spatiotemporal fractionation schemes may be a promising approach to reduce brain toxicities and improving the patients' quality of life.

9.3 Temporal optimization of the radiotherapy treatment course

Fractionation has historically been proposed to improve the tumor to normal tissue therapeutic ratio. However, fractionation also offer many other opportunities which are underutilized in current clinical practice. Besides altering the dose distributions in the different fractions as suggested by spatiotemporal fractionation, there are additional concepts that benefit from the fact that the dose can be delivered over multiple separate fractions. In this study, we considered two such approaches: combined proton-photon therapy and fraction-variant beam orientation optimization. In Chapter 6, we showed

that the quality of spatiotemporally fractionated radiotherapy treatments can be boosted by combination with fraction-variant beam orientation optimization. As different regions of the target volume are treated to a high dose in different fractions, and these regions may be situated at different anatomical locations, it may be meaningful to also consider different beam orientations for the delivery of each fraction. In Chapter 5, instead, we showed that spatiotemporal fractionation can be used also to simultaneously optimize different dose distributions obtained from using different treatment techniques and particle types. In the context of combined proton-photon therapy, the treatment planning algorithms developed for spatiotemporal fractionation can be used to determine the combination of proton and photon fractions that best utilize a limited number of proton fractions.

9.4 Practical considerations on the optimization and delivery of spatiotemporally fractionated treatments

Spatiotemporal fractionation schemes require the simultaneous optimization of multiple dose distributions. Thereby, both the computational cost for generating spatiotemporally fractionation schemes and the time needed for quality assurance increase linearly with the number of different fractions. In this thesis, several extensions to the optimization code have been made to enhance the computational efficiency, for example through the implementation of a non-uniform dose grid size. With the increased use of GPU-based optimization and recent developments in automated planning, the impact on the clinical resources of the longer computational time needed to generate spatiotemporally fractionated treatments does not appear to be a crucial problem. Also, with increased automation of patient-specific quality assurance the additional burden of quality assurance for spatiotemporal fractionation schemes is reduced.

In Chapter 8, we developed a treatment planning process which allow to generate clinically deliverable spatiotemporally fractionated treatments on a commercial treatment planning system. Although improvements in the dose calculation algorithms used for the research treatment planning system and additional testing of the implemented optimization algorithms may be needed to further improve the treatment plan quality to the level of commercial treatment planning systems, the work performed in Chapter 8 constitutes an important step towards the clinical implementation of spatiotemporal fractionation.

9.5 Outlook and conclusions

In conclusion, in this thesis we demonstrated that spatiotemporal fractionation is a very promising treatment approach to improve the therapeutic ratio compared to conventional uniform fractionation for some selected treatment sites, including patients with multiple brain metastases, liver cancer and large arteriovenous malformations. We developed and demonstrated different methods to account for both geometrical and biological uncertainties, such that robust spatiotemporally fractionated treatments can be obtained which still outperform conventional uniformly fractionated plans. While further research may be performed, for example to investigate the impact of inter-fractional anatomical changes on the tumor or include more accurate biological models, the work performed in this thesis together with the implementation of a treatment planning process to generate clinically deliverable spatiotemporally fractionated plans represent fundamental steps to facilitate the design of a clinical phase I trial to investigate the feasibility of spatiotemporal fractionation in the clinics.

Bibliography

[1] American Cancer Society (https://www.cancer.org/about-us/our-global-health-work/global-cancer-burden.html, Accessed: 09.11.2023)

[2] Deferal Statistical Office (https://www.bfs.admin.ch/bfs/en/home/statistics/health/state-health/diseases/cancer.html, Accessed: 09.11.2023)

[3] Gelband H, Jha P, Sankaranarayanan R, and Horton S (ed.). Cancer: Disease Control Priorities, vol. 3, chap. 14, 266-290 (The International Bank for Reconstruction and Development / The World Bank, 2015), third edn.

[4] Varian Medical Systems (https://www.varian.com/en-ch/products/radiotherapy/treatment-delivery/truebeam, Accessed: 09.11.2023)

[5] Romeijn, H. Edwin et al. "A Column Generation Approach to Radiation Therapy Treatment Planning Using Aperture Modulation." SIAM J. Optim. 15 (2005): 838-862

[6] Bortfeld T. IMRT: a review and preview. Phys Med Biol. 2006;51(13):R363-R379. doi:10.1088/0031-9155/51/13/R21

[7] Tai DT, Oanh LT, Phuong PH, et al. Dosimetric and radiobiological comparison in head-and-neck radiotherapy using JO-IMRT and 3D-CRT. Saudi J Biol Sci. 2022;29(8):103336. doi:10.1016/j.sjbs.2022.103336

[8] Teoh M, Clark CH, Wood K, Whitaker S, Nisbet A. Volumetric modulated arc therapy: a review of current literature and clinical use in practice. Br J Radiol. 2011;84(1007):967-996. doi:10.1259/bjr/22373346

[9] Dong P, Lee P, Ruan D, et al. 4Π non-coplanar liver SBRT: a novel delivery technique. Int J Radiat Oncol Biol Phys. 2013;85(5):1360-1366. doi:10.1016/j.ijrobp.2012.09.028

[10] Papp D, Bortfeld T, Unkelbach J. A modular approach to intensity-modulated arc therapy optimization with noncoplanar trajectories. Phys Med Biol. 2015;60(13):5179-5198. doi:10.1088/0031-9155/60/13/5179

[11] Garibaldi C, Jereczek-Fossa BA, Marvaso G, et al. Recent advances in radiation oncology. Ecancermedicalscience. 2017;11:785. Published 2017 Nov 30. doi:10.3332/ecancer.2017.785

[12] Hu, M., Jiang, L., Cui, X. et al. Proton beam therapy for cancer in the era of precision medicine. J Hematol Oncol 11, 136 (2018). doi:10.1186/s13045-018-0683-4

[13] Khan FM, Gibbons JP, Sperduto PW (ed.) Treatment Planning in Radiation Oncology (Lippincott Williams Wilkins, 2016).

[14] Landberg T, Chavaudra J, Dobbs J, et al. Icru report 50. Journal of the International Commission on Radiation Units and Measurements os26 (1993).

[15] Landberg T, Chavaudra J, Dobbs J, et al. Icru report 62. Journal of the International Commission on Radiation Units and Measurements os32 (1999).

[16] Francolini G, Desideri I, Stocchi G, et al. Artificial intelligence in radiotherapy: state of the art and future directions. Med Oncol 37 (2020).

[17] RadiologyKey (https://radiologykey.com/computer-assisted-treatment-planning-approaches-for-carbon-ion-beam-therapy/, Accessed: 09.11.2023)

[18] Ahnesjo A, Saxner M, Trepp A. A pencil beam model for photon dose calculation. Med Phys. 1992;19(2):263-273. doi:10.1118/1.596856

[19] Jabbari K. Review of fast monte carlo codes for dose calculation in radiation therapy treatment planning. J Med Signals Sens. 2011;1(1):73-86.

[20] Marks LB, Yorke ED, Jackson A, et al. Use of normal tissue complication probability models in the clinic. Int J Radiat Oncol Biol Phys. 2010;76(3 Suppl):S10-S19. doi:10.1016/j.ijrobp.2009.07.1754

[21] Fowler JF. The linear-quadratic formula and progress in fractionated radiotherapy. Br J Radiol 62, 679,Äì694 (1989).

[22] Unkelbach J, Craft D, Salari E, Ramakrishnan J, Bortfeld T. The dependence of optimal fractionation schemes on the spatial dose distribution. Phys Med Biol. 2013;58(1):159-167. doi:10.1088/0031-9155/58/1/159

[23] Williams MV, Denekamp J, and Fowler JF. A review of α/β ratios for experimental tumors: Implications for clinical studies of altered fractionation. Int J Radiat Oncol Biol Phys 11, 87,Äì96 (1985).

[24] Andruska N, Stowe HB, Crockett C, et al. Stereotactic Radiation for Lung Cancer: A Practical Approach to Challenging Scenarios. J Thorac Oncol. 2021;16(7):1075-1085. doi:10.1016/j.jtho.2021.04.002

[25] Ramadan S, Quan K, Schnarr K, et al. Impact of stereotactic body radiotherapy (SBRT) in oligoprogressive metastatic disease. Acta Oncol. 2022;61(6):705-713. doi:10.1080/0284186X.2022.2063067

[26] Correa RJM, Loblaw A. Stereotactic Body Radiotherapy: Hitting Harder, Faster, and Smarter in High-Risk Prostate Cancer. Front Oncol. 2022;12:889132. Published 2022 Jul 7. doi:10.3389/fonc.2022.889132

[27] Jardel P, Kammerer E, Villeneuve H, Thariat J. Stereotactic radiation therapy for breast cancer in the elderly. Transl Cancer Res. 2020;9(Suppl 1):S86-S96. doi:10.21037/tcr.2019.07.18

[28] Unkelbach J, Papp D. The emergence of nonuniform spatiotemporal fractionation schemes within the standard BED model. Med Phys. 2015;42(5):2234-2241. doi:10.1118/1.4916684

[29] Unkelbach J, Zeng C, Engelsman M. Simultaneous optimization of dose distributions and fractionation schemes in particle radiotherapy. Med Phys. 2013;40(9):091702. doi:10.1118/1.4816658

[30] Unkelbach J. Non-Uniform Spatiotemporal Fractionation Schemes in Photon Radiotherapy: World Congress on Medical Physics and Biomedical Engineering, Toronto, Canada, 7-12 June 2015. Springer; 2015.

[31] Unkelbach J, Bussière MR, Chapman PH, Loeffler JS, Shih HA. Spatiotemporal fractionation schemes for irradiating large cerebral arteriovenous malformations. Int J Radiat Oncol Biol Phys. 2016;95(3):1067-1074. doi:10.1016/j.ijrobp.2016.02.001.

[32] Unkelbach J, Papp D, Gaddy MR, Andratschke N, Hong T, Guckenberger M. Spatiotemporal fractionation schemes for liver stereotactic body radiotherapy. Radiother Oncol. 2017;125(2):357-364. doi:10.1016/j.radonc.2017.09.003

[33] Brenner AW, Patel AJ. Review of Current Principles of the Diagnosis and Management of Brain Metastases. Front Oncol. 2022;12:857622. Published 2022 May 24. doi:10.3389/fonc.2022.857622

[34] Sperduto PW, Mesko S, Li J, et al. Survival in Patients With Brain Metastases: Summary Report on the Updated Diagnosis-Specific Graded Prognostic Assessment and Definition of the Eligibility Quotient. J Clin Oncol. 2020;38(32):3773-3784. doi:10.1200/JCO.20.01255

[35] Kraft J, Zindler J, Minniti G, Guckenberger M, Andratschke N. Stereotactic radiosurgery for multiple brain metastases. Curr Treat Options Neurol. 2019;21(2):6. doi:10.1007/s11940-019-0548-3 .

[36] Kocher M, Wittig A, Piroth MD, et al. Stereotactic radiosurgery for treatment of brain metastases. A report of the DEGRO Working Group on Stereotactic Radiotherapy. Strahlenther Onkol. 2014;190(6):521-532. doi:10.1007/s00066-014-0648-7

[37] Tsao M, Xu W, Sahgal A. A meta-analysis evaluating stereotactic radiosurgery, whole-brain radiotherapy, or both for patients presenting with a limited number of brain metastases. Cancer. 2012;118(9):2486-2493. doi:10.1002/cncr.26515

[38] Churilla TM, Ballman KV, Brown PD, et al. Stereotactic radiosurgery with or without whole-brain radiation therapy for limited brain metastases: a secondary analysis of the north central cancer treatment group N0574 (Alliance) randomized controlled trial. Int J Radiat Oncol Biol Phys. 2017;99(5):1173-1178. doi:10.1016/j.ijrobp.2017.07.045

[39] Brown PD, Jaeckle K, Ballman KV, et al. Effect of radiosurgery alone vs radiosurgery with whole brain radiation therapy on cognitive function in patients with 1 to 3 brain metastases: a randomized clinical trial [published correction appears in JAMA. 2018 Aug 7;320(5):510]. JAMA. 2016;316(4):401-409. doi:10.1001/jama.2016.9839

[40] Chang EL, Wefel JS, Hess KR, et al. Neurocognition in patients with brain metastases treated with radiosurgery or radiosurgery plus whole-brain irradiation: a randomised controlled trial. Lancet Oncol. 2009;10(11):1037-1044. doi:10.1016/S1470-2045(09)70263-3

[41] Remick JS, Kowalski E, Khairnar R, et al. A multi-center analysis of single-fraction versus hypofractionated stereotactic radiosurgery for the treatment of brain metastasis. Radiat Oncol. 2020;15(1):128. doi:10.1186/s13014-020-01522-6

[42] Loo M, Pin Y, Thierry A, Clavier JB. Single-fraction radiosurgery versus fractionated stereotactic radiotherapy in patients with brain metastases: a comparative study. Clin Exp Metastasis. 2020;37(3):425-434. doi:10.1007/s10585-020-10031-5

[43] Sallabanda M, Garcia-Berrocal MI, Romero J, et al. Brain metastases treated with radiosurgery or hypofractionated stereotactic radiotherapy: outcomes and predictors of survival. Clin Transl Oncol. 2020;22(10):1809-1817. doi:10.1007/s12094-020-02321-x

[44] Deasy JO, Blanco AI, Clark VH. CERR: a computational environment for radiotherapy research. Med Phys. 2003;30:979

[45] Kelly DA. Treatment of multiple brain metastases with a divide-and-conquer spatial fractionation radiosurgery approach. Med Hypotheses. 2014;83(4):425-428. doi:10.1016/j.mehy.2014.04.024

[46] Nguyen TK, Sahgal A, Detsky J, et al. Single-fraction stereotactic radiosurgery versus hippocampal-avoidance whole brain radiation therapy for patients with 10 to 30 brain metastases: a dosimetric analysis. Int J Radiat Oncol Biol Phys. 2019;105(2):394-399. doi:10.1016/j.ijrobp.2019.06.2543

[47] Chen M, Wardak Z, Stojadinovic S, Gu X, Lu W. A general algorithm for distributed treatments of multiple brain metastases. Med Phys. 2021;48(4):1832-1838. doi:10.1002/mp.14722

[48] Mehta MP, Rozental JM, Levin AB, et al. Defining the role of radiosurgery in the management of brain metastases. Int J Radiat Oncol Biol Phys. 1992;24(4):619-625. doi:10.1016/0360-3016(92)90706-n

[49] Soliman H, Das S, Larson DA, Sahgal A. Stereotactic radiosurgery (SRS) in the modern management of patients with brain metastases. Oncotarget. 2016;7(11):12318-12330. doi:10.18632/oncotarget.7131

[50] Soike MH, Hughes RT, Farris M, et al. Does stereotactic radiosurgery have a role in the management of patients presenting with 4 or more brain metastases? Neurosurgery. 2019;84(3):558-566. doi:10.1093/neuros/nyy216

[51] Suh JH, Chao ST, Angelov L, Vogelbaum MA, Barnett GH. Role of stereotactic radiosurgery for multiple (>4) brain metastases. J Radiosurg SBRT. 2011;1(1):31-40

[52] Ali MA, Hirshman BR, Wilson B, et al. Survival patterns of 5750 stereotactic radiosurgery-treated patients with brain metastasis as a function of the number of lesions. World Neurosurg. 2017;107:944-951.e1. doi:10.1016/j.wneu.2017.07.062

[53] Kida Y, Mori Y. Radiosurgery for Patients with More Than Ten Brain Metastases. Cureus. 2020;12(1):e6728. doi:10.7759/cureus.6728

[54] Suh JH, Kotecha R, Chao ST, Ahluwalia MS, Sahgal A, Chang EL. Current approaches to the management of brain metastases. Nat Rev Clin Oncol. 2020;17(5):279-299. doi:10.1038/s41571-019-0320-3

[55] Palmer JD, Sebastian NT, Chu J, et al. Single-isocenter multi-target stereotactic radiosurgery is safe and effective in the treatment of multiple brain metastases. Adv Radiat Oncol. 2019;5(1):70-76. doi:10.1016/j.adro.2019.08.013

[56] Minniti G, Clarke E, Lanzetta G, et al. Stereotactic radiosurgery for brain metastases: analysis of outcome and risk of brain radionecrosis. Radiat Oncol. 2011;6:48. doi:10.1186/1748-717X-6-48

[57] Loo M, Clavier JB, Attal Khalifa J, Moyal E, Khalifa J. Dose-response effect and dose-toxicity in stereotactic radiotherapy for brain metastases: a review. Cancers (Basel). 2021;13(23):6086. doi:10.3390/cancers13236086

[58] Nieder C, Yobuta R, Mannsaker B. Second re-irradiation of brain metastases: a review of studies involving stereotactic radiosurgery. Cureus. 2018;10(12):e3712. doi:10.7759/cureus.3712

[59] Hall EJ, Giaccia AJ. Radiobiology for the Radiologist. 7th ed. Lippincott Williams Wilkins; 2012: 546 S

[60] Mizuta M, Takao S, Date H, et al. A mathematical study to select fractionation regimen based on physical dose distribution and the linear-quadratic model. Int J Radiat Oncol Biol Phys. 2012;84(3):829-833. doi:10.1016/j.ijrobp.2012.01.004

[61] Kim M, Stewart RD, Phillips MH. A feasibility study: selection of a personalized radiotherapy fractionation schedule using spatiotemporal optimization. Med Phys. 2015;42(11):6671-6678. doi:10.1118/1.4934369

[62] Pizarro F, Hernandez A. Optimization of radiotherapy fractionation schedules based on radiobiological functions. Br J Radiol. 2017;90(1079):20170400. doi:10.1259/bjr.20170400

[63] Kalinin EDJ. A method for fast 3-D IMRT dose calculations the quadrant infinite beam (QIB) algorithm. Paper presented at: 45th Annual Meeting of the American Association of Physicist in Medicine; 2003

[64] Dupic G, Brun L, Molnar I, et al. Significant correlation between gross tumor volume (GTV) D98% and local control in multifraction stereotactic radiotherapy (MF-SRT) for unresected brain metastases. Radiother Oncol. 2021;154:260-268. doi:10.1016/j.radonc.2020.11.021

[65] Wright SJ, Nocedal J. Numerical Optimization. Vol 2. Springer; 1999

[66] Bertsekas DP. Nonlinear Programming. Athena Scientific; 1999

[67] Bentzen SM, Dorr W, Gahbauer R, et al. Bioeffect modeling and equieffective dose concepts in radiation oncology-terminology, quantities and units. Radiother Oncol. 2012;105(2):266-268. doi:10.1016/j.radonc.2012.10.006

[68] Gaddy MR, Yildiz S, Unkelbach J, Papp D. Optimization of spatiotemporally fractionated radiotherapy treatments with bounds on the achievable benefit. Phys Med Biol. 2018;63(1):015036. doi:10.1088/1361-6560/aa9975

[69] Gaddy MR, Unkelbach J, Papp D. Robust spatiotemporal fractionation schemes in the presence of patient setup uncertainty. Med Phys. 2019;46(7):2988-3000. doi:10.1002/mp.13593

[70] Andersson B. Mathematical Optimization of Radiation Therapy Goal Fulfilment. MSc thesis. Uppsala University; 2017

[71] Unkelbach J, Alber M, Bangert M, et al. Robust radiotherapy planning. Phys Med Biol. 2018;63(22):22TR02. Published 2018 Nov 12. doi:10.1088/1361-6560/aae659

[72] Kaver G, Lind BK, Lof J, Liander A, Brahme A. Stochastic optimization of intensity modulated radiotherapy to account for uncertainties in patient sensitivity. Phys Med Biol. 1999;44(12):2955-2969. doi:10.1088/0031-9155/44/12/308

[73] Fabiano S, Torelli N, Papp D, Unkelbach J. A novel stochastic optimization method for handling misalignments of proton and photon doses in combined treatments. Phys Med Biol. 2022;67(18):10.1088/1361-6560/ac858f. Published 2022 Sep 8. doi:10.1088/1361-6560/ac858f

[74] Qi XS, Schultz CJ, Li XA. An estimation of radiobiologic parameters from clinical outcomes for radiation treatment planning of brain tumor. Int J Radiat Oncol Biol Phys. 2006;64(5):1570-1580. doi:10.1016/j.ijrobp.2005.12.022

[75] Kirkpatrick JP, Meyer JJ, Marks LB. The linear-quadratic model is inappropriate to model high dose per fraction effects in radiosurgery. Semin Radiat Oncol. 2008;18(4):240-243. doi:10.1016/j.semradonc.2008.04.005

[76] Joiner MC, Marples B, Lambin P, Short SC, Turesson I. Low-dose hypersensitivity: current status and possible mechanisms. Int J Radiat Oncol Biol Phys. 2001;49(2):379-389. doi:10.1016/s0360-3016(00)01471-1

[77] van Leeuwen CM, Oei AL, Crezee J, et al. The alfa and beta of tumours: a review of parameters of the linear-quadratic model, derived from clinical radiotherapy studies. Radiat Oncol. 2018;13(1):96. Published 2018 May 16. doi:10.1186/s13014-018-1040-z

[78] McMahon SJ. The linear quadratic model: usage, interpretation and challenges. Phys Med Biol. 2018;64(1):01TR01. Published 2018 Dec 19. doi:10.1088/1361-6560/aaf26a

[79] Onderdonk BE, Gutiontov SI, Chmura SJ. The Evolution (and Future) of Stereotactic Body Radiotherapy in the Treatment of Oligometastatic Disease. Hematol Oncol Clin North Am. 2020;34(1):307-320. doi:10.1016/j.hoc.2019.09.003

[80] Videtic GM. The role of stereotactic radiotherapy in the treatment of oligometastases. Curr Oncol Rep. 2014;16(7):391. doi:10.1007/s11912-014-0391-3

[81] Chen H, Louie AV, Higginson DS, Palma DA, Colaco R, Sahgal A. Stereotactic Radiosurgery and Stereotactic Body Radiotherapy in the Management of Oligometastatic Disease. Clin Oncol (R Coll Radiol). 2020;32(11):713-727. doi:10.1016/j.clon.2020.06.018

[82] Ahmed KA, Torres-Roca JF. Stereotactic Body Radiotherapy in the Management of Oligometastatic Disease. Cancer Control. 2016;23(1):21-29. doi:10.1177/107327481602300105

[83] Dengina N, Mitin T, Gamayunov S, Safina S, Kreinina Y, Tsimafeyeu I. Stereotactic body radiation therapy in combination with systemic

therapy for metastatic renal cell carcinoma: a prospective multicentre study. ESMO Open. 2019;4(5):e000535. Published 2019 Oct 13. doi:10.1136/esmoopen-2019-000535

[84] Tonse R, Tom MC, Mehta MP, Ahluwalia MS, Kotecha R. Integration of Systemic Therapy and Stereotactic Radiosurgery for Brain Metastases. Cancers (Basel). 2021;13(15):3682. Published 2021 Jul 22. doi:10.3390/cancers13153682

[85] Gaito S, Marvaso G, Ortiz R, et al. Proton Beam Therapy in the Oligometastatic/Oligorecurrent Setting: Is There a Role? A Literature Review. Cancers (Basel). 2023;15(9):2489. Published 2023 Apr 26. doi:10.3390/cancers15092489

[86] Grau C, Durante M, Georg D, Langendijk JA, Weber DC. Particle therapy in Europe. Mol Oncol. 2020;14(7):1492-1499. doi:10.1002/1878-0261.12677

[87] Loizeau N, Fabiano S, Papp D, et al. Optimal Allocation of Proton Therapy Slots in Combined Proton-Photon Radiation Therapy. Int J Radiat Oncol Biol Phys. 2021;111(1):196-207. doi:10.1016/j.ijrobp.2021.03.054

[88] Ten Eikelder SCM, den Hertog D, Bortfeld T, Perko Z. Optimal combined proton-photon therapy schemes based on the standard BED model. Phys Med Biol. 2019;64(6):065011. Published 2019 Mar 12. doi:10.1088/1361-6560/aafe52

[89] Unkelbach J, Bangert M, De Amorim Bernstein K, Andratschke N, Guckenberger M. Optimization of combined proton-photon treatments. Radiother Oncol. 2018;128(1):133-138. doi:10.1016/j.radonc.2017.12.031

[90] Fabiano S, Bangert M, Guckenberger M, Unkelbach J. Accounting for Range Uncertainties in the Optimization of Combined Proton-Photon Treatments Via Stochastic Optimization. Int J Radiat Oncol Biol Phys. 2020;108(3):792-801. doi:10.1016/j.ijrobp.2020.04.029

[91] Gao H. Hybrid proton-photon inverse optimization with uniformity-regularized proton and photon target dose. Phys Med Biol. 2019;64(10):105003. Published 2019 May 8. doi:10.1088/1361-6560/ab18c7

[92] Langendijk JA, Hoebers FJP, de Jong MA, et al. National Protocol for Model-Based Selection for Proton Therapy in Head and Neck

Cancer. Int J Part Ther. 2021;8(1):354-365. Published 2021 Jun 25. doi:10.14338/IJPT-20-00089.1

[93] Torelli N, Papp D, Unkelbach J. Spatiotemporal fractionation schemes for stereotactic radiosurgery of multiple brain metastases [published online ahead of print, 2023 Jun 15]. Med Phys. 2023;10.1002/mp.16457. doi:10.1002/mp.16457

[94] J.F. Fowler, 21 years of biologically effective dose, Br J Radiol, 83 (2010), pp. 554-568

[95] Wieser HP, Cisternas E, Wahl N, et al. Development of the open-source dose calculation and optimization toolkit matRad. Med Phys. 2017;44(6):2556-2568. doi:10.1002/mp.12251

[96] Travis EL, Tucker SL. Isoeffect models and fractionated radiation therapy. Int J Radiat Oncol Biol Phys. 1987;13(2):283-287. doi:10.1016/0360-3016(87)90141-6

[97] Paganetti H, Niemierko A, Ancukiewicz M, et al. Relative biological effectiveness (RBE) values for proton beam therapy. Int J Radiat Oncol Biol Phys. 2002;53(2):407-421. doi:10.1016/s0360-3016(02)02754-2

[98] van de Geijn J. Incorporating the time factor into the linear-quadratic model. Br J Radiol. 1989;62(735):296-298. doi:10.1259/0007-1285-62-735-296

[99] Tommasino F, Durante M. Proton radiobiology. Cancers (Basel). 2015;7(1):353-381. Published 2015 Feb 12. doi:10.3390/cancers7010353

[100] McNamara A L, Willers H, Paganetti H. Modelling variable proton relative biological effectiveness for treatment planning. Br J Radiol. 2020;93(1107):20190334. doi:10.1259/bjr.20190334

[101] Amstutz F, Fabiano S, Marc L, et al. Combined proton-photon therapy for non-small cell lung cancer. Med Phys. 2022;49(8):5374-5386. doi:10.1002/mp.15715

[102] Jeraj, M., Robar, V. (2004). Multileaf collimator in radiotherapy. Radiology and Oncology, 38(3). Retrieved from https://www.radioloncol.com/index.php/ro/article/view/1335

[103] Gerlach, S., Schlaefer, A. Robotic Systems in Radiotherapy and Radiosurgery. Curr Robot Rep 3, 9,Äì19 (2022). https://doi.org/10.1007/s43154-021-00072-3

[104] Convery DJ, Webb S. Generation of discrete beam-intensity modulation by dynamic multileaf collimation under minimum leaf separation constraints. Phys Med Biol. 1998;43(9):2521-2538. doi:10.1088/0031-9155/43/9/007

[105] Kallman P, Lind B, Eklof A, Brahme A. Shaping of arbitrary dose distributions by dynamic multileaf collimation. Phys Med Biol. 1988;33(11):1291-1300. doi:10.1088/0031-9155/33/11/007

[106] Yu CX. Intensity-modulated arc therapy with dynamic multileaf collimation: an alternative to tomotherapy. Phys Med Biol. 1995;40(9):1435-1449. doi:10.1088/0031-9155/40/9/004

[107] Dong P, Lee P, Ruan D, et al. 4œÄ noncoplanar stereotactic body radiation therapy for centrally located or larger lung tumors. Int J Radiat Oncol Biol Phys. 2013;86(3):407-413. doi:10.1016/j.ijrobp.2013.02.002

[108] Nguyen D, Rwigema JC, Yu VY, et al. Feasibility of extreme dose escalation for glioblastoma multiforme using 4œÄ radiotherapy. Radiat Oncol. 2014;9:239. Published 2014 Nov 7. doi:10.1186/s13014-014-0239-x.

[109] Rwigema JC, Nguyen D, Heron DE, et al. 4Π noncoplanar stereotactic body radiation therapy for head-and-neck cancer: potential to improve tumor control and late toxicity. Int J Radiat Oncol Biol Phys. 2015;91(2):401-409. doi:10.1016/j.ijrobp.2014.09.043

[110] Shepard DM, Earl MA, Li XA, Naqvi S, Yu C. Direct aperture optimization: a turnkey solution for step-and-shoot IMRT. Med Phys. 2002;29(6):1007-1018. doi:10.1118/1.1477415

[111] Otto K. Volumetric modulated arc therapy: IMRT in a single gantry arc. Med Phys. 2008;35(1):310-317. doi:10.1118/1.2818738

[112] Elith CA, Dempsey SE, Warren-Forward HM. Comparing four volumetric modulated arc therapy beam arrangements for the treatment of early-stage prostate cancer. J Med Radiat Sci. 2014;61(2):91-101. doi:10.1002/jmrs.52

[113] O'Connor D, Yu V, Nguyen D, Ruan D, Sheng K. Fraction-variant beam orientation optimization for non-coplanar IMRT. Phys Med Biol. 2018;63(4):045015. Published 2018 Feb 15. doi:10.1088/1361-6560/aaa94f.

[114] Gu W, O'Connor D, Ruan D, Zou W, Dong L, Sheng K. Fraction-variant beam orientation optimization for intensity-modulated proton therapy. Med Phys. 2020;47(9):3826-3834. doi:10.1002/mp.14340.

[115] Liang J, Atwood T, von Eyben R, et al. Trajectory Modulated Arc Therapy: A Fully Dynamic Delivery With Synchronized Couch and Gantry Motion Significantly Improves Dosimetric Indices Correlated With Poor Cosmesis in Accelerated Partial Breast Irradiation. Int J Radiat Oncol Biol Phys. 2015;92(5):1148-1156.

[116] Krayenbuehl J, Davis JB, Ciernik IF. Dynamic intensity-modulated non-coplanar arc radiotherapy (INCA) for head and neck cancer. Radiother Oncol. 2006;81(2):151-157. doi:10.1016/j.radonc.2006.09.004

[117] Smyth G, Bamber JC, Evans PM, Bedford JL. Trajectory optimization for dynamic couch rotation during volumetric modulated arc radiotherapy. Phys Med Biol. 2013;58(22):8163-8177. doi:10.1088/0031-9155/58/22/8163

[118] Smyth G, Evans PM, Bamber JC, et al. Non-coplanar trajectories to improve organ at risk sparing in volumetric modulated arc therapy for primary brain tumors. Radiother Oncol. 2016;121(1):124-131. doi:10.1016/j.radonc.2016.07.014

[119] Wild E, Bangert M, Nill S, Oelfke U. Noncoplanar VMAT for nasopharyngeal tumors: Plan quality versus treatment time. Med Phys. 2015;42(5):2157-2168. doi:10.1118/1.4914863.

[120] Popescu CC, Beckham WA, Patenaude VV, Olivotto IA, Vlachaki MT. Simultaneous couch and gantry dynamic arc rotation (CG-Darc) in the treatment of breast cancer with accelerated partial breast irradiation (APBI): a feasibility study. J Appl Clin Med Phys. 2013;14(1):4035. Published 2013 Jan 7. doi:10.1120/jacmp.v14i1.4035.

[121] Fix MK, Frei D, Volken W, et al. Part 1: Optimization and evaluation of dynamic trajectory radiotherapy [published online ahead of print, 2018 Jul 10]. Med Phys. 2018;10.1002/mp.13086. doi:10.1002/mp.13086.

[122] Mullins J, Renaud MA, Serban M, Seuntjens J. Simultaneous trajectory generation and volumetric modulated arc therapy optimization. Med Phys. 2020;47(7):3078-3090. doi:10.1002/mp.14155.

[123] Cassioli A, Unkelbach J. Aperture shape optimization for IMRT treatment planning. Phys Med Biol. 2013;58(2):301-318. doi:10.1088/0031-9155/58/2/301

[124] Peng F, Jia X, Gu X, Epelman MA, Romeijn HE, Jiang SB. A new column-generation-based algorithm for VMAT treatment plan optimization. Phys Med Biol. 2012;57(14):4569-4588. doi:10.1088/0031-9155/57/14/4569

[125] Mueller S, Guyer G, Volken W, et al. Efficiency enhancements of a Monte Carlo beamlet based treatment planning process: implementation and parameter study. Phys Med Biol. 2023;68(4):10.1088/1361-6560/acb480. Published 2023 Feb 13. doi:10.1088/1361-6560/acb480

[126] Telarovic I, Krayenbuehl J, Grgic I, et al. Probing spatiotemporal fractionation on the preclinical level. Phys Med Biol. 2020;65(22):22NT02. Published 2020 Nov 12. doi:10.1088/1361-6560/abbb75

[127] Uher K, Ehrbar S, Tanadini-Lang S, Dal Bello R. Reduction of patient specific quality assurance through plan complexity metrics for VMAT plans with an open-source TPS script [published online ahead of print, 2023 Mar 29]. Z Med Phys. 2023;S0939-3889(23)00011-9. doi:10.1016/j.zemedi.2023.02.003.

[128] Mueller S, Manser P, Volken W, et al. Part 2: Dynamic mixed beam radiotherapy (DYMBER): Photon dynamic trajectories combined with modulated electron beams [published online ahead of print, 2018 Jul 10]. Med Phys. 2018;10.1002/mp.13085. doi:10.1002/mp.13085.